

NISTIR 8415

**Material Research Support for the
Structural Performance of Nuclear
Power Plant Concrete Structures
Affected by Alkali-Silica Reaction**

Steven Feldman
Richard Eason
Peter Bajcsy
K.A. Snyder

This publication is available free of charge:
<https://doi.org/10.6028/NIST.IR.8415>

NIST
**National Institute of
Standards and Technology**
U.S. Department of Commerce

[BLANK]

NISTIR 8415

Material Research Support for the Structural Performance of Nuclear Power Plant Concrete Structures Affected by Alkali-Silica Reaction

Steven Feldman
Richard Eason
Engineering Laboratory

Peter Bajcsy
Information Technology Laboratory

K.A. Snyder
Engineering Laboratory

This publication is available free of charge:
<https://doi.org/10.6028/NIST.IR.8415>

May 2022



U.S. Department of Commerce
Gina M. Raimondo, Secretary

National Institute of Standards and Technology
Laurie E. Locascio, NIST Director and Under Secretary of Commerce for Standards and Technology

Certain commercial entities, equipment, products, or materials are identified in this document in order to describe a procedure or concept adequately. Such identification is not intended to imply recommendation or endorsement by the National Institute of Standards and Technology, nor is it intended to imply that the entities, products, materials, or equipment are necessarily the best available for the purpose.

**National Institute of Standards and Technology Interagency Report 8415
Natl. Inst. Stand. Technol. Interagency Rep 8415, 167 pages (May 2022)**

**This publication is available free of charge:
<http://doi.org/10.6028/NIST.IR.8415>**

PREFACE

This technical work was part of a comprehensive research program that was carried out by the Engineering Laboratory of the National Institute of Standards and Technology (NIST) on the structural performance of nuclear power plant concrete structures affected by alkali-silica reaction (ASR). The work was funded by the U.S. Nuclear Regulatory Commission (NRC) under Inter-agency agreement NRC-HQ-60-14-I-0004.

This publication is available free of charge: <https://doi.org/10.6028/NIST.JR.8415>

ABSTRACT

Alkali-silica reaction (ASR) can occur in concrete when aggregates within the concrete contain minerals that, when exposed to the high pH (> 9) pore solution, react to form a hygroscopic gel that can expand and create stresses sufficient to crack the concrete. If the damage becomes extensive enough, the concrete may not be able to perform its intended function. Although reliable tests exist for identifying the presence of the ASR reaction in concrete, there is little guidance for the assessment of the reaction regarding its effect on the structural properties, the degree of the reaction, and the extent to which the reaction will continue. The Engineering Laboratory at the National Institute of Standards and Technology undertook a research program, funded by the Nuclear Regulatory Commission, to develop measurement methods and tools for engineers to assess certain engineering properties (Tasks 1–3), and identify the extent and the anticipated progression of the reaction (Tasks 4 and 5). This Report summarizes the Task 4 and Task 5 materials research that used samples from an affected concrete to assess the degree of the alkali-silica reaction, and to estimate the extent to which the reaction will continue to progress. In addition, this Report summarizes the work done to develop the expansive mixture designs, which were used for both the structural and materials work.

At the core of the project was the design of three concrete mixtures having specific target values for the unconfined expansion (strain): 0.15 %, 0.30 %, and 0.50 %. An extensive mixture development effort was made to identify and procure materials, and then develop concrete mixtures that had the target expansions while meeting the placement and structural performance requirements for the following parameters: slump, 28-day compressive strength, and setting time. Although there are engineering guides for creating mixtures to meet specific target placement and structural performance requirements, there are no such guides for developing mixtures to meet specific target expansion values. Mixtures prepared with samples containing highly-reactive aggregates, including a New Mexico coarse aggregate (Placitas) and a Texas fine aggregate (Jobe sand) were the only materials known to meet the requirements. To ensure consistent performance for the more than 90 tons of aggregates required, quarry inspections were required, followed up by conformational testing upon receipt of the aggregate. Ultimately, sample mixtures were produced that achieved the target unconfined expansion in (75 mm x 75 mm x 280 mm) prisms within 200 days. In addition, a fourth control mixture was developed using a non-reactive aggregate for comparison purposes.

The mixture designs were used to make a number of samples for structural and materials testing. There were four large reinforced structural Blocks [115 cm (w) x 185 cm (h) x 500 cm (l)] that were instrumented and subsequently cored for structural and materials testing; these Blocks were cast using the four aforementioned mixtures for structural testing of cores (Task 1). There were expansive structural Beams (Task 2) made with the most expansive mixture (0.50 %). There were companion prisms and cylinders that were cast during the placement of the Blocks (four mixtures) and the Beams (one mixture). For the large Blocks and structural Beams, the companion prisms were used to monitor the corresponding unconfined expansion under similar environmental conditions (temperature and humidity).

The materials objectives were to identify a way for someone to assess an ASR affected concrete to estimate the degree of the reaction (where are we) and give some idea of how fast the reaction is advancing, along with some idea of how much further it will progress (where are we going, and how fast will we get there). The conceptual approach was to combine material property measurements of the concrete with petrographic examination of prisms and cores, and then correlate that information to the unconfined expansion. The general behavior of the ASR reaction is characterized by the time-dependent expansion, which has a consistent sigmoidal (logistic function) behavior, so knowing whether the reaction is in the first, middle, or last third of the reaction also discloses how fast the reaction is occurring. Although there may be disagreement regarding the direct relationship between the degree of the reaction and the extent of the expansion, from an engineering perspective a primary interest is knowing where the concrete exists on the expansion curve.

The material property measurements and the petrographic examinations were performed on a variety of samples. The material property measurements (mass change, ultrasonic pulse velocity, internal relative humidity, and electrical resistivity) were performed on the companion prisms and cylinders. These measurements were selected because there is a reason to believe that the relevant material properties correlate with the unconfined expansion. These measurements were performed over many months (and sometimes years) on samples made from all four mixture designs, and were performed on samples exposed to temperatures ranging from 25 °C to 50 °C. In addition, petrographic examinations and scanning electron microscopy were performed on cast prisms and on cores taken from the large Blocks.

The approach taken to estimate the ultimate degree of reaction was an existing residual expansion potential (REP) method. This method consists of extracting a core from a concrete, squaring the ends of the core and affixing measurement studs, and then monitoring expansion over a period of a few months. This approach had to rely on relatively limited data because extracting cores from the large Blocks was constrained by the requirements of the structural testing. Although the REP study by itself provided limited information, when combined with ultrasonic pulse velocity testing, the combined testing provided a qualitative measure of the degree of the expansion.

Petrographic examinations were used to characterize the aggregates used in the concrete mixtures and to develop a means of identifying and quantifying damage in ASR affected concrete. Optical microscopy was used to obtain the Damage Rating Index (DRI) on companion cast cylinders as a function of expansion. It was also used to identify ASR reaction products and resulting damage to the aggregate and paste, thus providing insight into the reaction mechanisms of the alkali-silica reaction in the concretes, specific to the materials used, and as a starting point for developing an alternate approach to estimating the extent of damage in a concrete. In this approach, a large (100 mm diameter) field of view is imaged by a scanning electron microscope (1300+ individual images stitched together) and used to train a convolutional neural net algorithm for identifying classes of damage that arose in these samples. The trained neural net was then used to evaluate subsequent Latin Hypercube sampling (77 images distributed across the sample) covering a similar (50 mm) spatial extent. An advantage to the approach that was developed was the significantly less effort needed to train the neural net. Unfortunately, the results are relatively specific to the particular aggregates and concrete proportions that were used.

Although a number of qualitative strategies were identified for characterizing the degree of the reaction and the rate of expansion, this project was not able to meet its objectives of finding relationships between material observations and quantitative estimations. Broadly, there were a number of factors contributing to this. The aggregate used in this study revealed the complexity that can arise when there are multiple mineral phases contributing to the ASR reaction. Even when there was evidence to suggest that the expansion rate scaled with temperature, the ultimate degree of reaction was different, suggesting a change in the nature of the reaction. There were also logistical challenges, such as the delay in exposing the large blocks to the elevated temperature and humidity, and in the limited ability to take cores from the large blocks. Finally, although material tests were conducted on the specimens, no consistently reliable method was found that related directly to either the rate of reaction/expansion or the expected future expansion.

Fortunately, the qualitative relationships found between certain material tests and the behavior of the reaction do show promise (summarized in Chapter 6), and they could be incorporated into existing monitoring and testing programs for a concrete structure that has exhibited evidence of an ASR reaction. Although these procedures, as described in this report, do not yield a quantitative result, when they are combined with engineering knowledge, they might be able to give experts a better understanding of the state of the reaction and the qualitative magnitude of any possible future expansion.

Keywords: alkali-silica reaction; cement hydration; concrete cracking; concrete petrography;

TABLE OF CONTENTS

Preface	v
Abstract.....	vi
List of Figures	xiii
List of Tables	xx
Acronyms and Abbreviations	xxii
Chapter 1 INTRODUCTION.....	1-1
1.1 Background	1-1
1.2 Scope.....	1-3
1.3 Report Outline.....	1-4
1.4 Measurement Practice and Duplicate Specimens.....	1-4
Chapter 2 MATERIAL SELECTION AND CONCRETE MIXTURE DESIGN.....	2-1
2.1 Material Selection	2-1
2.1.1 Initial characterization and evaluation of existing aggregate	2-1
2.1.2 Acquisition of additional reactive aggregate.....	2-5
2.1.3 Reactive aggregate mineralogy and texture	2-6
2.1.4 Isothermal Calorimetry	2-12
2.2 Concrete Mixture Design.....	2-13
2.2.1 Mixture Requirements	2-14
2.2.2 Development of Target Expansion Mixtures: Initial Screening	2-16
2.2.3 Final Target Mixture Designs.....	2-20
2.2.4 Quality Assurance for the Procurement of Bulk Reactive Aggregate.....	2-23
Chapter 3 TASK 1 and TASK 2 COMPANION EXPANSION MEASUREMENTS.....	3-1
3.1 Task 1 Expansion Measurements	3-1
3.1.1 Task 1 Companion Specimens	3-1
3.1.2 Task 1 Expansion Measurements	3-3
3.1.3 Prism Expansion Data	3-3
3.1.4 Cylinder Expansion Data.....	3-6

3.1.5	Summary Comparison	3-9
3.1.6	Deviations of Observed Expansion from Original Mix Design	3-11
3.1.7	Cube Expansion Data.....	3-12
3.2	Task 2 Expansion Measurements	3-16
3.2.1	Companion Specimens	3-16
3.2.2	3x3 Prism Expansion Data	3-16
Chapter 4	MATERIAL MEASUREMENTS	4-1
4.1	Degree of Reaction.....	4-1
4.2	Testing Plan	4-2
4.2.1	Task 1 Companion Specimens	4-3
4.2.2	Task 1 Temperature Exposure.....	4-4
4.2.3	Independent Temperature Studies	4-5
4.3	Material Property Measurements.....	4-5
4.4	Prism – Expansion vs. Temperature	4-5
4.4.1	Constant Temperature	4-5
4.4.2	Temperature Dependent Rate of Expansion	4-9
4.4.3	Variable Temperature Exposure.....	4-11
4.5	Prism – Relative Humidity	4-13
4.6	Prism - Mass Change	4-15
4.6.1	Temperature Dependence – Mass Change	4-19
4.7	Prism - Electrical Resistivity.....	4-20
4.7.1	Temperature Dependence – Resistivity	4-26
4.8	Prism - Ultrasonic Pulse Velocity.....	4-26
4.8.1	Measurements on Prisms.....	4-27
4.8.2	Temperature Dependence - UPV	4-31
4.8.3	Measurements on Cores	4-32
4.8.4	Diagnostic Tool – Pulse Velocity.....	4-34
4.9	Cast Cylinder - Damage Rating Index (DRI).....	4-34
4.9.1	Damage Rating Index Measurement Method	4-34
4.9.2	DRI Results.....	4-35
4.10	Block Core - Residual Expansion Potential (REP).....	4-38
4.10.1	REP Testing at 1 Year	4-39
4.10.2	REP Testing at 2 Years	4-43

4.10.3	Diagnostic Tool	4-44
Chapter 5	PETROGRAPHY	5-1
5.1	Petrography Sample Preparation	5-1
5.2	Sampling Plan	5-3
5.3	Observed Damage Mechanisms	5-6
5.3.1	Unique Damage Class	5-7
5.4	Relating Expansion to Degree of Reaction	5-10
5.5	Image Sampling Protocol.....	5-12
5.6	Automated Sampling.....	5-14
5.7	Convolutional Neural Net.....	5-14
5.7.1	Related Work.....	5-16
5.7.2	Methods	5-17
5.7.3	Results	5-24
5.7.4	Evaluate AI-Based Semantic Image Segmentation Models	5-30
5.7.5	CNN Weak Annotations and Accuracy Metrics	5-30
5.7.6	Discussion.....	5-33
Chapter 6	FINDINGS AND RECOMMENDATIONS.....	6-1
6.1	Concrete Mixture Designs	6-1
6.2	Expansion Measurement Statistics	6-1
6.3	Temperature Dependence	6-2
6.4	DEgree of the REaction.....	6-3
6.4.1	Damage Rating Index.....	6-3
6.4.2	Automated Neural Net	6-4
6.4.3	Ultrasonic Pulse Velocity	6-4
6.4.4	Residual Expansion Potential	6-5
6.5	Rate of Expansion	6-5
6.6	Ultimate Expansion	6-6
6.7	Recommended Testing.....	6-6
Chapter 7	REFERENCES.....	7-1
Appendix A	MARYLAND STATE HIGHWAY ADMINISTRATION AGGREGATE BULLETIN (2014).....	A-1
Appendix B	CEMENT MILL SHEET	B-1

LIST OF FIGURES

Figure 1-1. Schematic representation of alkali-silica reaction and cracking in concrete (from Deschenes et al. 2009). Hydroxyl and alkali species react with the reactive aggregate phases to form a gel that absorbs water, expands, and can ultimately generate sufficient stress to crack both the aggregates and the surrounding paste.	1-2
Figure 2-1. Comparison of ASTM C1260 measurements for (a) 14-day mortar bar (AMBT) expansion for the aggregates, and (b) expansion of the Luck #78 and #57 aggregates at 60 °C and 80 °C, and Chaney #67 aggregate at 60 °C in miniature (50 mm) concrete prisms. Results in (a) and (b) represent mean of triplicate and duplicate measurements, respectively, for qualitative comparison purposes.....	2-5
Figure 2-2. Placitas coarse aggregate components. Blond, red, and gray aggregate are volcanic components; clear are orthoquartzites.	2-6
Figure 2-3. (a) Estimated mass fractions of major cations of the Placitas bulk material and aggregate separates (individual XRF results from duplicate or triplicate samples, as indicated) and (b) chemical classification based on total alkali silica (TAS) content.	2-7
Figure 2-4. Phase composition of the Placitas bulk and aggregate components determined by XRD/Rietveld with internal standard.	2-8
Figure 2-5. Thin-section petrographic images under cross-polarization showing textural characteristics of the unaltered Placitas volcanic and quartzite rock types and components, grouped by classifications in Figure 2-4.....	2-10
Figure 2-6. Radial, fibrous/acicular crystal bodies as chalcedony (a) and spherulites (b,c) are some of the most highly reactive materials found in the Placitas felsic components....	2-11
Figure 2-7. Highly reactive spherulites in coarse Placitas aggregate SEM image (left) showing radial growth of fibers with EDS (x-ray) mapping of elemental composition (right).	2-12
Figure 2-8. Heat flow curves characterizing the reactivity of the 150 µm to 300 µm fraction of each of the Placitas aggregate components.....	2-13
Figure 2-9. Pail mixer used to develop concrete mixtures.....	2-13
Figure 2-11. A test block instrumented with an exterior and two internal thermocouples (left), and the recorded maximum internal temperatures and internal-external temperature differential were within target specifications for a concrete mixture having 350 kg/m ³ (right).	2-16
Figure 2-12. MCPT expansion in identical concrete mixtures batched with the Placitas coarse aggregate shows strong initial acceleration of expansion at high temperatures (a). ASR reaction is almost fully suppressed at 80 °C in a water soak solution due to alkali leaching, but proceeds normally at 40 °C (b). Light blue symbols were used to fit a line, merely to show the general trend. Results represent mean of 2 replicates; see discussion of uncertainty in text.	2-17

Figure 2-13. Comparison of mass change in specimens exposed to high temperature alkali soak solution (a), and a high temperature water soak solution (b); individual measurements are shown.2-18

Figure 2-15. Addition of the Jobe sand with the Placitas coarse aggregate substantially boosted expansion compared to Placitas aggregate alone. Use of a HRWR had an unintended benefit of boosting expansion after ≈ 25 days (circled).2-19

Figure 2-16. Overview of prism expansion measurements used to develop initial mixture designs for the large block specimens through 1 year or longer. Performance of preliminary Mixes 1 to 3 are shown.2-20

Figure 2-17. Revised prism expansion data for target Mixes 1 to 3, with the error bars representing one standard deviation from duplicate specimens.2-21

Figure 2-18. Quality assurance for the procurement of ≈ 96 tons of reactive aggregate was conducted, in part, by reconnaissance field visit to the quarry in Bernalillo, NM.2-23

Figure 2-19. ASTM C1260 14-day accelerated mortar bar expansion of the Placitas coarse aggregate from the 2016 bulk purchase was 23 % greater than the 2015 samples previously tested at NIST. Expansion values for the Jobe fine aggregate were comparable between the 2015 and the 2016 samples. Mineral heterogeneity among fluvial coarse aggregates processed (mined) at different times are the likely cause of the range of expansion values for the Placitas.2-24

Figure 3-1. Layout of prism molds and tools in preparation for the Task 1 casting.3-2

Figure 3-2. Sealed buckets modified for improved ASR expansion measurements have concrete prisms suspended over 1.8 L of deionized water with wicking blotter paper immersed in the water to provide a >95 % RH environment along the entire length of the prism columns. One prism is shown illustrating the plastic sleeve cast-in-place sleeve for internal RH measurement, and post-exposure sectioned specimens embedded in epoxy in preparation for SEM analysis.3-2

Figure 3-3. Setup for measuring prism expansion, with Invar reference bar.3-3

Figure 3-4. Linear expansion in 3x3 prisms cast from concretes for Task 1, Mixes 1 to 4. Results represent the mean and standard deviation from four replicates under 95+% RH, initially at 25 °C until day 280, and then exposed to 38 °C.3-4

Figure 3-5. Mean expansion of (12) 3x3 prisms held at 25 °C for the first 280 days for each of the Mixes 1 to 3; error bars represent the standard deviation of the mean.3-5

Figure 3-6. Expansion data for 4x4 prisms made with Task 1 Mixes 1-4, initially maintained at 25 °C and then moved to 38 °C after 280 days. Error bars represent the standard deviation of the mean from 2 replicates.3-6

Figure 3-7. Geometry of expansion measurements conducted on cast 4x8 cylinders from the Task 1 Mixes 1 to 4.3-7

Figure 3-8. Cylinder expansion data from Trial 1 Mixes 1 to 3. Indicated orientation is shown in Figure 3-7 above. The mean of three replicates is plotted, and the error bars indicate the sample standard deviation.3-8

Figure 3-9. Combined 3x3 and 4x4 prism, and 4x8 cylinder expansion data for each mix, following the temperature exposure of the large Blocks.3-10

Figure 3-10. Comparison of expansion in the prisms having exposure matching the large Blocks (left) to the laboratory supplemental batching with exposure to 38 °C immediately after demolding (right).....3-11

Figure 3-11. (a,b) The presence of minor alkali feldspars (Fd) and complex volcanic materials in the fine aggregate fraction of a representative Mix 1 prism (25 °C, 270 day) indicates that some reactive Jobe sand may have inadvertently been mixed in with Mix 1 materials during the batching of block specimen ASR 1.3-12

Figure 3-12. Coordinates used for 12-in block expansion measurements.3-13

Figure 3-13. 12-inch cubes from Task 1: (a) Mix 1; (b) Mix 2; and (c) Mix 3.3-14

Figure 3-14. Mix 1 individual expansion measurements from 12-in cubes.....3-14

Figure 3-15. Mix 2 individual expansion measurements from 12-in cubes.3-15

Figure 3-16. Mix 3 individual expansion measurements from 12-in cubes. Dotted lines in X-X' and the Z-Y' plots are averages Series 2 and Series 3.....3-15

Figure 3-17. Task 2 prism expansion measurements (mean and standard deviation of 4 replicates) for samples maintained at 38 °C and 95 % RH, and comparison with the mean Task 1 prism data for Mix 3 equilibrated initially at 25 °C and then moved to 38 °C after 280 days. Also shown are the average of two replicate prisms made with the Task 2 control mixture.3-17

Figure 4-1. The degree of expansion ξ as a function of time t , as characterized by Eq. 4-1 (from Larive, 1998). The latency time τ_L coincides with the inflection point, and the characteristic time τ_C has the geometrical relationship shown.....4-2

Figure 4-2. The sealed buckets modified for improved ASR expansion measurements have concrete prisms suspended over 1.8 L of deionized water and are lined with wicking blotter paper to provide a >95 % RH environment along the entire length of the prism columns.4-4

Figure 4-3. Expansion in 3x3 prisms made with Mix 1 and maintained at a constant temperature throughout. Symbols of the same color indicate the same series of testing.....4-6

Figure 4-4. Expansion in 3x3 prisms made with Mix 2 and maintained at a constant temperature throughout. Symbols of the same color indicate the same series of testing.....4-7

Figure 4-5. Expansion in 3x3 prisms made with Mix 3 and maintained at a constant temperature throughout. Symbols of the same color indicate the same series of testing.....4-8

Figure 4-6. Scaled data for Mix 1, where the 25 °C data are plotted as shown in Figure 4-3, the 38 °C prism ages were multiplied by 3, and the 55 °C prism ages were multiplied by 8..4-9

Figure 4-7. Scaled data for Mix 2, where the 25 °C data are plotted as shown in Figure 4-4, the 38 °C prism ages were multiplied by 5, and the 55 °C prism ages were multiplied by 22..4-10

Figure 4-8. Scaled data for Mix 3, where the 25 °C data are plotted as shown in Figure 4-5, the 38 °C prism ages were multiplied by 6, and the 55 °C prism ages were multiplied by 16..4-10

Figure 4-9. Effect of temperature change on Task 1 Mix 1 expansion in 3x3 prisms. Data for the first 280+ days are the mean of all 12 prisms held at 25 °C.4-11

Figure 4-10. Effect of temperature change on Task 1 Mix 2 expansion in 3x3 prisms. Data for the first 280+ days are the mean of all 12 prisms held at 25 oC.4-12

Figure 4-11. Effect of temperature change on Task 1 Mix 3 expansion in 3x3 prisms. Data for the first 280+ days are the mean of all 12 prisms held at 25 °C.4-12

Figure 4-12. Details of (left) the RH probe insertion tube to be cast in a prism, (middle) the RH measurement apparatus attached to a sealed specimen, and (right) the measurement arrangement for prisms stored in lidded pails.....4-14

Figure 4-13. Relative humidity (RH) calibration data from standard saturated solutions of 25 °C NaCl (75.4 %), KCl (84.7 %), and K₂SO₄ (97.4 %).4-14

Figure 4-14. Relative humidity (RH) measurements on Mixes 1 to 4 throughout the first 500 days.....4-15

Figure 4-15. Mix 4 (control) percent mass change in 3x3 prisms at 25 °C, 38 °C, and 55 °C, and corresponding values for 4x4 prisms at 38 °C. Average values shown, with error bars indicating the sample standard deviation.4-16

Figure 4-16. Percent mass change in 3x3 prisms from Task 1, maintained at 25 °C. Mean from four replicates show, along with the standard deviation of the mean.....4-17

Figure 4-17. Percent mass change in 3x3 prisms from Mixes 1 to 3, maintained at 38 °C. Mean from four replicates shown, and error bars indicate range of data from two replicates. ..4-18

Figure 4-18. Mix 1 percent mass change in 3x3 prisms at 25 °C, 38 °C, and 55 °C (Task 1 Temperature Exposure); also shown for 4x4 prisms at 38 °C. Average values shown, with error bars indicating the sample standard deviation.4-18

Figure 4-19. Mix 2 percent mass change in 3x3 prisms at 25 °C, 38 °C, and 55 °C (Task 1 Temperature Exposure); also shown for 4x4 prisms at 38 °C. Average values shown, with error bars indicating the sample standard deviation.4-19

Figure 4-20. Mix 3 percent mass change in 3x3 prisms at 25 °C, 38 °C, and 55 °C (Task 1 Temperature Exposure); also shown for 4x4 prisms at 38 °C. Average values shown, with error bars indicating the sample standard deviation.4-19

Figure 4-21. Mix 3 percent mass change in 3x3 prisms at 25 °C, 38 °C, and 55 °C, initiated immediately after demolding. Average values shown, with error bars indicating the sample standard deviation.4-20

Figure 4-22. Schematic representation of how a concrete surface resistivity device operates....4-21

Figure 4-23. Mix 4 (control) electrical resistivity in 3x3 prisms at 25 °C, 38 °C, and 55 °C; also shown for 4x4 prisms at 38 °C. Average values shown, with error bars indicating the sample standard deviation.4-22

Figure 4-24. Electrical resistivity of 3x3 prisms from Task 1, maintained at 25 °C. Symbols show the mean from four replicates, along with the standard deviation of the mean.4-23

Figure 4-25. Mix 1 electrical resistivity in 3x3 prisms at 25 °C, 38 °C, and 55 °C; also shown for 4x4 prisms at 38 °C. Average values shown, with error bars indicating the sample standard deviation.....4-24

Figure 4-26. Mix 2 electrical resistivity in 3x3 prisms at 25 °C, 38 °C, and 55 °C; also shown for 4x4 prisms at 38 °C. Average values shown, with error bars indicating the sample standard deviation.....4-24

Figure 4-27. Mix 3 electrical resistivity in 3x3 prisms at 25 °C, 38 °C, and 55 °C; also shown for 4x4 prisms at 38 °C. Average values shown, with error bars indicating the sample standard deviation.....4-25

Figure 4-28. Mix 3 electrical resistivity in 3x3 triplicate prisms at 25 °C, 38 °C, and 55 °C, along with the 4 prisms from Task 2. Average values shown, with error bars indicating the sample standard deviation.4-26

Figure 4-29. Image of UK1401 ultrasonic tester used to measure pulse velocity in prisms and cores.4-27

Figure 4-30. Mix 4 (control) ultrasonic pulse velocity in 3x3 prisms at 25 °C, 38 °C, and 55 °C; also shown for 4x4 prisms at 38 °C. Average values shown, with error bars indicating the sample standard deviation.4-28

Figure 4-31. Ultrasonic Pulse Velocity (UPV) of 3x3 prisms from Task 1, maintained at 25 °C. Symbols show the mean from 12 replicates prior to 280+ days and from four replicates thereafter, along with the standard deviation of the mean.....4-29

Figure 4-32. Mix 1 ultrasonic Pulse Velocity in 3x3 prisms at 25 °C, 38 °C, and 55 °C; also shown for 4x4 prisms at 38 °C. Average values shown, with error bars indicating the sample standard deviation.....4-30

Figure 4-33. Mix 2 ultrasonic Pulse Velocity in 3x3 prisms at 25 °C, 38 °C, and 55 °C; also shown for 4x4 prisms at 38 °C. Average values shown, with error bars indicating the sample standard deviation.....4-30

Figure 4-34. Mix 3 ultrasonic pulse velocity in 3x3 prisms at 25 °C, 38 °C, and 55 °C; also shown for 4x4 prisms at 38 °C. Average values shown, with error bars indicating the sample standard deviation.....4-31

Figure 4-35. Temperature dependence of 3x3 prism ultrasonic pulse velocity for Mix 3, a) at early times and b) at longer times.4-32

Figure 4-36. Ultrasonic pulse velocity of two replicate cores taken from the unconfined region of the Task 1 large Blocks. The first measurement shown was taken immediately after coring, and the error bars represent the standard deviation of four measurements (replicate measurements on two cores).....4-33

Figure 4-37. Ultrasonic pulse velocity of two replicate cores taken from the unconfined region of the Task 1 large Block for Mix 3. The first measurement shown was taken immediately after coring, and the error bars represent the standard deviation of four measurements (replicate measurements on two cores).....4-34

Figure 4-38. Raw Damage Rating Index for cast cylinders from Task 1. The nomenclature is (age/mix/temperature), and the color-coded damage class abbreviations are explained in Table 4-2. The coefficient of variation ranged between 4 % and 8 %.4-36

Figure 4-39. Comparison of corrected Damage Rating Index (red circles) to expansion data from 3x3 (blue) and 4x4 (red) prisms, and 4x8 cylinders (green). The DRI standard deviations are approximately equal the size of the symbol.....4-37

Figure 4-40. Gauge stud arrangement for the 10 cm diameter cores used to study Residual Expansion Potential at 1 year.4-39

Figure 4-41. Coring plan for 2018 residual expansion testing.....4-40

Figure 4-42. Linear and diametral expansion (left column), and mass change and pulse velocity data (right column), for the duplicate cores taken at 1 year from each of the three Task 1

Blocks (by row). Symbols indicate the average value, and the error bars indicated the sample standard deviation.	4-42
Figure 4-43. Gauge stud arrangement for the 10 cm diameter cores used to study Residual Expansion Potential at 2 years.....	4-43
Figure 4-44. Linear and diametral expansion (left), and mass change and pulse velocity (right), data for the duplicate cores taken at 2 years from the Task 1 Mix 3 Block. Symbols indicate the average value, and the error bars indicated the sample standard deviation. 4-44	
Figure 5-1. Equipment for impregnation and polishing of both Task 1 Block core specimens and companion prism sections (a,b, and c) in preparation for measurements by SEM-EDS. Sectioned 4x8 cylinders (b) are also polished here in preparation for DRI analysis.	5-2
Figure 5-2. Sampling and sectioning scheme for 3x3 prisms cast with the Task 1 Blocks made with Mixes 1 to 4.	5-3
Figure 5-3. Coring plan for the Mix 1 Block.....	5-4
Figure 5-4. Coring plan for Mix 2 Block.	5-5
Figure 5-5. Coring plan for Mix 3 Block.	5-6
Figure 5-6. Massive aggregate dissolution in both quartzite (Qz) and alkali feldspar (Fd) in a Mix 3 prism section after 270 days. Approximate original (unaltered) grain boundary for one aggregate particle is highlighted in yellow.	5-7
Figure 5-7. Multiple generations ('cycles') of ASR gel flowing into cement paste. Also shown are (a) dissolution pitting and (b) remobilization of emplaced silica from ASR gel and (c,d) increase in void space after dissolution.....	5-8
Figure 5-8. Reactive aggregate damage in orthoquartzites and feldspars is typically initiated as <i>external</i> 'chattering' which progresses to dissolution with appreciable mass loss over time (a-c). Damage in the highly-reactive volcanics is dominated by massive <i>internal</i> cracking and dissolution with substantial gel formation (d-f). A network of residual fine feldspar laths remaining after dissolution of noncrystalline volcanic glass is shown in (e).	5-9
Figure 5-9. Conceptual relationship between expansion curve and damage observed in the sample.	5-11
Figure 5-10. (a) 'Stitched' mosaic of 1360 SEM images mapped across the central 50 mm portion of a 70 mm diameter core specimen: Mix 3, Region 2, 180 d. (b) Single SEM image taken at 200 times magnification with a field of view of (1.1 mm x 1.4 mm); a pixel resolution of 1.47 μm	5-13
Figure 5-11. (Fig 2) Depiction of Latin Hypercube sampling over selected FOVs across the surface of a circular cross section (approximately 54 mm in diameter).....	5-13
Figure 5-12. An overview of the microscopic damage quantification, including field of view (FOV) sampling, FOV segmentation, and quantification of all segmented FOVs to generate statistics about damage sub-classes.....	5-15
Figure 5-13. An overview of two methods for creating training data sets.....	5-18
Figure 5-14. An overview of CNN-based segmentation modeling and evaluation using two training datasets.	5-19
Figure 5-15. Visual description of damage sub-classes (right column) based on SEM image intensities and shape characteristics of very dark intensity pixels (left columns).....	5-20

Figure 5-16. Visual description of contextual sub-classes based on SEM intensity and shape characteristics for gray (left) and very bright (right) image intensities and shape characteristics.5-21

Figure 5-17. Web-based visual validation system. Left – selection of a sample at the top and selection of quality score (good, correct, bad colors, bad pixels). Right – the updates of quality scores as experts inspect images.5-23

Figure 5-18. The set of 12 FOVs that were manually annotated and used for optimizing algorithmic parameters. Left – raw FOVs. Right – annotated FOVs. Bottom – color legend.5-25

Figure 5-19. Illustration of intermediate images during the sequence of steps in a damage-assisted segmentation.5-25

Figure 5-20. Illustration of intermediate images during the sequence of steps in a context-assisted segmentation.5-25

Figure 5-21. The distribution of samples in 12 manually annotated FOVs across contextual classes (left) and damage sub-classes (right).....5-27

Figure 5-22. A pipeline for computing and isolating the damage mask from background. DSC: Dice Similarity Coefficient; TP: True Positive; FP: False Positive; FN: False Negative.5-28

Figure 5-23. A pipeline for computing aggregate mask that corresponds to feldspar, quartzite, iron oxide, augite, and volcanic without dissolution.5-29

Figure 5-24. Classification of spatial annotation types.5-31

Figure 5-25. Visual inspection and validation of segmentation results obtained from the U-Net models trained on damage-assisted and context-assisted training datasets.5-33

LIST OF TABLES

Table 2-1. Aggregates initially screened for reactivity and published ASR expansion data.	2-3
Table 2-2. Particle size distribution (as % passing designated sieve size: 1" = 25.4 mm) and physical parameters of the principal coarse aggregates used in the study, as determined by ASTM C136 (interlaboratory 1s precision $\leq 3\%$ for all % retained).	2-4
Table 2-3. Particle size distribution, saturated surface dry (SSD) specific gravity (Sp. Gr.), water absorption, and fineness modulus (F.M.) of the Jobe reactive sand, as determined by ASTM C136 (interlaboratory 1s precision $\leq 3\%$ for all % retained).	2-4
Table 2-4. Mass fraction of minerals identified in the Placitas aggregate components (coarse aggregate - CA) and the bulk Jobe (fine aggregate - FA)	2-9
Table 2-5. Target mixture requirements for the large block structures.....	2-14
Table 2-6. Cement specifications for reactive Mixes 1 to 3. Uncertainties represent the estimated standard deviation. LOI: loss on ignition. Blaine Fineness refers to ASTM C 204.....	2-15
Table 2-7. Final mixture proportions for the target expansion mixtures (Mixes 1 to 3) and the control mixture (Mix 4).....	2-22
Table 4-1. Materials measurement plan for the cast specimens and the cores taken from the Blocks, for each of the Mixes 1 to 3. The number of replicate specimens (reps) is show in parentheses.	4-3
Table 4-2. Damage Rating Index (DRI) damage classes, their abbreviation, and the corresponding weighting factors (following Sanchez et al., 2013).	4-35
Table 4-3. Reported relationship between DRI, expansion, and loss in compressive strength – from Sanchez et al. (2018).	4-38
Table 4-4. Coring and initial measurement timetable for the residual expansion potential measurements on the Task 1 Blocks at 1 year.....	4-41
Table 4-5. Coring and initial measurement timetable for the residual expansion potential measurements on the Task 1 Mix 3 Block at 2 years.....	4-43
Table 5-1. Summary of acquired SEM images.....	5-16
Table 5-2. Objectives in all steps of AI-based semantic segmentation approach.	5-17
Table 5-3. A set of rules to determine damage sub-classes from contextual labels.	5-22
Table 5-4. Evaluations of two semi-automated methods, damage-assisted and context-assisted, for creating high-quality and large quantity of reference semantic segmentations under constraints described in Table 5-2. All methods start with a collection of 1360 FOVs and generate the number of annotated FOVs shown in the left column.....	5-27
Table 5-5. Definitions of the entries in Eq. 5-5 via the counts n_{ij} of the predicted labels Y_j (Est) at pixels with known reference labels X_i (Ground Truth (GT)) in multi-label segmentation.....	5-32

Table 5-6. Summary of test metrics (error, accuracy, and confusion matrix) for two training datasets and U-Net model. BKG: background; PD – paste damage; AD – aggregate damage; and AV – air voids.5-34

Table 6-1. Relative expansion rates for each Mix, relative to 25 °C. Values are taken from Figure 4-6 through Figure 4-8.6-3

Table 6-2. A qualitative characterization of the degree of the expansion based on combined UPV and REP measurements from a concrete core.....6-5

ACRONYMS AND ABBREVIATIONS

Acronyms:

AAR	Alkali-Aggregate Reaction
AMBT	Accelerated Mortar Bar Test
ACI	American Concrete Institute
ASR	Alkali-Silica Reaction
ASTM	ASTM International
CA	Coarse Aggregate
DRI	Damage Rating Index
DRUW	Dry Rodded Unit Weight
FA	Fine Aggregate
HRWR	High-Range Water Reducer
MCPT	Miniature Concrete Prism Test
NIST	National Institute of Standards and Technology
NRC	Nuclear Regulatory Commission
REP	Residual Expansion Potential
SEM	Scanning Electron Microscopy
SSD	Saturated Surface Dry

Abbreviations:

d	day
in	inches
psi	pounds per square inch

Chapter 1

INTRODUCTION

1.1 BACKGROUND

Alkali-silica reaction (ASR) was identified decades ago (e.g., Stanton, 1940) as a concrete deterioration mechanism whereby dissolved alkali hydroxide in the cement paste phase react with certain amorphous, poorly-ordered, or micro-crystalline siliceous phases in the aggregate to produce an expansive gel. The expansion caused by the gel ultimately leads to cracking and potential loss of strength of concrete (Hansen, 1944; Taylor, 1990). The gel forms initially in the aggregate as a low viscosity, high-alkali “sol”, and ultimately flows out of the aggregate, into the paste, whereby it picks up calcium via ion exchange (Rajabipour et al., 2015). Because the resulting gel is hygroscopic (i.e., it binds water to molecules), water is a key ingredient to the reaction and subsequent damage by cracking. Generally, the reaction rate is relatively slow, so the onset of cracking can occur years or decades after construction, depending on the reactivity of the mineral phases and the alkalinity of the pore solution.

This cracking may occur internally within the structural element, where water is more abundant, and it may take additional decades for a structure to begin showing external signs of distress from the reaction. From a safety perspective, an important consideration is the remaining capacity of a structure exhibiting distress due to ASR. For affected safety-related concrete structures that may operate for extended periods, a monitoring strategy is needed that can predict the future evolution of ASR may be needed to assure safe operation without significant increase in risk to public safety.

The conceptual model for ASR (see Figure 1-1) includes a series of sequential chemical reactions, and the consequent damage as shown schematically Figure 1-1, which is taken from Deschenes et al. (2009). Inside the concrete are aggregates containing reactive silica phases such as strained or cataclastic quartz, chert, opal, volcanic glass, and other silica materials that are high in silanol ($\equiv\text{Si-OH}$) groups.

The ASR process involves:

- 1) dissolution of these metastable forms of silica in reactive aggregate resulting from the highly alkaline pore solution environment created by the presence of soluble alkali species (e.g., K^+ and Na^+),
- 2) mobilization of alkali-stabilized dissolved silica species from the aggregate to the cement paste,
- 3) flocculation and formation of a colloidal silica gel by Ca^{2+} uptake from the cement paste, and
- 4) hygroscopic swelling of the ASR gel, generating expansive pressure and strain.

As the gel absorbs water (Step 4), it expands, generating tensile stresses that can be in excess of 10 MPa (nominally 1500 psi) (Rigden et al., 1995; Ferraris et al., 1997). These stresses are sufficient to generate cracking, both in the aggregate and in the surrounding hardened cement paste, and to cause macroscopic expansion of the structure.

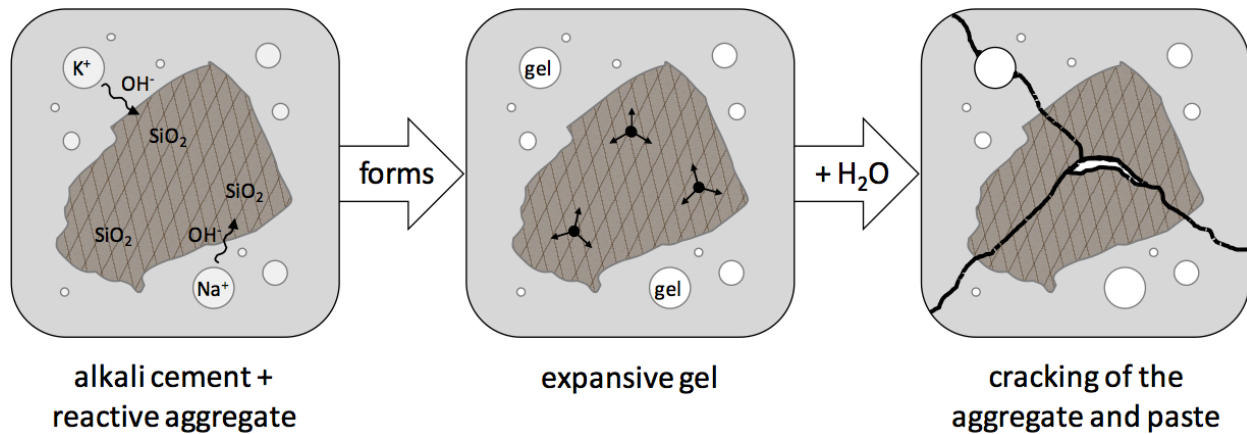


Figure 1-1. Schematic representation of alkali-silica reaction and cracking in concrete (from Deschenes et al. 2009). Hydroxyl and alkali species react with the reactive aggregate phases to form a gel that absorbs water, expands, and can ultimately generate sufficient stress to crack both the aggregates and the surrounding paste.

Within the alkaline pore solution, the concentration of the hydroxyl (OH^-) species are nearly equal to the combined concentration of the potassium (K^+) and sodium (Na^+) species. The reaction mechanisms of ASR are complex, and supply the pore solution with silica species that diffuse through the pore system and react with OH^- , Na^+ and K^+ to form a gel; this is the through-solution mechanism of gel production (Dron and Brivot, 1992, 1993). The gel incorporates water, either through absorption (Dent Glasser and Kataoka 1981) or through osmotic pressure (Diamond et al., 1981). A broader review of research on the ASR mechanism was performed by Helmuth et al. (1993). Although an understanding of the alkali-silica reaction helps to inform test method development, an exhaustive review of the fundamental studies of the reaction is not presented here.

One of the remaining technical challenges is predicting the reaction kinetics from information about the aggregate mineralogy, the pore solution composition, the temperature and moisture conditions, and the structure's geometry and location (environment). Part of the challenge is identifying and quantifying the rate-controlling processes. These may include the diffusion of pore solution through the aggregate and the dissolution rate at the reactive mineral phase surface. Depending on the mineral composition, the morphology of the aggregate, and the exposure conditions, ASR may not become evident until decades after construction.

The technical work presented in this report is part of a comprehensive research program carried out by the Engineering Laboratory of the National Institute of Standards and Technology (NIST) on the structural performance of nuclear power plant concrete structures affected by ASR. The research plan was based on a scoping study of ASR effects on concrete by the NIST (Snyder and Lew, 2013). The scoping study identified knowledge gaps in evaluating the present capacity of concrete structures affected by ASR, and predicting the future loss of structural capacity.

These gaps were identified through a comprehensive search of technical literature, including journal articles, standards, and codes related to ASR. Based on the identified gaps, a technical plan was proposed for closing these gaps.

The objective of the research plan was to develop a technical basis for generic regulatory guidance to evaluate Alkali Silica Reaction (ASR)-affected nuclear power plant (NPP) concrete structures throughout their service life with regard to the following: (1) significance and effects on structural performance and capability to perform intended function under design basis static and dynamic loads and load combinations, and (2) characteristics of an aging management program to adequately monitor and manage effects of ASR degradation such that intended functions are maintained through the period of extended operation of renewed licenses. The intended outcome is a methodology to determine, for an existing ASR-affected structure, its (1) in-situ structural capacity to resist design-basis static and dynamic loads, and (2) future structural capacity.

It should be noted that methodologies developed within the framework of this research program are generally applicable for evaluating the state of the ASR reaction in existing concrete structures. However, none of the data are intended for direct comparison to any specific structure due to differences in (1) the accelerated rate of ASR in the test environment, (2) use of mixes having both reactive fine and coarse aggregate to achieve specific target expansion, (3) levels of concrete confinement provided by steel reinforcing bars, and (4) other age-related degradations of concrete material properties experienced by a real structure under in-service, operating conditions.

1.2 SCOPE

The overall research program comprised five tasks. The first three tasks (Tasks 1, 2, and 3) sought to quantify the effects of ASR on the engineering properties of reinforced concrete structures, as they relate to the static and dynamic performance of structure. The other two tasks (Tasks 4 and 5) sought to identify and evaluate methods for determining the state and rate of the ASR reaction.

This report details Task 4 and Task 5 of the research program: *Assessing In-Situ Mechanical Properties of ASR-Affected Concrete*. These Tasks had the following objectives:

- Develop mixture designs for Tasks 1, 2 and 3 that would achieve desired levels of unconfined expansion while meeting specific placement (plastic state) and mechanical (hardened state) properties
- Use the smaller companion specimens to record their unconfined expansion for the purpose of informing the Task 1 and Task 2 sampling and testing schedules
- Identify relationships between material or petrographic measurements and the degree and the rate of the ASR reaction
- Identify relationships between material or petrographic measurements and the remaining potential for further expansion

1.3 REPORT OUTLINE

This Chapter describes the experimental program used to meet the objectives above for Task 4 and Task 5.

Chapter 2 presents the materials selection and qualification process for arriving at concrete mixture designs having specific unconfined expansion after 18 months of curing.

Chapter 3 presents the unconfined expansion data that was performed in support of Task 1 and Task 2.

Chapter 4 presents the material measurements (electrical resistivity, ultrasonic pulse velocity, relative humidity, mass change, Damage Rating Index, and Residual Expansion Potential) made on the companion prisms and cored cylinders.

Chapter 5 presents the petrographic analysis of the specific nature of the ASR reaction in the materials used, and the neural network scheme developed to estimate the total ASR damage in a specimen.

Chapter 6 summarizes the results.

1.4 MEASUREMENT PRACTICE AND DUPLICATE SPECIMENS

This project required taking measurements of many specimens, maintained in controlled environmental conditions, over long periods of time. In most cases, there were resources available to maintain at least three replicate specimens for each mixture and environmental condition considered. In a few cases, however, either there was insufficient material, insufficient storage space, or a specimen failed during exposure, resulting in only two replicate specimens. In these early tests, sometimes only duplicate specimens were available to assess the influence of starting materials or to quantify the response of a mixture, for a given exposure. Although only having two replicate specimens is not ideal, the purpose of these initial measurements was to gauge the relative performance of the materials, and to assess the anticipated affect in the large Blocks that would be tested for structural performance.

In the subsequent studies of materials performance, the number of replicates that are being reported on is provided. In some cases, only two replicate specimens were available. Although the uncertainty in the mean for duplicates is far greater than for triplicates, in the cases where duplicate specimens were used, the uncertainty of a measurement at any given time did not play a role in the conclusions drawn from the overall time-dependent behavior.

Chapter 2

MATERIAL SELECTION AND CONCRETE MIXTURE DESIGN

One of the objectives for the concrete materials research was to develop the concrete mixture designs to be used in the Tasks 1, 2, and 3 structural testing. These mixture designs would have requirements for the fresh properties (to facilitate placement), the mechanical hardened properties (desired structural performance), and the unconfined expansion (to characterize the effects of ASR expansion). Initially, the objective was to have three mixtures, with 'high', 'medium', and 'low' nominal levels of expansion. In time, however, the decision was made to have mixtures with specific unconfined expansions at 18 months: 0.15 %, 0.30 %, and 0.50 %. This proved to be quite challenging because it would require extensive mixture development and sufficiently reactive coarse and fine aggregate materials.

2.1 MATERIAL SELECTION

The three Task 1 reactive Block specimens were constructed using concretes with known, natural reactive aggregates and were designed to have pre-determined levels of unconfined expansion (i.e., expansion occurring without any type of mechanical restraint or reinforcement) at approximately 18 months of age. These included 'low', 'medium' and 'high' expansion concrete mixtures with target expansion (strain) levels of 0.15 %, 0.30 %, and 0.50 %, respectively. An additional (fourth) Block specimen was cast with concrete designed using non-reactive aggregate as a control.

The Task 2 reinforced concrete beams were constructed using the Task 1 concrete mixture with the 0.50 % target expansion, and the control specimens were made using the same concrete mixture, to which lithium nitrate was added for the purpose of reducing or eliminating the expansion due to ASR.

2.1.1 Initial characterization and evaluation of existing aggregate

Three sources of reactive aggregate were procured in the early stages of the project to meet the range of target expansions specified above. The first two were local aggregates that the 2014 Maryland State Highway Administration's Aggregate Bulletin (MSHA, 2014) had reported as having some measure of alkali reactivity: the i) the *Luck Stone*, a coarse aggregate meta-rhyolite, and ii) the *Chaney Enterprises fine aggregate*, a siliceous fluvial sand. The reported sieve data and aggregate properties are shown in Table 2-2. (Portions of the 2014 MSHA Aggregate Bulletin are included in Appendix B for reference.) The third aggregate source was a known highly-reactive *industrial fused silica* that was reported to be 99.7 % amorphous SiO₂, and having particle size ranging from (4.75 mm to 0.85 mm). The fused silica was originally thought to be required to achieve the highest target expansion levels (Table 2-1). Aggregate selections were based, in part, on the MSHA reported 14-day 'accelerated mortar bar test' (AMBT) ASR expansion measurements, based on the standardized ASTM C1260 test and used a crushed, graded aggregate, elevated temperatures, and strongly alkaline immersion solutions

where potentially deleterious behavior is indicated by expansion greater than or equal to 0.10 % (ASTM C1260-14, 2014).

On-site testing and verification of these reported AMBT expansion values in advance of mixture design development for the Luck Stone included crushed and graded fractions from both a #57 aggregate (38 mm or 1-1/2 in maximum size; 24 mm or 1 in nominal size) and a slightly smaller #78 aggregate (19 mm or 3/4 in maximum size; 13 mm or 1/2 in nominal size), both of which showed slow reactivity with average 14-day AMBT expansion of 0.257 %, or approximately one-half of the published value reported in the literature (Table 2-1; Figure 2-1a). Follow-up expansion test work using a larger (50 mm / 2 in.) miniature concrete prism test (MCPT) (Latifee and Rangaraju, 2015) with uncrushed Luck Stone coarse aggregate also showed relatively low expansion values of 0.183 % and 0.195 %, even under accelerated reaction conditions of 60 °C and 80 °C, respectively (Figure 2-1b). These results were likely due to variability in the testing, and the variability that can occur among aggregates taken from different regions of a quarry. Additional MCPT testing also established that the Chaney coarse (#67) aggregate was non-reactive with expansions ranging only from 0.009 % at 40 °C to 0.017 % at 60 °C.

Based on this initial screening, the Chaney coarse and fine aggregate were rejected as the primary reactive aggregates for this study; however, the Chaney fine sand was deemed feasible for use as an innocuous material to be blended with other more reactive aggregates in the development of final target mixtures. The Luck Stone was considered to be capable of achieving only the low- (0.15 %) and mid- (0.30 %) level expansion targets. The highly reactive fused silica (Teco-Sil) (<https://imerys-refractoryminerals.com/wp-content/uploads/Teco-Sil.pdf>) material, which showed expansions of 0.45 % (at 40 °C) and 0.60 % (at 60 °C) over 40 days at only 7.5 % (by volume) replacement of total aggregate, was a feasible alternative for the high expansion mixture, but was eliminated from further consideration in favor of natural aggregates to ensure that the project blocks and beams would exhibit the best representation of ASR effects observed in field structures. For these reasons, more highly reactive aggregate needed to be sourced to provide the 0.50 % target expansion mixture required for the project.

Table 2-1. Aggregates initially screened for reactivity and published ASR expansion data.

Aggregate	Source	Component	Type	Expansion (%)
Luck Stone Co.	Rockville, VA	Meta-rhyolite, phyllite, gneiss, strained quartz, chert	Coarse aggregate	0.47 ^{*, **}
Chaney Enterprises	Waldorf, MD	Interbedded fluvial sand; detrital quartz	Fine aggregate	0.13 ^{*, **}
Teco-Sil™	CE Minerals, Roswell, GA	Fused silica (amorphous SiO ₂)	-4+10 sieve fraction (2.0-4.76 mm)	0.50 [†]
Placitas	Vulcan Mat'ls Co., Bernalillo, NM	Fluvial gravel from rhyolitic-dacitic volcanics with quartzite	Coarse aggregate	0.82 ^{‡, **}
Jobe	Jobe Materials Co., El Paso, TX	Mixed rhyolitic volcanic, chert, quartz, alkali feldspar	Fine aggregate	0.64 ^{‡, **}

* MSHA. 2014. Aggregate bulletin – test data. Maryland State Highway Administration, Office of Materials Technology, Hanover, MD.

** ASTM C1260-14 'Accelerated' mortar bar test (ASTM, 2014).

† Tested in a non-reactive mixture at 7.5% volume replacement of Teco-Sil as fine aggregate.

‡ Ideker et. al., (2012).

Table 2-2. Particle size distribution (as % passing designated sieve size: 1" = 25.4 mm) and physical parameters of the principal coarse aggregates used in the study, as determined by ASTM C136 (interlaboratory 1s precision \leq 3 % for all % retained).

Sieve No.	Size	Placitas MA3-165	Luck #57 MA3-144	Luck #78 MA3-148	Millville (NR) MA3-40
--	1-1/2"	100	100	100	100
--	1"	100	95	100	100
--	3/4"	93	54	100	97
--	1/2"	39	19	83	56
--	3/8"	12	6	35	26
4	4.75 mm	2	1	8	4
8	2.36 mm	1	1	2	2
16	1.18 mm	1	1	1	0
30	pan	0	0	0	0
<hr/>					
SSD Sp. Gr.		2.5	2.6	2.6	2.8
Absorption, %		0.40	0.66	0.66	0.40
DRUW		100.6	--	96.2	102.4

Table 2-3. Particle size distribution, saturated surface dry (SSD) specific gravity (Sp. Gr.), water absorption, and fineness modulus (F.M.) of the Jobe reactive sand, as determined by ASTM C136 (interlaboratory 1s precision \leq 3 % for all % retained).

Retained on Sieve no.	Size Fraction	Cum % retained	% Passing
4	4.75 mm	7.7	92.3
8	2.36 mm	14.2	85.8
16	1.18 mm	21.8	78.2
30	0.6 mm	42.6	57.4
50	0.3 mm	87.5	12.5
100	150 μ m	97.9	2.1
200	75 μ m	99.7	0.3
pan	<76 μ m	100	0
<hr/>			
SSD Sp. Gr	2.57		
Absorption, %	1.15		
F.M.	2.7		

This publication is available free of charge: <https://doi.org/10.6028/NIST.JR.8415>

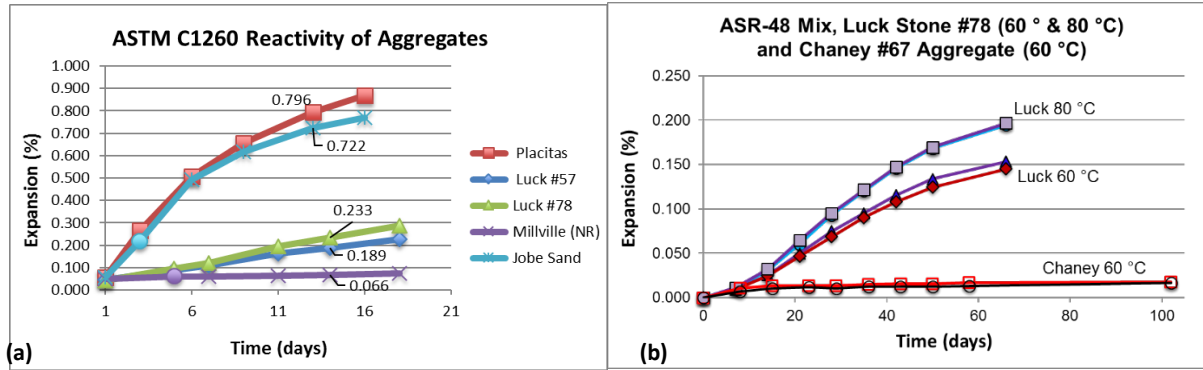


Figure 2-1. Comparison of ASTM C1260 measurements for (a) 14-day mortar bar (AMBT) expansion for the aggregates, and (b) expansion of the Luck #78 and #57 aggregates at 60 °C and 80 °C, and Chaney #67 aggregate at 60 °C in miniature (50 mm) concrete prisms. Results in (a) and (b) represent mean of triplicate and duplicate measurements, respectively, for qualitative comparison purposes.

2.1.2 Acquisition of additional reactive aggregate

With the elimination of fused silica glass as a highly reactive aggregate, two of the most highly alkali-reactive, commercially-available concrete aggregates in North America were sourced and procured for development of the concretes.

The Placitas coarse aggregate (Bernalillo County, NM) is a well-known, highly reactive fluvial/rounded gravel consisting of orthoquartzites and a variety of volcanics derived from the ancestral Rio Grande river (late Pleistocene to early Miocene) and ranging from blond to red rhyolites and dacites to gray andesites (Figure 2-2).

The Jobe fine aggregate (El Paso, TX), a highly reactive washed concrete sand also derived from mixed rhyolitic volcanics with quartz, chert, and feldspathic sand, was also sourced in November 2015 to further boost high expansion levels (Table 2-1). Testing verified the ASTM C1260 mortar bar expansion of the Placitas at 0.80 %, commensurate with values reported in the literature (Ideker et al. 2012). Mortar bar results for the Jobe also showed expansion levels on par with that of the Placitas coarse aggregate (Figure 2-1a).



Figure 2-2. Placitas coarse aggregate components. Blond, red, and gray aggregate are volcanic components; clear are orthoquartzites.

2.1.3 Reactive aggregate mineralogy and texture

Mineral Phase Composition:

The Placitas coarse aggregate comprises variable proportions of fine-grained rocks of felsic to intermediate composition containing poorly-ordered or noncrystalline reactive forms of silica that are particularly susceptible to ASR (FHWA, 2013). These range from yellowish-brown and yellowish-red siliceous end-members that are chemically classified as rhyolites to dark gray dacites and andesites of intermediate acidity (dominated by both Na-/K-feldspars as anorthoclase, and Ca-/Na-rich plagioclase as andesine with minor quartz). Elemental analysis was conducted by X-ray fluorescence (XRF) analysis on powder specimens. The blond and clear (opalescent) components are principally highly siliceous orthoquartzites, typically with >93 % SiO₂, mainly as strained quartz. As a composite of these component fractions, the bulk Placitas deposit has intermediate CaO, SiO₂, and alkali content with overall of rhyolitic composition (Figure 2-3a,b).

The component fractions (separates) of the Placitas have a wide range of accessory minerals present in trace amounts, primarily as alteration (devitrification) products of volcanic glass in the presence of available Ca, Na, and K (Figure 2-4, and Table 2-4).

As a predominantly fluvial deposit, the Placitas is extremely heterogenous, consisting of a complex mixture of highly siliceous orthoquartzites and volcanics ranging from rhyolites to andesites, each with distinctive phase composition, and texture. The alkali reactivity of the Placitas coarse aggregate is largely dependent on the *mineralogical (phase) composition* and *textural characteristics* of its components, both of which are fundamentally determined by the effects of fractional crystallization and cooling (devitrification) history of the magma and sedimentation history during transport.

The **Jobe** fine aggregate is a highly reactive fluvial material with mixed fluvial/volcanic (rhyolitic/dacitic) components. Mineral composition was characterized using quantitative X-ray (powder) diffraction (XRD) with Rietveld analysis using an internal standard. The mineral composition was similar to the bulk Placitas aggregate with respect to mineral and textural composition, but with appreciable chert (Figure 2-4, Table 2-4).

This publication is available free of charge: <https://doi.org/10.6028/NIST.JR.8415>

Sample	SiO ₂	Al ₂ O ₃	Fe ₂ O ₃	K ₂ O	Na ₂ O	CaO	MgO
Volcanics							(a)
Bulk 1	75.43	10.67	3.75	2.47	2.63	2.09	1.02
Bulk 2	77.51	9.21	3.91	2.00	2.16	2.16	0.84
Red 1	78.63	10.96	1.51	5.39	1.99	0.51	0.23
Red 2	72.75	12.94	4.24	2.70	4.58	1.34	0.68
Gray 1	69.31	12.68	5.95	2.60	2.91	3.31	1.30
Gray 2	60.21	15.54	9.37	1.81	2.83	6.41	1.64
Gray 3	68.73	13.1	4.41	2.55	2.73	4.65	1.50
Orthoquartzite							
Clear 1	97.97	0.11	0.81	0.02	0.01	0.05	0.01
Clear 2	94.86	0.45	1.51	0.04	0.01	0.83	0.35
Blond 1	93.59	3.11	0.93	2.00	0.40	0.06	0.02
Blond 2	86.38	6.89	1.34	0.20	2.64	0.95	0.14

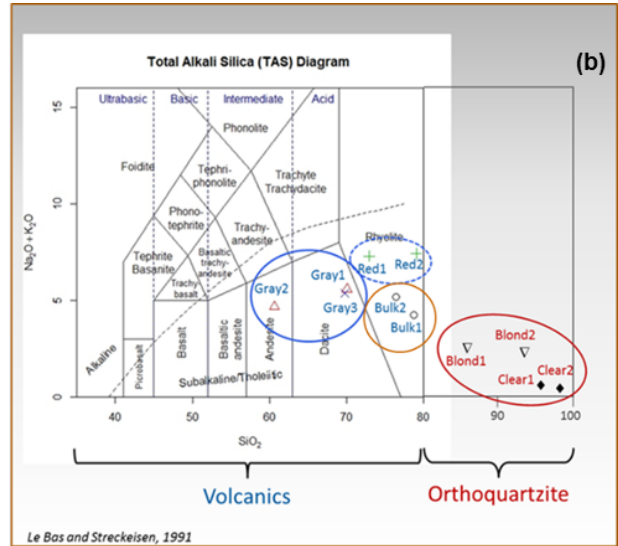


Figure 2-3. (a) Estimated mass fractions of major cations of the Placitas bulk material and aggregate separates (individual XRF results from duplicate or triplicate samples, as indicated) and (b) chemical classification based on total alkali silica (TAS) content.

Las Placitas Mineralogy

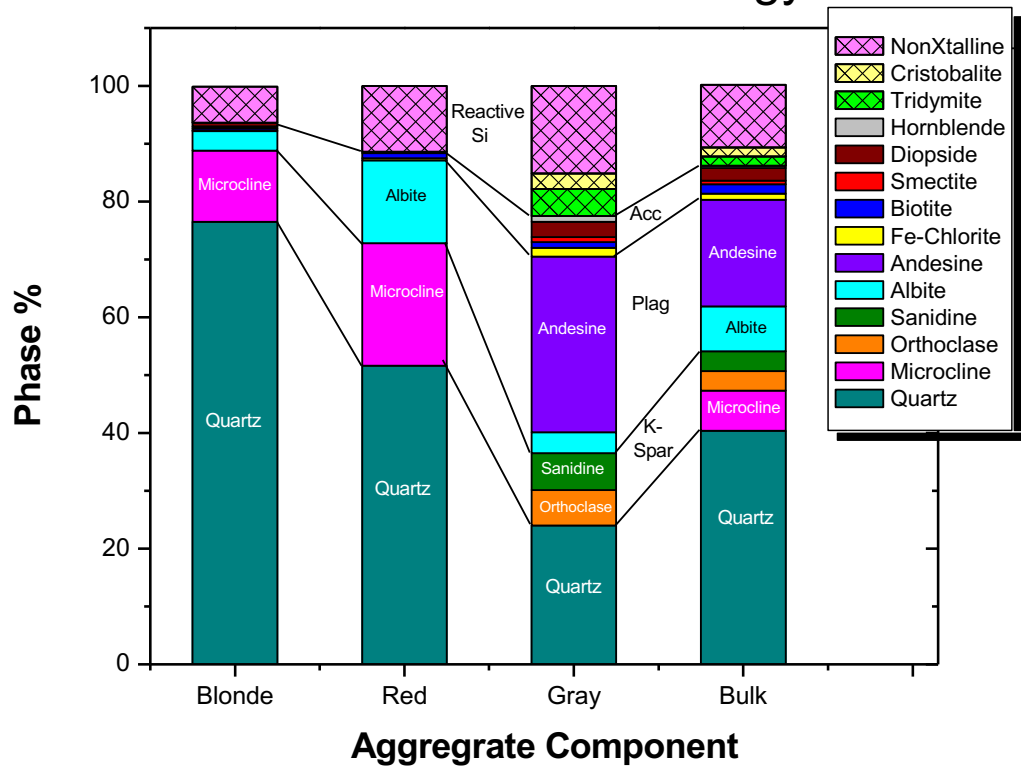


Figure 2-4. Phase composition of the Placitas bulk and aggregate components determined by XRD/Rietveld with internal standard.

This publication is available free of charge: <https://doi.org/10.6028/NIST.JR.8415>

Table 2-4. Mass fraction of minerals identified in the Placitas aggregate components (coarse aggregate - CA) and the bulk Jobe (fine aggregate – FA) .

AGGREGATE COMPONENT, Wt. %						
PHASE	PLACITAS, CA					JOBE, FA
	Clear	Blond	Red	Gray	Bulk	Bulk
Microcline		12.3 ± 0.13	21.2 ± 0.30		6.9 ± 0.50	10.6 ± 1.06
Sanidine				6.4 ± 0.21	3.4 ± 0.00	3.2 ± 0.57
Orthoclase				6.1 ± 0.16	3.4 ± 0.10	
Anorthoclase		3.4 ± 0.09	14.3 ± 0.35	3.6 ± 0.57	7.8 ± 0.30	6.2 ± 1.63
Andesine				30.4 ± 0.99	18.4 ± 0.25	9.6 ± 0.78
Fe-Chlorite		0.1 ± 0.05	0.4 ± 0.05	1.5 ± 0.28	1.1 ± 0.10	
Muscovite				tr		
Biotite		0.4 ± 0.05	0.9 ± 0.00	1.0 ± 0.17	1.6 ± 0.15	1.0 ± 0.21
Smectite	tr	tr	tr	0.9 ± 0.05	tr	tr
Pyrophyllite	tr					
Augite				2.6 ± 0.08	2.2 ± 0.00	1.9 ± 0.42
Calcite				tr		
Dolomite	tr					
Hornblende				1.0 ± 0.09	tr	
Quartz	87.9 ± 0.57	76.5 ± 1.24	51.6 ± 0.30	24.0 ± 0.76	40.4 ± 0.65	48.0 ± 1.27
Tridymite				4.7 ± 0.05	1.6 ± 0.05	
Cristobalite				2.7 ± 0.19	1.6 ± 0.10	tr
Noncrystalline	11.8 ± 0.78	6.3 ± 1.47	11.4 ± 0.90	15.1 ± 2.66	10.8 ± 0.10	19.0 ± 4.24

This publication is available free of charge: <https://doi.org/10.6028/NIST.JR.8415>

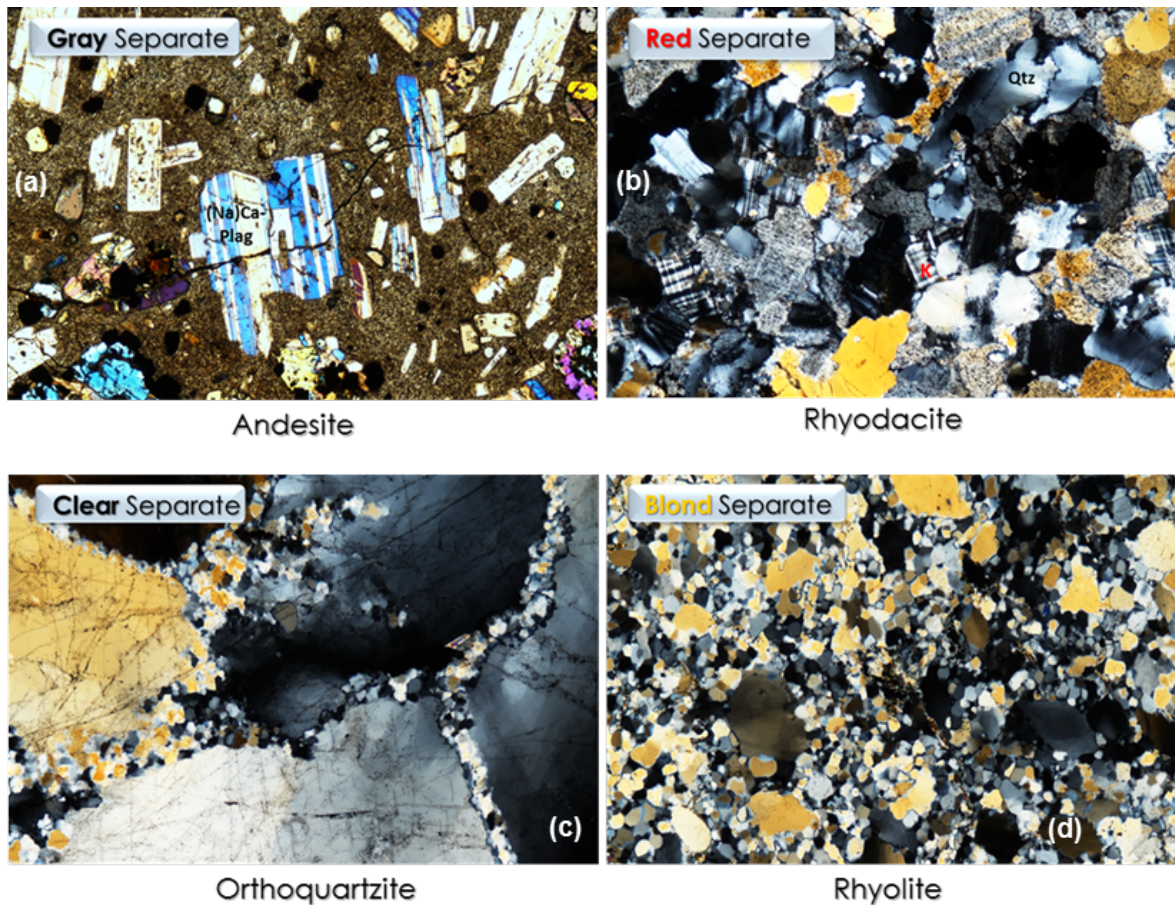


Figure 2-5. Thin-section petrographic images under cross-polarization showing textural characteristics of the unaltered Placitas volcanic and quartzite rock types and components, grouped by classifications in Figure 2-4.

Textural Characteristics:

Each of the respective rock types and components found within the Placitas and Jobe deposits also have unique grain texture characteristics resulting principally from primary and/or secondary igneous processes that have perhaps more influence on alkali-reactivity and rate of reaction than mineral phase composition alone.

The **dark gray andesite/dacite** component of the Placitas, for example, has characteristic aphanitic volcanic texture, with a bimodal distribution of blue-white plagioclase feldspar phenocrysts (largely as birefringent andesine) under crossed polars embedded within a fine-grained, highly-reactive, isotropic groundmass (Figure 2-5a). The groundmass, a product of devitrification associated with rapid cooling and crystallization of magma, is comprised of brownish volcanic glass consisting of finely-divided anorthoclase and sanidine feldspar intergrown with microcrystalline, high-temperature cristobalite and tridymite (opal-CT) and noncrystalline (opal-A) phases. The volcanic glass makes the dark gray andesite/dacite component among the most highly reactive of the Placitas aggregate components.

In contrast, the **red rhyolite/dacite** Placitas component consists of relatively well-crystalline, felsic mineral assemblages dominated by interlocking microcline/anorthoclase (alkali feldspars) and undulatory, strained quartz phases with little volcanic glass (Figure 2-5b). These phases formed under slower cooling of the magma and later crystallization, and are consequently dominated by framework (siloxane) surfaces with lower specific surface areas and equilibrium solubilities than the more poorly-crystalline and reactive gray/andesite component. For these reasons, the red component is only moderately alkali reactive (Figure 2-5b).

Alteration of alkali feldspars in both the red and gray Placitas fractions has been shown to provide a likely source of alkali to pore solutions thus potentially contributing to ASR over time (Constantiner and Diamond, 2003).

The **clear (orthoquartzite)** component (Figure 2-5c) is the most highly siliceous of all Placitas fractions with an average SiO_2 content of >90 %, principally as both massive (monocrystalline), undulatory, strained quartz and as polycrystalline/reprecipitated (secondary) silica. The large quartz crystals have irregular, sweeping extinction owing to the formation of subgrains after post-crystallization deformation. They have irregular (sutured) grain boundaries caused by pressure dissolution with reprecipitation of polycrystalline quartz at high-strain contact areas. The strained quartz component is moderately slowly reactive while the secondary reprecipitated quartz is highly alkali reactive.

The **blond** Placitas component is rhyolite transitional to orthoquartzite and is dominated by an advanced stage of secondary polycrystalline precipitation that includes polycrystalline quartz and a wide variety of ultra-reactive radial/acicular 'spherulite' and related chalcedony precipitates. Spherulites are radial arrays of fibrous microcrystals comprising micro- or cryptocrystalline acicular/fibrous zoned K/Na feldspars that formed by nucleation around a glassy opal-CT matrix during slow cooling/devitrification in felsic volcanic rocks, primarily rhyolites (Figure 2-6, Figure 2-7). They form coalesced bodies that are *extremely alkali-reactive*, typically resulting in mass dissolution features and disintegration of rock textures into a complex network of internal cracks and fissures well beyond the scope of linear aggregate cracking.

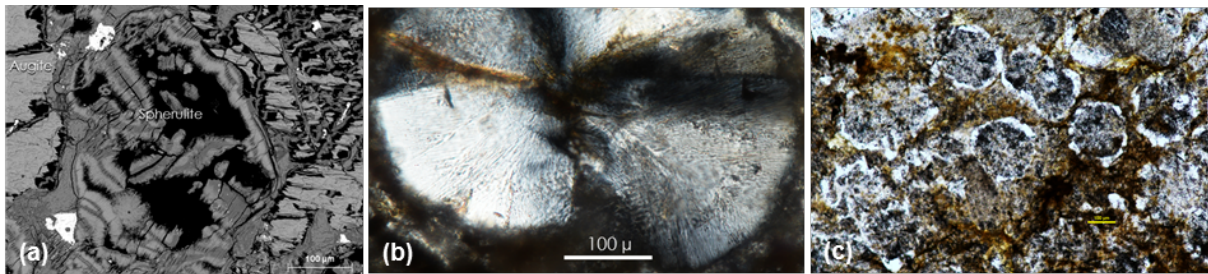


Figure 2-6. Radial, fibrous/acicular crystal bodies as chalcedony (a) and spherulites (b,c) are some of the most highly reactive materials found in the Placitas felsic components.

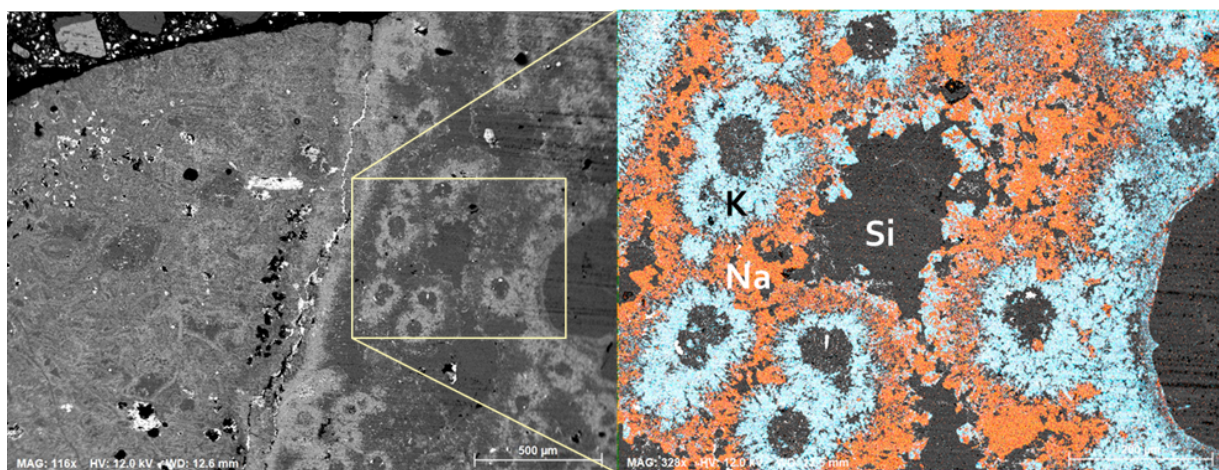


Figure 2-7. Highly reactive spherulites in coarse Placitas aggregate SEM image (left) showing radial growth of fibers with EDS (x-ray) mapping of elemental composition (right).

2.1.4 Isothermal Calorimetry

In advance of selective dissolution treatments to further identify and quantify the alkali-reactivity of aggregates used in this study, the heat flow of the bulk Jobe fine aggregate, along with the individual Placitas coarse aggregate components (blonde, red, gray, red, and clear) was measured by isothermal calorimetry in 1 mol/L NaOH aqueous solution at 80 °C. Each component was individually ground and sieved, and each specimen consisted of approximately 3.8 g from the fraction retained between the 150 µm and the 300 µm sieves.

The Gray Placitas (volcanic, andesite) component showed the highest heat flow, indicating the greatest alkali reactivity, as expected (Feldman, 2018; Feldman and Eason, 2018) (Figure 2-8). The Clear Placitas (monocrystalline orthoquartzite) was relatively slow to react, resulting from the dominance of strained quartz in this fraction. The bulk/composite Placitas was estimated from the average of the components.

Unfortunately, the complexity of the thermal properties of the individual Placitas phases prevented the use of isothermal calorimetry as a tool for charactering the reactivity of the aggregate. In particular, the endothermic behavior of the Clear Placitas negates much of the exothermic behavior of the other four phases.

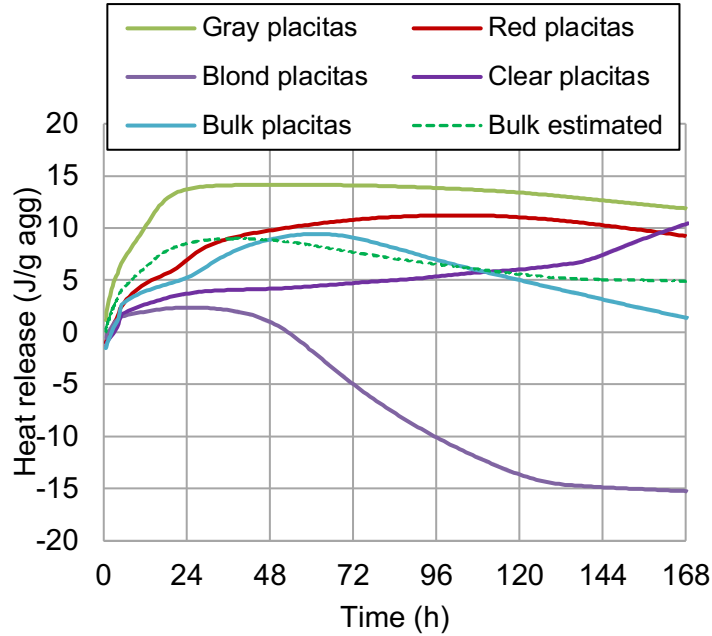


Figure 2-8. Heat flow curves characterizing the reactivity of the 150 μm to 300 μm fraction of each of the Placitas aggregate components.

2.2 CONCRETE MIXTURE DESIGN

Mixtures were developed in the laboratory in small batches, involving a pail mixer – see Figure 2-9. Typical batch volumes were 9 L.



Figure 2-9. Pail mixer used to develop concrete mixtures.

2.2.1 Mixture Requirements

Upon acquisition of a small sample of the reactive Placitas and Jobe aggregates, work continued toward development of concrete mixtures that met the requirements for expansion, strength, workability, placement, and mechanical consolidation as shown in Table 2-5.

Table 2-5. Target mixture requirements for the large block structures.

Property	Requirement	Component Vol. Fraction
Expansion Targets for Mixes	<0.04 %, 0.15 %, 0.30%, 0.50 %	
Compressive Strength (min)	28 MPa (~4 ksi)	
Maximum Cement Content	588 lb/yd ³ (350 kg/m ³)	
Maximum Aggregate Size	19 mm (0.75 in)	
Slump (target)	15 cm (6 in)	
Slump Retention	Up to ~1 hour	
Water / Cement	0.50	
Co. Aggregate		42.0 %
Fine Aggregate		27.4 %
Cement		11.1 %
Water		17.5 %
Air content		2 %

Concrete mixtures were developed using an ASTM C 150 Type-I/II high-alkali cement. The ASTM (2005) equivalent alkalinity (Na_2O_e) was 0.89 %; the mill sheet is shown in Appendix A. The alkali content of the concrete mixture was increased to 1.40 % (4.90 kg/m³ as Na_2O_e) in Mixes 1 to 3 by adding reagent-grade NaOH pellets dissolved into the batching water. Control Mix 4 was batched using a low-alkali Type I/II cement with no alkali additions. Mineralogy and selected physical and chemical properties of the cement used in both mixture design development and fabrication of the large blocks for Mixes 1 to 3 are shown in Table 2-5 and Table 2-6.

Concrete mixtures were designed to have relatively high paste volumes while maintaining a water:cement (w/c) mass ratio of 0.48 to 0.50. The high paste volume was needed to ensure a high volume fraction of alkaline pore solution to drive the alkali-silica reaction. It also helped to promote workability and facilitate flow of the concrete (between reinforcement bars), which was an important consideration for the highly instrumented Task 1 Blocks.

Table 2-6. Cement specifications for reactive Mixes 1 to 3. Uncertainties represent the estimated standard deviation. LOI: loss on ignition. Blaine Fineness refers to ASTM C 204.

Cement Specifications (Reactive Mixes 1-3)			
<i>Mineral Phase</i> *	<i>Wt %</i>	<i>Chemical</i> **	<i>Wt %</i>
C3S	60.3 ± 1.3	SiO ₂	19.3
β-C2S	13.9 ± 1.3	Al ₂ O ₃	4.1
C4AF	8.0 ± 0.8	Fe ₂ O ₃	2.8
orthorh-C3A	1.4 ± 0.3	CaO	61.4
cubic-C3A	5.0 ± 0.1	MgO	4.2
Periclase	2.8 ± 0.1	SO ₃	3.5
Gypsum	2.3 ± 0.0	LOI †	2.3
Bassanite	2.1 ± 0.1		
Portlandite	tr	<i>Other</i>	
Calcite	1.7 ± 0.2	Equiv. Alkalis (Na ₂ O _e)	0.89
Quartz	0.4 ± 0.0	Blaine Fineness (m ² /kg)	405
Arcanite	1.0 ± 0.1		
Syngenite	1.0 ± 0.4		

* Determined by XRD/Rietveld.

** Holcim Cement Material Certification Report, March 9, 2017

An additional requirement in mixture proportioning was the limit on the total cement content to prevent excessive heat of hydration and possible thermal and delayed ettringite (DEF) cracking effects, both of which could damage the blocks and confound long-term ASR measurements. Published specifications for mass concrete thermal control state that, “the maximum temperature in concrete after placement shall not exceed 158 °F (70 °C)” and that, “the maximum temperature difference between center and surface of placement shall not exceed 35 °F” (ACI Committee 301, 2010).

Hydration temperatures for a proposed maximum target cement content were verified directly through fabrication of a ≈1/3-scale concrete test block (1.1 m x 1.6 m x 1.8 m) that was outfitted with interior and exterior thermocouples. The measured maximum internal temperature for a trial concrete mixture containing 350 kg/m³ (588 lb/yd³) of cement was 66.8 °C (152 °F), with an interior-exterior temperature difference ($\Delta T_{(int-ext)}$) of 20 °C, demonstrating that heat of hydration within the first 7 days was well within target specification at this cement content (Figure 2-10). Following this test, cement content was fixed at 350 kg/m³ (588 lb/yd³) in the subsequent mixture design work involving the large blocks and companion prism specimens.

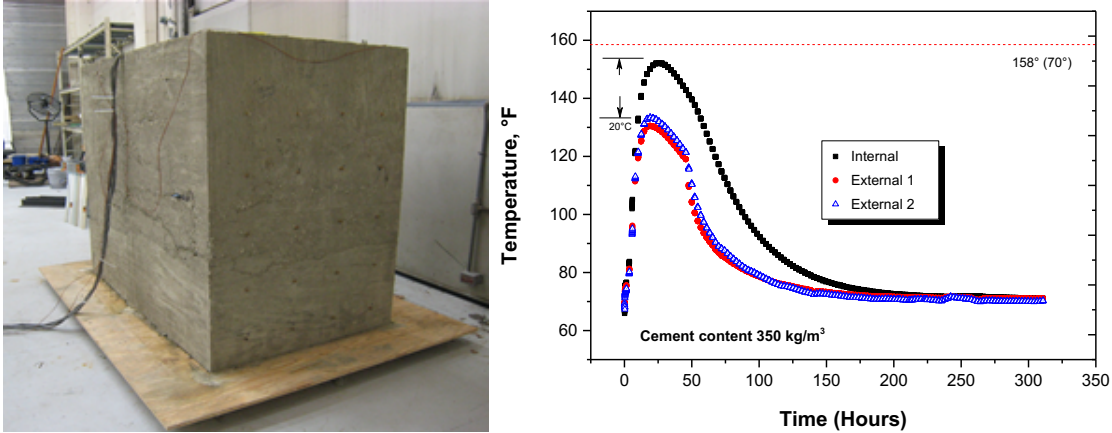


Figure 2-10. A test block instrumented with an exterior and two internal thermocouples (left), and the recorded maximum internal temperatures and internal-external temperature differential were within target specifications for a concrete mixture having 350 kg/m³ (right).

With total cement content and w/c ratio fixed at 350 kg/m³ and 0.5, respectively, mixtures with different coarse to fine aggregate proportions were tested until a slump of at least 10 cm (4 in) was achieved. High-range water reducer was then added to the optimum mixture until a slump of 18.5 cm (7.25 in) was achieved with no bleeding and no evidence of segregation. Additional measurements using this optimized mixture showed that 54 % of the initial slump was retained at 45 minutes after placement, and that 41 % of the slump remained with good workability at 60 minutes.

2.2.2 Development of Target Expansion Mixtures: Initial Screening

Mixtures having the target expansion values were developed using the reactive Placitas coarse and Jobe fine aggregates. The mixtures were cast into prisms for expansion measurements, based on the 'miniature concrete prism test' (MCPT) method of Latiffie and Rangaraju (2015). The MCPT modifies the ASTM C1293 (one-year) prism test in the following ways:

- smaller 50 mm x 50 mm x 273 mm (2 in x 2 in x 11 in) prisms than the conventional 75 mm x 75 mm x 273 mm (3 in x 3 in x 11 in) prisms specified in ASTM C1293,
- partial immersion of prisms in either 1 mol/L NaOH or deionized water where specimens are covered with a cloth during the test to wick the soak solution across the entire prism surface, and
- equilibration temperatures ranging from 40 °C (104 °F) to 80 °C (176 °F).

An initial MCPT test at a relatively high cement content of 394 kg/m³ (663 lb/yd³), and using the Placitas coarse aggregate with the non-reactive Chaney fine sand, showed expansion in excess of 0.115 % after 90 days when soaked in alkali solution (Figure 2-11a). For this mixture, two different temperature exposure conditions were used: 40 °C and 80 °C. Initially, expansion was greater in the specimens conditioned at 80 °C. After day ≈60, however, the expansion was greater in the samples conditioned at 40 °C. Expansion continued, but at diminishing rates at both temperatures through the 90-day test period.

This same concrete mixture equilibrated in water, rather than an alkali soak solution, also showed rapid initial expansion at 80 °C, but the reaction was strongly curtailed near day 20, suggesting that the ASR reaction was effectively halted by diffusion and preferential leaching of alkalis from the cement paste, even for cements boosted to Na_2O_e levels in excess of 1.35 % (Figure 2-11b). Comparable prisms conditioned at 40 °C continued to expand through 90 days before the reaction began to slow. Alkali leaching, particularly in the water soak solution, is exacerbated at temperatures above 60 °C where suppression of normal primary ettringite formation during cement hydration occurs, resulting in an increase in the ratio of $(\text{SO}_4^{2-} / \text{OH}^-)$ in pore solution and lowering of local pH, which slows the dissolution of reactive silica and ASR gel formation. These conditions can also foster late-stage expansion as delayed ettringite formation which can confound ASR expansion (Divet and Randriambolona, 1998).

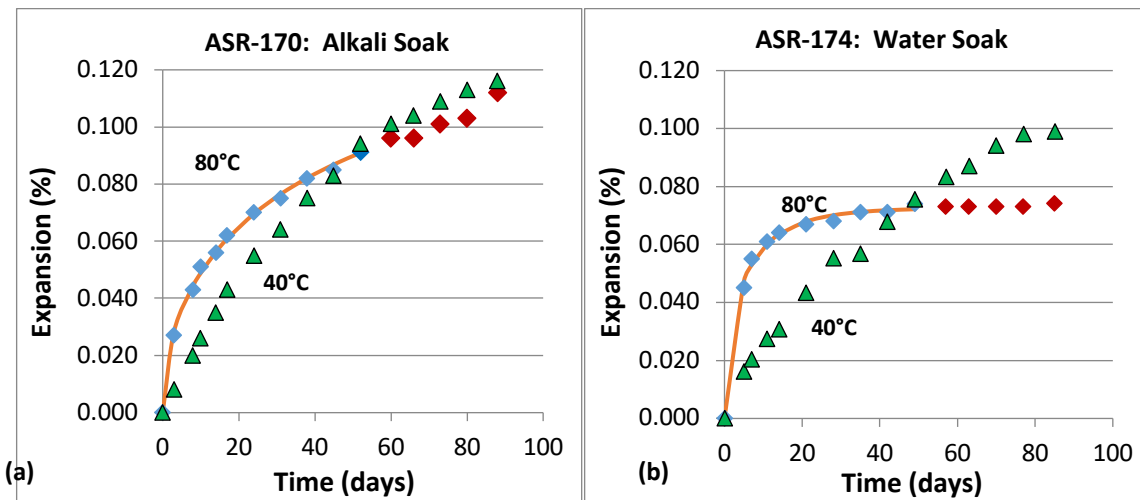


Figure 2-11. MCPT expansion in identical concrete mixtures batched with the Placitas coarse aggregate shows strong initial acceleration of expansion at high temperatures (a). ASR reaction is almost fully suppressed at 80 °C in a water soak solution due to alkali leaching, but proceeds normally at 40 °C (b). Light blue symbols were used to fit a line, merely to show the general trend. Results represent mean of 2 replicates; see discussion of uncertainty in text.

Additionally, prisms undergoing continuous expansion normally exhibit mass increase commensurate with moisture uptake associated with formation and hydration of alkali-silica gel and other cement hydration processes. However, exposing prisms to 80 °C is a particularly aggressive treatment, especially under an alkali soak, resulting in disruption of normal cement hydration processes and degradation of prism integrity associated with silica gel exudation, minor cracking, and mass loss (Figure 2-12). The significance of the effect is demonstrated by the fact that each measurement value is shown, so the difference in replicate measurements are an indication of the uncertainty. When stored in water solution, however, predictable weight gain attributable to ASR gel formation and normal hydration processes occurs at both 40 °C and 80 °C (Figure 2-12b).

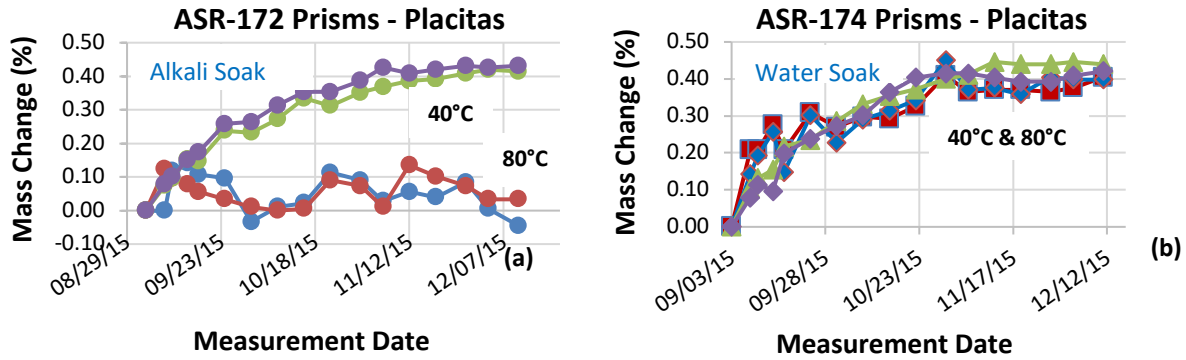


Figure 2-12. Comparison of mass change in specimens exposed to high temperature alkali soak solution (a), and a high temperature water soak solution (b); individual measurements are shown.

These results indicate that i) expansion studies on prisms held at 40 °C in water provide a more accurate representation of long-term ASR reaction in the large block specimens (i.e., the blocks will not be soaked in alkali solution) than prism studies under more aggressive, accelerated conditions, and ii) the Placitas aggregate alone is insufficient to attain the higher (0.50 %) expansion target, and will need to be supplemented with additional reactive aggregate.

For these reasons, prism expansion measurement techniques were modified further to include the following:

- 50 mm x 50 mm prisms were eliminated in favor of larger 75 mm x 75 mm prisms to i) reduce alkali leaching and ii) provide a greater prism:aggregate length ratio for a 19 mm nominal aggregate size,
- prisms were suspended vertically over water at $\approx 95\%$ RH in sealed containers in accordance with ASTM C1293 to more accurately reflect conditions of the large blocks in the environmental chamber,
- expansion measurements for target mixture design were conducted at 38 °C,
- cement content for all trial mixtures was capped at 350 kg/m^3 (588 lb/yd^3), and
- electrical resistivity, ultrasonic pulse velocity, percent mass change, and internal RH within prisms were recorded for all samples with each expansion measurement.

Trial mixtures were repeated under these new conditions, with combinations of all aggregates, and with and without a high-range water reducer. The addition of the Jobe sand to the Placitas coarse aggregate and use of 75 mm x 75 mm (3 in x 3 in) prisms resulted in more than a two-fold boost in expansion compared to that of the Placitas aggregate alone in the MCPT 50 x 50 mm (2 in x 2 in) prisms submersed in either alkali or water (Figure 2-13). The Placitas + Jobe mixture, however, began to exhibit evidence of alkali leaching and curtailed ASR expansion beginning at day ≈ 60 , continuing through day 75 and beyond.

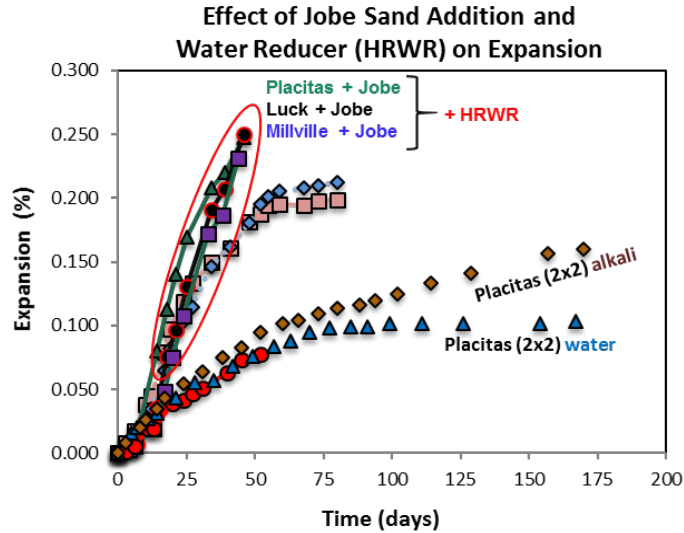


Figure 2-13. Addition of the Jobe sand with the Placitas coarse aggregate substantially boosted expansion compared to Placitas aggregate alone. Use of a HRWR had an unintended benefit of boosting expansion after ≈ 25 days (circled).

The trial mixtures were also conducted to ensure the suitability of the high-range water reducer (HRWR) selected to provide acceptable slump, and adequate workability and flow during the casting of the large Blocks. The HRWR – principally a polycarboxylate polymer based on a sodium salt - initially showed innocuous behavior up to day ≈ 20 for three aggregate mixtures, but at later ages had the effect of boosting expansion (circled), either by contributing alkalis to the pore solution or by initiating unanticipated reactions (Figure 2-13, Figure 2-14). This enhanced expansion effect was an unexpected benefit that was observed in concretes with three different aggregates in combination with the Jobe sand, suggesting that the latter is both extremely reactive and alkali-sensitive.

Longer-term prism expansion measurements (Figure 2-14) provided a more comprehensive understanding of the mixes would perform. For almost all the prisms, the expansion slowed or halted due to alkali leaching sometime in the range 75 d to 100 d. Expansion in the concrete with Placitas+100 % Jobe as fine aggregate (Mix 3) exceeded 0.40 % after ≈ 125 days, and was favorable for the high expansion (0.50 %) target mixture. The concrete with Placitas coarse aggregate and 50 % volume replacement of the non-reactive Chaney fine aggregate by the Jobe sand (Mix 2), as per the specifications of the 0.30 % target mixture, did not perform as expected, with diminished rate of expansion after \approx day 50 due to alkali leaching. The concrete with Placitas and 100% non-reactive Chaney sand (Mix 1) was close to meeting the 0.15 % expansion at day ≈ 150 .

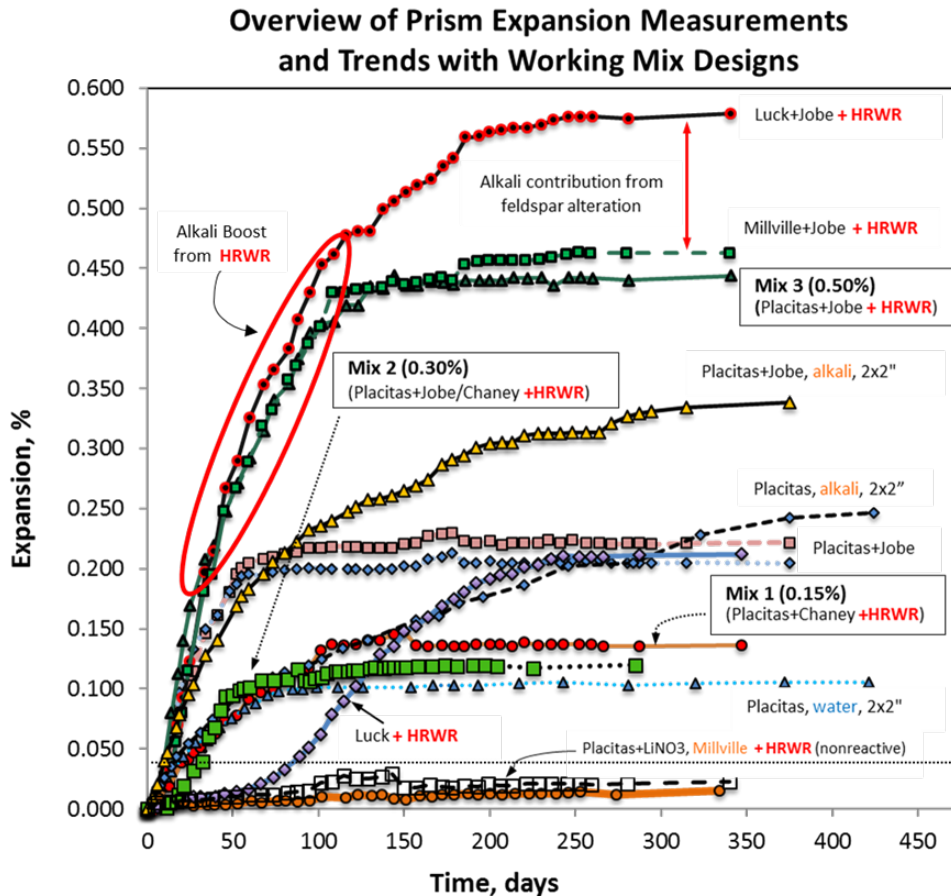


Figure 2-14. Overview of prism expansion measurements used to develop initial mixture designs for the large block specimens through 1 year or longer. Performance of preliminary Mixes 1 to 3 are shown.

Also shown in the expansion data in Figure 2-14 are the results from additional trial mixtures using other aggregates and aggregate combinations. These mixtures included two different control concretes developed using either innocuous aggregate or reactive Placitas aggregate in combination with LiNO_3 . Also shown in Figure 2-14 are results from a mixture using the Luck aggregate, which was very slowly reactive owing to the presence of strained quartz as the dominant reactive aggregate phase. Concrete with the Luck stone was below the 0.04 % level and would be classified as innocuous by ASTM C1293 through ≈ 80 days of reaction.

2.2.3 Final Target Mixture Designs

Prism specimens for each of the three preliminary reactive mixtures (indicated as Mix 1, Mix 2, and Mix 3 in Figure 2-14) were cast and conditioned using the improved experimental and measurement parameters described above. Expansion results for these re-cast prisms (Figure 2-15) showed that concrete Mix 1 met target expansion levels at 0.161 % by 160 days, with expansion in Mixes 2 and 3 achieving 0.24 % and 0.33 % expansion, respectively, within 250 days. Expansion trends continued for all mixtures through >266 days, suggesting substantially

reduced alkali leaching from the prism. The control specimen remained non-reactive with values below the 0.04 % ASTM C1293 threshold for innocuous aggregate. Final mixture proportions for the target mixtures and control specimen are detailed in Table 2-7.

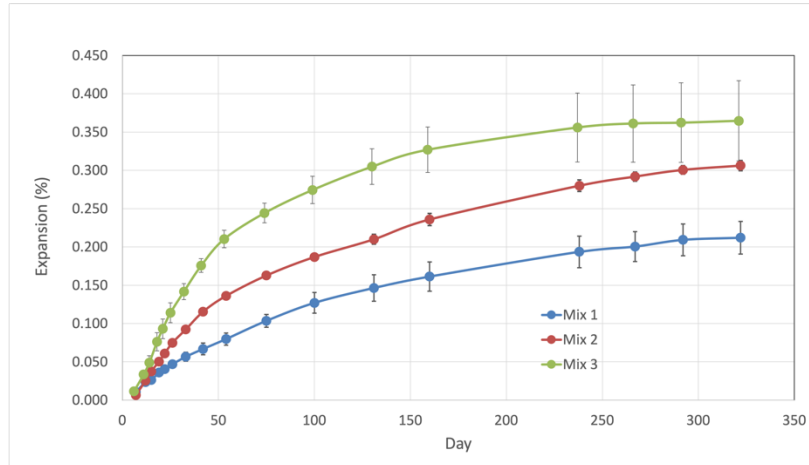


Figure 2-15. Revised prism expansion data for target Mixes 1 to 3, with the error bars representing one standard deviation from duplicate specimens.

Although expansion in laboratory prism specimens for Mixes 2 and 3 are slightly below target levels, unconfined expansion in the large block specimens based on these mixture designs is expected to meet or exceed target expansion levels. Expansion in large block specimens and field structures is reported to occur at appreciably slower rates than for small-scale laboratory prism and mortar bar samples, but to continue for a longer duration, resulting in greater long-term expansion (Thomas et al., 2006). This effect is largely due to the accelerated diffusion and leaching of alkalis from reaction sites in small lab specimens that is otherwise negligible in large lab specimens.

Table 2-7. Final mixture proportions for the target expansion mixtures (Mixes 1 to 3) and the control mixture (Mix 4).

Mix Designation	Cement			Coarse Aggregate			Fine Aggregate			Alkalis	Water	Water Reducer	Paste Volume
	Type	kg/m ³ (lb/yd ³)	Volume Fraction	Type	kg/m ³ (lb/yd ³)	Volume Fraction	Type	kg/m ³ (lb/yd ³)	Volume Fraction	kg/m ³ (lb/yd ³)	kg/m ³ (lb/yd ³)	mL/kg (fl oz/cwt)	(%)
Mix 1: 0.15 %	Type I/II high alkali (≥0.87 % Na ₂ O _e)	350 (588)	0.111	Placitas	1050 (1767)	0.420	Chaney	713 (1199)	0.274	2.9 (4.9)	174 (294)	130 — 975 (2 – 15)	28.6
Mix 2: 0.30 %	Type I/II high alkali (≥0.87 % Na ₂ O _e)	350 (588)	0.111	Placitas	1050 (1767)	0.420	Jobe	423 (711)	0.274	2.9 (4.9)	174 (294)	130 — 975 (2 – 15)	28.6
							Chaney	285 (480)					
Mix 3: 0.50 %	Type I/II high alkali (≥0.87 % Na ₂ O _e)	350 (588)	0.111	Placitas	1050 (1767)	0.420	Jobe	705 (1185)	0.274	2.9 (4.9)	174 (294)	130 — 975 (2 – 15)	28.6
Mix 4: Control	Type I/II (≤0.87 % Na ₂ O _e)	343 (578)	0.115	# 57	1071 (1805)	0.399	Washed #33 Sand	822 (1385)	0.295	< 1 (< 2)	174 (294)	1105 (17)	28.6

This publication is available free of charge: <https://doi.org/10.6028/NIST.JR.8415>

2.2.4 Quality Assurance for the Procurement of Bulk Reactive Aggregate

Once the mixture designs had been finalized, large quantities of the Placitas and Jobe sand were procured. As these are natural products that can exhibit variable properties from different portions of the quarry, and given the significance of the work in this project, the properties of the material to be shipped would have to be validated before shipment.

A field visit to assess the characteristics, quality, and uniformity of aggregate was undertaken prior to procuring the ≈ 96 tons of bulk aggregate (Figure 2-16). Quality assurance of the bulk reactive aggregate was evaluated by accelerated mortar bar testing (ASTM C1260) using representative cone-and-quartered samples of bulk coarse and fine aggregate delivered to NIST for the large block pour to ensure that aggregate reactivity for the 2016 delivered materials was comparable to the 2015 material used to develop the mixture designs. The average prism expansion (3 replicates) of coarse aggregate samples from the 2016 Placitas bulk material was 23 % greater than the expansion observed in the 2015 samples at 14 days, owing to mine and deposit variability (Figure 2-17). Expansion values for the 2016 Jobe fine aggregate bulk purchase material are comparable to those of the 2015 Jobe material. Results suggest that ultimate expansion in the large Blocks may be greater than that previously estimated based on mixture development using the 2015 aggregate.



Figure 2-16. Quality assurance for the procurement of ≈ 96 tons of reactive aggregate was conducted, in part, by reconnaissance field visit to the quarry in Bernalillo, NM.

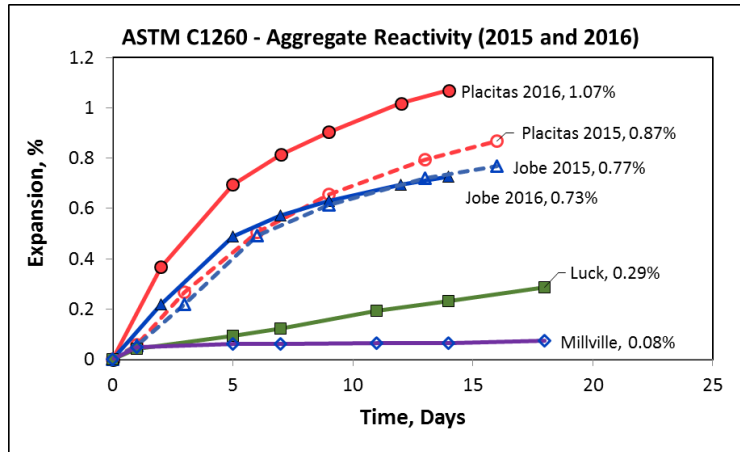


Figure 2-17. ASTM C1260 14-day accelerated mortar bar expansion of the Placitas coarse aggregate from the 2016 bulk purchase was 23 % greater than the 2015 samples previously tested at NIST. Expansion values for the Jobe fine aggregate were comparable between the 2015 and the 2016 samples. Mineral heterogeneity among fluvial coarse aggregates processed (mined) at different times are the likely cause of the range of expansion values for the Placitas.

Chapter 3

TASK 1 AND TASK 2 COMPANION EXPANSION MEASUREMENTS

During the casting of the Task 1 large Blocks (114 cm (w) x 185 cm (h) x 500 cm) and the Task 2 beams (28 cm x 33 cm x 350 cm), smaller companion prisms, cylinders, and small cubes were cast for use as a reference for the unconfined expansion. The schedule for the mechanical testing to be conducted during Task 1 and Task 2 was designed to coincide with target values of unconfined expansion. The following is a summary of the unconfined expansion data obtained for the Task 1 and Task 2 concrete mixes.

3.1 TASK 1 EXPANSION MEASUREMENTS

3.1.1 Task 1 Companion Specimens

For each of the three concrete mixes used in the large Block specimens in Task 1, a series of companion laboratory specimens were prepared to independently measure unconfined expansion:

- *75 mm x 75 mm x 285 mm (3 in x 3 in x 11.25 in) prisms (ASTM C1293)*: For each concrete mix, three sets of four (4) replicate prisms were cast for measurement of unconfined expansion; each set of four would be exposed to a different temperature: 25 °C, 38 °C, and 55 °C. These prisms are referred to in the text as “3x3 prisms”.
- *100 mm x 100 mm x 285 mm (4 in x 4 in x 11.25 in) prisms*: Two (2) replicate prisms of larger size were cast for each mix to examine the size effect on rate-limiting parameters such as alkali leaching. These prisms are referred to in the text as “4x4 prisms”.
- *300 mm x 300 mm x 300 mm (12 in x 12 in x 12 in) cubes*. Three (3) cubes were cast per mix. These specimens are referred to in the text as “12-in cubes”.
- *100 mm x 200 mm (4 in x 8 in) cylinders*: Three (3) replicate cylinders were cast per mix to provide both complementary expansion measurements, and to provide specimens for measuring the Damage Rating Index (DRI) discussed in Chapter 4. These specimens are referred to in the text as “4x8 cylinders”.

Expansion in the prisms was measured using gauge pins that were embedded directly into each prism during casting. The 12-in cubes and the 4x8 cylinders had steel gauge reference studs (with a machined ‘demec point’ at the end) installed into small holes (that were drilled into the hardened concrete), and were affixed using a shrinkage-free, rapid-setting epoxy. The details of the arrangement of the studs are discussed below.

The prisms and cylinders were also used for making the material property measurements discussed in Chapter 4. By making these measurements directly on the prisms and cylinders being used to measure expansion, there is a more direct relationship between changes in a material property and expansion.

The general setup for casting the prisms is shown below in Figure 3-1. The prism molds are assembled and sprayed with form release, and tools are made ready. A few of the prisms in the

background have yellow plastic inserts which create a cavity in the prism from which one can measure the internal relative humidity (RH). The storage and measurement of these RH prisms is shown in Figure 3-2.



Figure 3-1. Layout of prism molds and tools in preparation for the Task 1 casting.

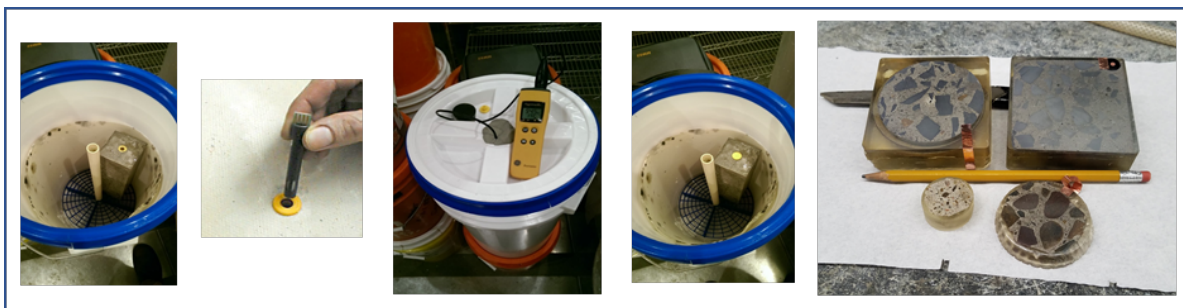


Figure 3-2. Sealed buckets modified for improved ASR expansion measurements have concrete prisms suspended over 1.8 L of deionized water with wicking blotter paper immersed in the water to provide a >95 % RH environment along the entire length of the prism columns. One prism is shown illustrating the plastic sleeve cast-in-place sleeve for internal RH measurement, and post-exposure sectioned specimens embedded in epoxy in preparation for SEM analysis.

3.1.2 Task 1 Expansion Measurements

After casting, the prisms and cylinders were demolded at (24 ± 0.5) h, as per ASTM C1293. An initial length measurement was taken on each prism using a digital comparator with an accuracy of 0.001 mm and a calibrated Invar (nominally, 36 % nickel, 64 % iron) standard reference bar as specified in ASTM C 490/490M (see Figure 3-3). The companion 4x8 cylinders were drilled at the ends, and the pins were epoxied in place. An initial length measurement was taken using Vernier calipers. Subsequent length measurements readings were taken weekly for the first 2 weeks, biweekly through 60 days, and then monthly thereafter.



Figure 3-3. Setup for measuring prism expansion, with Invar reference bar

The prisms and cylinders were stored in 7-gallon pails with vapor-proof lids, and the pails were stored in walk-in chambers maintained at a constant temperature to within ± 0.2 °C of the target temperature. The pails were modified by adding a grate (shelf) to suspend the prisms above 1.7 L of water, and a wicking blotter paper was immersed in the water and surrounded the container interior to ensure at least a 95 % relative humidity environment (Figure 3-2). To provide meaningful companion specimens to Task 1, the pails were initially held at 25 °C while the Task 1 large Blocks were maintained at ambient room temperature. When the heating system was implemented for the large Blocks and the environmental chamber temperature increased to 38 °C, the pails were moved to a 38 °C walk-in chamber to mimic the exposure.

All prism and cylinder expansion measurements were conducted in a walk-in chamber maintained at 25 °C. Specimens exposed to temperatures other than 25 °C were first moved to the walk-in chamber either the night before or a few hours prior to measurement. After the measurement, the specimens were immediately returned to their exposure environment.

3.1.3 Prism Expansion Data

The expansion measurements from the 3x3 prisms are shown in Figure 3-4. The average of the four replicate specimens is plotted, with error bars representing the sample standard deviation. At approximately 280 d, the heating system was turned on for the large Blocks, and the prism specimens were moved from 25 °C to 38 °C. After this age, there is a noticeable increase in the rate of expansion. After nearly 1000 d, the average expansions were 0.32 % (Mix 1), 0.29 % (Mix 2), 0.31 % (Mix 3), and 0.014 % (Control Mix 4).

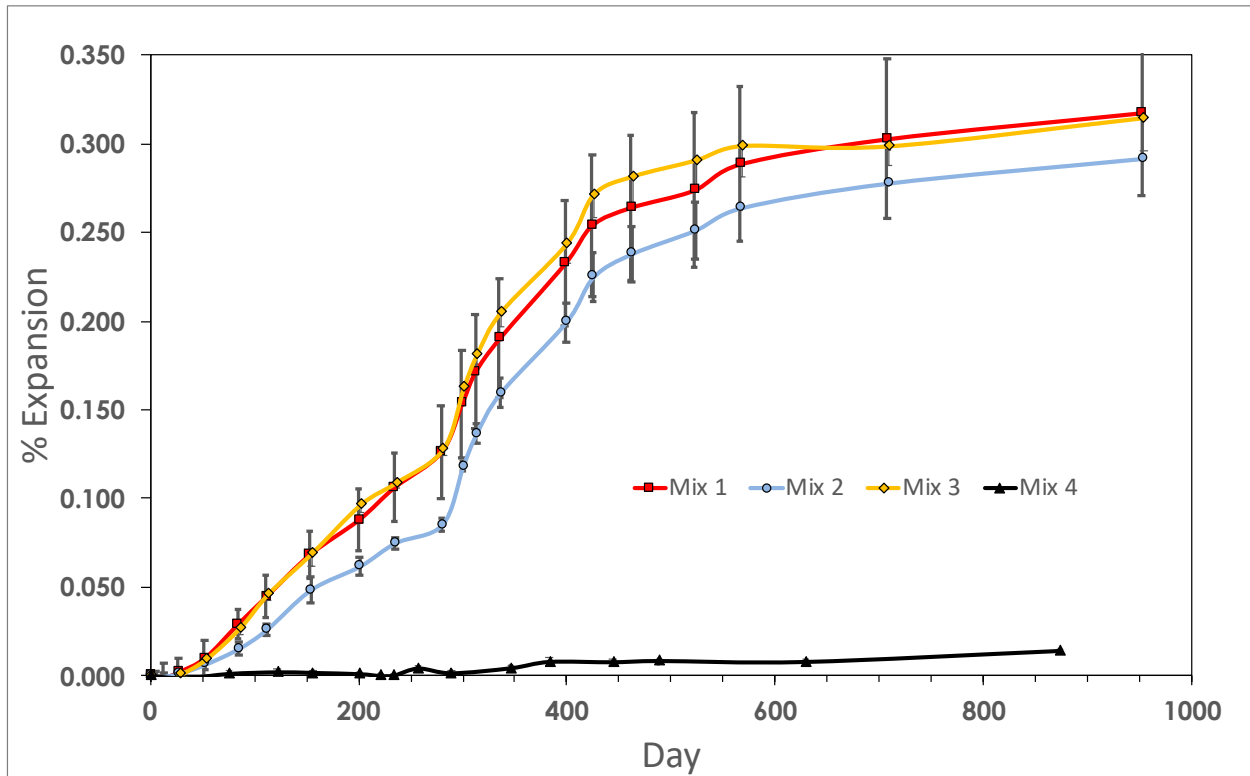


Figure 3-4. Linear expansion in 3x3 prisms cast from concretes for Task 1, Mixes 1 to 4. Results represent the mean and standard deviation from four replicates under 95+% RH, initially at 25 °C until day 280, and then exposed to 38 °C.

The expansion data for the 3x3 prisms was unexpected. The results suggest that there was relatively little difference among the three expansive mixes. This seemed implausible, given the time and effort put into developing the mixture designs. There were a number of possible explanations: the variability in the 3x3 prisms was greater than expected; holding the mixture at 25 °C for 280+ days prior to 38 °C exposure had unforeseen consequences; the concrete mixing and delivering was a very complex procedure, during which an unintentional action could have taken place (e.g., cross contamination of aggregates).

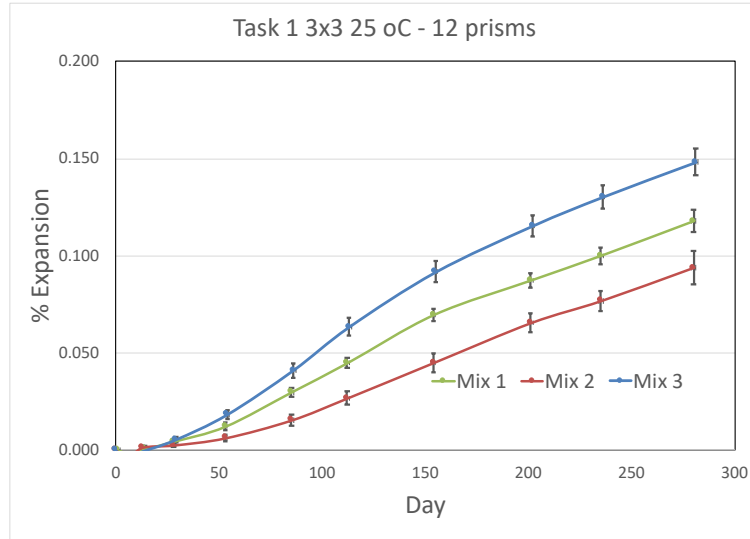


Figure 3-5. Mean expansion of (12) 3x3 prisms held at 25 °C for the first 280 days for each of the Mixes 1 to 3; error bars represent the standard deviation of the mean.

To study this further (and to confirm this unexpected outcome), additional 3x3 prisms were cast from Mixes 1 to 4, and an exposure plan was made to replicate the exposure of the large Blocks. For each mix, separate quadruple replicate 3x3 prisms were designated for 25 °C, 38 °C, and 55 °C exposure. Initially, however, all three sets of prisms were kept at 25 °C. After 280 d, the replicates designated for 38 °C and 55 °C exposure were moved to chambers maintained at those temperatures. (For the subsequent discussion of the expansion data for each Mix, during the initial 280 days there were (12) 3x3 prisms exposed to 25 °C.)

The mean 3x3 prism expansions for each mix, for the first 280 d exposure to 25 °C, are shown in Figure 3-5; the error bars are the standard deviation of the mean. With this larger sample of prisms, the data seem to confirm that the observed ordering from the 3x3 prisms cast with the concretes used in the large Blocks; Mix 2 exhibited the smallest expansion of the three.

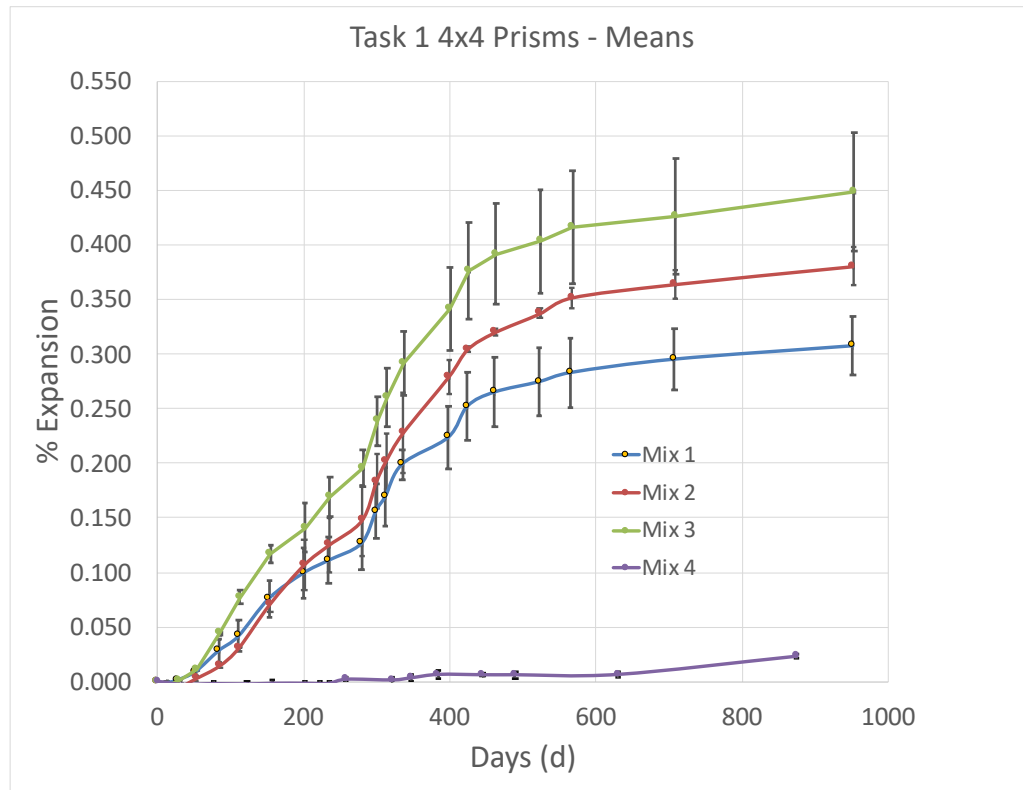


Figure 3-6. Expansion data for 4x4 prisms made with Task 1 Mixes 1-4, initially maintained at 25 °C and then moved to 38 °C after 280 days. Error bars represent the standard deviation of the mean from 2 replicates.

By contrast, the expansion measurements from the companion 4x4 prisms (from the casting of the large Blocks) are shown in Figure 3-6. The values shown are the average of the two replicate prisms (error bars representing the standard deviation of the mean). The 4x4 prisms also exhibited the noticeable change in expansion upon transition to 38 °C, but the ordering of the expansion was consistent with the intended mixture designs. Unfortunately, the uncertainties associated with the small sample size are relatively large, and the measured expansion in Mix 1 was nearly twice the target ultimate expansion of 0.15 %.

Given the contradiction between the 3x3 prism expansion data and the 4x4 prism expansion data, it is difficult to use the prism data to draw a definitive conclusion regarding the progression of the expansion in the large Blocks. Furthermore, the prisms were always stored in a humid environment, whereas the large Blocks were exposed to ambient laboratory relative humidity during the first 280 days.

3.1.4 Cylinder Expansion Data

The arrangement of the gauge studs on the 4x8 cylinders were more involved than for the prisms. The studs were placed on the sides and the ends of the cylinder (see Figure 3-7). The gauge studs on the side of the cylinder were located at two sets of diametrically opposite lines, one set located 38 mm (1.5 in) from the bottom of the cylinder, and the other set located 38 mm (1.5 in) from the top (Figure 3-7). The studs on the ends were used to obtain linear expansion values, and the studs on the sides were used to obtain diametrical expansion data.

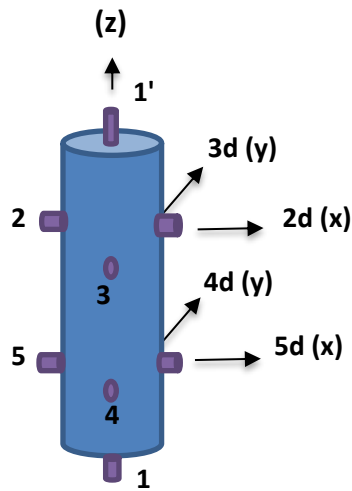


Figure 3-7. Geometry of expansion measurements conducted on cast 4x8 cylinders from the Task 1 Mixes 1 to 4.

The linear and diametrical expansion data are shown below in Figure 3-8 for cylinders initially held at 25 °C for 280 d, and then transferred to 38 °C. For each mix, the mean of three replicate 4x8 cylinders is plotted, and the error bars represent the sample standard deviation. The linear expansion (between the pins labeled 1-1') data are nearly equal for all three mixes. The linear and diametrical measurements are labelled according to the pairs of gauge studs being measured; the diametrical measurements are in similar pairs: 2-2d, 3-3d, 4-4d, 5-5d. The values are roughly consistent with the prism data for Mix 1 and Mix 2, but consistently below the prism expansion data from Mix 3. For this reason, only the linear expansion values were used when comparing the cylinder expansion with the 3x3 prism and 4x4 prism expansion data.

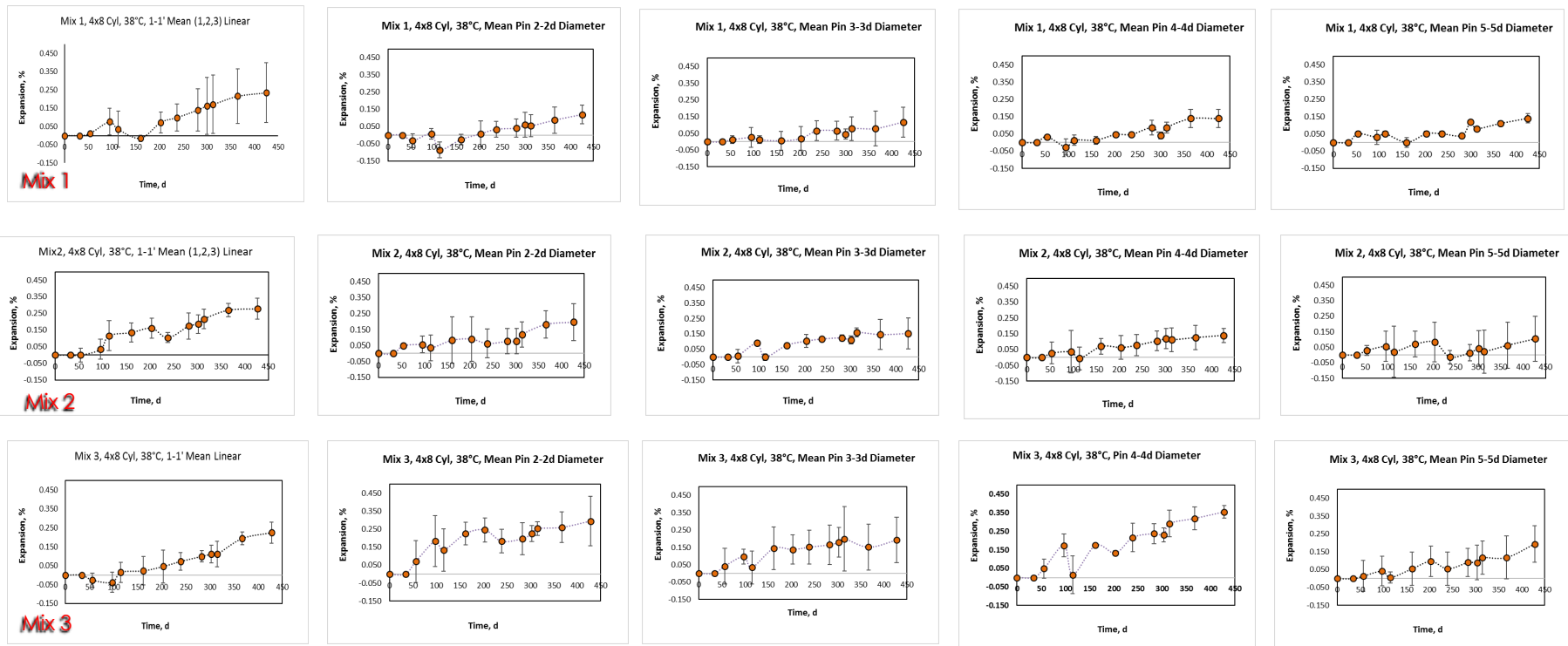


Figure 3-8. Cylinder expansion data from Trial 1 Mixes 1 to 3. Indicated orientation is shown in Figure 3-7 above. The mean of three replicates is plotted, and the error bars indicate the sample standard deviation.

3.1.5 Summary Comparison

For completeness, all the prism and cylinder (linear) expansion data for each mix, following the temperature exposure of the large Blocks, are shown below in Figure 3-9. For Mix 2 and Mix 3, there is a distinction in the apparent expansion from the 3x3 prisms and the 4x4 prisms.

One might conclude that the 4x4 prism data might be more accurate because of the larger ratio of the prism width to the nominal coarse aggregate size, and the overall larger volume of the specimen. Unfortunately, the 4x8 cylinder data do not help resolve this. Although these specimens also have a similar ratio of specimen width to nominal coarse aggregate size, it would appear that the shorter length contributed to a smaller total volume, and a resulting increased variability. Moreover, the 4x8 cylinder data appear to agree better with the 4x4 prism data for Mix 2, but appear to agree better with the 3x3 prism data for Mix 3.

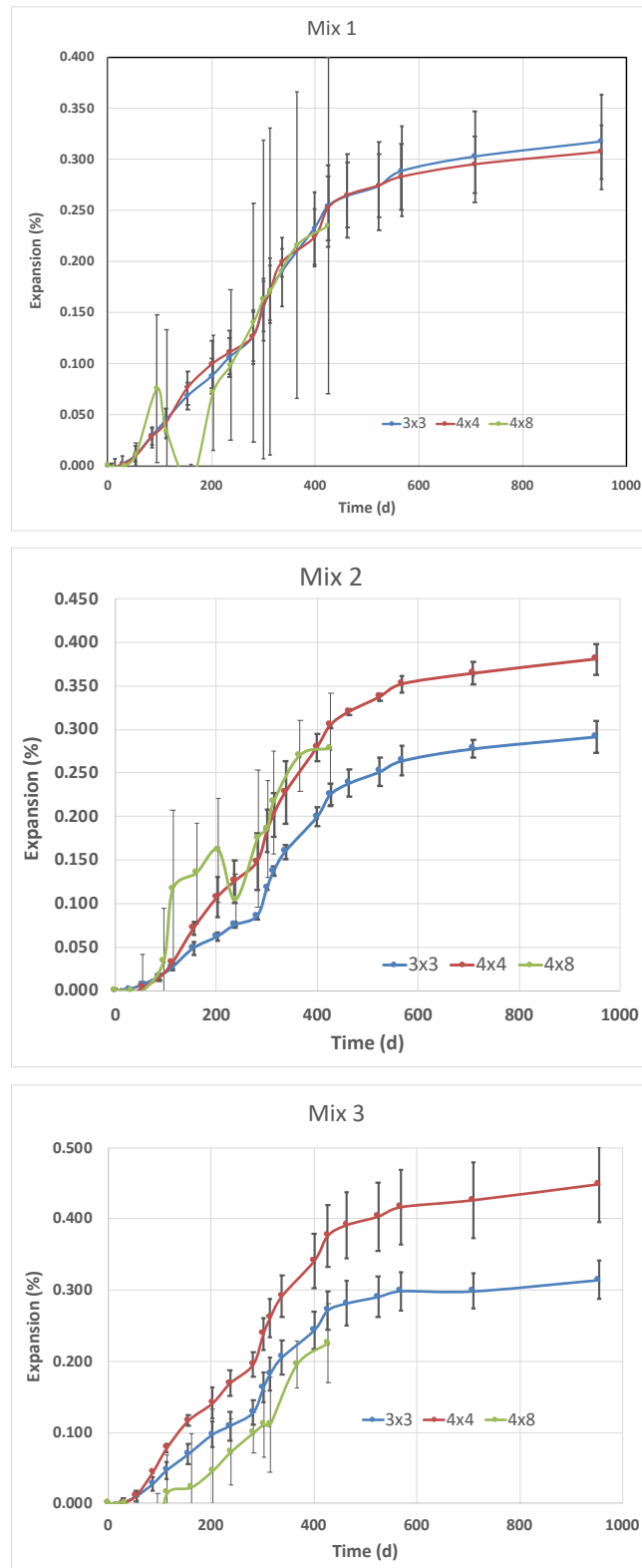


Figure 3-9. Combined 3x3 and 4x4 prism, and 4x8 cylinder expansion data for each mix, following the temperature exposure of the large Blocks.

3.1.6 Deviations of Observed Expansion from Original Mix Design

To confirm the validity of the concrete mixture designs, the prism expansion measurements were repeated (again) with the target mixture designs. Replicate 3x3 prisms were re-cast using the Task 1 concrete mix designs for Mix 1 to Mix 3. The prisms were stored in the sealed pails, suspended over water, and stored in an environmental chamber. Contrary to the Task 1 specimens, however, the prisms were maintained at 38 °C the entire time.

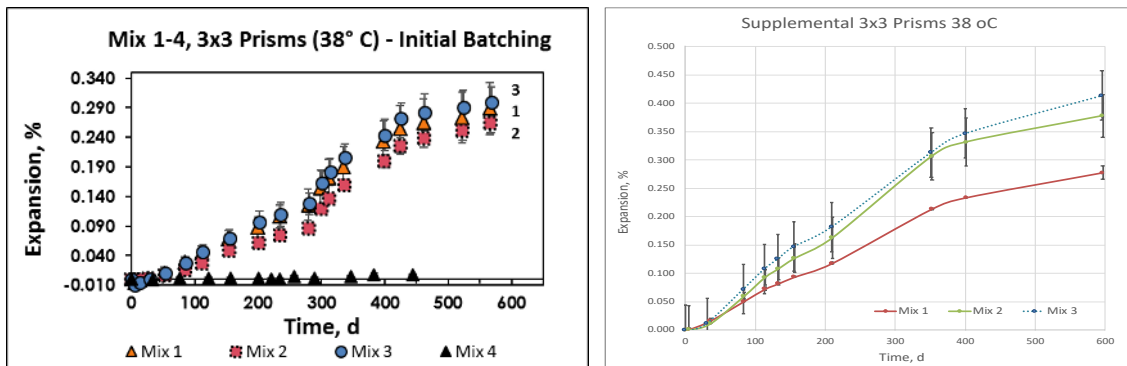


Figure 3-10. Comparison of expansion in the prisms having exposure matching the large Blocks (left) to the laboratory supplemental batching with exposure to 38 °C immediately after demolding (right).

Linear expansion of the original Task 1 prisms (held under ambient conditions for 270+ days before exposure to 38 °C) is compared to the recast prisms (exposure to 38 °C immediately after demolding) in Figure 3-10. Although the mean expansion of the three re-cast mixes was in the intended order of (Mix 1 < Mix 2 < Mix 3), there was considerable variability in the results, and results from Mix 2 and Mix 3 are relatively indistinguishable. However, the Mix 1 expansion for the recast prisms was unquestionably lower than the expansion for Mix 2 and Mix 3. Moreover, it would seem both interesting and odd that the initial 280 d exposure to 25 °C would affect the different mixtures disproportionately. Therefore, deeper study was needed to explain the observed behavior.

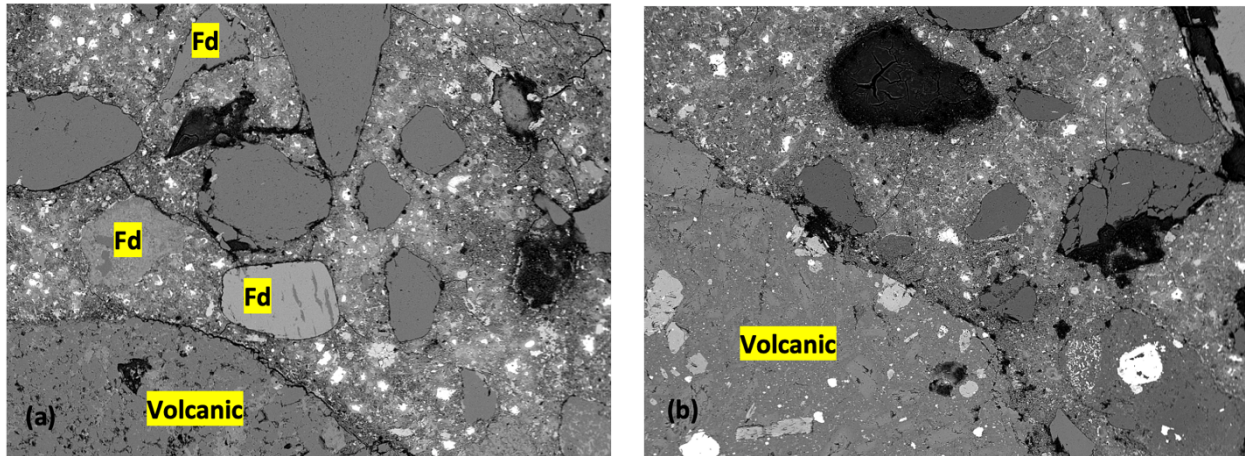


Figure 3-11. (a,b) The presence of minor alkali feldspars (Fd) and complex volcanic materials in the fine aggregate fraction of a representative Mix 1 prism (25 °C, 270 day) indicates that some reactive Jobe sand may have inadvertently been mixed in with Mix 1 materials during the batching of block specimen ASR 1.

Follow up petrographic analysis of the companion prisms cast with Mix 1 of the Task 1 Blocks identified the presence of minor reactive alkali feldspars (anorthoclase) and complex volcanics partially intermixed with the fine aggregate fraction (Figure 3-11); these were also observed in cores taken from the Mix 1 large Block. Because these phases are found in the Jobe sand, this suggests that some minor amount of the reactive Jobe sand may have been introduced to Mix 1 during batching. Mix 1 was designed to have no reactive material in the fine aggregate fraction; the reactive material was only in the coarse aggregate fraction. Although an exhaustive analysis of the unreactive sand was not performed, and although one cannot rule out the possibility of very small amounts of these reactive phases in the nonreactive sand, it is unlikely. This suggests that the enhanced expansion observed in the ASR 1 large block and Mix 1 companion prisms may have been due to some contamination of materials.

3.1.7 Cube Expansion Data

Initially, the 12-in cubes were not meant for companion expansion testing, so their handling was different from that of the prisms. After initial casting, the 12-in cubes were demolded at (24 ± 0.5) h and held at ambient conditions for approximately 30 days, during which no measurements were made on the cubes. After the initial 30 days, it was decided to transfer them to the companion unconfined expansion testing program. The cubes were drilled and gauge studs affixed with epoxy, and after the epoxy cured, the initial dimension measurements were taken. The cubes were then wrapped in burlap, soaked with water, and wrapped in plastic to retain moisture. The cubes remained in ambient laboratory temperature, during which time the cubes were periodically re-wetted to avoid surface drying. When the heating system for the large Blocks was initiated, the cubes were uncovered and moved to the large environmental chamber to experience the same temperature (38 °F) and moisture exposure as the large Blocks.

Prior to taking expansion measurements, the chamber heating and humidifying system was shut off and the temperature and humidity allowed to approach ambient laboratory conditions overnight. Expansion measurements on the 12-in cubes were made from four gauge pins located on each of the five exposed faces of the cube. The measurements were made along

each of three mutually orthogonal directions, including one direction perpendicular to the casting plane. The geometry of the arrangement is shown in Figure 3-12, and images of the blocks are shown in Figure 3-13. Measurements were made using digital calipers that could span 30 cm (12 inches).

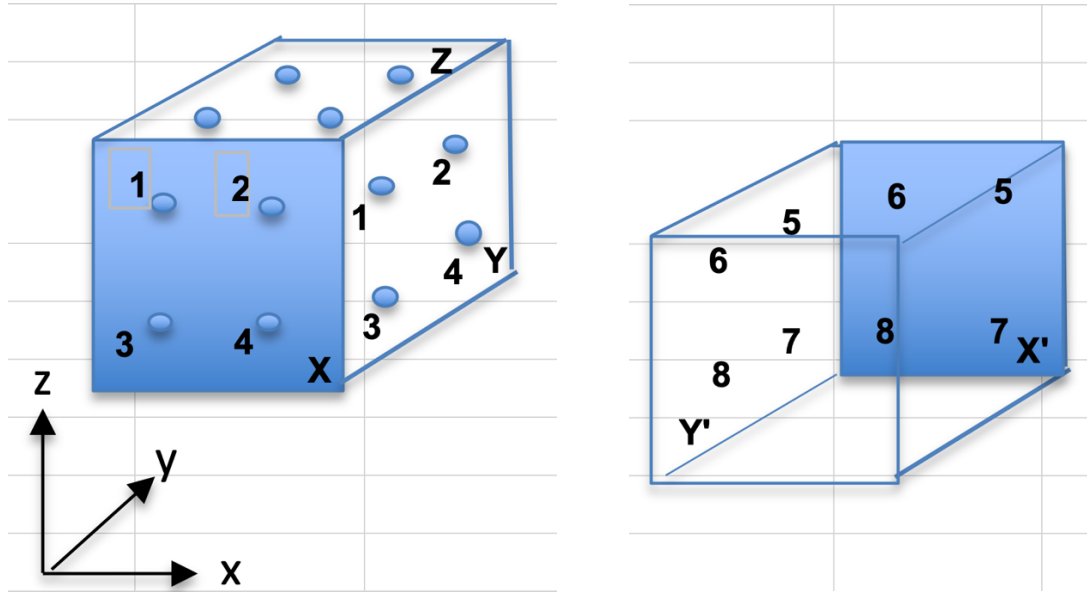


Figure 3-12. Coordinates used for 12-in block expansion measurements.

The expansion direction nomenclature is as follows. The direction X represents the average expansion measured between the two pairs of studs 1-2 and 3-4 of the blue shaded face on the left cube in Figure 3-12. The direction X' represents the average expansion measured between studs 5-6 and 7-8 in the blue shaded face on the right cube in Figure 3-12. The designation X-X' represents the average of the four pairs of studs for each cube. A similar convention is used for directions Y and Y'.

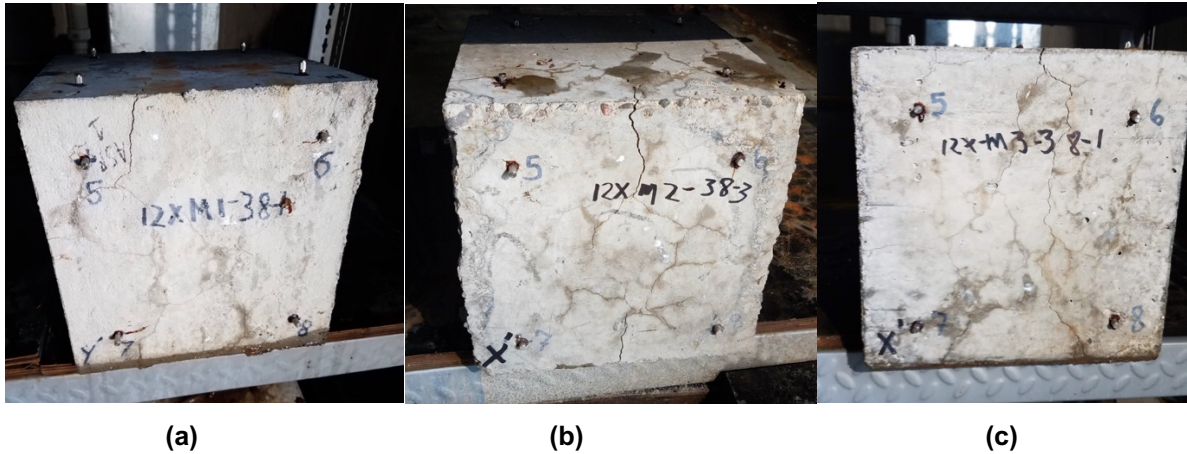


Figure 3-13. 12-inch cubes from Task 1: (a) Mix 1; (b) Mix 2; and (c) Mix 3.

Unconfined expansion measurements for 12-in cubes cast with Mixes 1 to 3 are shown in Figure 3-14 through Figure 3-16; each datum represents an individual measurement, and the variability of values at a given time is an indications of the uncertainty. The average value for each of the three replicate cubes is shown. For the first 300 days, there is little evidence of expansion. After this time, coinciding with increased temperature and humidity generation, the specimens begin to expand noticeably.

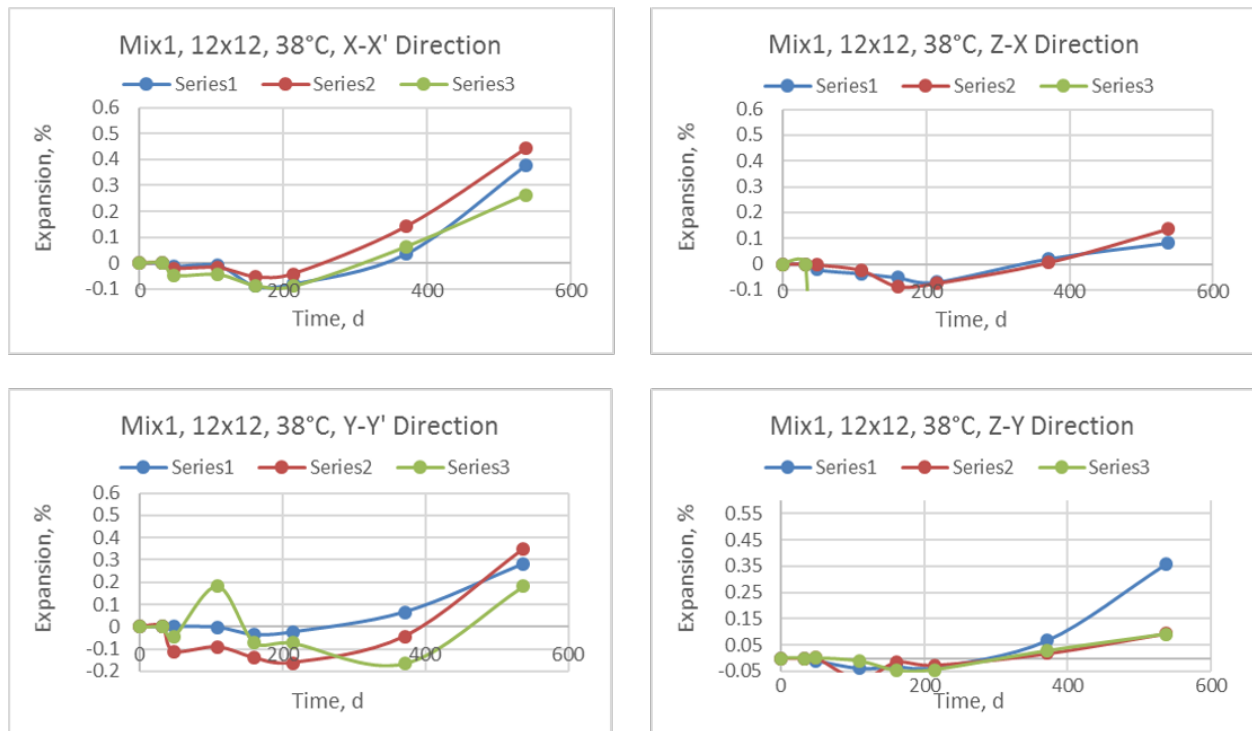


Figure 3-14. Mix 1 individual expansion measurements from 12-in cubes.

This publication is available free of charge: <https://doi.org/10.6028/NIST.IR.8415>

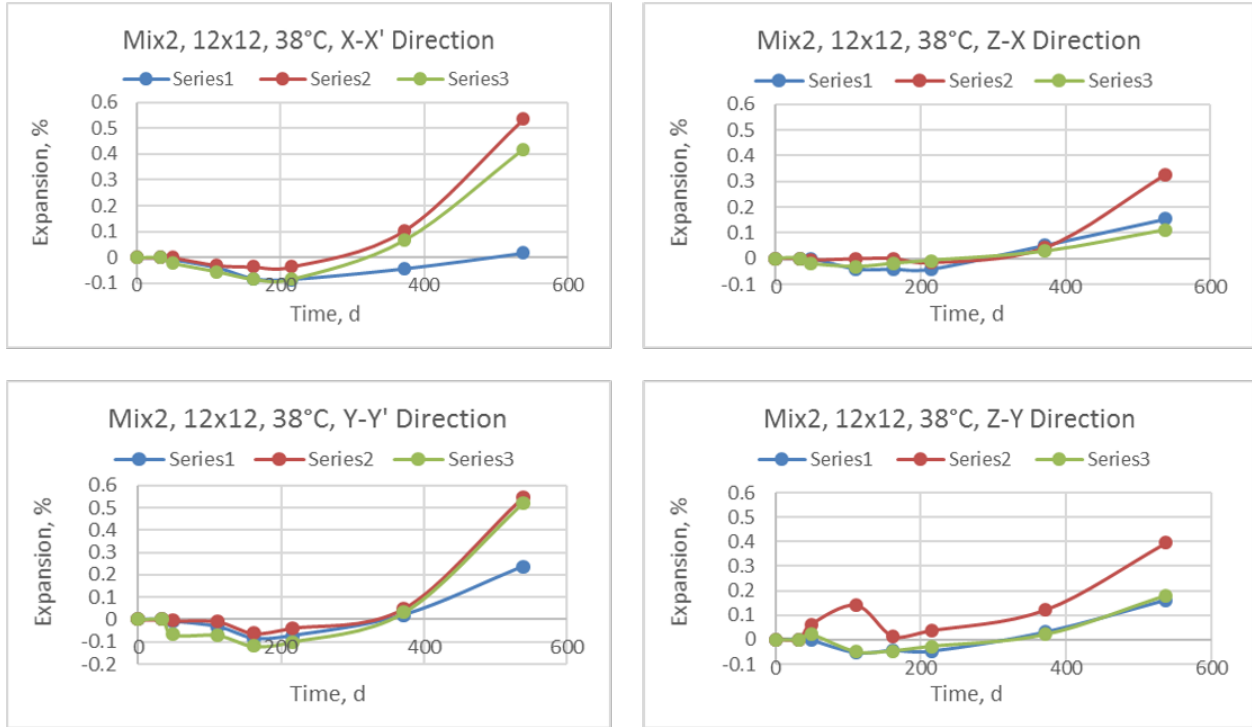


Figure 3-15. Mix 2 individual expansion measurements from 12-in cubes.

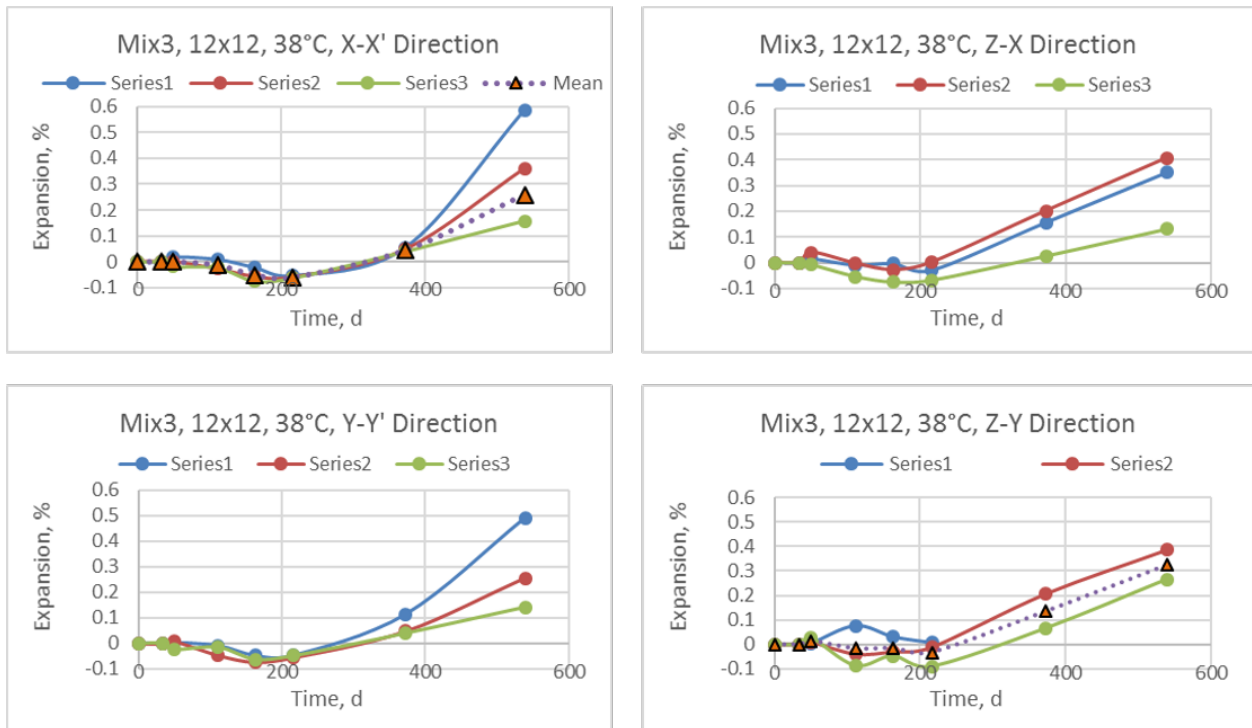


Figure 3-16. Mix 3 individual expansion measurements from 12-in cubes. Dotted lines in X-X' and the Z-Y' plots are averages Series 2 and Series 3.

The data for the X-X' and the Y-Y' pairs are consistent for a given mix, but the data contain sufficient uncertainty/variability that it is difficult to distinguish among the different mixes.

The absence of measurable expansion in the 12-in cubes during the first 300 days is rather perplexing. The cubes were kept moist after the first 30 days of curing, and the temperature exposure was very similar to the large Blocks. This was also surprising because the 12-in cubes were considered large enough to avoid the effects of evaporation. The results suggest that surface expansion measurements may be extremely sensitive to the exposure conditions, and may not be a reliable indicator of interior ASR expansion reaction.

Late-stage expansion measurements occurring after ≈ 400 days were confounded by cracks of ≈ 1 mm or greater in width, which led to the studs becoming loose, and to the measurements becoming unreliable.

These data suggest that surface crack mapping of ASR-affected concrete, and/or surface measurements of concrete expansion may not be a reliable indicator of long-term damage effects in variable climate conditions where the concrete surface can become dry.

3.2 TASK 2 EXPANSION MEASUREMENTS

Task 2 consisted of testing 19 reinforced concrete beams made with the most expansive mix (Mix 3). At predetermined degrees of unconfined expansion for Mix 3, the beams were tested to failure.

A control mixture was made from Mix 3 by adding lithium nitrate. This was done on-site by adding the lithium nitrate to the remaining concrete in the mixer, after all the reactive beams had been cast. Through this process, there was uncertainty in amount of concrete that remained in the mixer. Although a recommended dosage was used, the precise dosage is unknown.

3.2.1 Companion Specimens

For the Task 2 beams study, four (4) companion 3x3 prisms were cast using the concrete supplied for the beams. In addition, two 3x3 prisms were cast using the concrete in the control Beam 11. After 24 h of curing, the prisms were demolded, placed into pails (identical to the Task 1 prisms), and immediately moved into a 38 °C chamber. The pails remained at these conditions until each expansion measurement was conducted. As was done with the Task 1 companion specimens, the prisms were first equilibrated at 25 °C before conducting expansion measurements.

3.2.2 3x3 Prism Expansion Data

The four expansion measurements for Task 2 Mix 3 were averaged, and the results are shown below in Figure 3-17. The data indicate that the Task 2 mixtures exhibited unconfined expansion as expected, reaching approximately 0.50 % at 400 days of exposure to 38 °C.

Also shown in the figure are the average values of the 3x3 prism expansion measurements from the Task 1 Mix 3. There is a noticeable difference in the expansion behavior between Task 1 and Task 2, as would be expected. After approximately 150 days, the mean expansion for the Task 2 prisms exceeded the final expansion of the Task 1 prisms. The primary difference in the material properties between these two specimens is the modulus of the material when the specimen was exposed to 38 °C. Data provided in the next Chapter will show that the ultrasonic

pulse velocity data increases by approximately 20 % over the first 200 days. This would suggest that the expansion that occurs during the early time exposure to the higher temperature, before the concrete has its fully developed stiffness, is critical to the overall expansion for these mixtures.

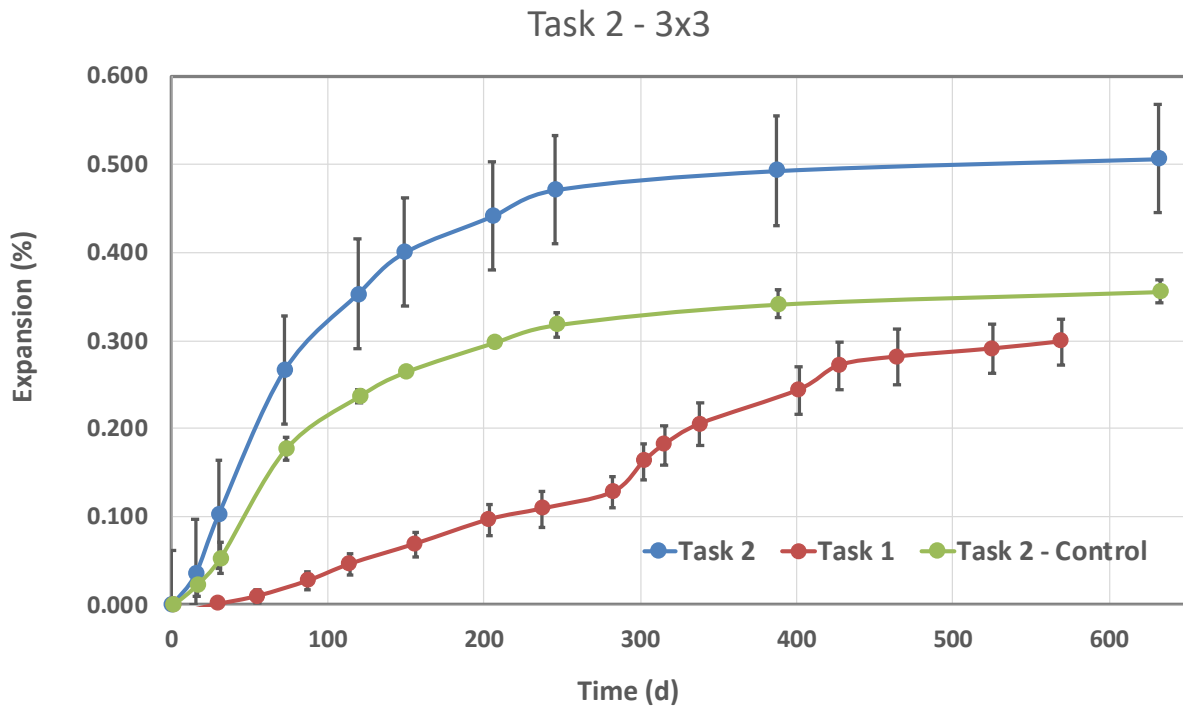


Figure 3-17. Task 2 prism expansion measurements (mean and standard deviation of 4 replicates) for samples maintained at 38 °C and 95 % RH, and comparison with the mean Task 1 prism data for Mix 3 equilibrated initially at 25 °C and then moved to 38 °C after 280 days. Also shown are the average of two replicate prisms made with the Task 2 control mixture.

Also shown in Figure 3-17 are the expansion data for the Task 2 control mixture during casting of beam 11. The symbols indicate the average from the two specimens, and the error bars indicate the standard deviation. At 73 d of age, the mean expansion was 0.18 % expansion. The expansive nature of the mixture is the combined result of the uncertainty in the amount of concrete remaining in the mixer, and the unknown, precisely required dosage.

Chapter 4

MATERIAL MEASUREMENTS

As ASR progresses, the expansive forces can initiate cracking, and the reaction can change the chemistry and microstructure of the hardened cement paste that binds the aggregate. For this project, a number of material properties were measured to help characterize the changes that occurred in the physical and chemical properties, as a function of time and temperature. The objective was two-fold. First, these measurements may be used to study the reaction for the purpose of creating a better understanding of the reaction mechanisms involved, and possibly identify evermore meaningful material parameters. Second, by relating the changes in the properties to the macroscopic expansion observed, one might identify of how far the ASR reaction has progressed.

4.1 DEGREE OF REACTION

When confronted with an existing concrete structure that is exhibiting distress due to ASR, one objective is to determine the *degree of the reaction*. The general concept of a reaction is that there are one or more reactants, and the fraction of the reactants consumed is the degree of the reaction. In the case of ASR, however, one of the reactants is water, which, for the reaction to proceed to completion, may have to be supplied from an outside source. Moreover, the reaction itself can be quite complex, with multiple mineral phases contributing, as was shown in the isothermal calorimetry data in Chapter 2.

From the practical perspective of an existing concrete with ASR, however, one may also be concerned with how much additional expansion is expected to occur. Because of the possible complexity of the reaction, there is no reason to assume that the volume of gel produced (stress generation) is directly proportional to the volume of reactants consumed, at any stage of the reaction. Also, there is no reason to assume that the stress generation (expansion) is directly proportional to the volume of gel produced because the initial gel produced will fill existing void spaces. It is possible, however, that phases that react more slowly (thus contributing more to 'late stage' reaction) may produce either more or less gel per volume of reacted phase. Moreover, the rate of production and the physical properties (e.g., viscosity) of the gel play important roles in the expansive stress development.

As a means of simplifying the situation, the *degree of the expansion* is used as a surrogate for the degree of reaction. Because the expansion is the cause of the cracking and subsequent damage, even if the degree of the reaction is known, one would still need to translate this information into the relevant amount of expansion that would have occurred. In this case, the objective is to relate expansion to material property measurements made on the concrete, and to relate the amount of expansion or change in expansion to the material measurement or the change in the material measurement.

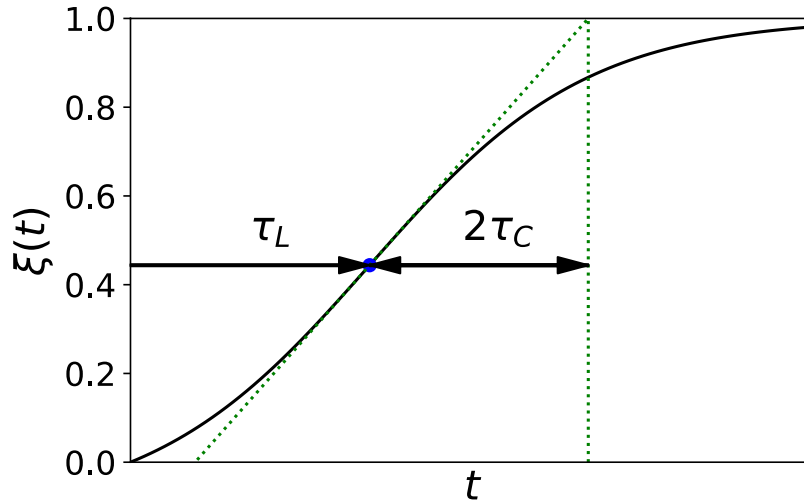


Figure 4-1. The degree of expansion ξ as a function of time t , as characterized by Eq. 4-1 (from Larive, 1998). The latency time τ_L coincides with the inflection point, and the characteristic time τ_C has the geometrical relationship shown.

The expansion that occurs in an unconfined specimen has general form that is relatively common among specimens with ASR. Figure 4-1 is a schematic representation of the relationship, showing the time dependent expansion that could occur over time. The expansion (dimensionless strain) ε can be represented by a product of a time dependent function ξ and the ultimate expansion ε_∞ (from Larive, 1998):

$$\varepsilon(t) = \xi(t) \varepsilon_\infty = \left[\frac{1 - e^{-t/\tau_C}}{1 + e^{-(t-\tau_L)/\tau_C}} \right] \varepsilon_\infty \quad (4-1)$$

The dimensionless function $\xi(t)$ serves as the *degree of the expansion*. The ultimate expansion is defined as $\varepsilon_\infty = \varepsilon(t \rightarrow \infty)$, and it cannot be measured – it must be estimated from the observed data. Equation 4-1 was developed so that identifiable features in Figure 4-1 can be related to parameters in the equation: τ_L is the latency time and $\xi(\tau_L)$ corresponds to the inflection point, and τ_C is the characteristic time and has the geometrical relationship shown in the figure. It is expected that the parameters τ_L and τ_C are a function of temperature and availability of water (a function of the degree of saturation). The ultimate expansion ε_∞ is assumed to be a function of the concrete materials and mixture proportions. The question of whether ε_∞ is temperature dependent, however, is uncertain.

4.2 TESTING PLAN

The following is a summary of the material measurements conducted on samples produced from Mixes 1 to 4. In many cases, the prism and cylinder specimens used for the material measurements were cast at the time of constructing the Task 1 Blocks. For some of the temperature dependence studies, however, separate small batches of prisms were made in the laboratory using one or more of Mixes 1 to 3. Additional material measurements were conducted on drilled cores extracted from the Task 1 Blocks.

Most of these material measurements were conducted at the same time as the Task 1 companion expansion measurements discussed in Chapter 3, using the same specimens. As was done for the expansion measurements, the other material measurements were conducted when the specimens had been equilibrated in a 25 °C environmental chamber prior to performing measurement.

4.2.1 Task 1 Companion Specimens

Table 4-1 provides a summary of the measurements conducted on specimens created at the time of casting the Task 1 Blocks. The cast specimens included the 3x3 prisms, the 4x4 prisms, the 4x8 cylinders, and the 12-in cubes that were discussed previously in Chapter 3. In addition, cores were taken for analysis of residual expansion potential measurements after the Blocks were nearly a year old.

In addition to the expansive mixes (Mixes 1 to 3), Mix 4 was developed as a control mixture (nonreactive aggregate) that was designed not to expand. Materials measurements made using companion specimens from Mix 4, and subsequently exposed to different temperatures, served as a means for comparing the differences between temperature effects and mixture effects.

Table 4-1. Materials measurement plan for the cast specimens and the cores taken from the Blocks, for each of the Mixes 1 to 3. The number of replicate specimens (reps) is show in parentheses.

Sample Type	Temp, °C	Linear Expansion	Diametral Expansion	Electrical Resistivity	Ultrasonic Pulse Velocity	% Mass Change	Internal Relative Humidity	'Soak' Solution Chemistry	Petrographic/ SEM-EDS Analysis	Damage Rating Index (DRI)	Residual ASR Expansion Potential
Cast Specimens (reps)											
3 in x 3 in prisms	25 °, 38 °, 55 °C*										
Measurement (4)		X		X	X	X		X			
Destructive (2)							X	X	X		
4 in x 4 in prisms (2)	38 °C	X		X	X	X		X	X		
12 in x 12 in cubes (3)	38 °C	X [†]									
4 in x 8 in cylinders	38 °C	X	X							0.5%, 1.0% of ϵ_t [†]	
Drilled Cores											
2.75 in x 8 in (2)	38 °C										0.5%, 1.0% of ϵ_t [†]



Figure 4-2. The sealed buckets modified for improved ASR expansion measurements have concrete prisms suspended over 1.8 L of deionized water and are lined with wicking blotter paper to provide a >95 % RH environment along the entire length of the prism columns.

4.2.2 Task 1 Temperature Exposure

The original plan for the companion specimens was to cast them and expose replicate specimens to different temperatures (25 °C, 38 °C, and 55 °C) shortly after demolding the specimens. Due to logistical constraints, however, the Task 1 Blocks were cast and maintained at 25 °C for more than 280 days before the heating and humidity generation were initiated. This was done to provide support to the structural testing by monitoring the equivalent unconfined expansion in specimens in similar exposure conditions to the large Blocks. As a result, all the companion prisms and 4x8 cylinders were kept at 25 °C until the heating and humidity systems were turned on for the large Blocks. At that time, the prisms and cylinders were divided into three groups, and each group of replicates was exposed to either 25 °C, 38 °C, or 55 °C until measurements ceased.

When the Task 1 large Block heating system was turned on, the age of the specimens at the time of this transition was different for the different mixes. For Mixes 1 to 3, this age ranged from 280 to 282 days, so this transition date is referred to as “280+ days” for these mixtures. For Mix 4 (control), which was cast a little more than 200 days later, the transition date is referred to as “200+ days.” When referring to the entire group of Mixes 1 to 4, this transitional temperature exposure is referred to as the *Task 1 Temperature Exposure*.

As described in Chapter 3, the prisms and cylinders exposed to 25 °C and 38 °C were placed into air-tight lidded pails, suspended over water, and stored in walk-in chambers. The specimens exposed to 55 °C were placed in lidded plastic containers, suspended (horizontally) over water, and stored in ovens. Measurements were carried out for nearly 1000 days at 25 °C and 38 °C. The measurements at 55 °C ceased when the plastic containers began failing after approximately 500 days. The numbers in parentheses in Table 4-1 indicate the number of replicate prisms or cylinders that were exposed to each of these temperatures.

Because the samples all experienced the same temperature for the first 200 to 280 days, the resulting measurements do not reflect a strict temperature dependence, in the typical sense. It does, however, provide a measure of how the material properties discussed in Section 4.3 might change due to a change in temperature – albeit only at one given age.

4.2.3 Independent Temperature Studies

To provide a more thorough understanding of the nature of the temperature dependence of the material properties, an additional series of specimens were cast in the lab using the same mixture designs. The number of replicates used for each series is stated explicated in the text describing the results from the measurements.

4.3 MATERIAL PROPERTY MEASUREMENTS

The material measurements conducted on the prisms and cylinders are summarized as follows:

- Linear expansion
- Percent mass change
- Electrical (surface) resistivity
- Ultrasonic pulse velocity
- Relative humidity
- Damage Rating Index
- Residual Expansion Potential

4.4 PRISM – EXPANSION VS. TEMPERATURE

Periodically, throughout the course of this project, 3x3 prisms were cast using one of the mixes, and then exposed to a constant temperature, starting immediately after demolding the specimens. This was done for different mixes and different constant temperatures. The combined data from all these measurement series were used to assess the influence of temperature on the rate of the expansion.

4.4.1 Constant Temperature

The expansion measurements for each of these series of tests were conducted as described in Chapter 3, and are shown in Figure 4-3 through Figure 4-5 for each of Mixes 1, 2, and 3, respectively. The individual expansion measurements are shown with a filled circle. The color of the symbol indicates the series of the test; the color coding is consistent across all three figures. Specifically, the blue symbols indicate individual measurements taken on companion prisms from Task 1 (25 °C, all mixes) and Task 2 (38 °C, Mix 3). The other colors correspond to various other trials conducted throughout the project, but do not correspond to any other data discussed previously.

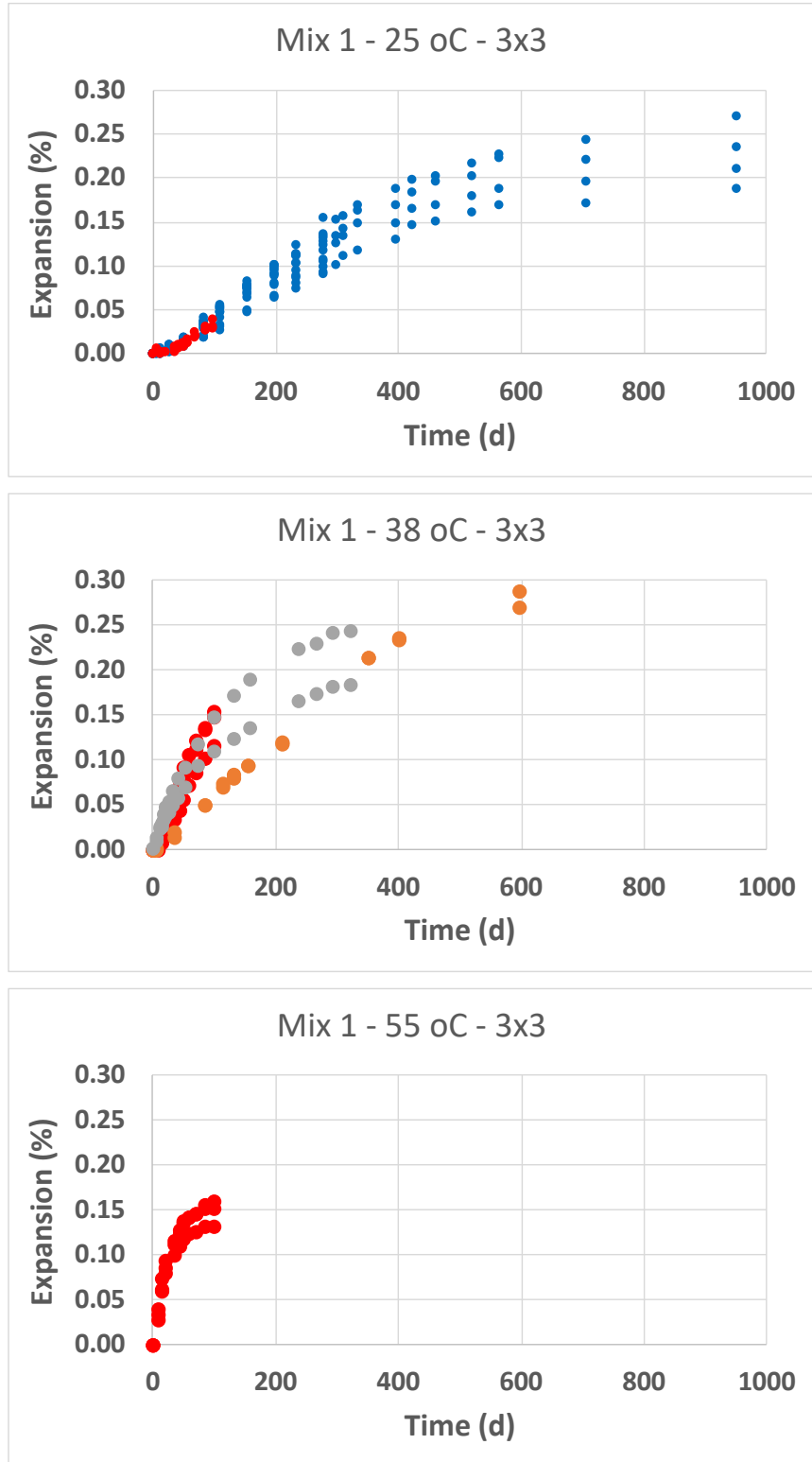


Figure 4-3. Expansion in 3x3 prisms made with Mix 1 and maintained at a constant temperature throughout. Symbols of the same color indicate the same series of testing.

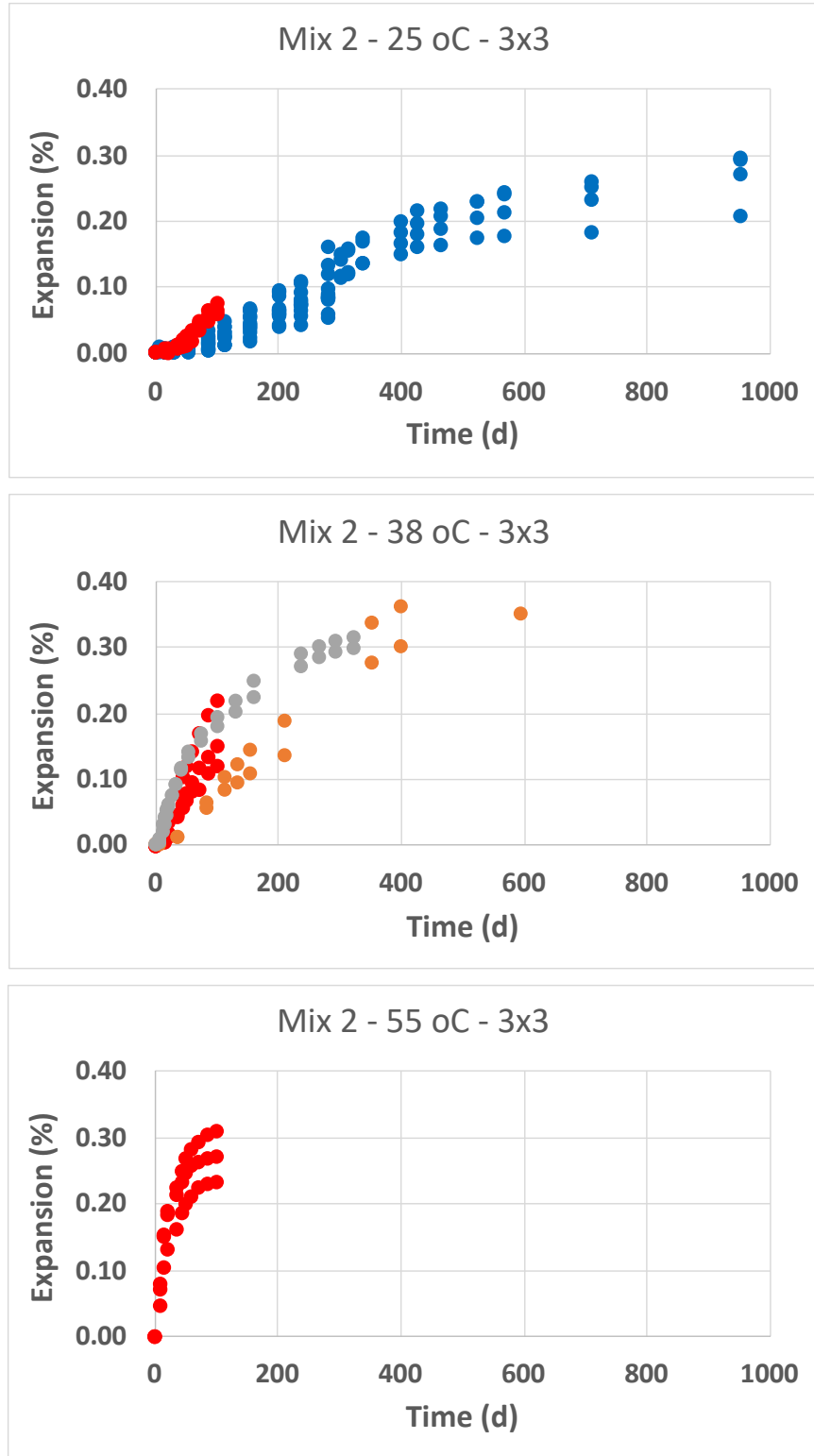


Figure 4-4. Expansion in 3x3 prisms made with Mix 2 and maintained at a constant temperature throughout. Symbols of the same color indicate the same series of testing.

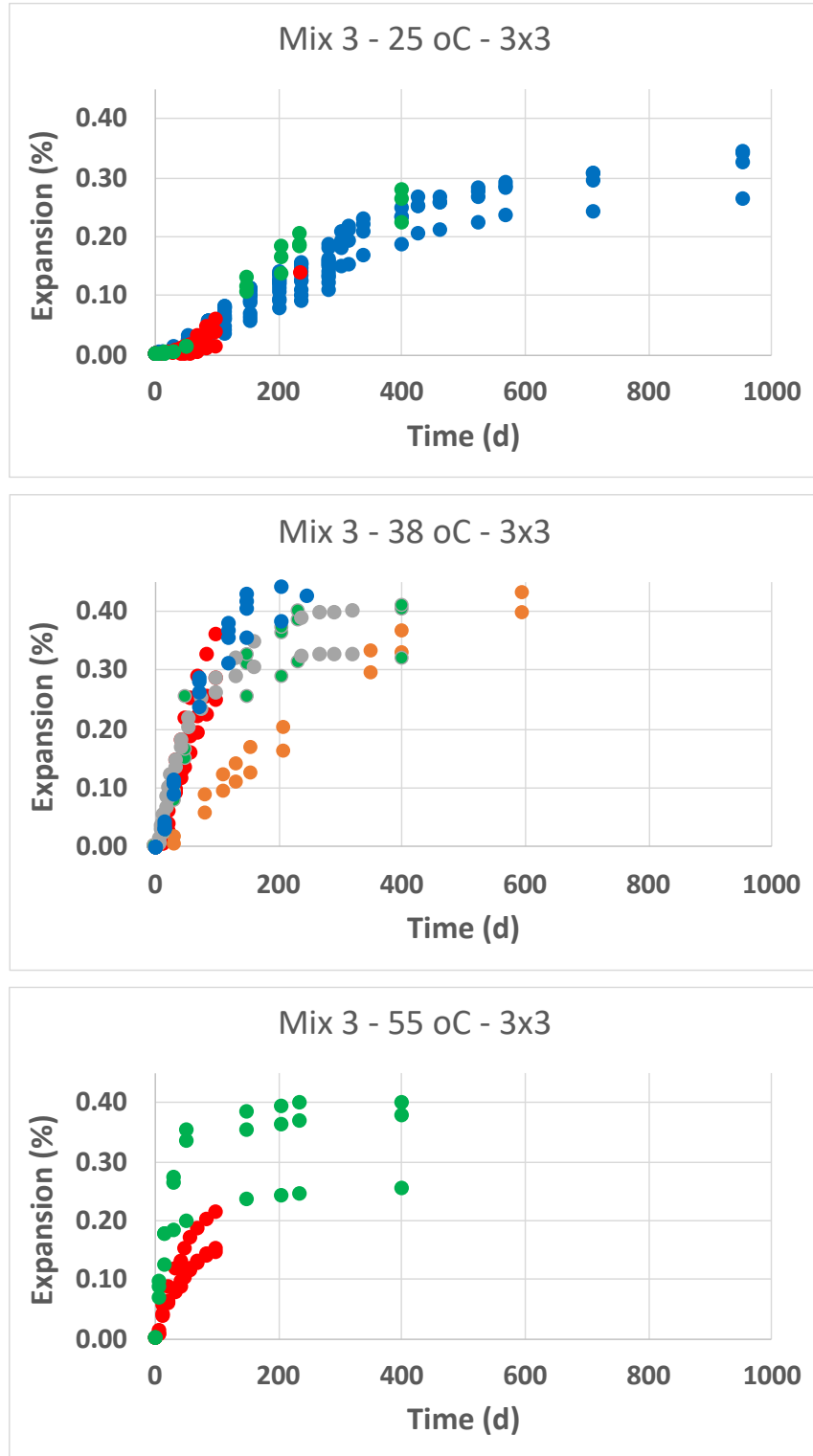


Figure 4-5. Expansion in 3x3 prisms made with Mix 3 and maintained at a constant temperature throughout. Symbols of the same color indicate the same series of testing.

A common assumption of the temperature dependence of a reaction is that changing the temperature merely changes the rate of the reaction; i.e., the nature of the reaction and the ultimate degree of the reaction are unchanged. For a given concrete mix, this implies that there exists a way of scaling the time dependence in such a way so that the data for all the temperatures fall on a single curve.

4.4.2 Temperature Dependent Rate of Expansion

One can observe from the data in Figure 4-3 through Figure 4-5 that as the temperature increases, the rate of expansion increases. If the reaction remains the same but only its rate changes, the curves would only differ from one another by a scaling of the time axis. Assuming this to be true, using the 25 °C data from each mix as a point of reference, the age of the prism at a different temperature could be multiplied by a constant so that the data fall on the 25 °C data.

As an illustrative example, the data in Figure 4-3 through Figure 4-5 are plotted in Figure 4-6 through Figure 4-8, but with the 38 °C prism ages and the 55 °C prism ages multiplied by separate scaling factors denoted in the figure captions. The individual scaling factors were chosen in a somewhat ad hoc manner; the values were adjusted until achieving the “tightest” envelope of data cluster around common behavior.

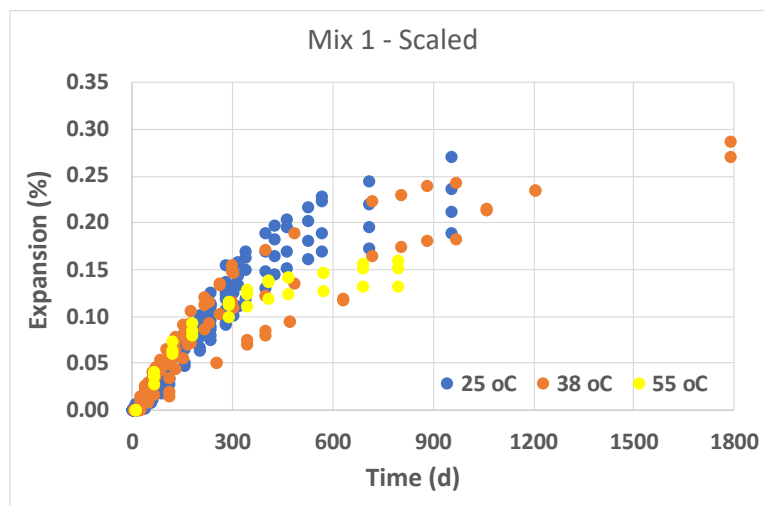


Figure 4-6. Scaled data for Mix 1, where the 25 °C data are plotted as shown in Figure 4-3, the 38 °C prism ages were multiplied by 3, and the 55 °C prism ages were multiplied by 8.

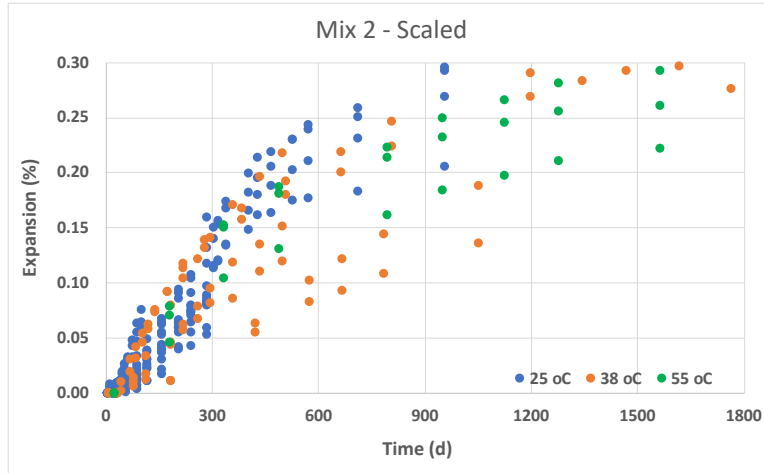


Figure 4-7. Scaled data for Mix 2, where the 25 °C data are plotted as shown in Figure 4-4, the 38 °C prism ages were multiplied by 5, and the 55 °C prism ages were multiplied by 22.

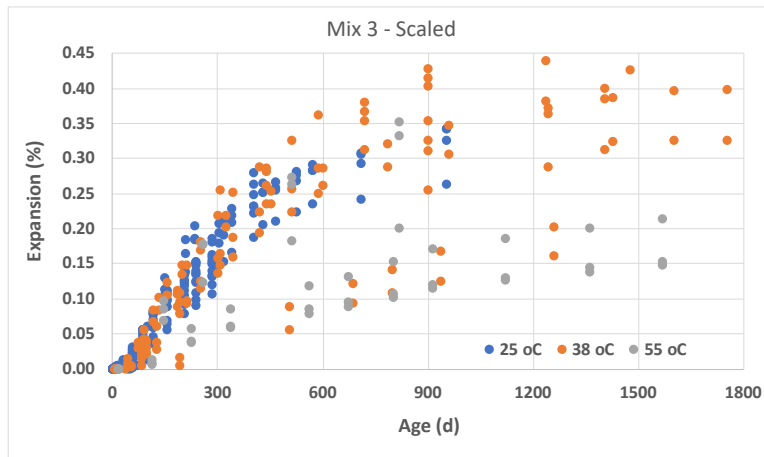


Figure 4-8. Scaled data for Mix 3, where the 25 °C data are plotted as shown in Figure 4-5, the 38 °C prism ages were multiplied by 6, and the 55 °C prism ages were multiplied by 16.

Scaling the data, even in this ad hoc manner, is illustrative for a couple of reasons. Primarily, it reveals the underlying variability/uncertainty in the measurement process. This includes the inherent uncertainty due to specimen-to-specimen variability, revealed in the width of the envelope of data when multiple replicates are superimposed. It also reveals the series-to-series variability; these are replicates of the same mixture, cast on a different day. In large part, the majority of the data fall within a reasonably-defined envelope. A few of the composite images, however, exhibit data that span a much wider envelope. The occurrence of this different behavior was not obvious at the time of the measurements, and it is only after direct comparison with other series that one can recognize the ‘outlier’ nature of a given series.

A major outcome of these results is the demonstrated need for multiple measurement series when working with prism widths that are only 2 to 3 times the size of the largest aggregate. Casting additional prisms for a single series does not overcome the series-to-series variability that can occur.

Another observation is applicability of the symmetric function in Eq. 4-1 to these data. The equation exhibits an initiation phase, followed by a gradually increase rate of expansion. The experimental data exhibit either a very short initiation phase (Mixes 2 and 3), or virtually no initiation phase (Mix 1). Therefore, either different specific ASR reaction types require different shaped expansion curves, or the highly accelerated nature of these experiments cannot be easily translated into a “typical” curve that would be applicable to field concrete.

4.4.3 Variable Temperature Exposure

The Task 1 companion specimens can be used to study how a change in temperature affects the subsequent reaction rate. This effect was provided by the *Task 1 Temperature Exposure* process whereby the temperature exposure changed at 280+ days. The resulting expansion of the prisms is shown Figure 4-9 through Figure 4-11, where the symbols indicate the mean value, and the error bars are the standard deviation of the mean. The data before 280+ days are from the twelve prisms (four replicates for three temperature exposures), and the data after this time are for the four replicates for each temperature.

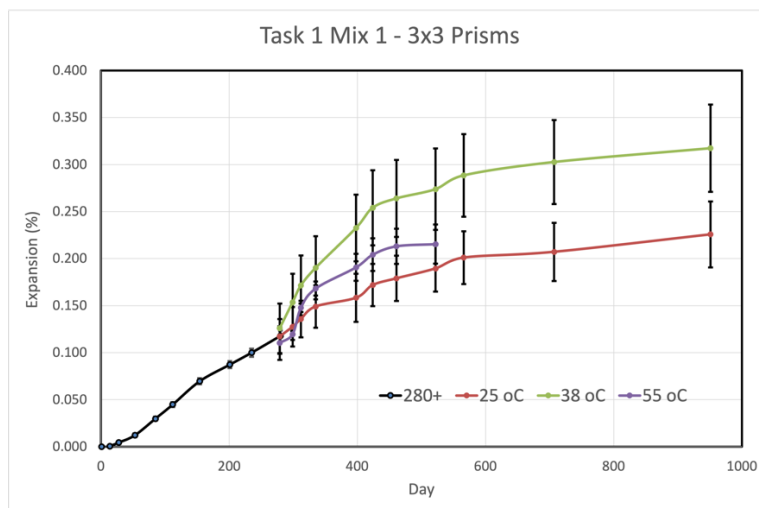


Figure 4-9. Effect of temperature change on Task 1 Mix 1 expansion in 3x3 prisms. Data for the first 280+ days are the mean of all 12 prisms held at 25 °C.

The 3x3 prism expansion data for Mix 1 are shown in Figure 4-9. The 25 °C data after 280+ days appear to be a natural continuation of the data prior to 280+ days. The initial rate of change in expansion after 280+ days, however, appears to be greatest for the samples moved to 38 °C, with dehydration likely affecting the 55 °C samples.

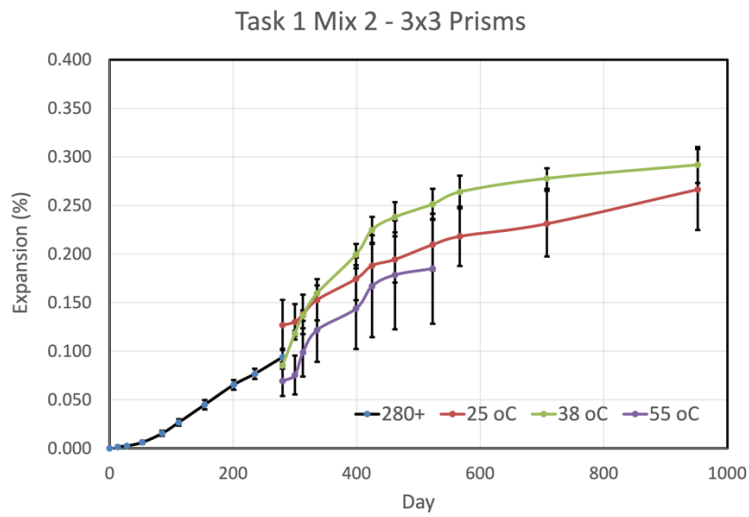


Figure 4-10. Effect of temperature change on Task 1 Mix 2 expansion in 3x3 prisms. Data for the first 280+ days are the mean of all 12 prisms held at 25 °C.

The 3x3 prism expansion data for Mix 2 are shown in Figure 4-10. Although the 25 °C data and the 55 °C data appear to have a discontinuous jump at 280+ days, the slope of the data before and after 280+ days is qualitatively similar. The initial rate of change in expansion after 280+ days appears to be qualitatively equal for the 38 °C and 55 °C data.

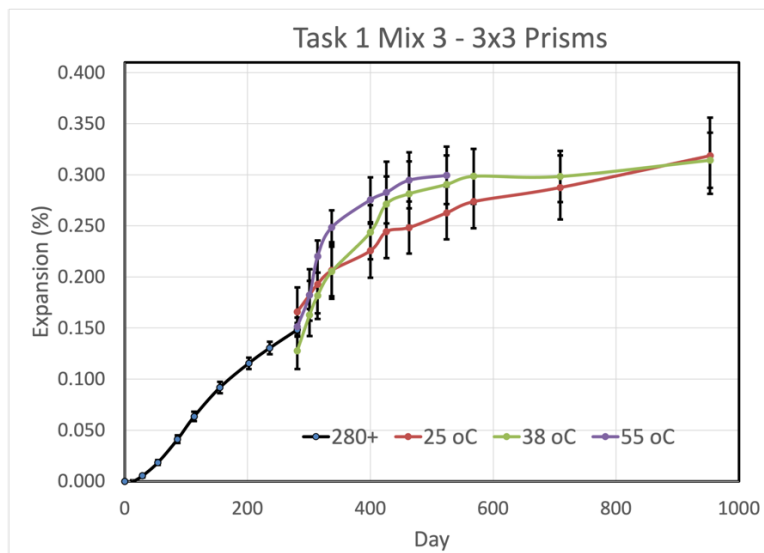


Figure 4-11. Effect of temperature change on Task 1 Mix 3 expansion in 3x3 prisms. Data for the first 280+ days are the mean of all 12 prisms held at 25 °C.

The 3x3 prism expansion data for Mix 3 are shown in Figure 4-11. As with the Mix 2 data, the 25 °C data before and after 280+ days appear to have a discontinuous jump, yet the slope of the data before and after 280+ days is qualitatively equal. The initial rate of change in expansion after 280+ days appears to be greatest for the 55 °C data.

If the time scaling from Section 4.4.2 applies throughout the exposure, one would expect that the change in slope after 280+ days should be consistent with the scaling factors from Figure 4-6 through Figure 4-8. For example, upon the temperature transition at 280+ days for Mix 1, in comparison to the 25 °C data, one would expect the slope of the 38 °C data would be 3 times greater, and the slope of the 55 °C data would be 8 times greater. Similar arguments could be made for the Mix 2 and Mix 3 data, using the corresponding scaling factors.

Note, however, that only for Mix 3 was the expansion for subsequent 55 °C exposure noticeably greater than for the other temperatures. This suggests that there is more to the temperature dependence than merely a scaling of the time. The age at which expansion occurs is a very important aspect of the overall expansion.

This is consistent with the fact that the mechanical properties of the concrete are continuously changing. This is especially true at early ages. The mixtures were designed to expand quickly (at early ages), when the mechanical properties were still changing. Note that the expansion data in Chapter 2 indicated that, for all three expansive mixes, 75 % of the expansion had occurred by approximately 150 d. This could explain why holding the samples at 25 °C for 280+ days prior to 38 °C exposure had a significant effect on the overall expansion, in comparison to samples exposed to 38 °C from the time of demolding. Assuming that, given enough time, the ultimate amount of expansive force generated by a particular mix design is not temperature dependent (it only depends on the mineralogy and the availability of water), the expansion exhibited is a function of the pressure and the mechanical properties of the material. If the majority of the expansive force occurs after the concrete has developed most of its ultimate strength, there will be less expansion than if more of the expansive forces had occurred while the concrete was still developing strength.

4.5 PRISM – RELATIVE HUMIDITY

For each mix and for each temperature exposure, two prisms were specially cast with a re-sealable cavity at one end for making relative humidity (RH) measurements. These prisms were subjected to the *Task 1 Temperature Exposure* and tested periodically after first being equilibrated to 25 °C. A cavity was cast into the prism (see Figure 4-12) to obtain RH measurements at a nominal depth of 73 mm. A commercial RH probe was inserted into the cavity, creating a tight seal, and remained therein until a steady value was recorded (after equilibrating for no less than 6 h). The commercial device was capable of internally correcting for temperature.



Figure 4-12. Details of (left) the RH probe insertion tube to be cast in a prism, (middle) the RH measurement apparatus attached to a sealed specimen, and (right) the measurement arrangement for prisms stored in lidded pails.

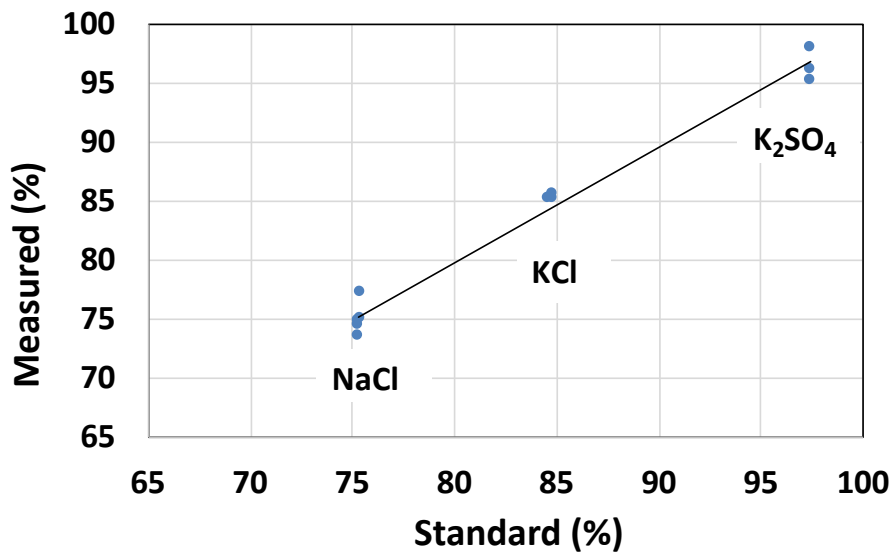


Figure 4-13. Relative humidity (RH) calibration data from standard saturated solutions of 25 °C NaCl (75.4 %), KCl (84.7 %), and K₂SO₄ (97.4 %).

The commercial probe was first calibrated using saturated salt solutions of NaCl, KCl, and K₂SO₄, which are a function of temperature. At 25 °C, the standard RH values are (NaCl) 75.3 %, (KCl) 84.3 %, and (K₂SO₄) 97.3 % (Greenspan, 1977). The calibration data are shown in Figure 4-13, and the regression line relating the Standard value (x) to the Measured value (y) is shown below in Equation (4-2):

$$y = 0.970 x + 2.28 \quad (4-2)$$

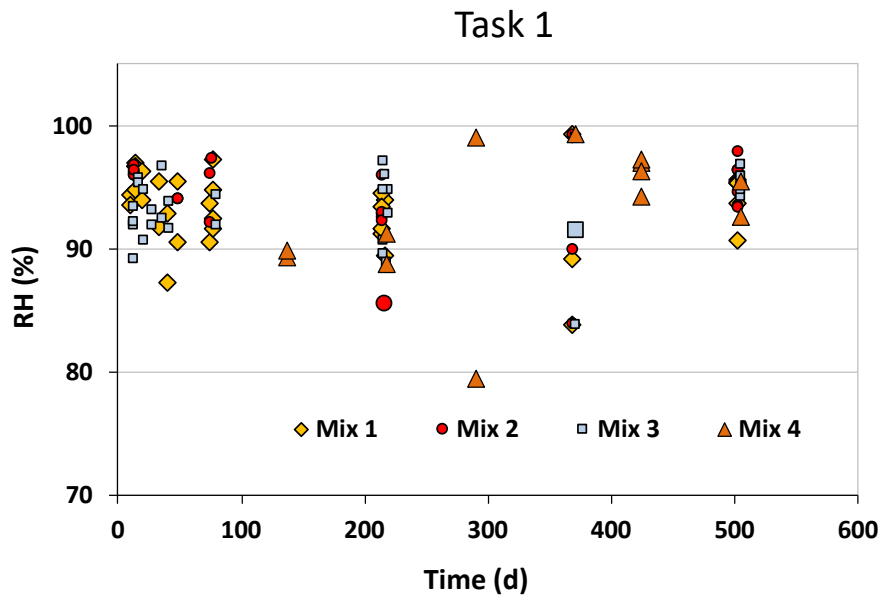


Figure 4-14. Relative humidity (RH) measurements on Mixes 1 to 4 throughout the first 500 days.

The RH measurements on prisms made from Mixes 1 to 4 are shown in Figure 4-14. There is no general distinction among the mixes; no mixture had RH readings that were consistently greater than or less than the other mixtures. Also, the RH values remain relatively constant throughout the first 500 days. As expected, all the RH measurements were above the 75 % RH threshold required for ASR expansion to occur (Poyet et al., 2006). Therefore, as a diagnostic tool for specimens that are expected to be saturated, RH is not a sensitive measure of the ASR degree of reaction.

4.6 PRISM - MASS CHANGE

The mass change measurements were taken from the 3x3 prisms and the 4x4 prisms (Table 4-1), and were conducted under saturated surface dry (SSD) conditions. The premise for making these measurements is that as the prism cracks in a humid environment, the void space and the ASR gel will take up water, thus increasing the mass of the specimen.

The baseline mass change for a submerged, non-reactive concrete can be estimated from the chemical shrinkage that occurs during cement hydration. During cement paste hydration under water, the cement paste will take on water in proportion to the degree of hydration. The quantity of the chemical shrinkage can be estimated using ASTM C1608 (Standard Test Method for Chemical Shrinkage of Hydraulic Cement Paste).

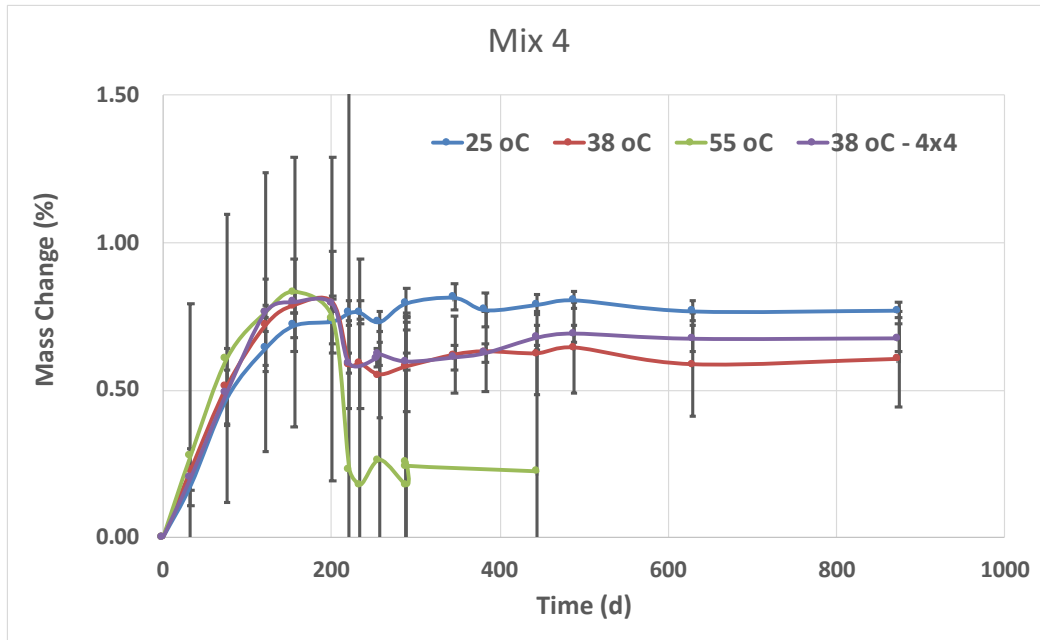


Figure 4-15. Mix 4 (control) percent mass change in 3x3 prisms at 25 °C, 38 °C, and 55 °C, and corresponding values for 4x4 prisms at 38 °C. Average values shown, with error bars indicating the sample standard deviation.

For comparison purposes, the percent mass change in the Mix 4 (control) prisms is shown in Figure 4-15. All of the specimens were held at 25 °C for the first 180+ days. During these first 180+ days, the 3x3 prisms exhibit increasing mass, which can be explained by the chemical shrinkage that would occur during hydration. The chemical shrinkage of pure portland cement is approximately (0.06 g water / g cement) (Bentz et al., 2005). Given that the cement used was approximately 85 % portland cement and 15 % limestone, and that for Mix 4 the cement constituted approximately 14 % of the mass of concrete, the expected chemical shrinkage for Mix 4 is approximately (0.008 g water / g concrete). This estimated value is consistent with the values shown. Moreover, the rate of mass gain during the first 180+ days appears to increase with increasing temperature; the underlying uncertainty prevents any definitive statement.

After 180+ days, when the specimens were exposed to different temperatures, there was greater mass loss with increasing temperature exposure. For cementitious materials, the moisture content is a function of relative humidity and temperature. At a constant relative humidity, the moisture content decreases with increasing temperature (Poyet, 2009). If the specimens were fully saturated, the mass should remain constant at all temperatures (neglecting any small differences in degree of hydration that would occur after 180+ days). Because there was a mass loss with increasing temperature indicates the samples were not fully saturated.

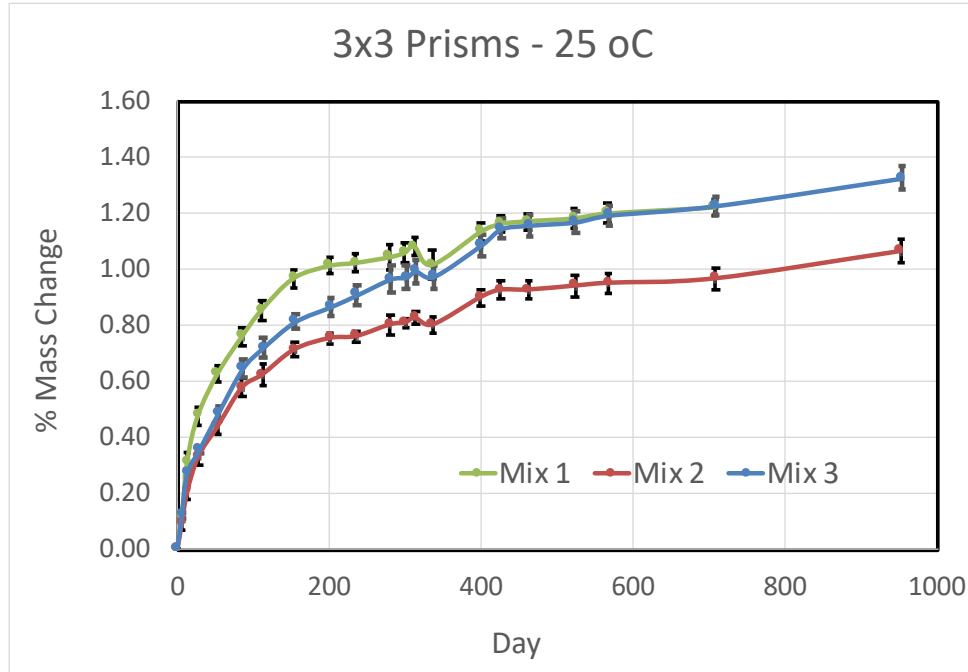


Figure 4-16. Percent mass change in 3x3 prisms from Task 1, maintained at 25 °C. Mean from four replicates show, along with the standard deviation of the mean.

The percent mass change for specimens made with Mixes 1 to 3 and kept at 25 °C throughout are shown in Figure 4-16. Even when the exposure temperature was the same as the measurement temperature, there was an observable “step change” sometime after 300 days. The source of this behavior is unknown and inexplicable. It does, however, provide some measure of insight into the underlying uncertainty of the procedure.

For comparison, the corresponding percent mass change for the same mixes, but maintained at 38 °C throughout are shown in Figure 4-17. These samples also exhibit something of a “step change” in mass, but at closer to 400 days. This suggests that the corresponding behavior in the data for the 25 °C exposure was not unique.

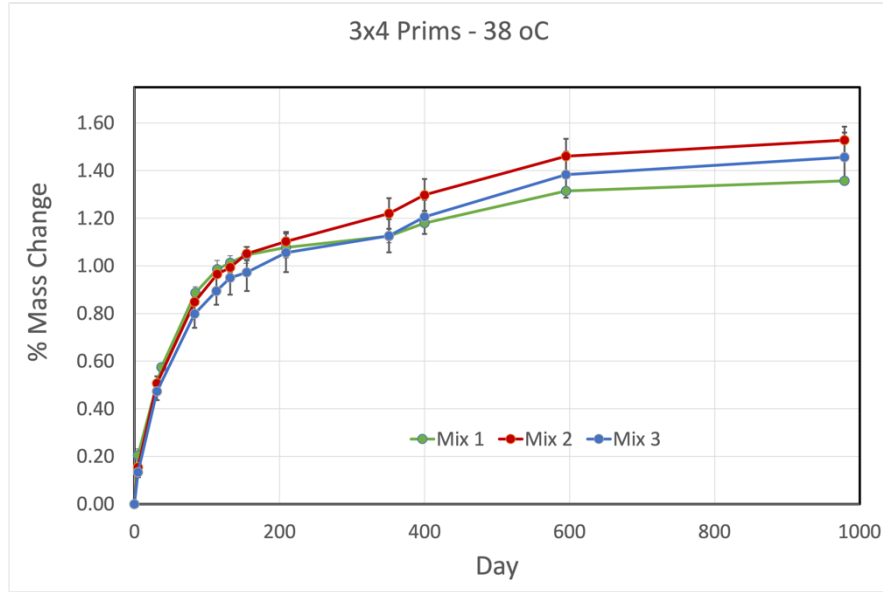


Figure 4-17. Percent mass change in 3x3 prisms from Mixes 1 to 3, maintained at 38 °C. Mean from four replicates shown, and error bars indicate range of data from two replicates.

The percent mass change for Mixes 1 to 3, subject to the Task 1 Temperature Exposure, are shown in Figure 4-18 through Figure 4-20. For the 3x3 prisms, the greater the temperature exposure at 280+ days, the greater the percent mass loss at that time – similar to the control specimens, which suggests a strictly temperature effect (not directly related to the ASR reaction).

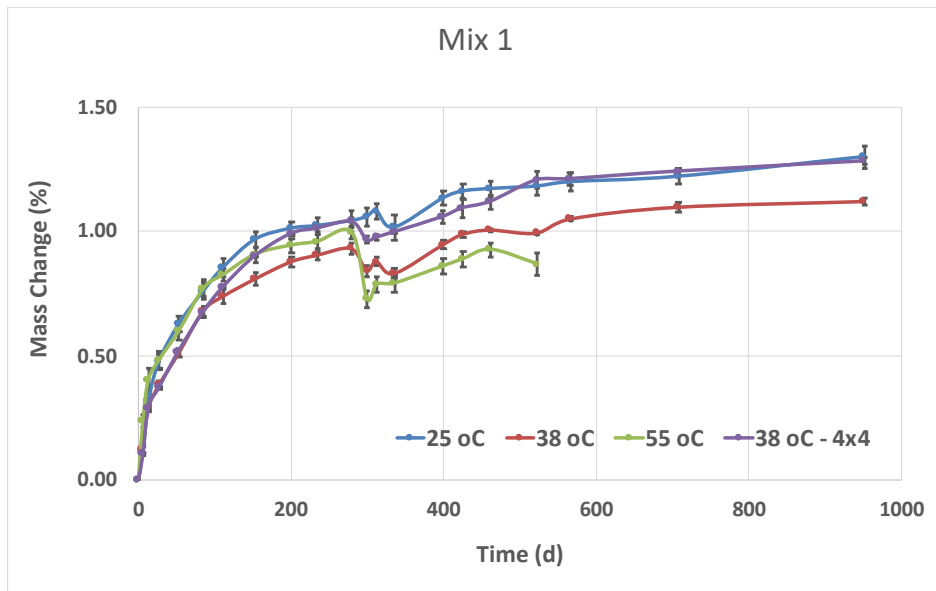


Figure 4-18. Mix 1 percent mass change in 3x3 prisms at 25 °C, 38 °C, and 55 °C (Task 1 Temperature Exposure); also shown for 4x4 prisms at 38 °C. Average values shown, with error bars indicating the sample standard deviation.

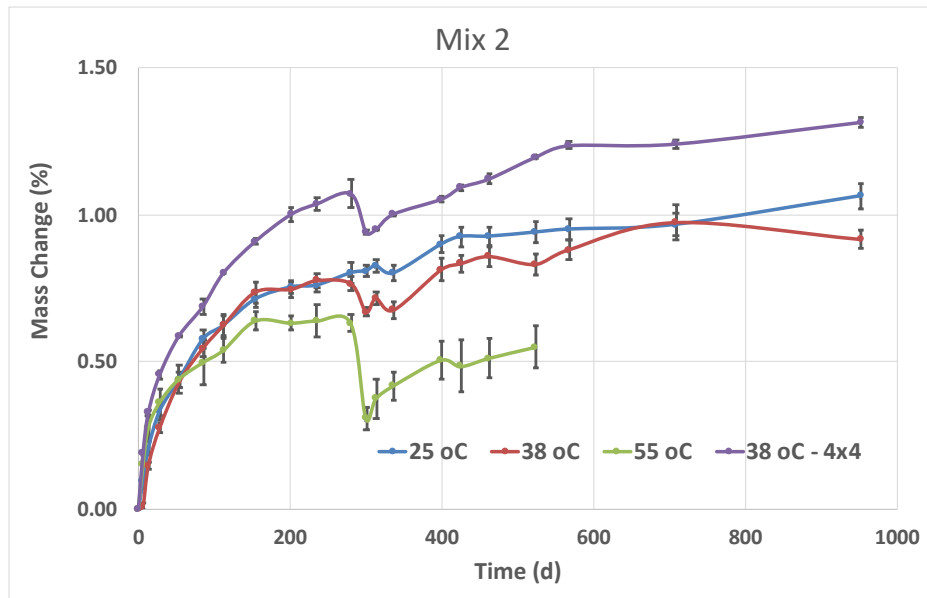


Figure 4-19. Mix 2 percent mass change in 3x3 prisms at 25 °C, 38 °C, and 55 °C (Task 1 Temperature Exposure); also shown for 4x4 prisms at 38 °C. Average values shown, with error bars indicating the sample standard deviation.

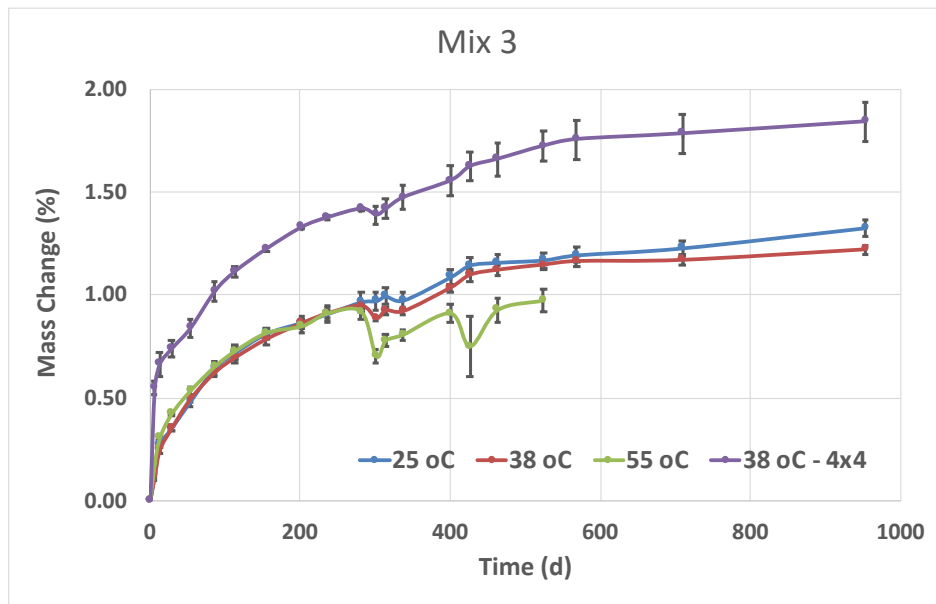


Figure 4-20. Mix 3 percent mass change in 3x3 prisms at 25 °C, 38 °C, and 55 °C (Task 1 Temperature Exposure); also shown for 4x4 prisms at 38 °C. Average values shown, with error bars indicating the sample standard deviation.

4.6.1 Temperature Dependence – Mass Change

Percent mass change was also recorded from a different set of Mix 3 prisms exposed to different constant temperatures immediately after demolding. The recorded values are plotted

in Figure 4-21. The results suggest that, even for the most expansive mix, there is no discernable difference in mass change. Moreover, the rate of increase is the same, despite the different rates of hydration and the different rates of ASR expansion. Therefore, percent mass change is not a reliable means of monitoring expansion (or ASR reaction) in these mixtures.

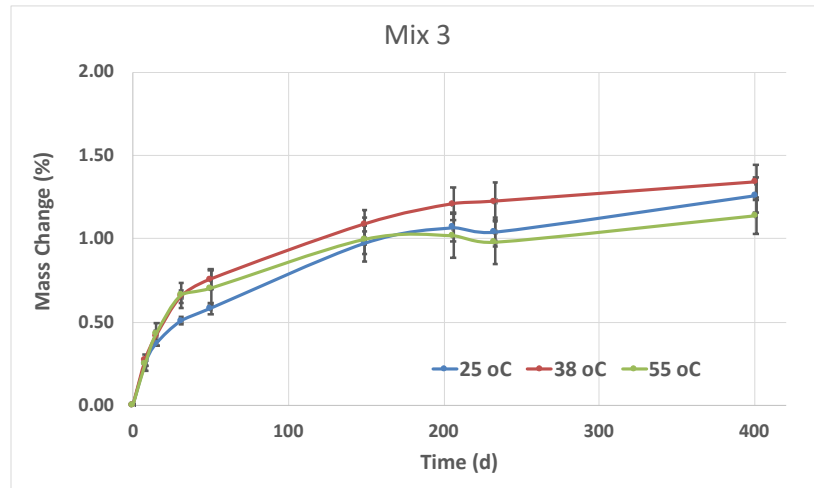


Figure 4-21. Mix 3 percent mass change in 3x3 prisms at 25 °C, 38 °C, and 55 °C, initiated immediately after demolding. Average values shown, with error bars indicating the sample standard deviation.

4.7 PRISM - ELECTRICAL RESISTIVITY

When an electrical potential is placed across a concrete specimen, the current is conducted through the water-filled pore space. The electrical resistivity of a concrete, therefore, depends upon a number of material properties: the pore volume, the degree of water saturation, the connectivity and tortuosity of the water-filled pore space, and the electrical conductivity of the pore solution.

In most intact concretes, the greatest contribution of water-filled porosity is in the hardened cement paste, not the aggregate; the paste porosity is typically 10 % to 20 %, and the pore solution conductivity is typically 10 S/m to 20 S/m (Snyder et al, 2003, and references therein). Cracking, however, can change the electrical properties of the concrete significantly. If the cracks become filled with (highly conductive) pore solution, not only will they increase the water-filled pore volume, their spatial extent can act as “super-highways” of electrical conduction. As a result, one would expect dramatic changes in electrical conductivity as a function of internal cracking (assuming that the cracks are random, or they extend in the direction of the electrical current).

Electrical resistivity was measured using a commercial device designed for measuring the surface resistivity of a cast 4x8 cylinder (Proceq Resipod model 381-20-001). The device has four electrodes, spaced 38 mm (1.5 in) apart, and reports the resistivity to a precision of ± 0.2 k Ω -cm. A schematic of the operation of the device is shown in Figure 4-22, which is based on the Wenner four-electrode method (Wenner, 1916). The measurement consists of four co-linear probes separate by a constant distance a . An alternating current (I) is applied across the

outside pair of probes, and the resulting alternating voltage (V) is measured between the inside pair of probes. The measured resistance (R) is the ratio V/I . The resistivity is calculated from the resistance and geometry factor that depends on the geometry of the specimen. For all the measurements conducted here, the result is the average of four measurements, equally distributed around the specimen. The specifics depend on the geometry of the specimen.

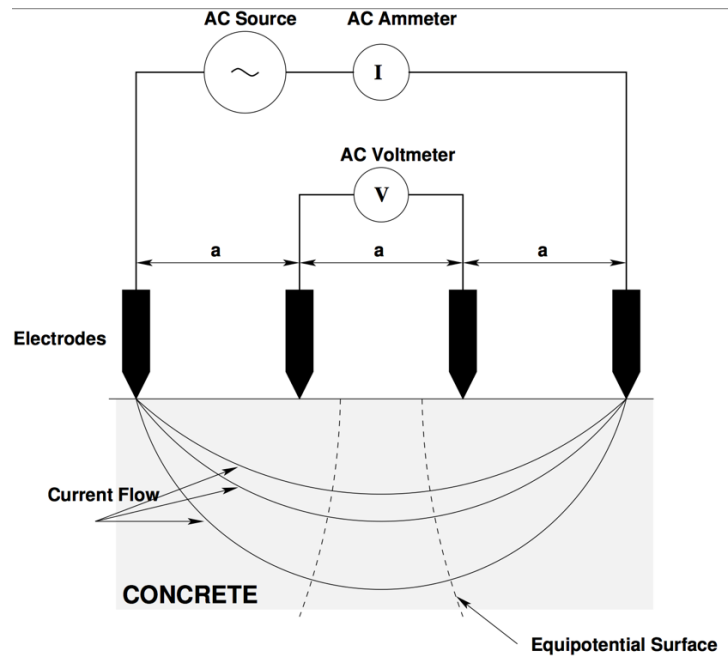


Figure 4-22. Schematic representation of how a concrete surface resistivity device operates.

Wenner developed the method for measuring the resistivity of soils, and the measurement is conducted by placing meter-long probes into the ground at even intervals (over distances on the order of the size of the region being characterized). For this application, resistivity ρ is calculated from the measured resistance R :

$$\rho = 2\pi aR \quad (4-3)$$

This equation uses $2\pi a$ as the geometry factor because it assumes that the region being studied is a semi-infinite half-space. When the technique is used on a finite sample, like a 4x8 cylinder or a 3x3 prism, there is an additional geometric correction factor that must be applied to Eq. (4-3) (Morris et al., 1996). The correct geometric correction factor is required to accurately estimate the resistivity. If, however, the ratio of the measured resistivity to the initial resistivity is sought, the geometry factor cancels out (i.e., it is equivalent to the ratio of the measured resistances).

Unfortunately, most commercial concrete surface resistivity devices do not incorporate this geometrical correction, so the user must be aware of how the device operates and, if necessary, apply the corrected geometric factor, as was done for these measurements. Moreover, the commercial devices were intended for measurements on cylinders. The geometrical corrections for prisms are different. For the measurements done on the prisms from Mixes 1 to 4, the four

probes are arranged longitudinally along the center line of one surface of the prism, and are centered between the ends of the prism. The commercial software COMSOL Multiphysics was used to calculate the correction factors when using 38 mm electrode spacings on 3x3 and 4x4 prisms (285 mm long): 3x3 – 2.11; 4x4 – 1.53 (the device-reported value must be divided by these geometric correction factors).

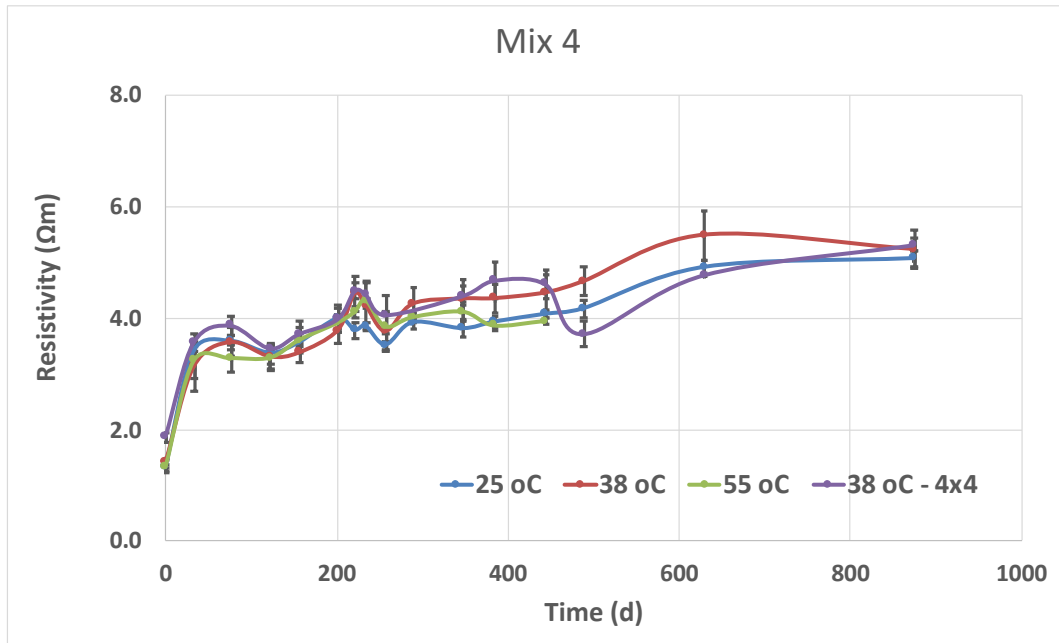


Figure 4-23. Mix 4 (control) electrical resistivity in 3x3 prisms at 25 °C, 38 °C, and 55 °C; also shown for 4x4 prisms at 38 °C. Average values shown, with error bars indicating the sample standard deviation.

The electrical (surface) resistivity of the control mixture (Mix 4) is shown in Figure 4-23. The prisms were subjected to the *Task 1 Temperature Exposure*. The behavior after 280+ days was very similar to the behavior before 280+ days. Moreover, the resistivity is steadily increasing throughout the measurement period, indicating the system continued to hydrate as expected, which is consistent with the conceptual model that a hydrating paste is perpetually filling in void space with reaction product under typical hydration conditions.

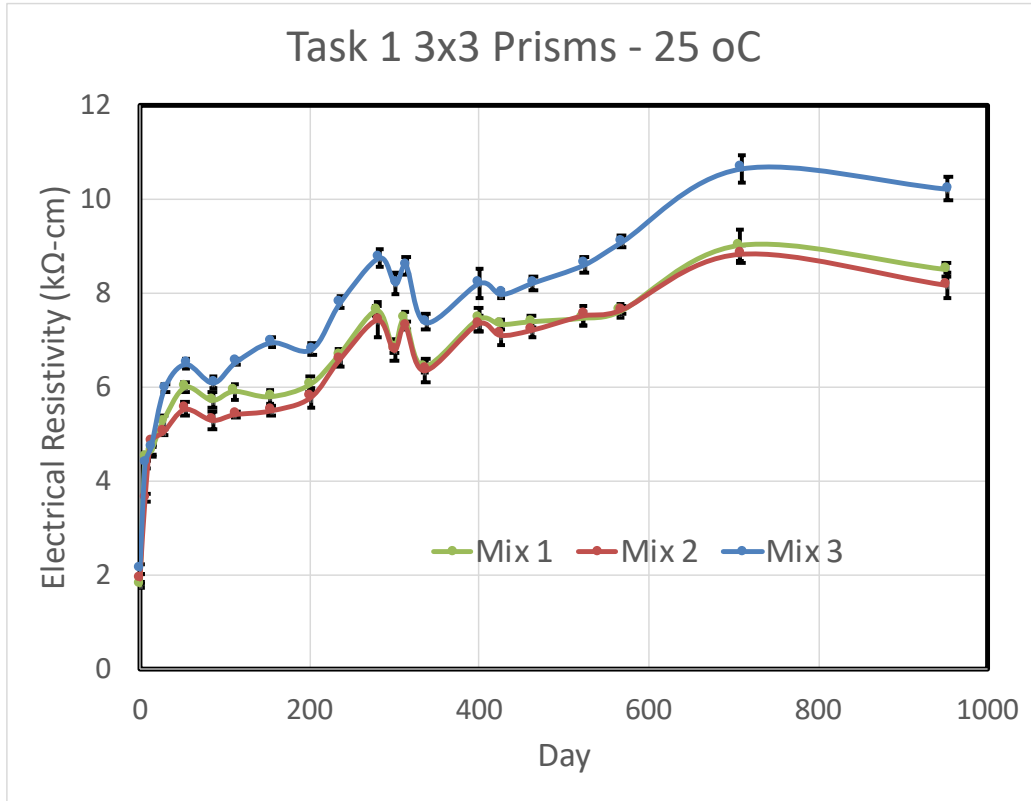


Figure 4-24. Electrical resistivity of 3x3 prisms from Task 1, maintained at 25 °C. Symbols show the mean from four replicates, along with the standard deviation of the mean.

The Mixes 1 to 3 electrical resistivity measurements from specimens maintained at a constant 25 °C are shown in Figure 4-24. As for the control mixture, the resistivity appears to increase somewhat monotonically, at least through the first 800 days. One possible explanation (for the absence of any indication of a deleterious reaction) is that because the rate of the ASR reaction is slowest for this temperature, if the rate of gel formation is only slightly greater than the rate of crack formation, the ASR gel is filling in void space and newly formed cracks at roughly the same rate as they are forming.

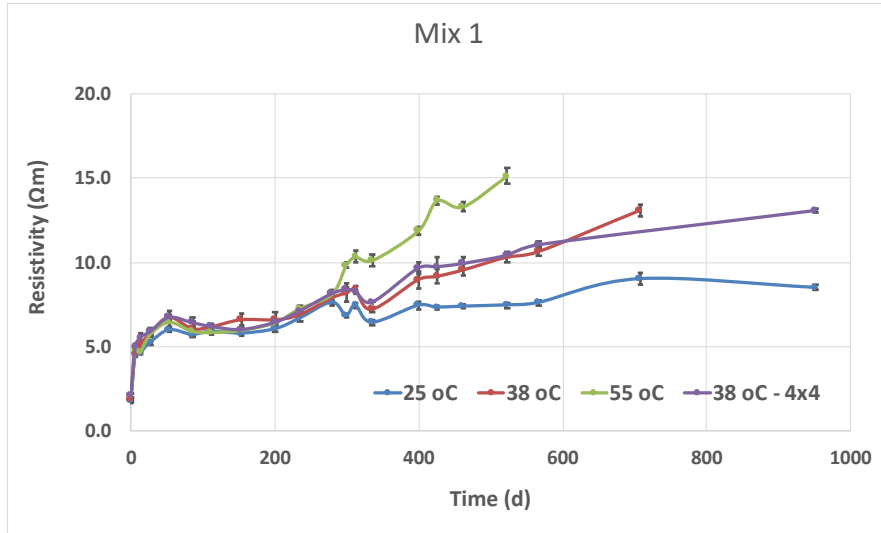


Figure 4-25. Mix 1 electrical resistivity in 3x3 prisms at 25 °C, 38 °C, and 55 °C; also shown for 4x4 prisms at 38 °C. Average values shown, with error bars indicating the sample standard deviation.

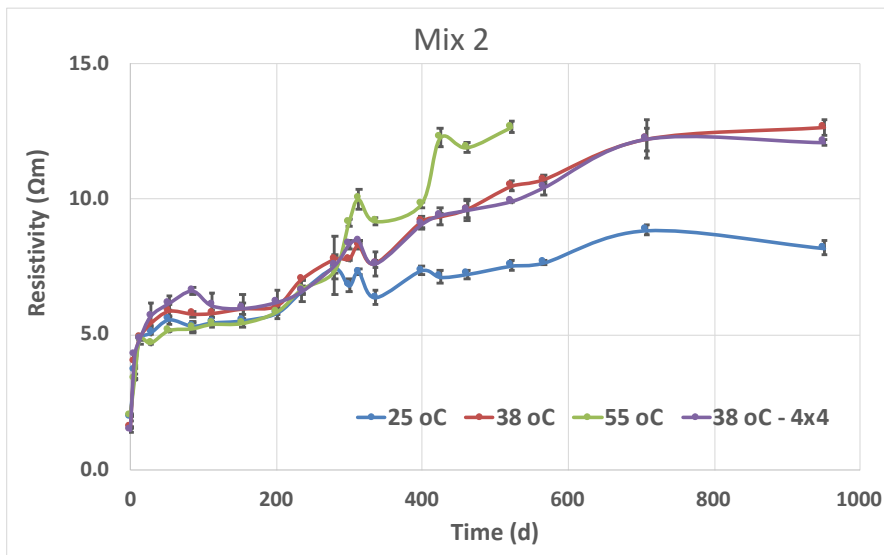


Figure 4-26. Mix 2 electrical resistivity in 3x3 prisms at 25 °C, 38 °C, and 55 °C; also shown for 4x4 prisms at 38 °C. Average values shown, with error bars indicating the sample standard deviation.

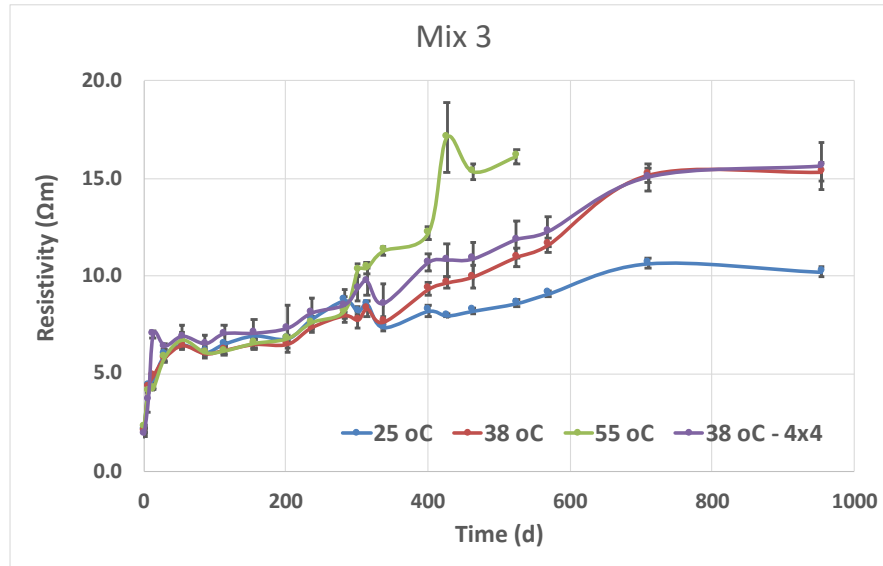


Figure 4-27. Mix 3 electrical resistivity in 3x3 prisms at 25 °C, 38 °C, and 55 °C; also shown for 4x4 prisms at 38 °C. Average values shown, with error bars indicating the sample standard deviation.

The electrical resistivity of the 3x3 and 4x4 prisms from Mixes 1 to 3 subjected to the *Task 1 Temperature Exposure* are shown in Figure 4-25 through Figure 4-27, respectively. For a given mixture, the differences among electrical resistivity measurements are minimal during the first 280+ days. Increasing the temperature after 280+ days increased both the rate of the change in resistivity, and the maximum resistivity attained; this is in contrast to the temperature behavior of the Mix 4 prisms (Figure 4-23) that also underwent the *Task 1 Temperature Exposure*.

This would indicate that increasing the temperature had the effect of increasing the rate of gel formation in such a way as to increase the overall resistivity. There are a number of plausible mechanisms that could account for this. Greater amounts of gel could fill a greater volume fraction of available porosity. In addition, the gel incorporates alkalis from the pore solution (OH⁻ is the greatest contribution to pore solution conductivity), having the effect of reducing the pore solution conductivity. Moreover, over time the gel can solidify, thus becoming a low conductivity solid phase in the paste.

4.7.1 Temperature Dependence – Resistivity

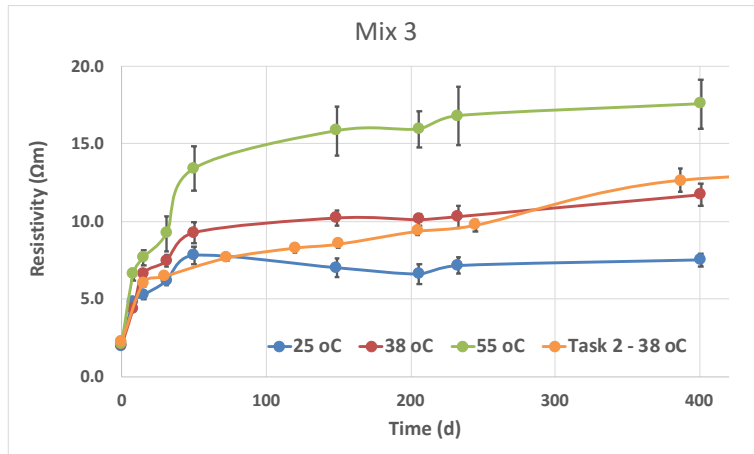


Figure 4-28. Mix 3 electrical resistivity in 3x3 triplicate prisms at 25 °C, 38 °C, and 55 °C, along with the 4 prisms from Task 2. Average values shown, with error bars indicating the sample standard deviation.

The electrical resistivity of prisms made from Mix 3 and exposed to different temperatures immediately after demolding is shown in Figure 4-28. The specimens include a separate temperature dependence experiment with triplicate specimens, and the companion 3x3 prisms made for the Task 2 beams. The initial slope in the electrical resistivity seems to increase with increasing temperature. In addition, the electrical resistivity plateaus at a value that increases with increasing temperature.

This temperature dependence suggests that changes in temperature for an expansive mix have a different effect on the microstructure than for a non-expansive mix. Whereby temperature had no significant effect on Mix 4 (Figure 4-23), it had a noticeable effect on Mixes 1 to 3, for both the *Task 1 Temperature Exposure* and for different constant temperature exposures. The increasing resistivity with exposure temperature, however, is contrary to the increasing rate of damage that one would expect with increasing temperature. One must assume that the internal damage is happening in such a way as to either reduce porosity, reduce available free water, reduce the connectedness of the pore space, or reduce the conductivity of the pore solution. As a result, electrical conductivity does not appear to be good candidate as a diagnostic tool for assessing the state of ASR, or the damage that may have occurred. The resistivity *increased more* in cases that are thought to have more internal damage, contrary to what one would expect.

4.8 PRISM - ULTRASONIC PULSE VELOCITY

The ultrasonic pulse velocity (speed of sound) measurements were conducted using an ACS UK1401 (Surfer) ultrasonic tester designed for use with concrete (see Figure 4-29). It is a hand-held device with two dry-contact probe tips that are affixed 150 mm apart. The device is placed

against the surface of the concrete specimen, and the pulse velocity is estimated from the 50 kHz p-wave propagation time between the probes. For a pulse velocity measurement v , the instrument specifications indicate that the measurement uncertainty is $(0.01 v + 10 \text{ m/s})$. The values recorded in this study ranged from 3500 m/s to 5000 m/s, so the precision of individual measurements was less than 1.5 % for the values shown.



Figure 4-29. Image of UK1401 ultrasonic tester used to measure pulse velocity in prisms and cores.

Surface pulse velocity measurements have the advantage of not requiring access to both sides of a concrete element and the measurement values can be applicable to reinforced concrete elements. The effect of the rebar is to increase the measured wave speed, to an extent that depends, in part, on the ratio of the pulse velocity through steel V_s to the pulse velocity through plain concrete V_c ; the value of which is approximately 1.4 to 1.7. For a concrete cover thickness c and surface UPV probe separation distance L , the contribution of the rebar to the measured wave speed becomes negligible if the ratio satisfies the following relationship (Malhotra and Carino, 2004):

$$\frac{c}{L} > \frac{1}{2} \sqrt{\frac{V_s - V_c}{V_s + V_c}} \quad (4-4)$$

Using the midpoint of the ratio of pulse velocities ($V_s/V_c = 1.55$) and the instrument probe spacing, if the depth of rebar is greater than 75 mm, the rebar should have minimal effect on the measured pulse velocity.

For a concrete with expansive aggregate, there could conceivably be four processes contributing to changes in the UPV: hydration; changing moisture content; cracks/damage creation from ASR expansion stresses; and the filling in of void/crack space by the ASR gel. Processes that densify the microstructure (hydration, increased moisture content, and void/crack filling by ASR gel) should increase the UPV. Decreasing moisture content and the creation of cracks or other types of ASR damage should reduce the UPV.

4.8.1 Measurements on Prisms

Ultrasonic pulse velocity data were measured along the length of each prism, with one measurement taken on each of the 4 sides of a prism. These four values were averaged to

represent the ultrasonic pulse velocity of the specimen. When damage occurs in a concrete specimen, the pulse velocity should decrease because the elastic constants of the bonds between the various components (paste, fine aggregate, and coarse aggregate) decrease, and the existence of voids means that the path of the sound waves becomes more tortuous.

The pulse velocity of the control mix (Mix 4) is shown in Figure 4-30. During the first month, hydration is densifying (reducing porosity within) the microstructure. After this, the microstructure stabilizes, as does the measured pulse velocity. This is to be expected because there is no reason to expect the pulse velocity to change.

The exception was the specimens exposed to 55 °C. After 221 days of exposure, there was a significant decrease in the pulse velocity. One possible explanation for this could be that, at this particular age, the temperature change (i.e., moving between the 55 °C exposure temperature and the 25 °C testing temperature) was sufficient to induce damage (via dehydration), which continued to manifest itself during each subsequent measurements (which required additional “cycling” to 25 °C), resulting in a steady decrease in UPV.

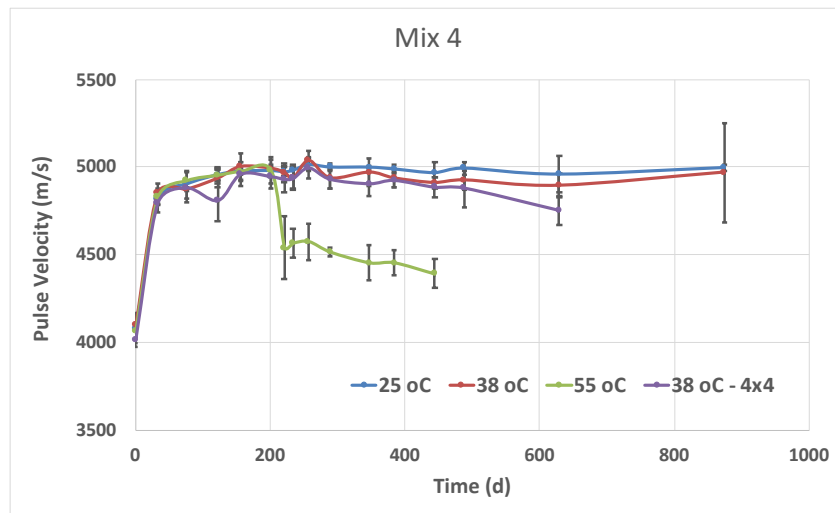


Figure 4-30. Mix 4 (control) ultrasonic pulse velocity in 3x3 prisms at 25 °C, 38 °C, and 55 °C; also shown for 4x4 prisms at 38 °C. Average values shown, with error bars indicating the sample standard deviation.

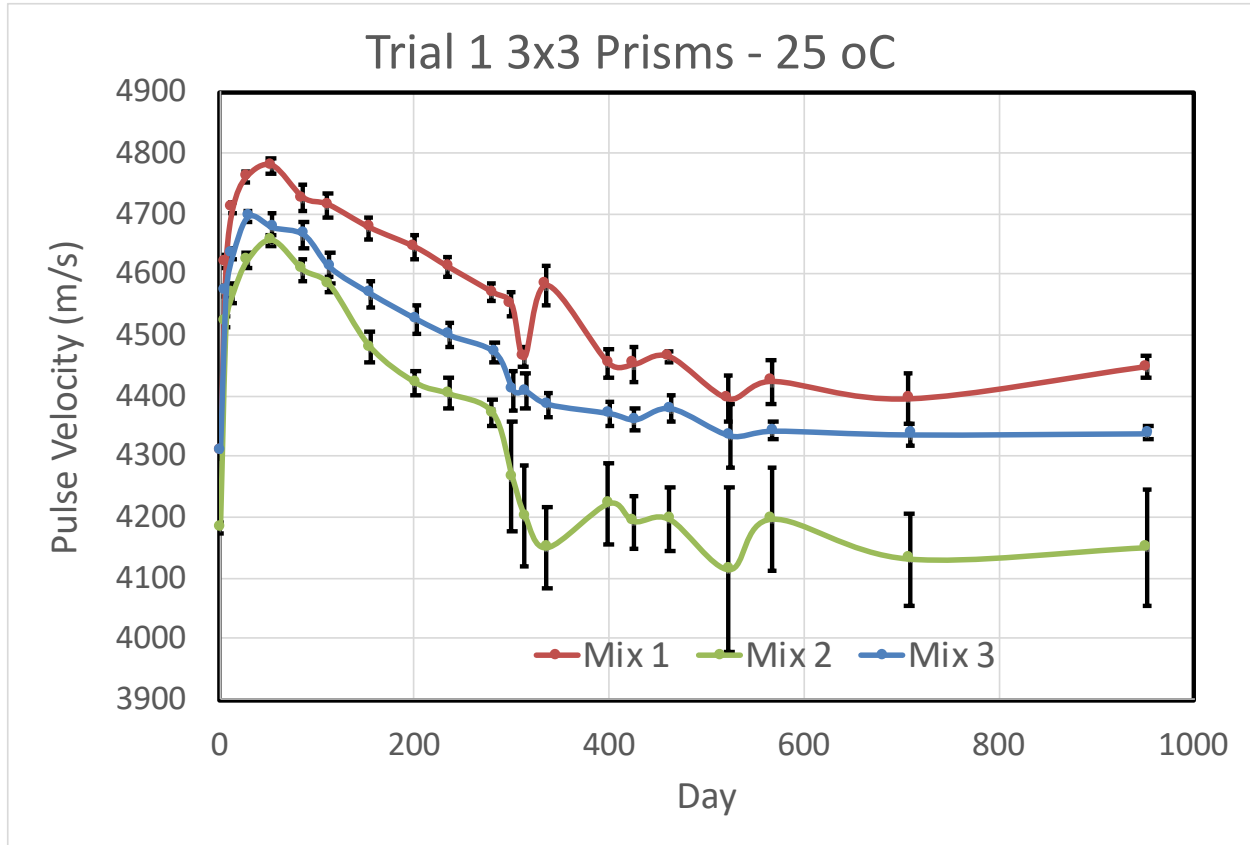


Figure 4-31. Ultrasonic Pulse Velocity (UPV) of 3x3 prisms from Task 1, maintained at 25 °C. Symbols show the mean from 12 replicates prior to 280+ days and from four replicates thereafter, along with the standard deviation of the mean.

The pulse velocity for the Mixes 1 to 3 prisms maintained at 25 °C is shown in Figure 4-31. After an initial increase due to hydration, the three mixes exhibited a monotonic decrease in pulse velocity, plateauing after approximately 500 d. The pulse velocity values at the plateaus suggest that the damage is greatest in Mix 2, with Mix 1 and Mix 3 having similar amounts/types of damage.

Another mitigating factor is the nature of the ASR gel that is formed from the reaction. Initially, the gel is a liquid. Over time, however, the gel can become more viscous and harden. Even though the expansion continues to increase between 400 and 800 days, the UPV was relatively constant. The plateau value is probably a function of both the degree and nature of the damage created by the expansion, and the mechanical properties of the hardened gel. Ergo, the UPV seems to be a more sensitive measure of damage during the early stages of the expansion, but not the later stages.

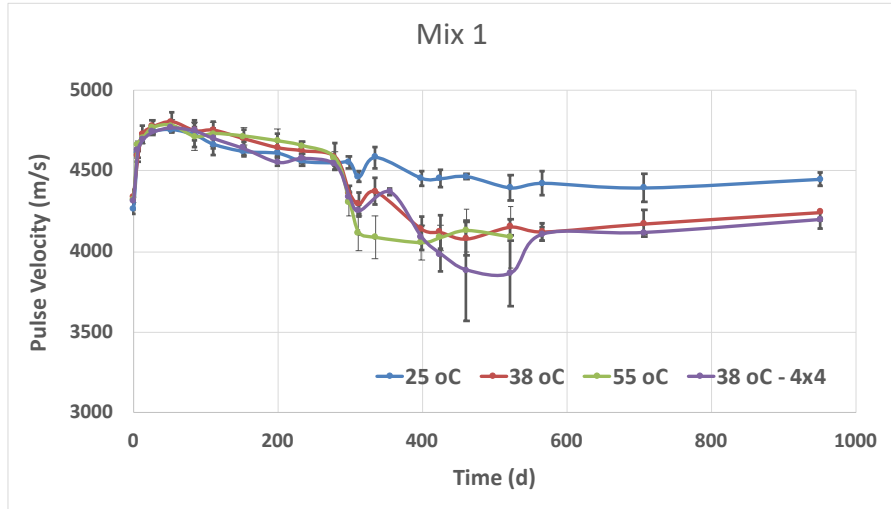


Figure 4-32. Mix 1 ultrasonic Pulse Velocity in 3x3 prisms at 25 °C, 38 °C, and 55 °C; also shown for 4x4 prisms at 38 °C. Average values shown, with error bars indicating the sample standard deviation.

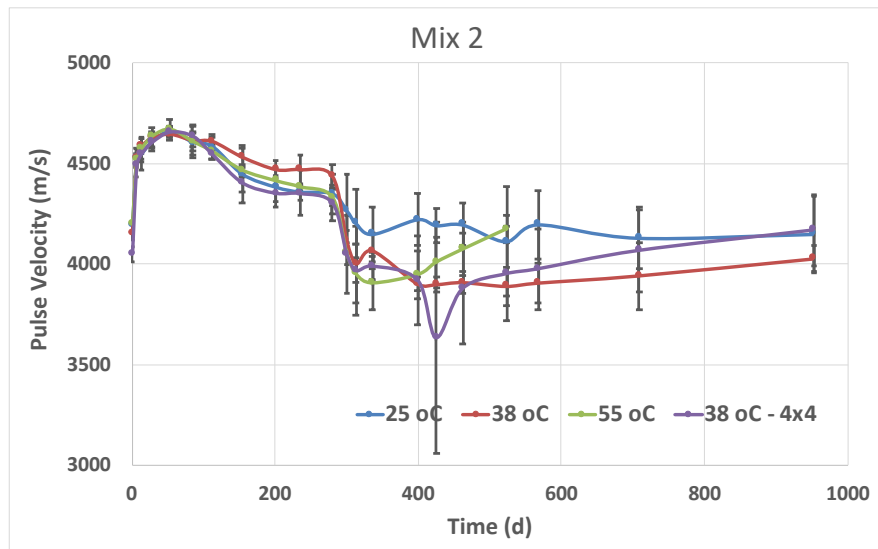


Figure 4-33. Mix 2 ultrasonic Pulse Velocity in 3x3 prisms at 25 °C, 38 °C, and 55 °C; also shown for 4x4 prisms at 38 °C. Average values shown, with error bars indicating the sample standard deviation.

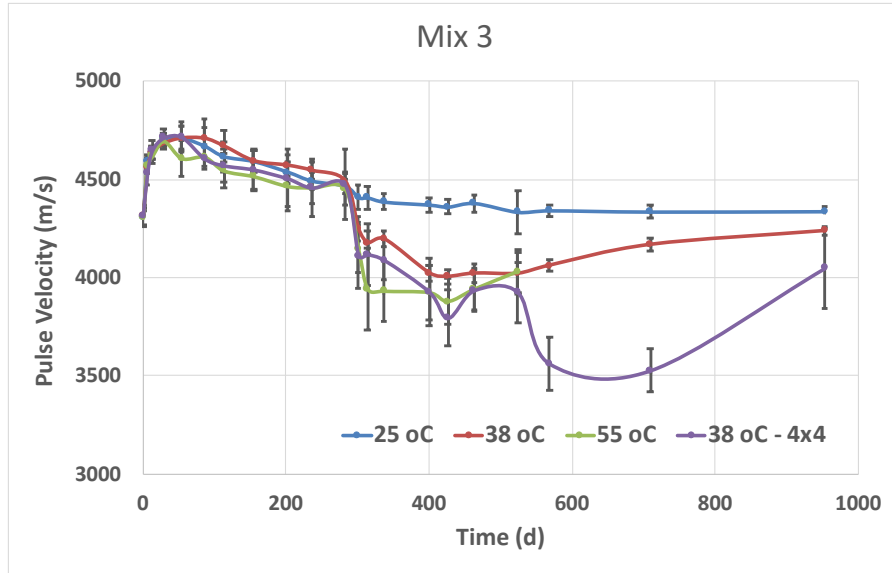


Figure 4-34. Mix 3 ultrasonic pulse velocity in 3x3 prisms at 25 °C, 38 °C, and 55 °C; also shown for 4x4 prisms at 38 °C. Average values shown, with error bars indicating the sample standard deviation.

The pulse velocity of the prisms from Mixes 1 to 3 subjected to the *Task 1 Temperature Exposure* are shown in Figure 4-32 through Figure 4-34. By comparison to the other temperature exposures, the 25 °C exposures exhibited a relatively gradual monotonic decrease after the first month of hydration, indicative of limited ASR damage. The change in pulse velocity values for the 38 °C and the 55 °C exposures was more dramatic. Because the 38 °C transition in Mix 4 (Figure 4-30) created no apparent change in behavior, one may conclude that the 38 °C transition for Mixes 1 to 3 caused a change in the rate and quantity of damage for all three mixes. The 55 °C transitions appear to have created damage, too, but the magnitude is difficult to infer because of its demonstrated temperature effect on Mix 4.

4.8.2 Temperature Dependence - UPV

The ultrasonic pulse velocity measurements from triplicate 3x3 prisms cast from Mix 3 and exposed to 25 °C, 38 °C, and 55 °C (starting immediately after demolding) are shown in Figure 4-35, along with the four companion 3x3 prisms cast with the Task 2 beams. The figure is divided between early times (left) and later times (right). The early time data show that the UPV increased at 7 d and 14 d for the 25 °C and the 38 °C samples, respectively. The 55 °C data, however, decrease monotonically for the first 30 days. At later times, the 25 °C data decrease monotonically from 7 d to 400 d, while the 38 °C and the 55 °C specimens reach a minimum UPV at 150 d and 50 d, respectively.

These results are consistent with the expected behavior mentioned above. The data suggest that ASR gel filling of the cracks outpaces the new crack formation at 150 d and 50 d for the 38 °C and the 55 °C exposures, respectively. As a result, the UPV increases after these ages. For the 25 °C exposure, the UPV continues to decrease through to the end of the measurements at 400 days. Therefore, one might conclude that the crack formation is faster than ASR gel filling over the first 400 d.

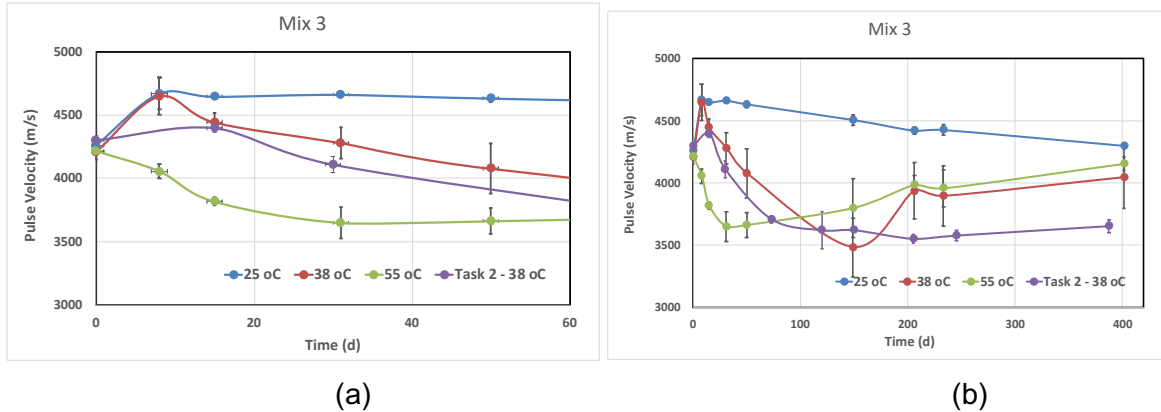


Figure 4-35. Temperature dependence of 3x3 prism ultrasonic pulse velocity for Mix 3, a) at early times and b) at longer times.

The immediate decrease in pulse velocity for exposure to 55 °C suggests that the nature of the ASR reaction is different at this temperature. Noting that the pulse velocity of the 38 °C specimens also decreased a similar amount, but only after an initial increase, suggests that the rate of increasing damage at 55 °C is greater than the rate of hydration, at all times. Assuming the rate of damage production at 38 °C is lower than at 55 °C, the decrease in pulse velocity in the 38 °C specimens would occur after the rate of hydration had decreased to a point where the rate of damage was greater.

4.8.3 Measurements on Cores

The UPV measurements on Task 1 Block cores were limited by specimen availability. As the Blocks aged, the concrete became more susceptible to breakage. Also, coring in the confined regions was restricted to critical structural testing needs because coring would alter the degree of confinement. Therefore, UPV measurements on cores was limited to cores taken on the unconfined (middle) sections of the Task 1 large Blocks.

Coring in the unconfined regions of all three expansive Task 1 Blocks was conducted at approximately 370 d of age, and a subsequent coring of the unconfined region of the Mix 3 Block was conducted at approximately 700 days. Each coring operation resulted in two replicate specimens. Each replicate specimen was cut to square off the ends, and the UPV was measured longitudinally. The cores were wrapped in plastic and stored in a lidded bucket, suspended over water, to prevent drying. The buckets were stored at 38 °C, like the Blocks. Prior to UPV measurements, the buckets were moved to a 25 °C chamber.

The initial and subsequent UPV measurements are plotted below in Figure 4-36 for the coring at 370 days, and in Figure 4-37 for the coring at 700 days. At a given age, a result consisted of two replicate measurements on each replicate core. In the figure, the symbol indicates the mean value (of the four measurements), and the error bars indicate the resulting sample standard deviation. The initial measurement for each mix was taken at the time of coring.

The data in Figure 4-36 indicate fairly constant UPV values over the subsequent 100 days after the initial coring. Based on the companion prism UPV and expansion data discussed previously, the coring from the large Blocks occurred after the majority of the expansion had already occurred and the UPV value was approaching a constant.

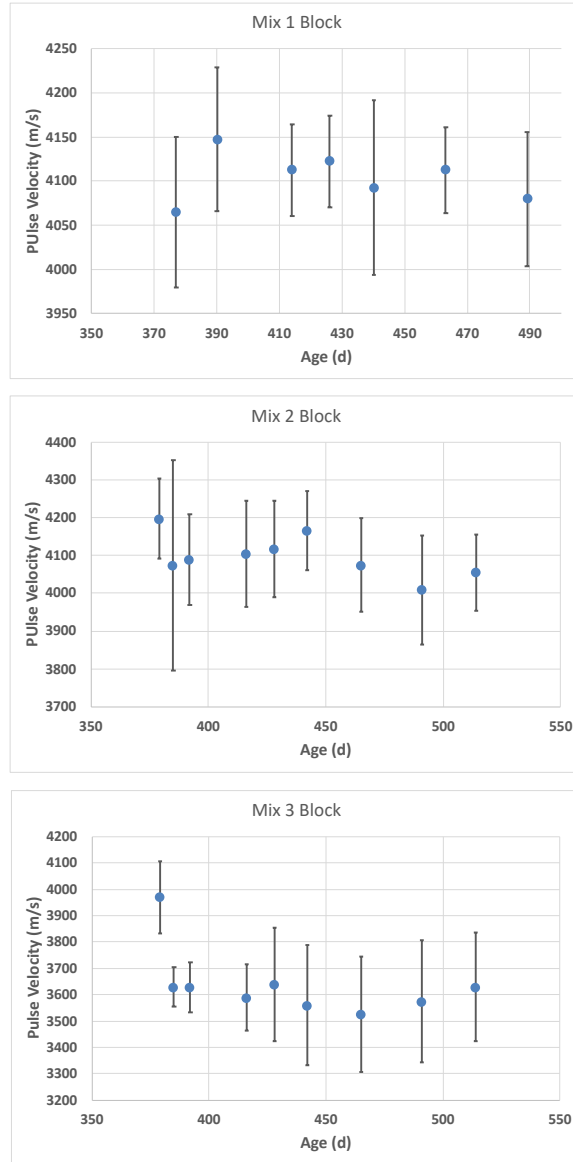


Figure 4-36. Ultrasonic pulse velocity of two replicate cores taken from the unconfined region of the Task 1 large Blocks. The first measurement shown was taken immediately after coring, and the error bars represent the standard deviation of four measurements (replicate measurements on two cores).

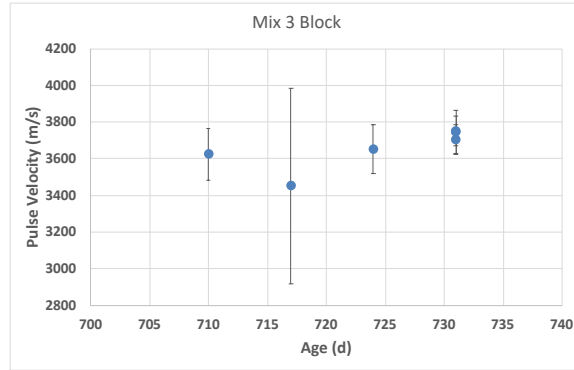


Figure 4-37. Ultrasonic pulse velocity of two replicate cores taken from the unconfined region of the Task 1 large Block for Mix 3. The first measurement shown was taken immediately after coring, and the error bars represent the standard deviation of four measurements (replicate measurements on two cores)

For the coring performed at approximately one year of age, the pulse velocity showed relatively little change over time while resting in an unconfined state. The exception was Mix 3, which exhibited a relatively rapid decrease in pulse velocity, followed by relatively constant values. In contrast, pulse velocity measurements on Mix 3 cores taken at two years of age showed relatively little change over the subsequent 3 weeks.

4.8.4 Diagnostic Tool – Pulse Velocity

The ultrasonic pulse velocity shows promise as a diagnostic tool for detecting damage due to ASR. The change in pulse velocity is greatest during the early and middle stages of the expansion. Although the absolute value of the pulse velocity is not meaningful, a record of change in pulse velocity could be very informative. The UPV is not, however, sensitive to changes that occur during the later stages of the expansion. Once the ASR reaction has progressed considerably, and the concrete has aged considerably, the measurement performed on cored samples seems to have limited sensitivity to the ongoing reaction.

4.9 CAST CYLINDER - DAMAGE RATING INDEX (DRI)

Evaluating the Damage Rating Index (DRI) was conducted on Task 1 companion 4x8 cylinders cast with Mixes 1, 2, and 3 (see Table 4-1). The DRI measurements were conducted at times intended to roughly correspond to $\varepsilon = (0.33 \varepsilon_{\infty}, 0.67 \varepsilon_{\infty}, 0.99 \varepsilon_{\infty})$ from Eq. (4-1).

The DRI is based on a petrographic examination of a polished concrete section whereby the petrographer tallies the number of predefined damage classes that are observed, and which represent damage in both the hardened paste and the aggregate (Villeneuve et al., 2012). Conceptually, the DRI value is expected to be correlated to the amount of reaction or expansion that has taken place.

4.9.1 Damage Rating Index Measurement Method

The DRI method is a destructive test of the 4x8 cylinder. The cylinder is cut in half longitudinally, and the exposed (10 cm x 20 cm) surface is polished. Optical microscopy, using

a stereo-microscope at a magnification of 16x, was used for identifying and tallying the occurrences of specific types of damage on the polished surface (Rivard, et al., 2002). A (1 cm x 1 cm) grid is overlain on the surface, and within each grid cell a tally is taken of the 7 damage classes shown in Table 4-2 (following Sanchez et al., 2013). When completed, the number of occurrences for each damage class is summed across all the grid cells, arriving at a total damage number for the entire area analyzed. Each summed damage class is then multiplied by a weighting factor shown in Table 4-2. In the subsequent data presented, each damage class is abbreviated as shown in Table 4-2.

Table 4-2. Damage Rating Index (DRI) damage classes, their abbreviation, and the corresponding weighting factors (following Sanchez et al., 2013).

	Petrographic Features	Abbreviation	Weighting Factor
Aggregate	Cracks in Co. Agg.	CCA	0.25
	Opened Cracks in Co. Agg.	OCA	2
	Cracks with Reaction Products in Co. Agg.	OCAG	2
	Co. Agg. Debonded	CAD	3
	Disaggregation/Corroded	DAP	2
Paste	Cracks in Cement Paste	CCP	3
	Cracks with Reaction Products in Cement Paste	CCPG	3

To be applicable to any concrete specimen, the DRI is normalized by the total area analyzed. The 'standard' area is 100 cm², so for a given analyzed area A , the weighted sum of damage classes, across the entire area, is multiplied by the ratio $(100/A)$, where A is expressed in units of cm². The weighed sum of damage classes before the area correction are referred to here as 'raw' DRI, and after the correction they are referred to as 'corrected' DRI. For the instance of the 4x8 cylinders analyzed here, the raw total was multiplied by 1/2 to arrive at the corrected DRI.

4.9.2 DRI Results

The Damage Rating Index (DRI) measurements for Mixes 1 to 3 are shown in Figure 4-38, grouped by exposure temperature. The raw values are plotted, with the labelling along the x-axis denoting the age (# days) and the mix (M1, M2, M3), grouped by the Task 1 Temperature Exposure temperature (25, 38, 55). In addition, the contribution of each damage class (Table 4-2) is color coded.

The precision (repeatability) of a DRI value is analogous to a point count; the variance is approximately equal to the number of observations. The sum of raw counts (occurrence of a damage) for a given specimen ranged from 200 to 1000. These raw counts were weighted by damage class (via Table 4-2), and were corrected for total area. The coefficient of variation of the corrected DRI values ranged from 4 % to 8 %. The person-to-person variability of the test (reproducibility) has not been quantified.

For a given temperature exposure, the DRI generally increases with mix number and age. For the ASR reactions occurring in Mixes 1 to 3, the largest contributors to the DRI are the (reaction product) gel-filled cracks in the large aggregate (OCAG), disaggregation or corrosion (DAP), and gel-filled cracks in the cement paste (CCPG).

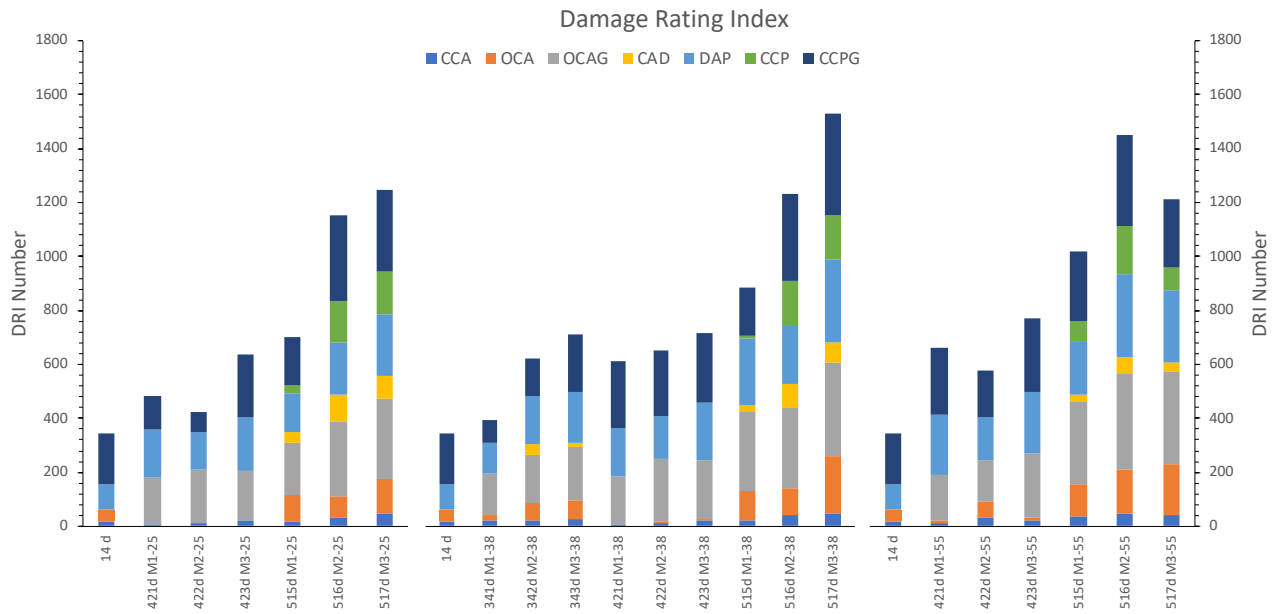


Figure 4-38. Raw Damage Rating Index for cast cylinders from Task 1. The nomenclature is (age/mix/temperature), and the color-coded damage class abbreviations are explained in Table 4-2. The coefficient of variation ranged between 4 % and 8 %.

In Figure 4-39 below, the 24 corrected DRI values are compared with the unconfined expansion observed in the 3x3 prisms, the 4x4 prisms, and the 4x8 cylinders. The DRI axis scale was chosen somewhat arbitrarily for comparison to the expansion values, but a single (fixed) scaling was used for all mixtures and temperatures. Ideally, each DRI value is associated with a specific value for the expansion, but the data demonstrate that there is rarely an unambiguous expansion value associated with a particular DRI value.

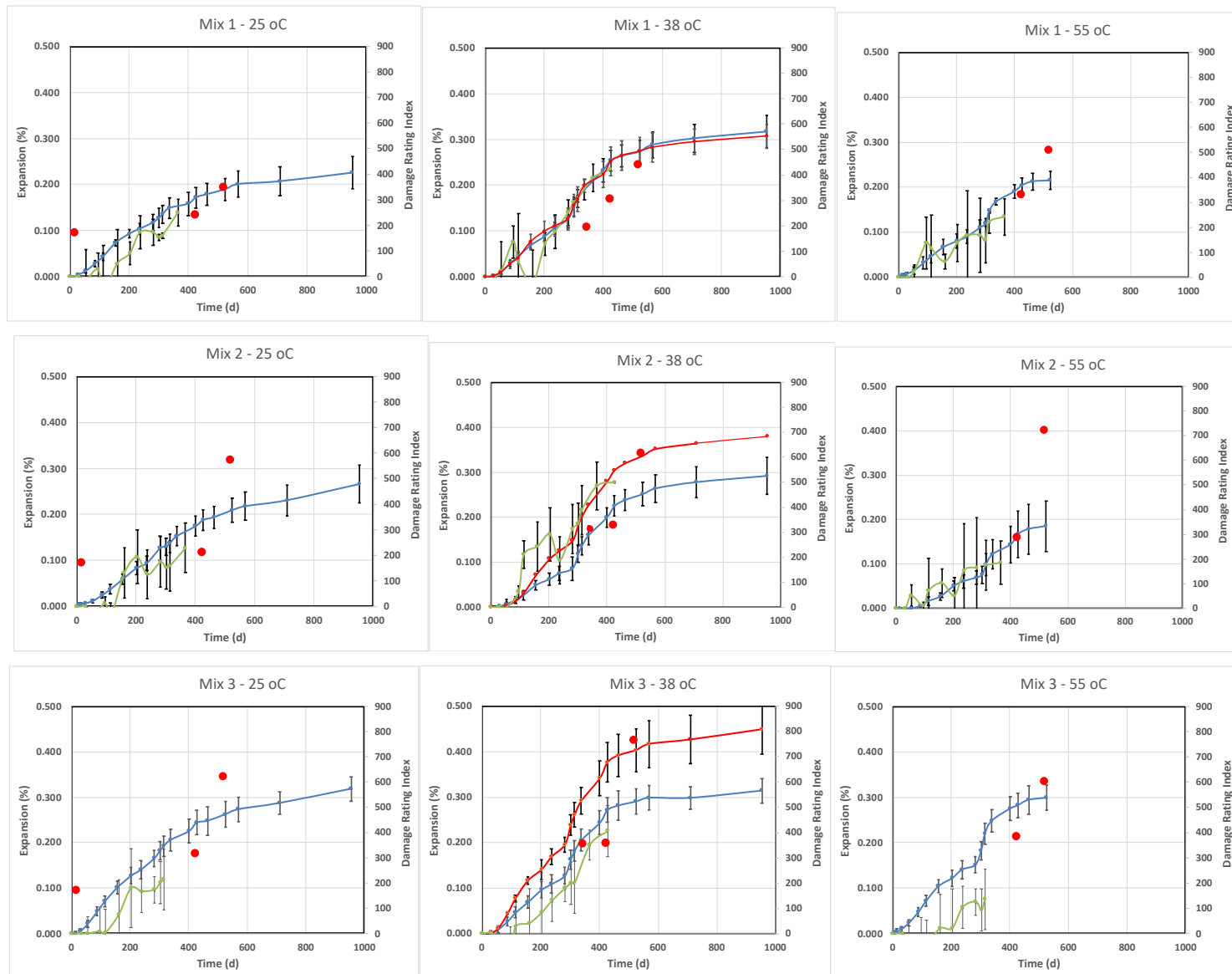


Figure 4-39. Comparison of corrected Damage Rating Index (red circles) to expansion data from 3x3 (blue) and 4x4 (red) prisms, and 4x8 cylinders (green). The DRI standard deviations are approximately equal the size of the symbol.

For a given mixture, it is interesting to note the consistency of DRI values. For each Mix, at a given age, the DRI values are roughly equal for all three temperatures. Given that these cylinders were exposed to 25 °C for the first 270+ days, the subsequent temperature differences seem to have relatively little effect on the DRI. Therefore, if DRI is proportional to damage, these results suggest that the damage (in a given Mix, at a given age) was consistent across all three temperatures.

Table 4-3. Reported relationship between DRI, expansion, and loss in compressive strength – from Sanchez et al. (2018).

DRI	Damage Classification	Expansion (%)	Compressive Strength Loss (%)
100 – 155	Negligible	0.00 – 0.03	-
210 – 400	Marginal	0.04 +/- 0.01	15 – 60
330 – 500	Moderate	0.11 +/- 0.01	0 – 20
500 – 765	High	0.20 +/- 0.01	13 – 25
600 – 925	Very High	0.30 – 0.50	20 – 35

Sanchez et al. (2018) developed a general relationship among DRI, expansion, and loss in compressive strength (see Table 4-3. Rather than a strict 1:1 relationship between DRI and expansion or compressive strength loss, the table suggests that, at best, one can only classify damage in broad ranges. Furthermore, this is corroborated by the data in this Study. Even though there are measurable differences among the expansion values for the different temperatures at later ages, the DRI values are not capable of distinguishing among these differences. Furthermore, the general relationship between DRI and total expansion suggests that DRI is not a good indicator of the degree of the expansion; i.e., it is difficult to infer how much more expansion will occur from a DRI result.

4.10 BLOCK CORE - RESIDUAL EXPANSION POTENTIAL (REP)

The Residual Expansion Potential (REP) is a test designed to characterize the capacity of an ASR-affected concrete to continue reacting. To conduct the test, a core is taken from the affected concrete, and the ends are cut off square and drilled for epoxying gauge studs in place. The subsequent expansion is measured over time. The implicit assumption is that, comparatively, a specimen exhibiting a greater subsequent expansion corresponds to a greater residual expansion potential.

There are a few challenges with the test method. The first is that the amount of subsequent expansion can be due to a number of causes. The primary assumption is that the cause is unreacted phases in the aggregate, which will continue reacting and cause additional expansion in the structure. However, another possible source of residual expansion can be the change from confinement to unconfinement when sampling from a reinforced concrete structure. Inside the structure, the expansion stresses of the ASR reaction have been restrained by the steel reinforcement, thus confining the concrete within. Even if the ASR reaction had become depleted, the act of removing the core from the structure can result in expansion as the sample

achieves a new mechanical equilibrium. For this reason, extracted cores for REP measurement were typically equilibrated until stabilized before measurements were taken.

Another challenge is identifying a suitable accelerated conditioning protocol to achieve meaningful results in a timely manner; which is typically achieved by heating the specimen in a humid environment. Not only is the conditioning temperature an important consideration, but so is the time to wait before imposing the elevated temperature.

The method that was used for this study is an accelerated method based on the one proposed by Merz and Leeman (2013) – see also Sellier et al. (2009) and RILEM TC 259-ISR (2017). To help eliminate the effects of confinement in this study, specimens were cored from the unreinforced sections (Region 2) of the Task 1 Blocks; given the size of the Task 1 Blocks, there is an overbearing pressure that confines the specimen, but this pressure should be far less than the ASR expansion confinement pressure in the reinforced region. Given all the variabilities in a field specimen, there is no consensus on how to equilibrate or condition cores after extraction, nor consensus on what time to use as “time zero”.

In this study, the cores were extracted and immediately wrapped in plastic film and conditioned in air-tight lidded pails kept at 38 °C and 95 % RH; the plastic film was used to reduce moisture loss at 38 °C (Merz and Leemann, 2013). After one week, gauge studs were epoxied to the ends and the side of the cylinder, arranged as shown in Figure 4-40. Initial measurements (taken at 25 °C) of linear and diametral expansion, mass, and ultrasonic pulse velocity were taken, and the cores returned to the pails and the 38 °C chamber. Expansion, mass, and pulse velocity measurements were repeated over the following 100 days.

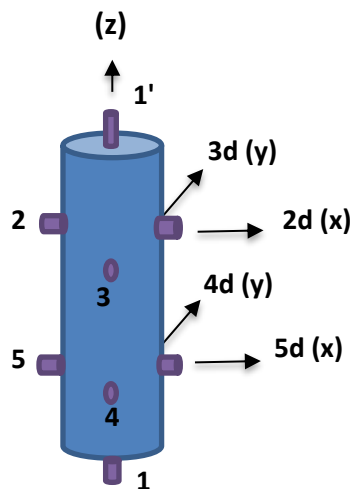


Figure 4-40. Gauge stud arrangement for the 10 cm diameter cores used to study Residual Expansion Potential at 1 year.

4.10.1 REP Testing at 1 Year

Replicate 10 cm (4 in) diameter cores were taken from the unconfined regions of Task 1 Blocks made with Mixes 1 to 3. The location of each core is shown in Figure 4-41. The cores were all

taken on the same day, and the measurements commenced the following week. The schedule is shown below in Table 4-4, including the age of the Blocks at the corresponding date.

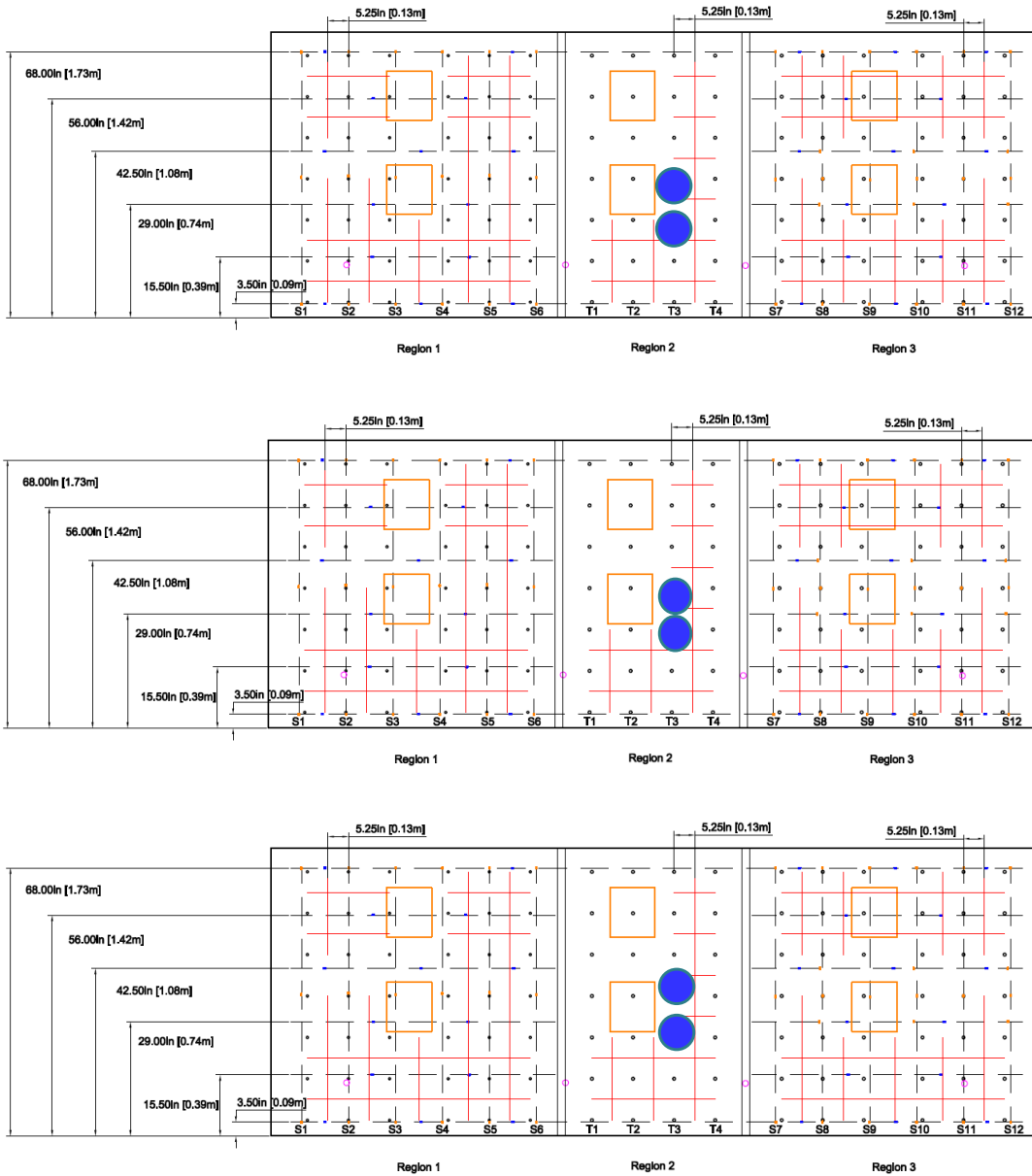


Figure 4-41. Coring plan for 2018 residual expansion testing.

Table 4-4. Coring and initial measurement timetable for the residual expansion potential measurements on the Task 1 Blocks at 1 year.

MIX	DATE		
	Cast	Core	Initial Measurement
Block/Mix 1	03/23/2017	03/28/2018 (370 d)	04/04/2018 (377 d)
Block/Mix 2	03/22/2017	03/28/2018 (371 d)	04/04/2018 (378 d)
Block/Mix 3	03/21/2017	03/28/2018 (372 d)	04/04/2018 (379 d)

The linear and diametral expansion measurements for Mixes 1 to 3 are plotted in Figure 4-42 as a function of the time passed since the day of the coring. The symbols indicated the mean value, and the error bars indicate the sample standard deviation; the lines are provided to merely guide the eye, and not meant to suggest specific behavior of the specimen between measurements.

All of the expansion measurements exhibit a similar response, divided into three regions. There is an initial increase in expansion during the first 14 days, which appears to be correlated with the mass of water uptake occurring over the same period, and a decrease in pulse velocity (for Mix 1 and Mix 3). Between 14 d and 60 d there is a simultaneous increase in both the expansion and the mass. Between 60 days and 120 days the expansion in all three mixes appears to reach a plateau. With the possible exception of Mix 2, the steady-state expansion behavior is consistent with relatively constant mass and pulse velocity.

The data suggest that the response of the Mix 1 cores was qualitatively different from that of the Mix 2 and Mix 3 cores. For Mix 1, there was no significant change in linear expansion after 25 days, and the average UPV increased over the first 25 days. By contrast, both Mix 2 and Mix 3 specimens exhibited additional linear expansion after 25 days, and the average UPV decreased during the first 25 days. However, there was considerable variability in the UPV results, so no definitive statement can be made in this regard. It should be noted, also, that by the end of the measurements some of the Mix 2 and Mix 3 cores lost integrity and broke apart.

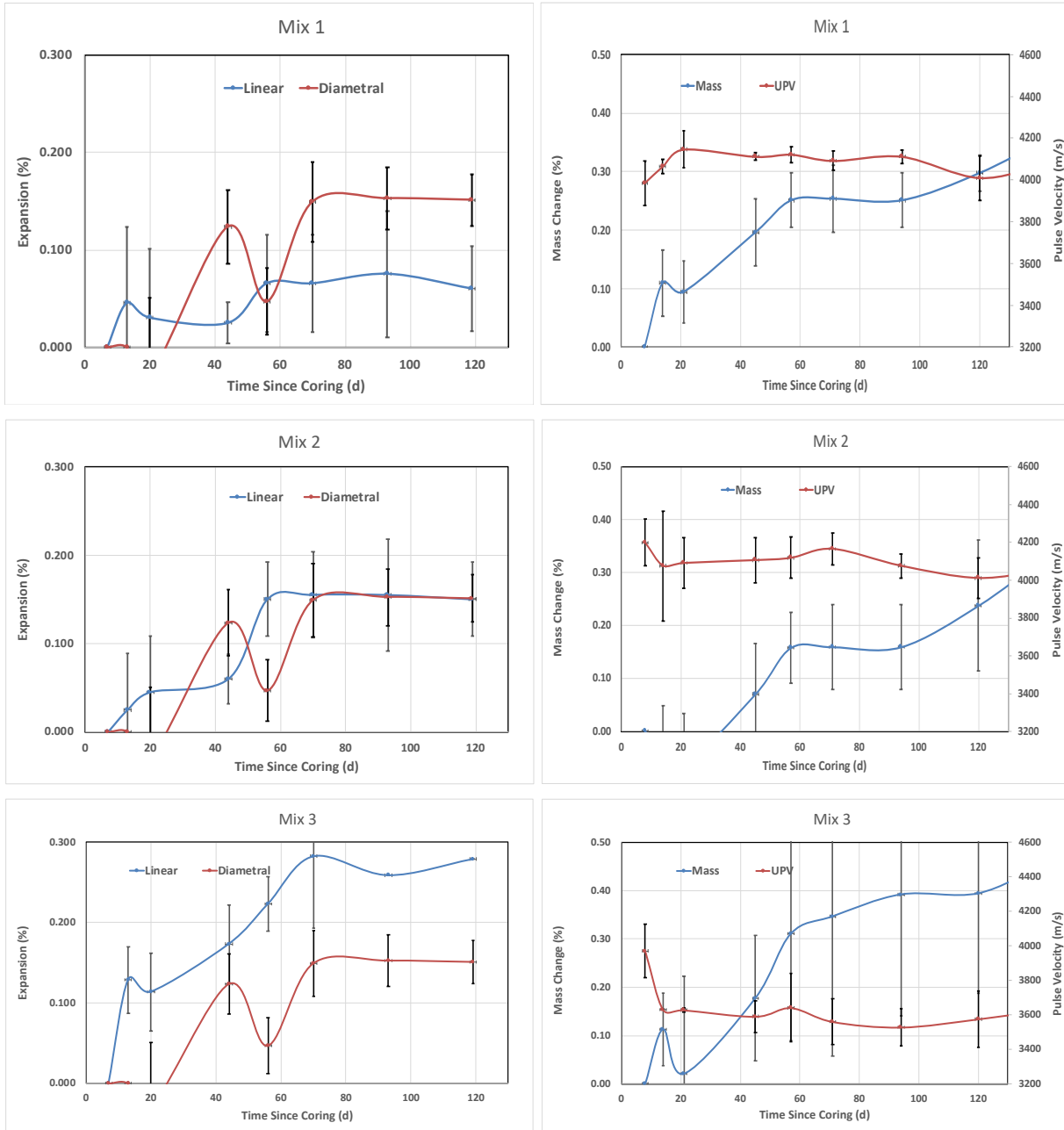


Figure 4-42. Linear and diametral expansion (left column), and mass change and pulse velocity data (right column), for the duplicate cores taken at 1 year from each of the three Task 1 Blocks (by row). Symbols indicate the average value, and the error bars indicated the sample standard deviation.

4.10.2 REP Testing at 2 Years

When the Task 1 Blocks were nearly 2 years old, the residual expansion potential test was performed again, using cores extracted in duplicate from the unconfined portion of the Mix 3 Block. The measurement procedure was nearly the same as was used in the previous year's testing. One small difference was the arrangement of the gauge studs on the core for evaluating expansion (see Figure 4-43).

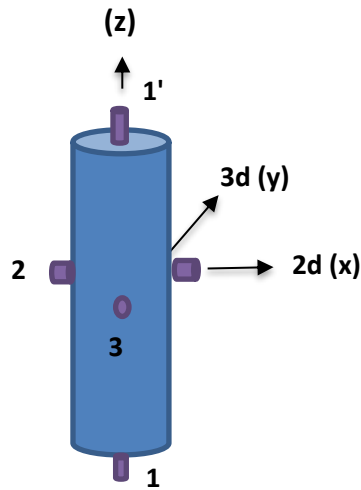


Figure 4-43. Gauge stud arrangement for the 10 cm diameter cores used to study Residual Expansion Potential at 2 years.

Table 4-5. Coring and initial measurement timetable for the residual expansion potential measurements on the Task 1 Mix 3 Block at 2 years.

MIX	DATE		
	Cast	Core	Initial Measurement
Block/Mix 3	03/21/2017	02/25/2019 (706 d)	03/01/2019 (710 d)

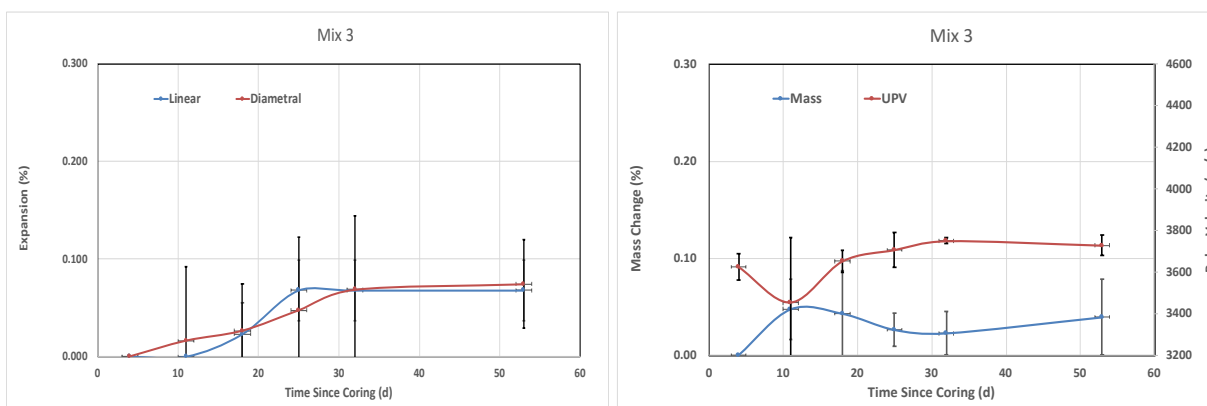


Figure 4-44. Linear and diametral expansion (left), and mass change and pulse velocity (right), data for the duplicate cores taken at 2 years from the Task 1 Mix 3 Block. Symbols indicate the average value, and the error bars indicated the sample standard deviation.

The expansion, mass change, and pulse velocity data from the replicate cores are plotted in Figure 4-44, using the same axis scales as for the data from the previous coring shown in Figure 4-42. For these specimens, expansion halted approximately 25 days after coring. This inference was corroborated by the mass change and pulse velocity data showing a relatively steady mass and a pulse velocity that had recovered its initial value after coring. Moreover, the expansion plateau value was less than 0.1 %. Therefore, not only did the expansion reach a plateau faster than in the previous coring study, the plateau value was smaller. It is also interesting to note that these initial pulse velocity values were approximately equal to the previous pulse velocity values after 120 days of residual expansion.

4.10.3 Diagnostic Tool

The REP shows promise as a diagnostic tool for characterizing residual expansion. There was considerable residual expansion, especially for Mix 2 and Mix 3 at one year of age. There was even measurable expansion in the Mix 3 cores after 2 years of age. Given the insensitivity of the UPV at these ages, the REP could be an effective complementary tool to UPV, whereby measurable REP in the absence of measurable changes in UPV might suggest that the concrete is in the late stages of expansion.

Chapter 5

PETROGRAPHY

Extensive petrographic examination of prisms and cores was used to develop a more complete understanding of the nature of the degradation occurring in the Task 1 Mixes 1 to 3. The petrographic examinations used scanning electron microscopy (SEM) (in combination with energy-dispersive X-ray spectroscopy (EDS)) and optical microscopy. The specimens that were analyzed included the Task 1 cast prisms and large Block cores.

Detailed analysis of the ASR reaction and the changes in the microstructure, in both cast companion prisms and extracted cores, was performed to achieve a number of specific objectives. The first was to verify whether damage to the concrete is indeed caused by ASR and not by other mechanisms such as drying shrinkage, or damage caused by sample preparation. For damage associated with ASR, the next objective was to assess the severity and extent of deterioration at the microstructural level, which includes changes to both aggregates and hardened paste. By relating the type of damage to the degree of the expansion, the analysis provided support for developing a correlation between internal ASR damage and any degradation or changes in structural capacity of the concrete (*e.g.*, surface cracking, compression strength, elastic modulus), along with providing a possible means of relating damage to the *potential* for further expansion.

To quantitatively relate the observed damage to the degree of expansion, a strategy was developed for quantifying damage from microscopy images using artificial intelligence based image segmentation models. The approach comprised three strategies: 1) a sampling strategy to ensure acquisition of spatially and temporally representative data; 2) a sample preparation and imaging strategy that would facilitate automating the image capture on a scanning electron microscope and incorporate the tradeoffs between imaging time per field of view and spatial coverage; and 3) a trusted modeling strategy that leverages accuracy of neural network based segmentation algorithms, multiple approaches to preparing high quality and large quantity of training data, and incorporating microstructural semantic features according to experts into the models to distinguish among different types of damage and quantify the resulting damage.

5.1 PETROGRAPHY SAMPLE PREPARATION

The cored specimens and the prism specimens are sectioned with a cut-off saw into disks with parallel surfaces of 2 mm to 3 mm in thickness. They are then immediately treated by solvent exchange to stop ASR reactions and cement hydration, and to preserve reaction products. The chemical treatment was a serial concentration method using 200-proof ethanol (ETOH) in water. Disks are first immersed into 50 % (by volume) ETOH for 24 h, with subsequent 24 hour treatments in 75 % and 100 % ETOH:water solutions. Afterwards, specimens were dried in an oven at low temperature (40 °C) to drive off any excess ETOH with minimal effect on calcium silicate hydrate or ASR gel.

Specimens for analysis via optical (polarized light) microscopy were also sent to outside laboratories for thin sectioning and polishing, primarily for initial characterization of fresh (unaltered) reactive coarse and fine aggregate. The prepared specimens were analyzed using reflected light and in plane or cross-polarized transmitted light.

Specimens for SEM-EDS analysis were impregnated using a low viscosity (8 mPa s) epoxy resin and hardener. After the epoxy cured, the specimens were prepared by grinding with 60-grit silica carbide paper to attain microscopically flat surfaces, and then by polishing with resin-bonded diamond discs at 220-, 500-, 1200-, 2000-, and 4000-grit using water as lubricant. Final polishing was accomplished with 3 μm , 1 μm , and 0.25 μm diamond suspensions, respectively, in a non-aqueous medium. Finally, samples were carbon coated to prevent charging and analyzed in an SEM with backscattered electron and energy-dispersive detectors operating at 12 kV with a spot size of 5.2 \AA .

Figure 5-1 shows the equipment used for specimen preparation. The large device in Figure 5-1a is an automated specimen polisher that can polish large specimens. These included both the 10 cm diameter cores and the transverse sections of the 4x4 prisms, shown in Figure 5-1c.

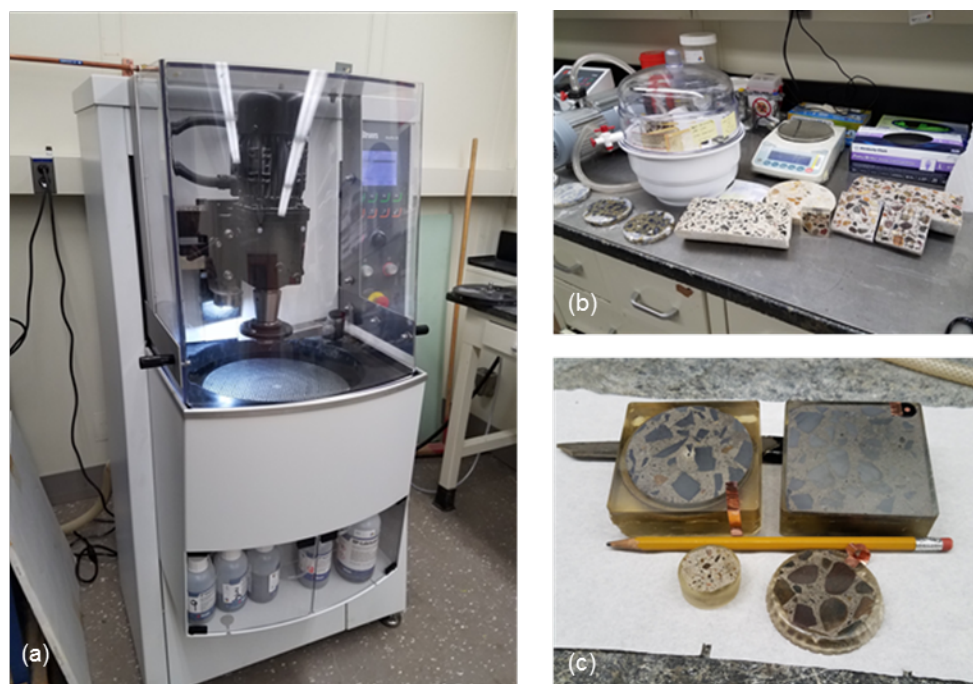


Figure 5-1. Equipment for impregnation and polishing of both Task 1 Block core specimens and companion prism sections (a,b, and c) in preparation for measurements by SEM-EDS. Sectioned 4x8 cylinders (b) are also polished here in preparation for DRI analysis.

Backscattered SEM imaging was typically conducted at 15 kV accelerating voltage, a 0.8 nA beam current, and using an indicated magnification of 200X or higher. One field of view (FOV) acquired by the microscope at 200X consists of 1024×768 pixels, which represents $1.5 \text{ mm} \times 1.1 \text{ mm}$ at a pixel spacing of $1.47 \mu\text{m}$. The FOVs were stored in an uncompressed TIFF file format with 8 bits per pixel (BPP). The acquisition of one FOV took between 1 min to 3 min.

5.2 SAMPLING PLAN

A sampling plan was devised to ensure observation of ASR reaction products and damage throughout the duration of expansion. The specimens included the Task 1 companion prisms and cores extracted from the large Blocks. The petrographic specimens from the 3x3 prisms were obtained by cutting the prism transversely, exposing a (75 mm x 75 mm) surface. The cores from the Blocks were generally 70 mm (2.75 in) in diameter, and the analysis was performed on transverse sections that were (400 mm to 500 mm) from the concrete surface.

The schedule for the 3x3 prism sample preparation is shown in Figure 5-2. Dividing the degree of expansion roughly into thirds along the vertical axis, the scheduling was devised to ensure samples were taken during each of these thirds, with the exception of Mix 4.

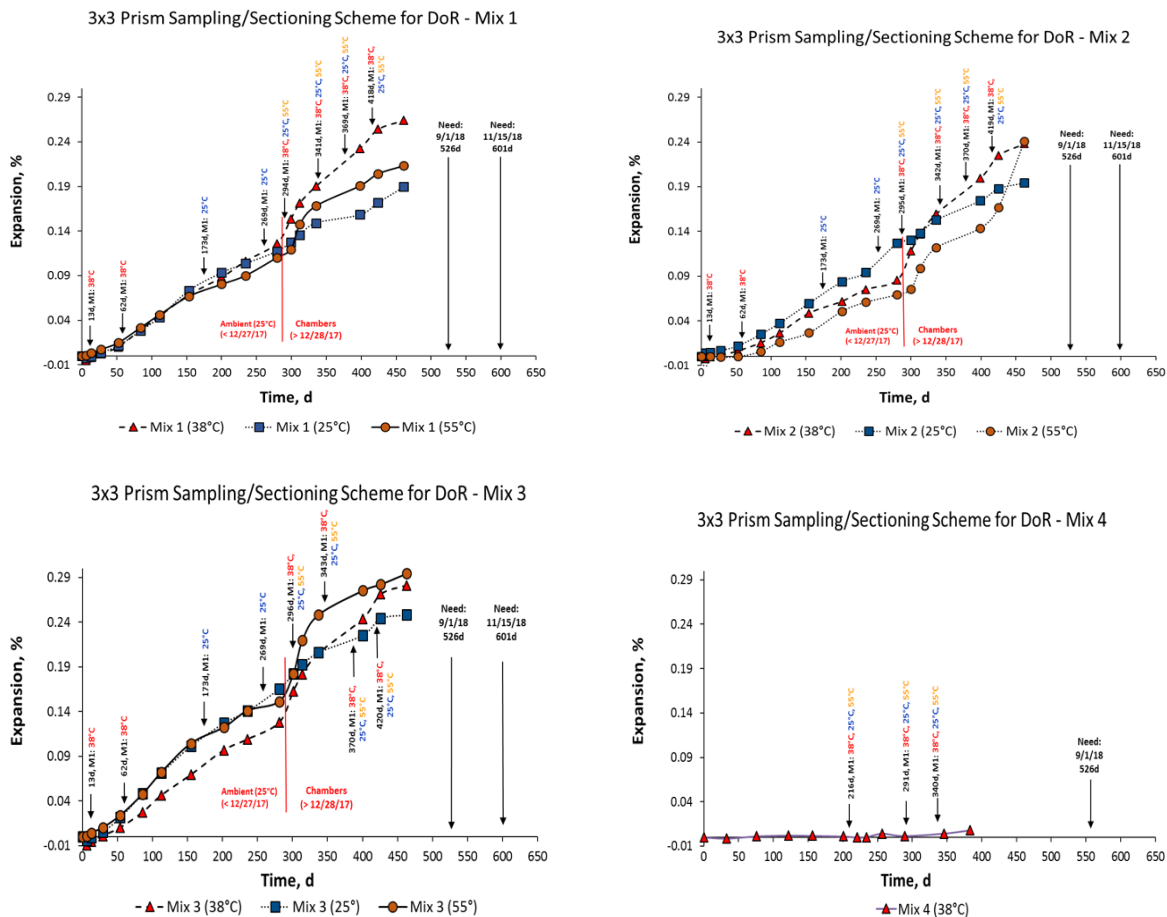


Figure 5-2. Sampling and sectioning scheme for 3x3 prisms cast with the Task 1 Blocks made with Mixes 1 to 4.

Twenty-nine core specimens were taken from the large Blocks for Mixes 1 to 3. The location of each core is shown below in Figure 5-3 through Figure 5-5 as a colored circle, labeled with the sequential number of the core. The coring was conducted at approximately 180 d and 365 d of age, denoted with red and blue symbols, respectively. The scheduling and location of the

coring conducted in Region 1 and Region 2 was constrained by the demands of the structural testing research plan for Tasks 1 to 3.

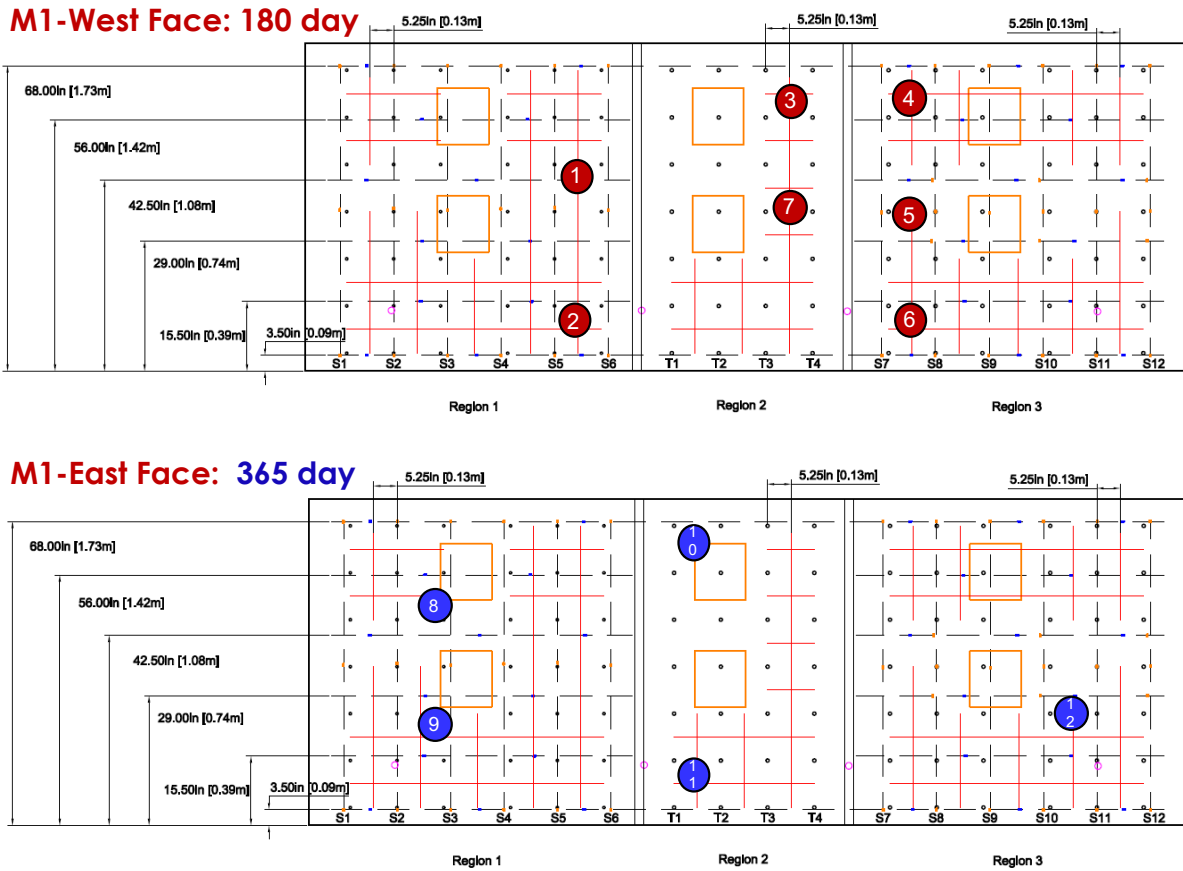


Figure 5-3. Coring plan for the Mix 1 Block.

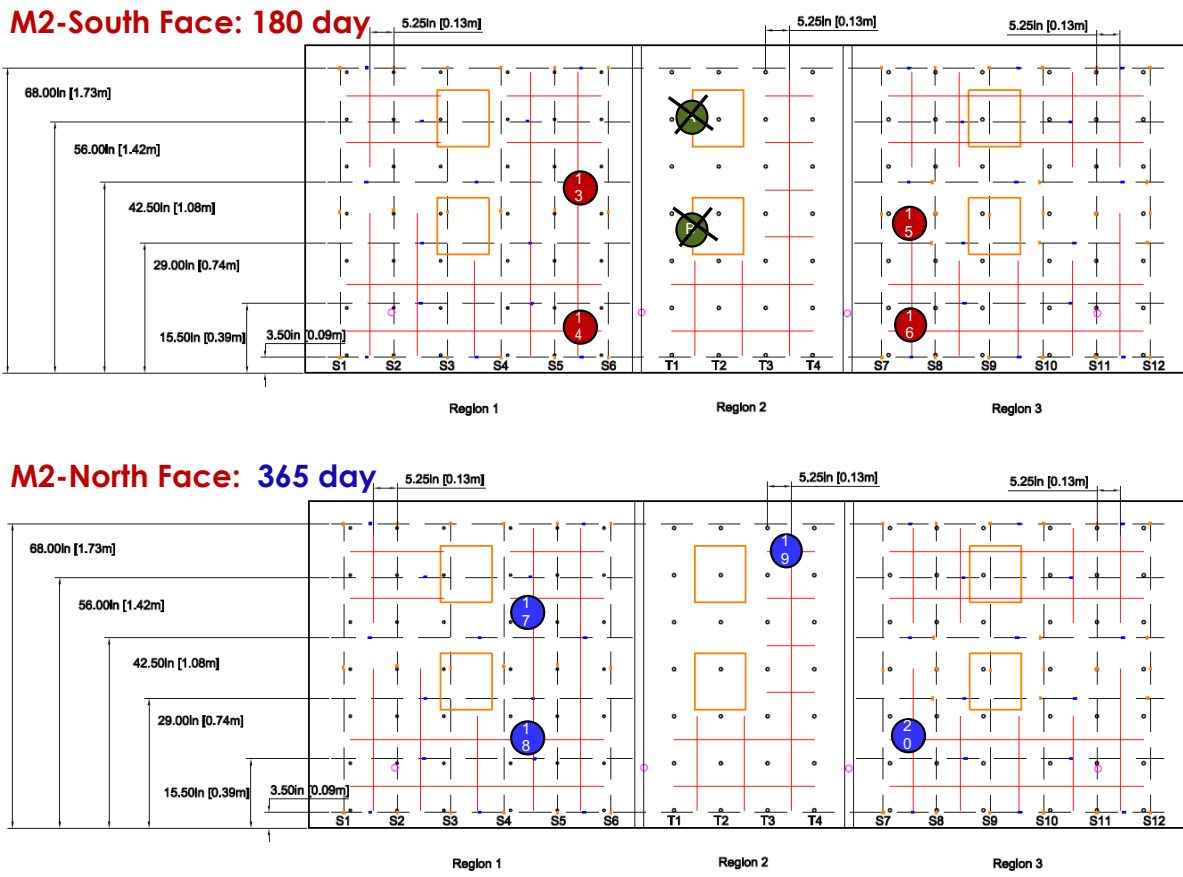


Figure 5-4. Coring plan for Mix 2 Block.

This publication is available free of charge: <https://doi.org/10.6028/NIST.JR.8415>

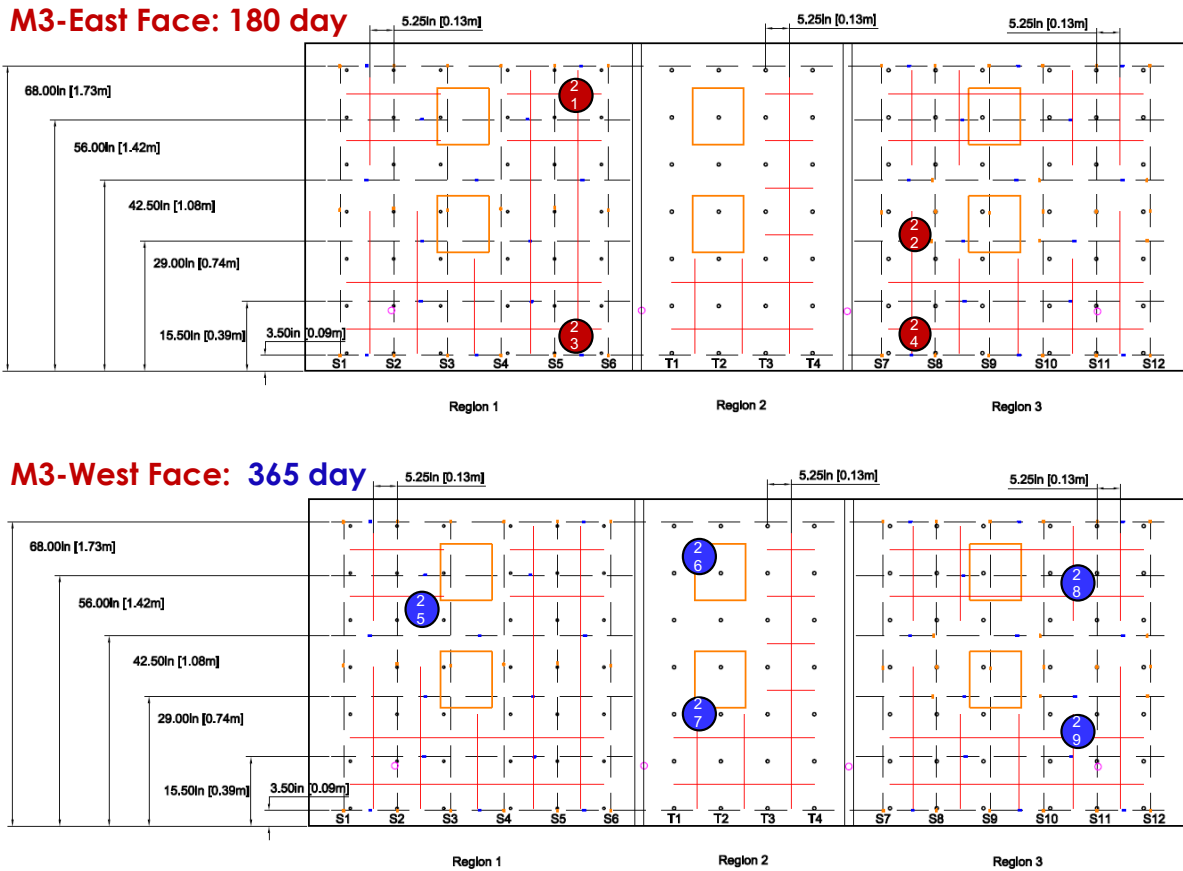


Figure 5-5. Coring plan for Mix 3 Block.

5.3 OBSERVED DAMAGE MECHANISMS

One of the reasons for conducting this more in-depth petrographic analysis was that a large fraction of the observed damage seen in Mixes 1 to 3 was not captured in the DRI damage criteria (discussed in Chapter 4), which rely heavily on cracking; the different DRI damage classes largely refine the details of the cracking (paste vs aggregate; empty vs gel-filled).

One unexpected outcome of this work – from a qualitative viewpoint – is the magnitude and extent of ASR alteration damage resulting not only from aggregate (or paste) *cracking*, but from massive aggregate *dissolution* that results in a substantial mass loss and increase in void space within the microstructure. Figure 5-6 shows an example of the effect. The quartz (Qz) aggregate has partially dissolved. The yellow outline in the figure denotes the approximate original outline of the aggregate. Visually, the black space is a void, but is not a crack. Therefore, this feature is not counted as part of the DRI analysis (Chapter 4); identifying the nature of the void space requires a measure of expertise on the part of the petrographer.

Increased void space resulting from massive dissolution is largely a function of the type and amount of reactive aggregate in the concrete. In these highly alkali-reactive systems, the extent

of the aggregate dissolution is significant. Generally, an increase in void space in a concrete should result in a loss of both compressive strength and reinforcement bond strength. The dissolution, however, results in reactants that can form gel elsewhere. Therefore, a loss of mechanical properties in one location may be offset by the increase in properties in another. The net effect, however, can only be determined from mechanical testing.

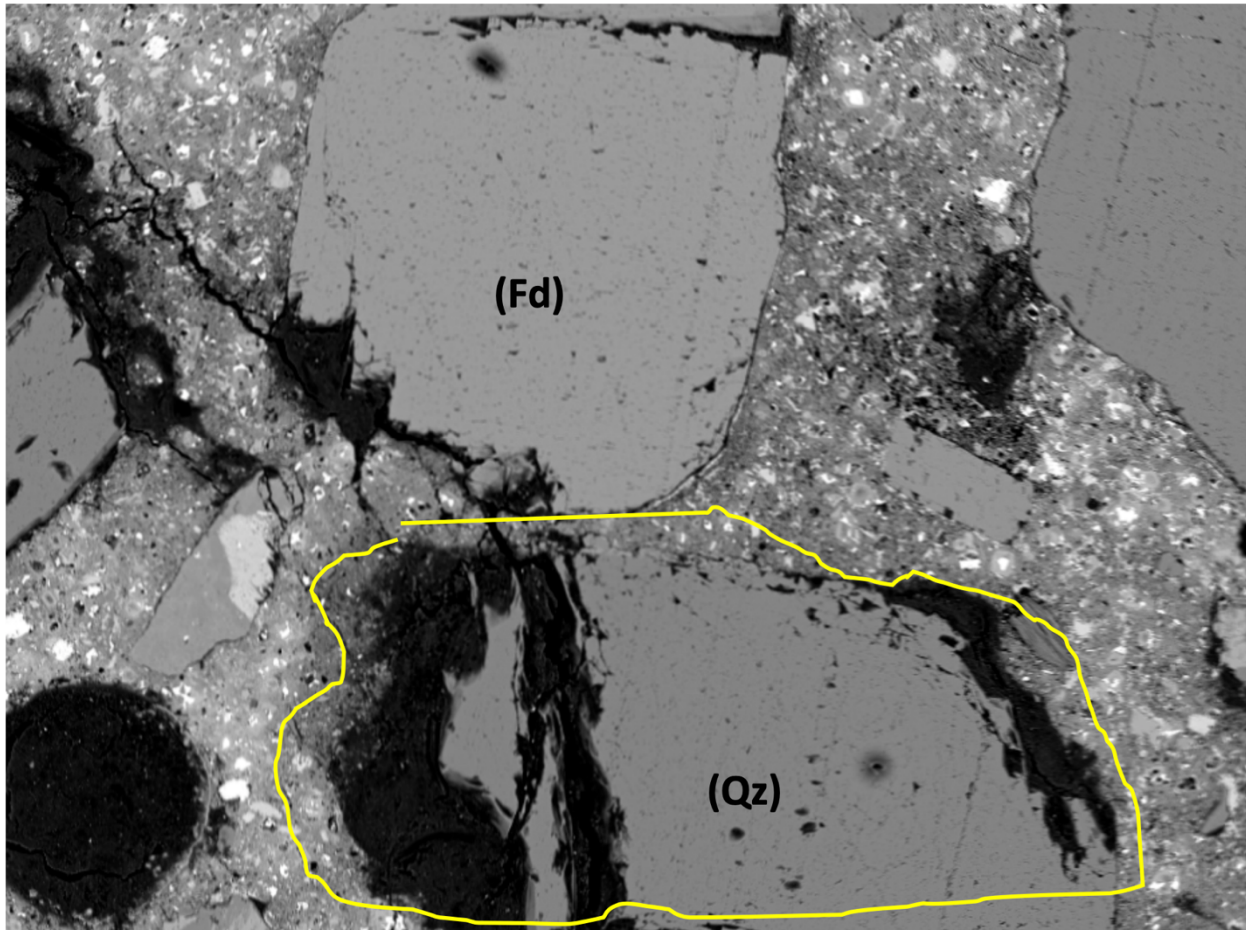


Figure 5-6. Massive aggregate dissolution in both quartzite (Qz) and alkali feldspar (Fd) in a Mix 3 prism section after 270 days. Approximate original (unaltered) grain boundary for one aggregate particle is highlighted in yellow.

5.3.1 Unique Damage Class

Simply adding *aggregate dissolution* to the DRI list of damage classes is problematic because the dissolution damage can be diffuse and difficult to reliably interpret. Whereas a crack is generally a well-defined entity with a degree of permanence, the aggregate dissolution and pitting is more subtle. Routine SEM analysis of core and prism sections as a function of specimen age and damage showed that ASR gel deposition in paste and aggregate is deposited in multiple generations (cycles), typically punctuated by periods of extensive dissolution pitting and silica remobilization (Figure 5-7, a-b).

After the dissolution, there will be void spaces left behind within the aggregates (or, more specifically, voids in the mineral phases within the aggregate that have dissolved) (Figure 5-7, c-d). These features are important contributions to the indicators of damage, but they require a trained eye to distinguish from other features. Furthermore, during these cycles, previously dissolved voids can re-fill with gel, but the region will not be shaped like a crack.

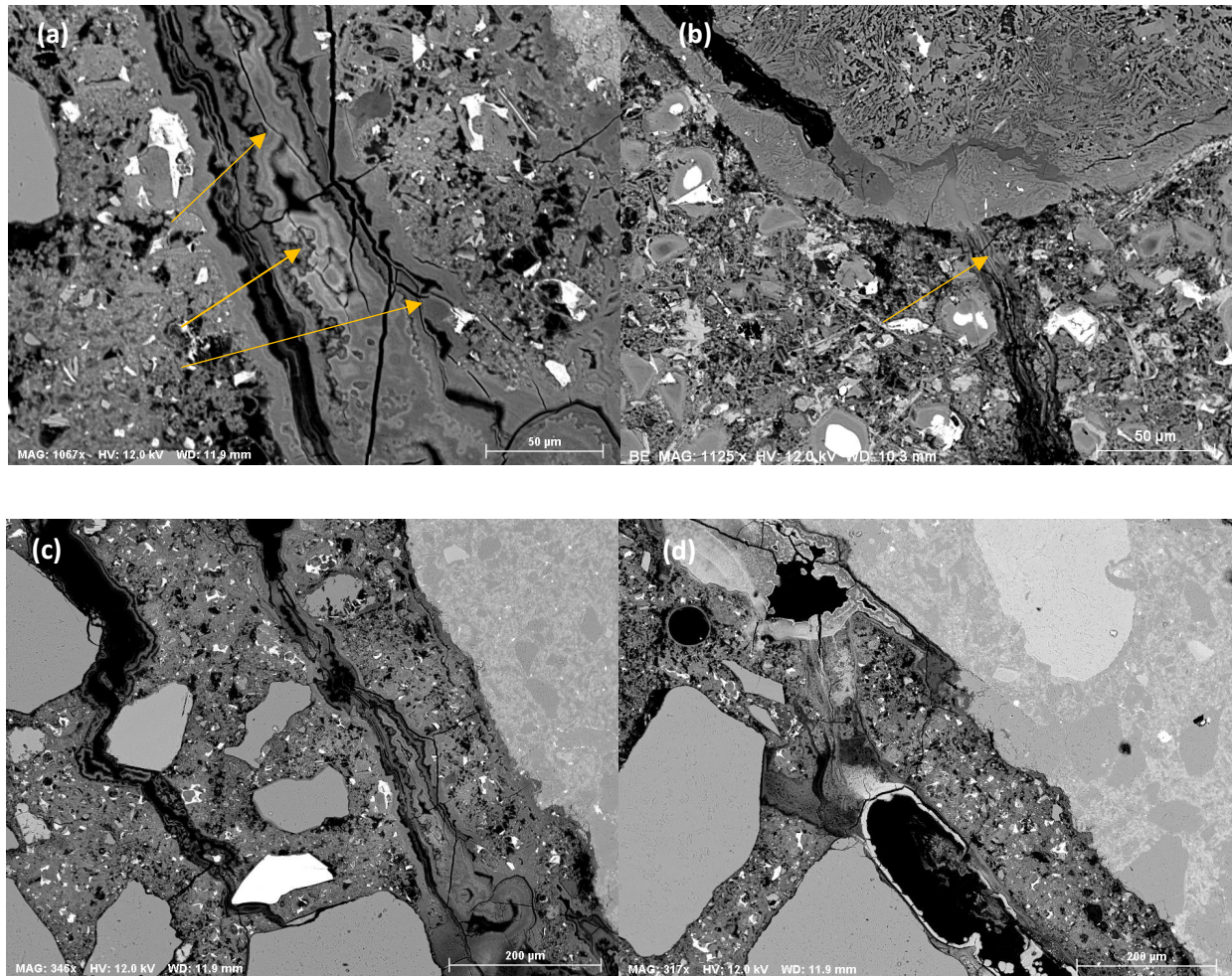


Figure 5-7. Multiple generations ('cycles') of ASR gel flowing into cement paste. Also shown are (a) dissolution pitting and (b) remobilization of emplaced silica from ASR gel and (c,d) increase in void space after dissolution.

The subtlety and complexity are demonstrated further in Figure 5-8. For the Placitas aggregate, damage occurred in the orthoquartzites and feldspars (Figure 5-8, a-c). For these phases, the nature of the damage evolved over time. Initially, the phases exhibited chattering (small, curved fractures on mineral surfaces) that progressed to dissolution with substantial mass loss. Moreover, the damage was largely *external* in orthoquartzites and both *internal* and massive in the highly reactive volcanics (e.g., amorphous volcanic glass and spherulites), with correspondingly large gel production.

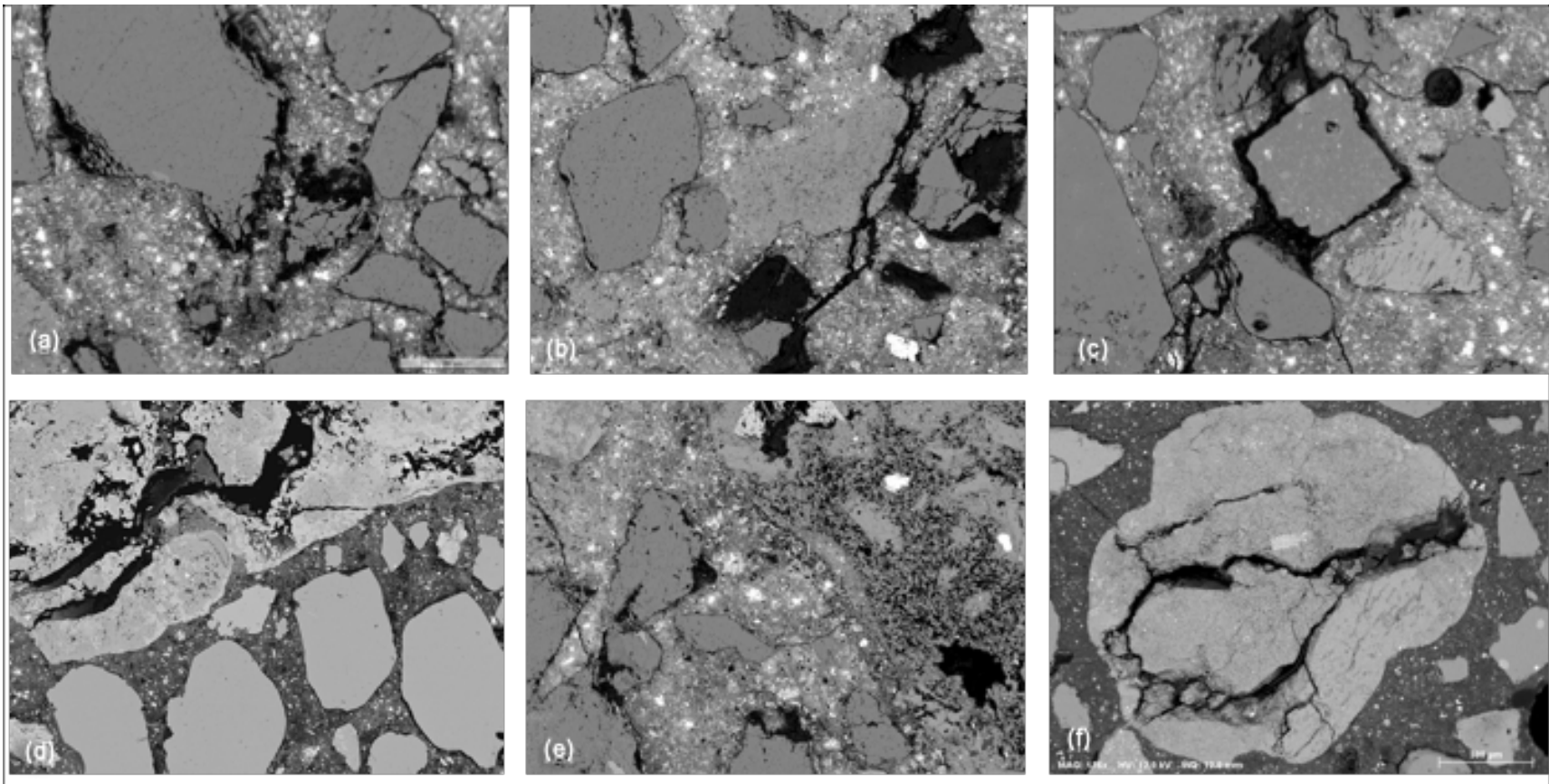


Figure 5-8. Reactive aggregate damage in orthoquartzites and feldspars is typically initiated as *external* ‘chattering’ which progresses to dissolution with appreciable mass loss over time (a-c). Damage in the highly-reactive volcanics is dominated by massive *internal* cracking and dissolution with substantial gel formation (d-f). A network of residual fine feldspar laths remaining after dissolution of noncrystalline volcanic glass is shown in (e).

It is hypothesized that the combined mineral phase dissolution and silica recycling are mechanisms that can impact the long-term residual effects of ASR. The recycling/regeneration of silica (gel) might originate as an ion exchange phenomenon where potassium and/or sodium in the low-viscosity gels (that formed in the aggregate) flow into the calcium-rich cement paste, resulting in uptake of calcium by the gel. Calcium-rich gels have lower surface charge and higher viscosity than alkali gels and are, therefore, relatively immobile.

It is the release of alkalis to solution, however, that results in localized areas of high pH, which can promote i) further dissolution of aggregate *and* ii) 'cannibalistic' attack and dissolution of existing gel with remobilization and deposition of silica, or 'secondary' gel cycles elsewhere (Figure 5-7).

The cycling of silica provides a regenerating supply of reactive surfaces available for further dissolution. In principle, this could create new material for continuing reaction after the initial supply of reactive aggregate is exhausted. Furthermore, secondary silica dissolution results in the appreciable increase of void space and loss of concrete integrity in the long term, in addition to alterations from reactive aggregate.

5.4 RELATING EXPANSION TO DEGREE OF REACTION

When the damage classes are combined with evidence of reaction, one has a more complete characterization of the ASR reaction. Borrowing from Saouma (2015), Figure 5-9 relates specific ranges of the degree of expansion to observed evidence of reaction or damage over time. Generally, early on in the reaction, one observes evidence of reaction products at the perimeter of aggregates – so-called 'reaction rims'. As reaction progresses, one finds evidence of the aggregates cracking, and then cracks propagating into the paste. The next stage is gel-filled aggregates where the gel is exhibiting desiccation cracking. Finally, there is evidence of aggregate dissolution.

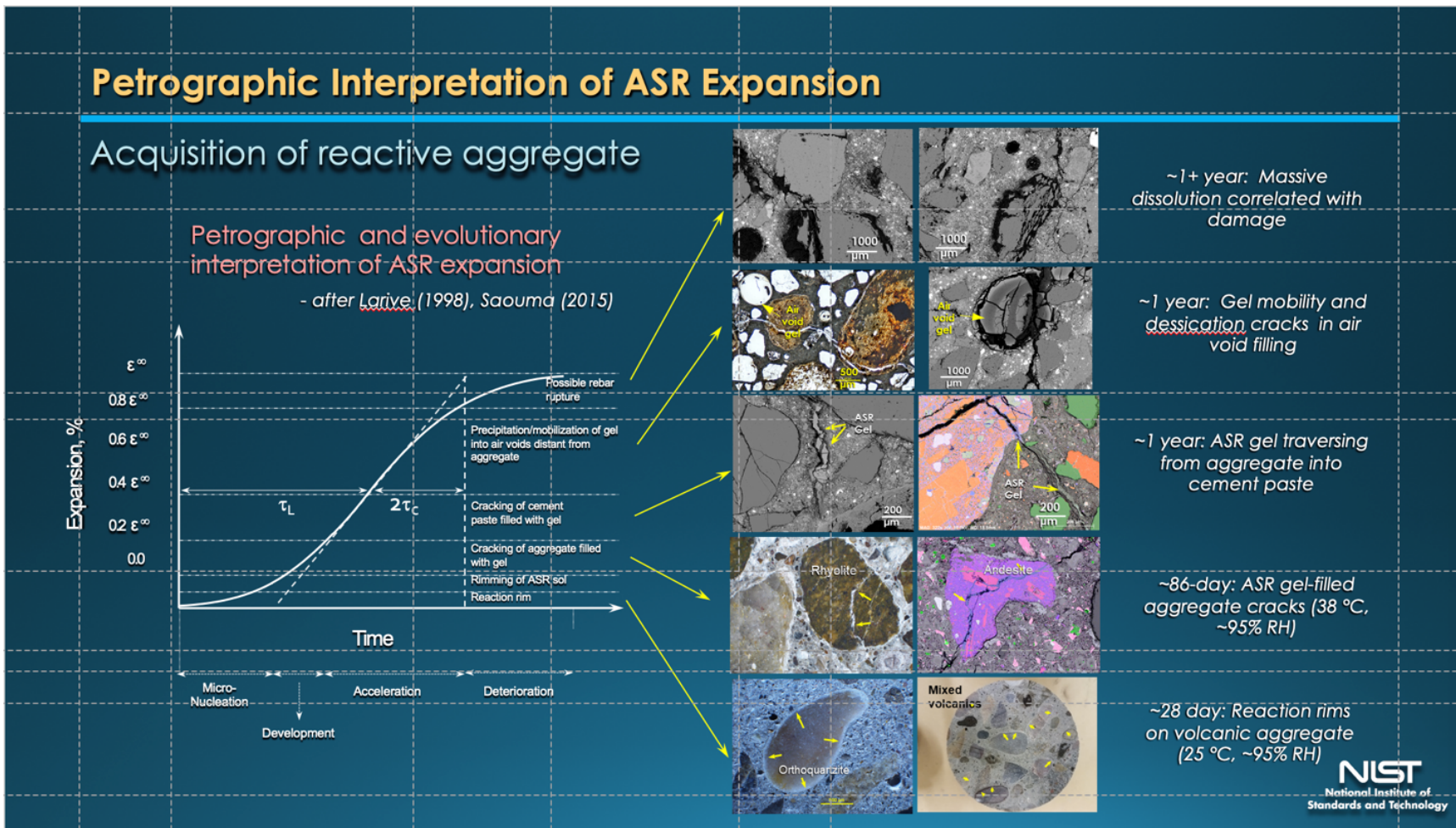


Figure 5-9. Conceptual relationship between expansion curve and damage observed in the sample.

5.5 IMAGE SAMPLING PROTOCOL

The next step was to identify methods to accurately assess the amount of damage in a specimen based on features from images taken of the polished surface. The challenge is two-fold: there needs to be sufficient magnification to identify and quantify the areas of aggregate dissolution; and the field of view needs to be sufficiently wide to capture the large spatial extent of the damage.

Furthermore, determining an adequate spatial extent must consider the heterogeneity of the aggregate, and whether the fine and/or coarse aggregate is reacting. For the Placitas aggregate analyzed in Chapter 2, there were multiple mineral phases contributing reactive aggregate, each contributing differently to the overall reaction. In bulk, the aggregate contained approximately 10 % (by mass) reactive phases. The Jobe sand, by comparison, contained approximately 20 % (by mass) reactive phases.

Given the relatively small fraction of reactive phases, an approach was developed to image the majority of the polished surface in an automated way. At 200X magnification, 1,360 individual SEM images are required to entirely cover the measurable area of a 70 mm core sample (50 mm diameter center section, allowing for exclusion of the outer 10 mm perimeter) as shown for the stitched mosaic in Figure 5-10. Focusing on the inner region ensures avoiding polishing or drilling artifacts at the specimen edges. By creating a stitched mosaic map of all 1360 images, a measure of 'ground truth' for the entire core section was obtained, which afforded the opportunity to observe spatial relationships between cementitious materials, aggregates, and ASR damage across an entire core.

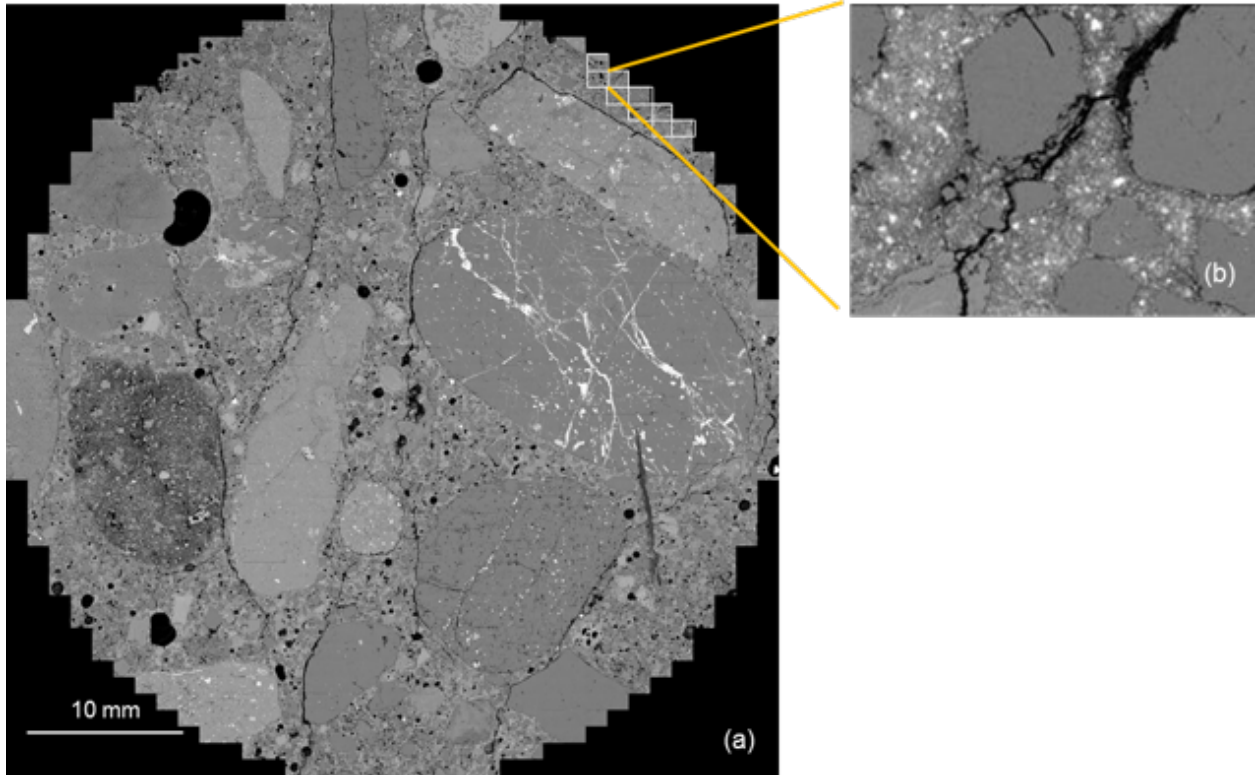


Figure 5-10. (a) 'Stitched' mosaic of 1360 SEM images mapped across the central 50 mm portion of a 70 mm diameter core specimen: Mix 3, Region 2, 180 d. (b) Single SEM image taken at 200 times magnification with a field of view of (1.1 mm x 1.4 mm); a pixel resolution of 1.47 μm.

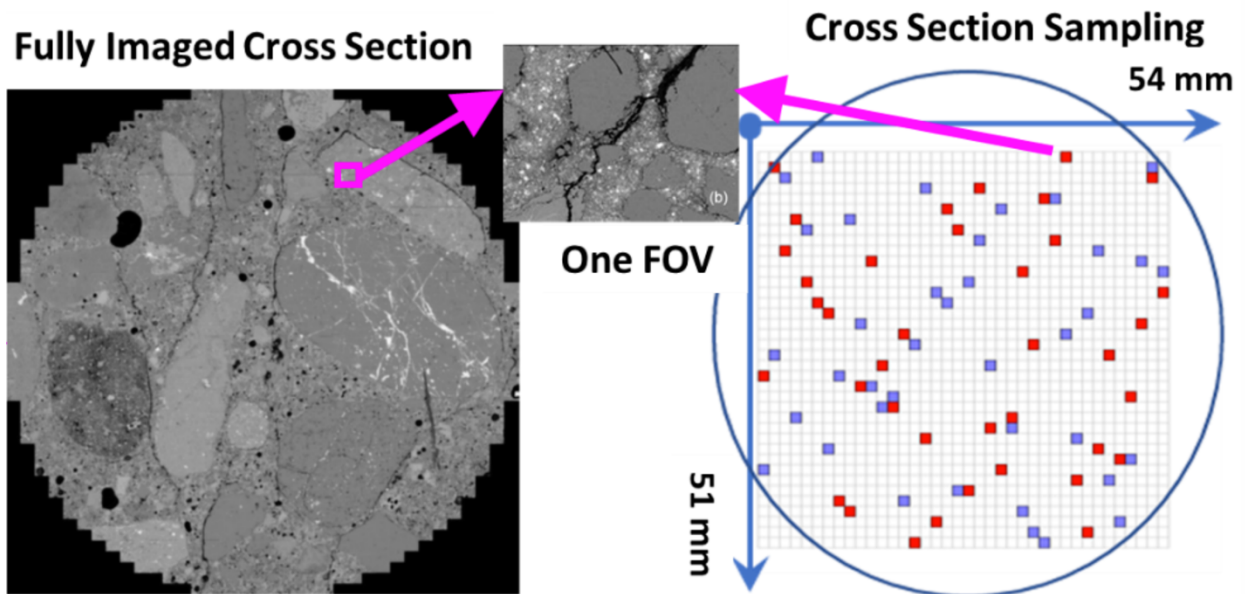


Figure 5-11. (Fig 2) Depiction of Latin Hypercube sampling over selected FOVs across the surface of a circular cross section (approximately 54 mm in diameter).

With an exorbitant amount of SEM instrument time (≈ 72 h) required to acquire mosaic images for each sample, and many core and prism samples to examine, time constraints and existing resources did not allow for an exhaustive mapping of each core or prism sample. Therefore, several contending sampling protocols were evaluated to define a representative subset of these possible 1360 images for analysis. These included i) a completely randomized design, ii) random stratified sampling (with strata consisting of the concrete damage classes), and iii) Latin Hypercube Sampling (Tang 1993).

To reduce the imaging time even more, a modified two-dimensional Latin Hypercube (LHC) method was applied to the FOVs covering the 36 x 46 grid positions; see the layout in Figure 5-11. The LHC sampling strategy during imaging generated a near-random distribution of sampling points whereby we increased the observations from one image (depicted by the blue points in Figure 5-11) in each row and column to two images per row (depicted by red in Figure 5-11). We applied the LHC sampling strategy to a grid of size 36 x 46 positions as established for the fully imaged case, and used it over each core or prism section. This sampling approach yields 72 FOVs per core or prism section (2 FOVs times 36 rows). Depending on the quality of sample and edge artifacts, the number 72 FOVs varied between 61 to 74 FOVs.

5.6 AUTOMATED SAMPLING

Collecting the more than 1300 SEM images to create a mosaic of the surface of each sample, or even the 76 images required to conduct the modified LHC sampling, in an image-by-image basis would be intractable. The automated imaging capabilities on the scanning electron microscope were leveraged for image acquisition. The electron microscope stage has x-y stepping motors for moving the sample under the beam. The focus of the electron beam, however, is controlled by the electron optics. Once the automatic image collection begins, the focal distance cannot be adjusted. Keeping the sample in focus across the entire surface requires that, not only does the surface need to be very flat, the top surface must be parallel to the base to ensure that the microscope remains in focus over the entire surface.

In addition, the concrete sample preparation process consists of multiple variables that can affect the SEM image quality. There can be variations of image quality across core and prism samples due to concrete surface epoxy-coating, grinding and polishing. The SEM imaging can be a source of variations due to sample tilt and SEM settings.

5.7 CONVOLUTIONAL NEURAL NET

A method was developed to automate the process of categorizing features within the microstructure of a concrete specimen. The method requires creating a large quantity of high-quality training segmentation masks from images taken by a scanning electron microscope (SEM). The images are acquired from concrete samples that exhibit progressive amounts of degradation resulting from alkali-silica reaction (ASR). The target damage classes in concrete seen in the SEM images are defined as paste damage, aggregate damage, air voids, and no damage. The segmentation problem was attacked by applying Convolutional Neural Network (CNN) based methods to identify and assign damage classes (due to ASR) to each image pixel. The challenges in using the CNN-based methods lie in preparing large numbers of high-quality training labeled images, while having limited human resources. To address these challenges, damage- and context-assisted approaches were designed to lower the requirements of human

resources. The accuracy of CNN-based segmentation methods was evaluated using the datasets prepared with these two approaches.

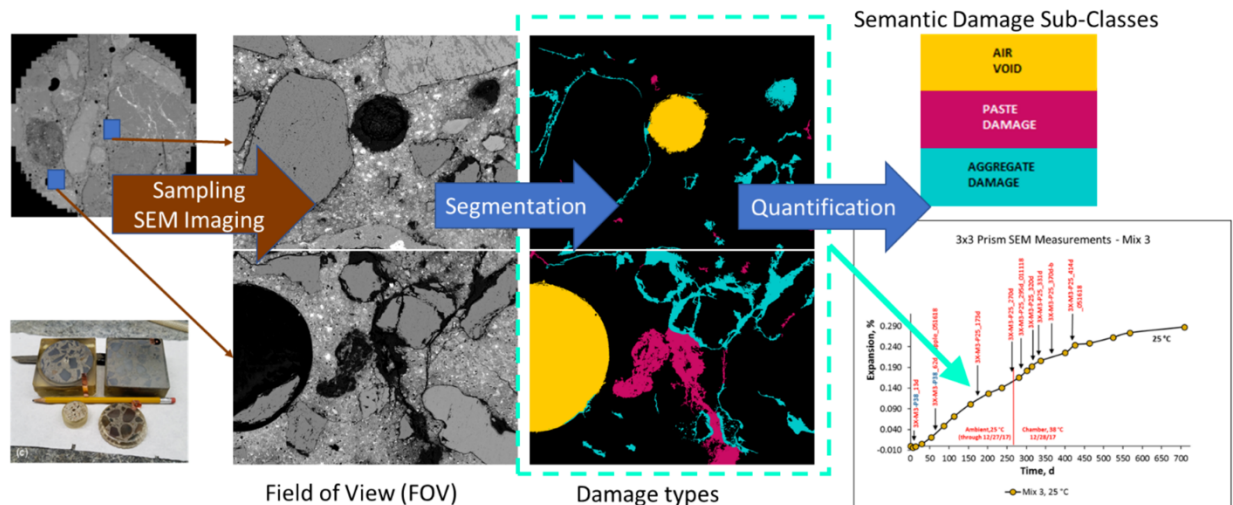


Figure 5-12. An overview of the microscopic damage quantification, including field of view (FOV) sampling, FOV segmentation, and quantification of all segmented FOVs to generate statistics about damage sub-classes.

Acquired SEM images were segmented into physical areas/volumes that correspond to microscopic damage types. The application-driven motivation for the approach lies in automated accurate image-based quantification of damage types from laboratory prepared concrete samples that were extracted from the companion prisms and from cores taken from the large Blocks, as shown schematically in Figure 5-12.

The computational problem of image-based quantification involves several challenges including (1) accurate and reliable automated segmentation across image variations, (2) computational scalability over large image collections, and (3) visual inspection and validation by quantifying the accuracy of segmentation results. First, the image variations come from a large spectrum of complex sample compositions, including degree of ASR damage over time, some variability resulting from the preparation of large numbers of over-sized concrete polished sections, and SEM imaging variability. Next, the size of image collections becomes apparent when one enumerates the ideal number of image acquisitions over time, structural conditions, environmental conditions, sample preparation protocols, and settings during SEM imaging: terabytes of image data and millions of images. Finally, visual validation of results is needed because of the increasing popularity of black-box segmentation modeling tools and the importance of applications where these laboratory and field damage measurements would be used for decision making. The computational motivation for this work lies in creating large quantities of high-quality image segmentation masks to be used for training Convolutional Neural Network (CNN)-based segmentation models applied to concrete images.

Convolutional Neural Network segmentation methods have been proven to outperform traditional machine learning (TML) models (Hesamian et al., 2019; and Simonyan and Zisserman, 2015). In addition, visual validation is also useful for comparing the results coming from the “white-box” and “black-box” models. The white-box models include traditional

supervised machine learning (TML) models with feature engineering and unsupervised clustering models with image processing (pipeline engineering).

The main contributions of this work are (1) in the experimental design of this study, and (2) in the fully automated CNN-based SEM image quantification of ASR damage sub-classes over time using a large number of quality-controlled training data. The key technical contributions are techniques for incorporating *a priori* knowledge about the SEM imaging of concrete samples a means of automating the training data preparation, and a framework for generating a large quantity of high quality training images, while minimizing the human effort. The main novelty of the work lies in (1) designing and evaluating top-down and bottom-up approaches to creating multi-class training data sets, and (2) disseminating 4594 SEM images of raw fields of views (FOVs) with their damage-assisted, context-assisted, and U-Net predicted target microstructural masks within an interactive web-based validation system (<https://isg.nist.gov/deepzoomweb/data>) for advancing segmentation models of damage in concrete.

The summary of acquired SEM images is provided in Table 5-1. The total number of SEM images for cored samples is 1360 (from 1 complete specimen) + 1161 (sampled from portions of 16 specimens). For prism samples, the number of SEM images is 2821, distributed across 29 difference prism specimens.

Table 5-1. Summary of acquired SEM images.

Variables	Number of physical samples	Represented number of time points	Spatial coverage with FOVs	Total number of SEM Images
Core Samples	17	3	1 full + 16 sampled	2073
Prism Samples	29	12	29 sampled	2821

FOV = field of view. SEM = scanning electron microscopy.

5.7.1 Related Work

Related work elsewhere is categorized based on relevance to (1) the experimental design of this study and (2) the objective of a fully automated artificial intelligence (AI) based image quantification of damage sub-classes. First, the experimental design is related to Ben Haha's PhD thesis (Ben-Haha, 2006) and a journal paper (Ben-Haha et al., 2007), both of which studied ASR damage in concrete. The concrete samples in this project exceeded more than 100 times the number of controlled structural and environmental evaluations presented in Ben-Haha et al. (2007). The authors in Ben-Haha (2006) and Ben-Haha et al. (2007) report "At a magnification of 200x, 100 images were found to be sufficient to consider and take into account about 5000 independent aggregates". Here, by contrast, 4.5 times more images were collected because the experimental design spanned a much larger spectrum of reactive phases.

Second, the SEM image quantification of damage sub-classes can leverage the past work on crack damage detection in macroscopic and microscopic images for training supervised AI-based models. The AI-based models have been trained on manually prepared segmentation of macroscale color or grayscale images of cracks in pavements, roads, buildings, tunnels, steel structures, or cityscapes (Chambon and Moliard, 2011; Cha et al., 2017, 2018; Liu et al., 2019;

Choi and Cha, 2019; and Cordts et al., 2016). These training sets are of unknown quality and acquired at very different scales than SEM images, even though they were obtained for the related task of detecting cracks or classifying damage. For example, the Crack Forest Dataset comprised 118 color images acquired by a smartphone (Shi et al., 2016), the Crack Dataset comprised merely 5 sets of gray-scale images (Amhaz et al., 2013), and the DeepCrack Dataset comprised 537 color image pairs collected from asphalt and concrete for the purpose of determining either a *crack* or a *no-crack* classification (Liu et al., 2019).

5.7.2 Methods

The task of semantic image segmentation is to classify each pixel into a predefined semantic class. An AI-based semantic image segmentation approach consists of three steps: (1) create a collection of high-quality reference image segmentations, (2) generate a large quantity of such reference image segmentations that equally represent all semantic classes, and (3) apply AI-based models for segmentation and train them on the collection of reference image segmentations. These three steps are executed under multiple maximization and minimization objectives as summarized in Table 5-2.

Table 5-2. Objectives in all steps of AI-based semantic segmentation approach.

	Maximization Objective	Minimization Objective
Step 1	accuracy of manually annotated image segments	time/effort to create pixel-level annotations
Step 2	number of pixel-level annotations	imbalance between classes
Step 3	model accuracy by optimizing architecture design, loss function, accuracy metric, and parameter selection	execution time

Given the objectives for all three steps, two methods were devised for creating training data sets and evaluated two AI-based segmentation architectures, particularly, U-Net (Ronneberger et al., 2015) and SegNet (Badrinarayanan et al., 2015) convolutional neural network architectures. Figure 5-13 shows an overview of the two methods for creating training data sets.

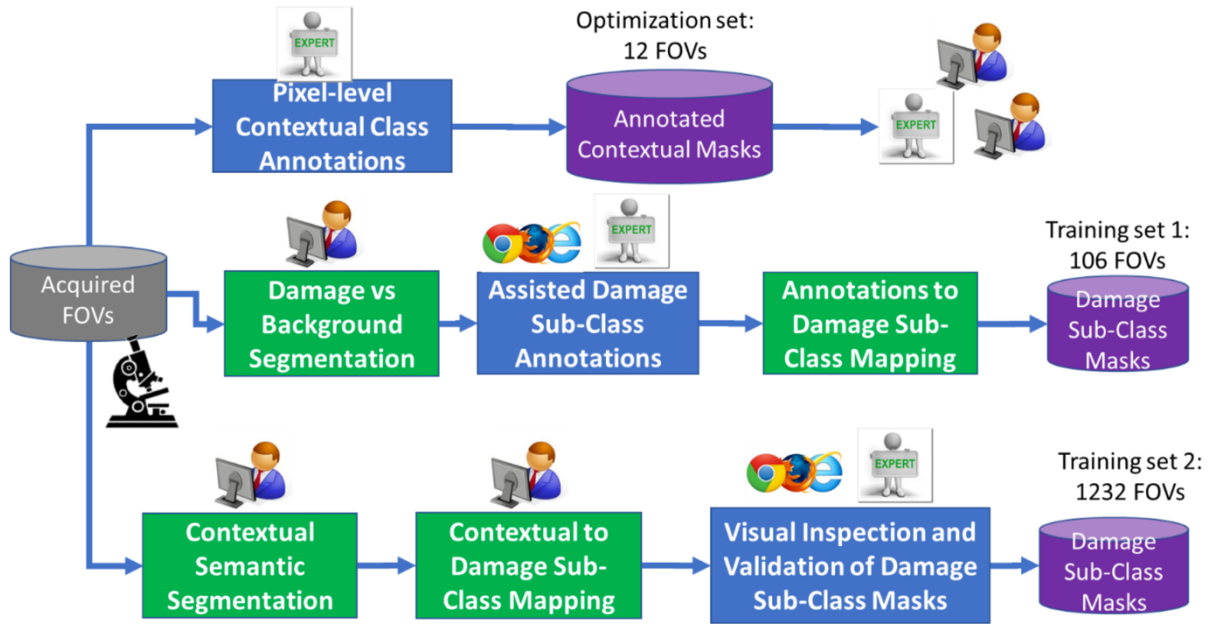


Figure 5-13. An overview of two methods for creating training data sets.

The blue boxes denote manual operations by a concrete domain expert while the green boxes refer to automated operations by a computer program applied on acquired FOVs. The optimization dataset is used for finding optimal values of algorithmic parameters in automated operations assisting in preparation of the two training datasets. The icons denote concrete and computer experts, as well as their interactions when the optimization dataset is used for knowledge transfer to computer experts. Figure 5-14 illustrates the CNN-based segmentation modeling and its accuracy validation.

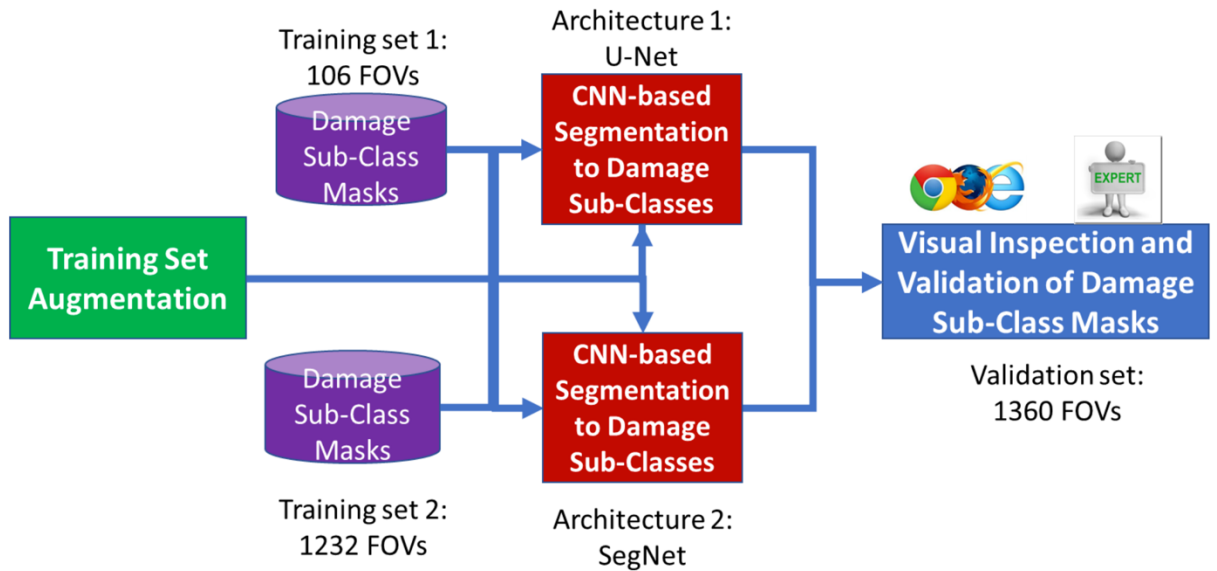


Figure 5-14. An overview of CNN-based segmentation modeling and evaluation using two training datasets.

The methods designed to meet the three objectives shown in Table 5-2 are described as follows:

Step 1: Create High-Quality Reference Image Segmentation

When creating a high-quality reference image segmentation, one must consider the accuracy of spatial annotations and semantic categorical labels. Labeling every pixel in an image containing millions of pixels is time consuming, and its spatial accuracy depends on many factors (e.g., capabilities of annotation tools, fatigue and meticulousness of annotators). Labeling pixels into many sub-classes lowers the error margin on intensity-based discrimination and is more time consuming than labeling a few sub-classes. Such considerations lead to a choice of spatial and class labeling schemes.

Spatial labels: To incorporate the accuracy maximization and effort minimization objectives (see Table 5-2), partial (weak) spatial annotations were analyzed because some of them have been studied in the past (Hong et al., 2017; and Papandreou et al., 2015). More information about the weak annotations is provided in Section 5.7.5 below.

Semantic categorical labels: In the case of SEM images of concrete samples, the categories of interest are damage sub-classes, such as damage in aggregate, damage in cement paste (paste cracking or de-bonding), and other by-stander sub-classes such as air voids and background. Our definition of aggregate damage includes aggregate cracks, partial or complete dissolution of intact grains (typically quartzites), and dissolution of finely-divided volcanic glass or spherulite bodies represented by dark interior sections of rhyolites, dacites, and andesites. The aggregate sub-classes consequently include quartzite, potassium rich and/or sodium rich (K/Na) feldspars as discrete or exsolved species, spherulites or volcanic glass, free iron oxides, and augite. The cement paste represents the matrix phase of the concrete and consists of cement powder plus water plus fine aggregate with minor free iron oxides. The two sets of semantic labels of interest are defined below:

- A set of damage sub-class labels $SD = \{\text{air void, aggregate damage, paste damage, background}\}$
- A set of contextual labels $SC = \{\text{paste, air void, quartzite, feldspar, augite, iron oxide, dissolution, volcanic, and damage cracks}\}$

The intersection of the two sets contains air voids ($SC \cap SD = \{\text{air void}\}$) and the background components are the union of certain aggregate and paste labels, which forms a subset of the set of contextual labels ($\text{background} = \cup \text{quartzite, feldspar, augite, iron oxide, paste} \subset SC$).

Step 2: Create Large Quantity of Reference Image Segmentations

To incorporate the maximization and minimization objectives for both steps 1 and 2 (see Table 5-2), we leveraged *a priori* knowledge about (1) SEM imaging (Goldstein et al., 2018; and Donovan et al., 2003) and (2) appearance of concrete component classes (e.g., paste, aggregate, sand). Based on knowledge of the compositional back-scattered electron (BSE) mode of the SEM, and the interpretation of phase composition from chemical analysis by energy-dispersive spectroscopy (EDS), the higher the average atomic number, the brighter the signal intensity will appear in the image. Thus, damage super-class containing structures with low atomic numbers represent dissolution or void space and, therefore, appear much darker than aggregate and paste classes for the majority of SEM pixels.

Note that although air-voids are classified as a type of damage, the purpose is to use shape characteristics to distinguish them from other damage classes. When characterizing the total damage of a specimen, the portion of the image classified as air void can be omitted.

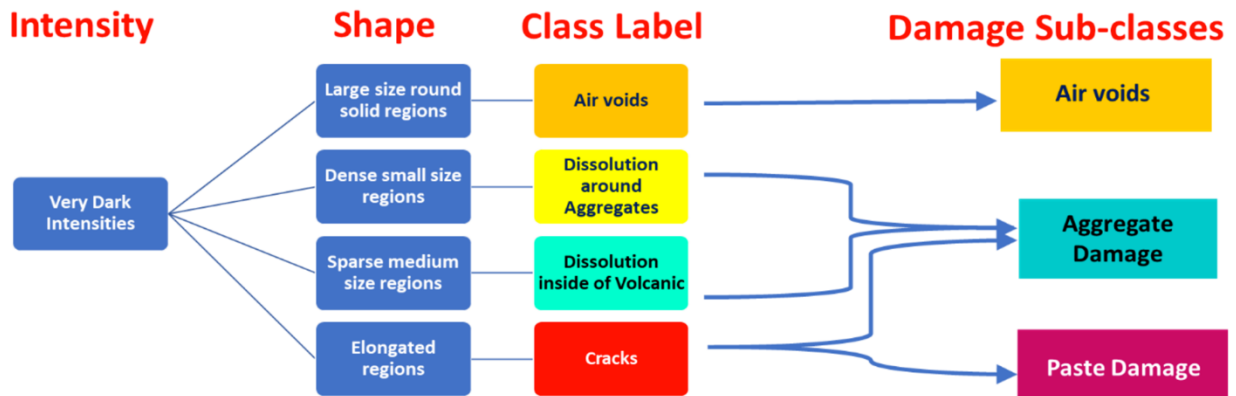


Figure 5-15. Visual description of damage sub-classes (right column) based on SEM image intensities and shape characteristics of very dark intensity pixels (left columns).

This publication is available free of charge: <https://doi.org/10.6028/NIST.IR.8415>



Figure 5-16. Visual description of contextual sub-classes based on SEM intensity and shape characteristics for gray (left) and very bright (right) image intensities and shape characteristics.

Training dataset #1 created by a damage-assisted method: Knowledge of the phase composition and microstructural interpretation based on contrast mechanism in SEM BSE analysis was leveraged for creating a training dataset #1. The method is based on automatically separating dark regions (damage versus everything else denoted as background in Figure 5-13) and presenting the damage masks overlaid on top of raw images for manual annotations. The damage super-class masks are spatially more accurate than those created by hand. The algorithm for damage versus background separation consists of intensity-based thresholding followed by morphological filtering. The algorithmic parameters (threshold and kernel sizes) are optimized against manually created pixel-level reference segmentation masks. The damage masks and raw images are presented in a zoomable web-based interface with transparent overlays and annotations tools using the Web Image Processing Pipeline (WIPP) system (Bajcsy et al., 2018). This overall method reduces the level of effort for the annotator from labeling each pixel to drawing rectangles around regions in masks that belong to a damage sub-class. False regions in damage masks are skipped and new regions could be potentially drawn as well. The mapping from annotations to damage sub-classes is done programmatically and it can incorporate color, shape and text clues from annotations to create the final multi-label training masks.

Training dataset #2 created by a context-assisted method: This dataset leverages *a priori* knowledge about the appearance of SEM images from concrete polished sections. The knowledge is represented via visual characteristics of semantic classes defined by experts as illustrated in Figure 5-15 for damage sub-classes and in Figure 5-16 for contextual sub-classes of aggregate and paste. To create a large quantity of high-quality training segmentations, these visual characteristics are turned into automated image processing pipelines that generate binary masks for each sub-class. The pipelines encode the intensity and shape models into a sequence of parametric algorithmic operations, such as thresholding, clustering, connectivity analysis, morphological filtering, filtering by region size or region solidity, filling holes, and Boolean math. The parameters of these image processing pipelines can be optimized by using manually created pixel-level reference segmentation masks. The set of image processing pipelines is represented as “Contextual Semantic Segmentation” in Figure 5-13 and the parameter optimization is performed using the collection denoted as ‘Optimization set’.

After generating 9 contextual labels (paste, air void, quartzite, feldspar(s), augite, iron oxide, dissolution, volcanic glass, and damage cracks), one must codify a set of rules applied by experts to determine damage sub-classes based on surrounding pixels with (a) contextual semantic labels and (b) damage labels. Figure 5-15 illustrates that the four damage class labels need contextual labels, and that the final damage sub-classes need rules for other than one-to-one mapping. Figure 5-13 shows this step as “Contextual to Damage Sub-class Mapping” and

Table 5-3 summarizes the set of rules to derive damage sub-classes from contextual labels. While encoding a priori knowledge into a set of image processing pipelines and a set of codified rules applied to damage sub-class labeling for creating a large collection of semantic segmentation masks, one must also ensure the high-quality of training data by enabling a visual validation of the segmentation masks. To meet the objectives for Steps 1 and 2 summarized in Table 5-2, a web-based visual validation system was designed that displays the raw image and the masks with damage sub-classes and contextual labels. The visual inspection and validation system require two mouse clicks to assign a quality score and move to the next image segmentation evaluation. Figure 5-17 shows the user interface and quality scores. The good or correct scores correspond to at least 90 % or 75 % correct assignment of labels to pixel locations. The other two scores refer to (a) less than 75 % of semantic labels were assigned to correct pixel locations (bad colors) or (b) less than 75 % of pixel locations were assigned to correct labels (bad pixels).

Table 5-3. A set of rules to determine damage sub-classes from contextual labels.

Contextual Label in Damage Superclass	Applied Rule	Damage Subclass Label
Air Void	None	Air Void
Dissolution	None	Aggregate Damage
Damage Cracks	Surrounded by Paste	Paste Damage
Damage Cracks	Between Aggregate and Dissolution	Aggregate Damage
Damage Cracks	Between Paste and Dissolution and Connected to Dissolution	Aggregate Damage
Damage Cracks	Between Paste and Dissolution and not Connected to Dissolution	Paste Damage
Damage Cracks	Surrounded by Dissolution	Aggregate Damage
Damage Cracks	Neighboring with Air Void	Air Void
Damage Cracks	Surrounded by Volcanic	Volcanic

Home Sample M3_Day180 1-1-S5-6-W-31-180d **1-2-T3-4-W-37-180d** 2-1-S4-5-N-48-365d 2-1-S5-6-S34-180d 2-2-T1-2-S-36-180d

2-2-T1-2-S-59-180d 3-1-S-4-5-E-62-623d 3-1-S5-6E-37-180d 3-1-S-5-6-E-64-180d 3-2-T1-2-W-61-365d 3-2-T3-4-60-180d 3-2-T3-4-E-37-180d

1-2-T3-4W-59-180d 3-2-T3-4-60-180d_BadFocus

Segmentation verification - 1-2-T3-4-W-37-180d

FOV name: Sample__10_10_ome.png

Raw FOV Damage Labels Contextual Labels

Previous Next

How would you classify this semantic segmentation?

Good Correct Bad Colors Bad Pixels

How would you classify this semantic segmentation?

Good Correct Bad Colors Bad Pixels

Current classification: badPixels

Your classification for this dataset

Download the CSV file

Display CSV below

- Sample__10_10_ome.png.correct
- Sample__10_29_ome.png.correct
- Sample__10_3_ome.png.badColors
- Sample__10_7_ome.png.badPixels
- Sample__11_15_ome.png.good
- Sample__11_21_ome.png.good
- Sample__11_26_ome.png.good
- Sample__11_5_ome.png.good
- Sample__12_10_ome.png.good
- Sample__12_19_ome.png.good
- Sample__12_23_ome.png.good
- Sample__12_3_ome.png.good
- Sample__13_12_ome.png.good
- Sample__13_26_ome.png.good
- Sample__13_31_ome.png.good
- Sample__14_16_ome.png.good
- Sample__14_20_ome.png.good
- Sample__14_22_ome.png.good
- Sample__14_8_ome.png.good
- Sample__15_19_ome.png.good
- Sample__15_30_ome.png.good
- Sample__15_6_ome.png.good
- Sample__16_11_ome.png.good
- Sample__16_14_ome.png.good

Figure 5-17. Web-based visual validation system. Left – selection of a sample at the top and selection of quality score (good, correct, bad colors, bad pixels). Right – the updates of quality scores as experts inspect images.

Step 3: Apply AI-based Models for Semantic Image Segmentation

The architectures of U-Net and SegNet convolutional neural networks have been implemented according to Ronneberger et al. (2015) and Badrinarayanan et al. (2015). The implementation is based on the TensorFlow library 2.0 with the default hyper-parameters described in the original papers. The TensorFlow library is already optimized for Graphics Processing Unit (GPU) execution of training and inference.

Augmentation of Training Datasets: While the above approaches to creating training datasets can yield hundreds or thousands of image pairs (raw image and multi-class segmentation mask), the CNN models like U-Net and SegNet have millions of unknown coefficients to be optimized. Although there are multiple approaches to this optimization problem as described in Section 5.7.1, we chose the data augmentation approach because it would benefit the most from our prior knowledge. Data augmentation implies that previously created training data can be altered digitally to increase the number of training instances. Sample placement is a random variable. Hence as dictated by the LHC sampling method, it is reasonable to assume that a segmentation model should be translation, rotation, and reflection invariant as experimentally documented in Majurski et al. (2018). Thus, our training datasets are augmented by applying these three geometrical transformations with the rotation angles selected randomly from $[0, 360)$, translation varying within $[0 \%, 10 \%)$ of the image size, and random choice of horizontal and vertical reflections.

Class Imbalance in Training Datasets: One of the objectives for the training dataset in Table 5-2 is to select (approximately) equal numbers of samples per class (i.e., to minimize class imbalance). Given that classes are unevenly distributed across FOVs, and given that the damage class is one of the less frequently occurring classes in FOVs, one cannot form a class-balanced dataset directly from annotated FOVs. The between-class imbalance has been approached in the literature (He and Garcia, 2009) via (a) sampling methods, (b) cost-sensitive methods, (c) kernel-based and active learning methods, and (d) additional methods using one-class learning or forecasting techniques for multivariate data. Here, a sampling method is used. As the AI model is trained by processing batches (subsets) of training datasets, each batch is formed by sampling from all classes to have each class equally represented.

Visual Inspection and Validation: The same web-based system was used for visual inspection and validation of U-Net models trained on the two training datasets as before for the context-assisted method. In this case, a user is presented with the raw and two segmented images, and selects whether both segmentations are valid or invalid, or whether only one of them is valid.

5.7.3 Results

The evaluations of the AI-based semantic image segmentation approach were divided according to the three steps described above. Since Steps 1 and 2 target the creation of training data, they are jointly evaluated because both quality and quantity of training data are equally important. Step 3 is focused on building a segmentation model with the emphasis on accuracy and speed over two CNN architectures.

To generate a baseline for creating training datasets, we fully annotated (by hand) 12 selected FOVs containing representative class samples from the set SC with 9 contextual semantic labels. The raw and manually annotated images are shown in Figure 5-18. We have also experimented with weak annotations of 31 additional FOVs where rectangles and circles inside of each region were drawn per contextual class. These weak annotations were only used for qualitative comparisons. (There were a total of 106 weak annotations.)

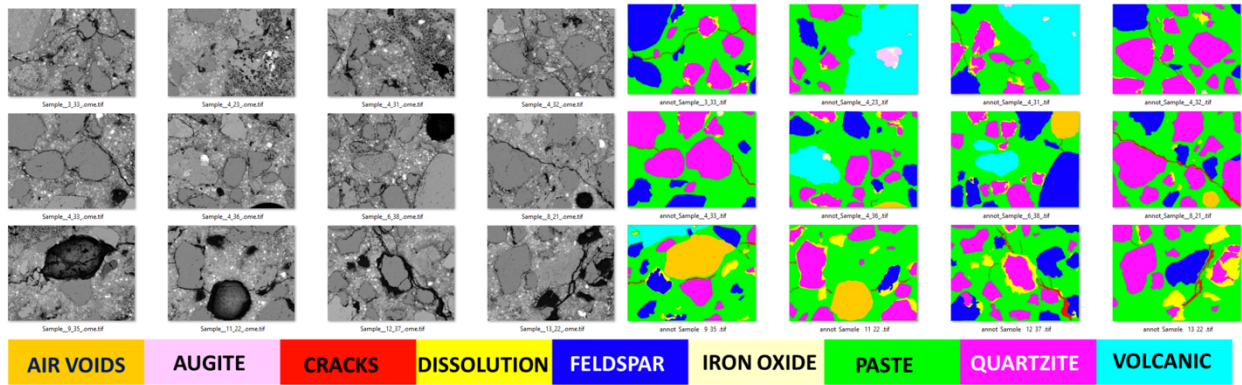


Figure 5-18. The set of 12 FOVs that were manually annotated and used for optimizing algorithmic parameters. Left – raw FOVs. Right – annotated FOVs. Bottom – color legend.

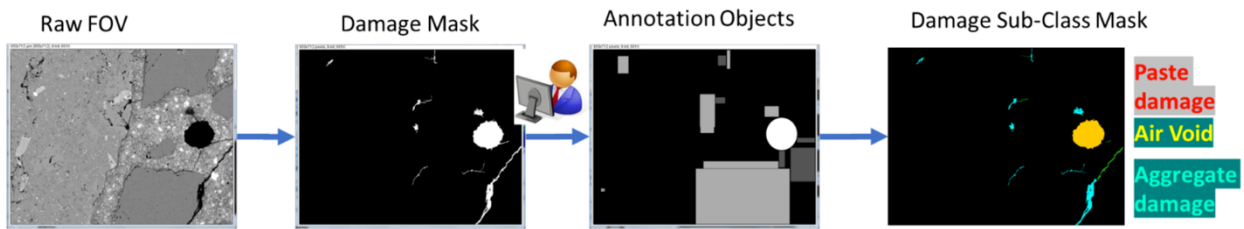


Figure 5-19. Illustration of intermediate images during the sequence of steps in a damage-assisted segmentation.

In Section 5.7.2, two sets of semantic labels were introduced (SC – contextual, and SD – damage), and two training datasets were created by using damage-assisted (#1) and context-assisted (#2) methods. The 12 FOVs fully annotated (i.e., annotated by hand) were used to optimize algorithms and their parameters for creating the two training datasets. The intermediate image results for both damage-assisted and context-based segmentation methods are illustrated in

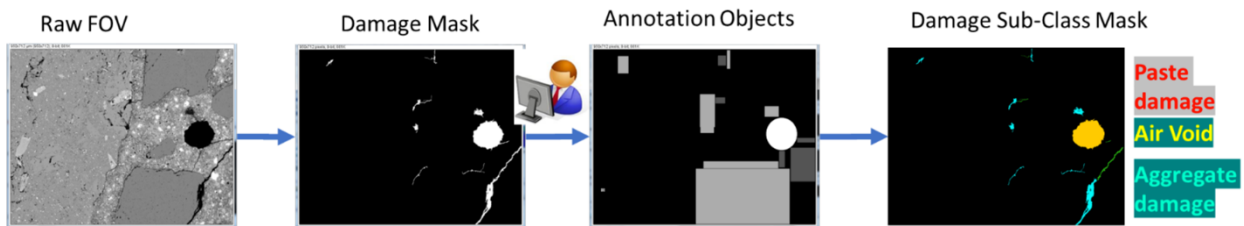


Figure 5-19 and Figure 5-20, respectively, with a human operator icon indicating the manual inputs.

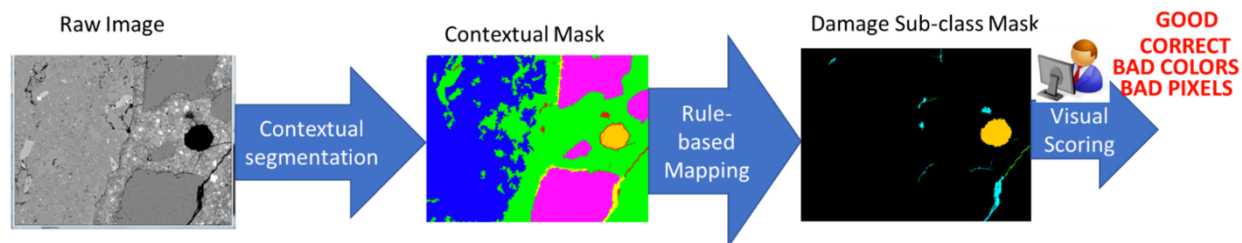


Figure 5-20. Illustration of intermediate images during the sequence of steps in a context-assisted segmentation.

Evaluations: To evaluate accuracy, coverage, and required levels of effort, a comparison was conducted of the manual method with the damage-assisted (#1) and context-assisted (#2) methods, and the results shown in

Table 5-4. The main goal of these evaluations was to understand the tradeoffs between accuracy, coverage, and level of effort to generate high-quality and high-quantity training datasets. This comparison considers both spatial and semantic aspects of the assigned labels. Spatial accuracy is defined as the accuracy of labeling local details. The spatial accuracy delivered by a human is limited by the narrow and jagged shape of cracks, capabilities of annotation tools (i.e., mouse click location, display resolution) and level of effort. Thus, the manual annotation method has a low spatial accuracy when labeling each pixel, and medium spatial accuracy when drawing bounding boxes as opposed to an automated method based on pixel intensities. The spatial coverage is defined as the percentage of pixels annotated per FOV. Semantic accuracy is defined as our confidence that the semantic (color) label is correct.

While all annotations created by hand have high semantic accuracy, the drawing of rectangles and circles as a part of the damage-assisted method has shape and location limitations in reassigning damage mask pixels into damage sub-classes. Thus, semantic errors, such as overlapping rectangles with different labels or missing damage pixels, occur and hence the method is labeled with medium semantic accuracy. Semantic coverage corresponds to the percent of labels being assigned. In our case, the union of two sets of labels (SC and SD) yields 12 unique labels. The methods summarized in

Table 5-4 show the semantic coverage as 3, 9, or 12 out of 12 labels.

Finally, the level of effort per FOV was approximated by estimated annotation time. The number of generated annotated FOVs varies because the total level of effort per method also varies (e.g., Manual \approx 24 h to 48 h; Weak manual \approx 3.6 h to 7.2 h; Damage-assisted \approx 26.5 h; Context-assisted \approx 1360 x 16 s = 6 h). The 106 FOVs obtained using the damage-assisted method were manually sampled from the set of 1360 FOVs – comprising a full-coverage stitched mosaic of an entire core section surface - due to the total time needed for annotating all FOVs. On the other hand, there were 1232 FOVs obtained using the context-assisted method after scoring all 1360 FOVs. The 1232 FOVs were scored as “Good” or “Correct”, and obtained 90.6 % accuracy for the context-based method.

Table 5-4. Evaluations of two semi-automated methods, damage-assisted and context-assisted, for creating high-quality and large quantity of reference semantic segmentations under constraints described in Table 5-2. All methods start with a collection of 1360 FOVs and generate the number of annotated FOVs shown in the left column.

Annotation Method	Annotation Operation	Spatial Accuracy	Spatial Coverage [%]	Semantic Accuracy	Semantic Coverage [%]	Annotation Level of Effort per FOV
Manual (12 FOVs)	Polygon + Color + Text	Low	100	High	75	2 h to 4 h
Weak Manual (31 FOVs)	Rectangle or Circle + Color + Text	Low	≈35	High	75	7 min to 14 min
Damage-assisted (106 FOVs)	Rectangle or Circle + Color + Text	Medium	100	Medium	25	15 min
Context-assisted (1232 FOVs)	Click on Score Button	High	100	High	100	16 s

Class imbalance: In addition, the problem of class imbalance was documented in Figure 5-21. The distributions of samples in 12 manually annotated FOVs was divided into 9 contextual classes and 3 damage sub-classes. The class percentages are used by AI-model training routines to form batches of samples with uniform class representation.

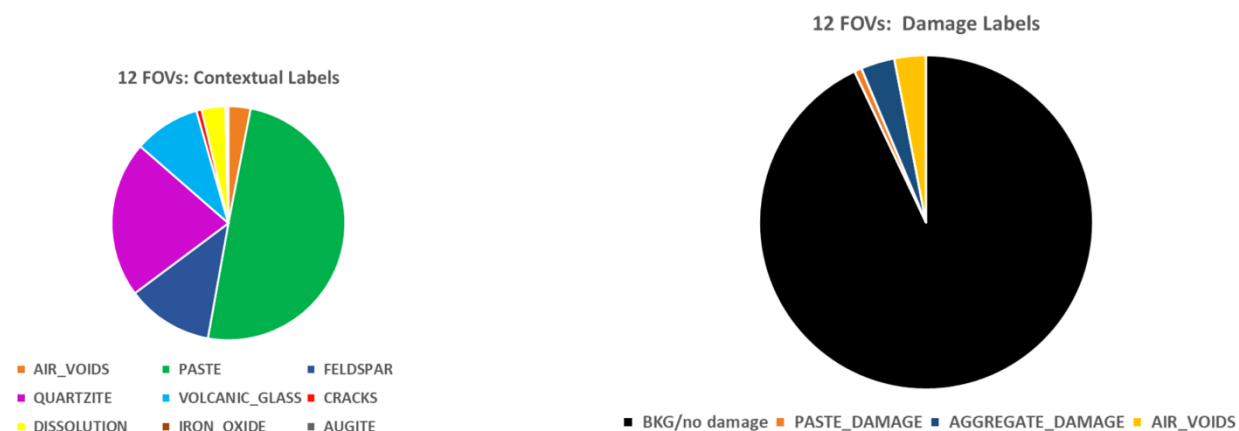


Figure 5-21. The distribution of samples in 12 manually annotated FOVs across contextual classes (left) and damage sub-classes (right).

Optimization of algorithmic parameters: The set of computational pipelines for creating 9 contextual masks and the damage mask consists of several algorithmic parameters. Figure 5-22

illustrates the pipeline for computing the damage mask using intensity-based thresholding and filtering by size. Similarly, Figure 5-23 shows the pipeline for computing feldspar, quartzite, iron oxide, and augite masks using K-means clustering, hole filling, filtering by size, and morphological filtering. The decision behind the choice of K-means clustering was based on *a priori* knowledge about the mapping between SEM intensities and average atomic numbers of concrete components (Goldstein et al., 2018). During the experimental design and sample preparation, concrete samples were measured for the presence of several components (e.g., feldspar, quartzite, iron oxide, augite, and volcanic without dissolution). These components in concrete form spatially homogeneous regions in SEM images that could be identified by simple intensity-based clustering. Unfortunately, the intensity calibration of a SEM instrument might not always be perfect, and the sample surface might not be perfect. Thus, the intensities defining all components might shift along the dynamic range (256 unique values). K-means clustering with a fixed set of intensity seeds can incorporate the intensity-to-component mapping and provide enough flexibility to adapt the cluster to the shift of the initial seeds.

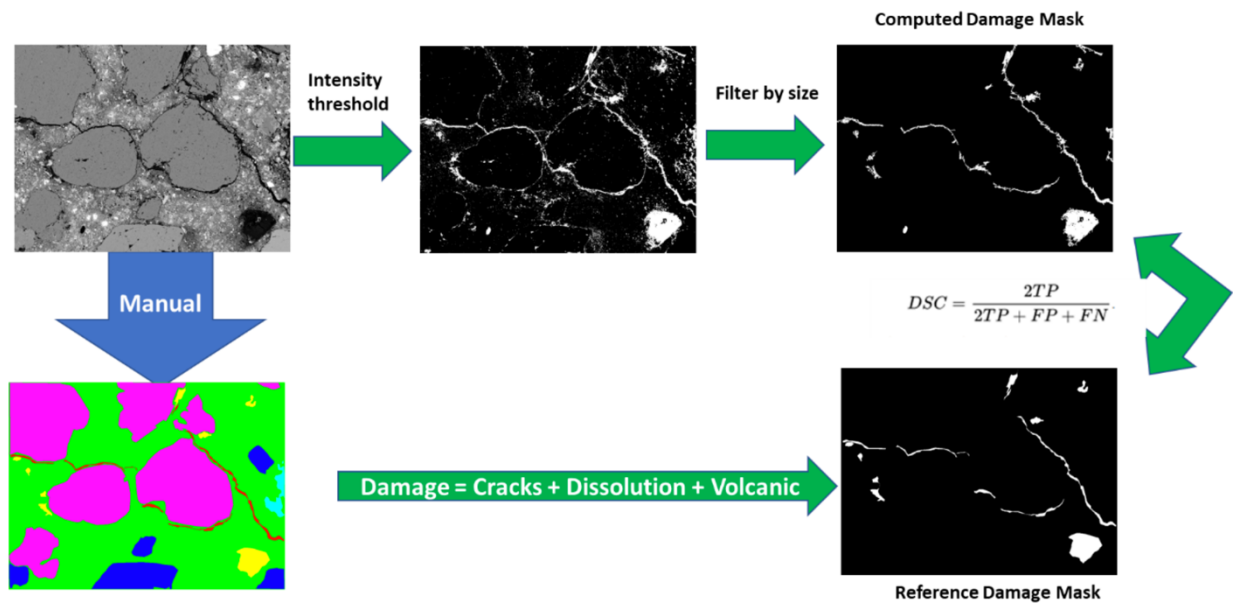


Figure 5-22. A pipeline for computing and isolating the damage mask from background. DSC: Dice Similarity Coefficient; TP: True Positive; FP: False Positive; FN: False Negative.

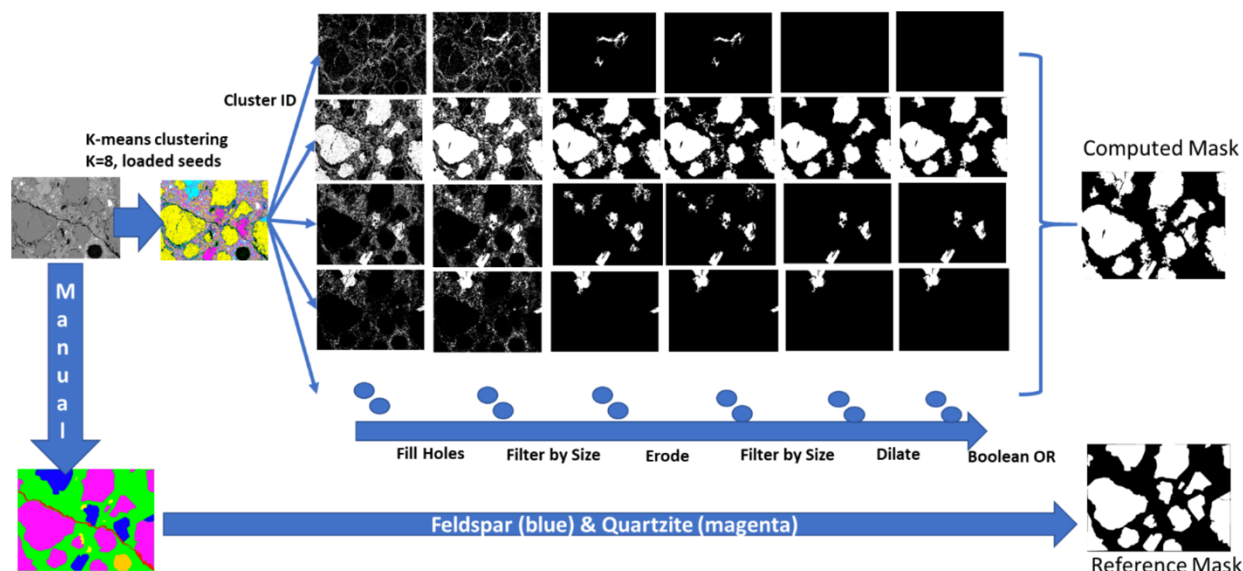


Figure 5-23. A pipeline for computing aggregate mask that corresponds to feldspar, quartzite, iron oxide, augite, and volcanic without dissolution.

These high-dimensional parametric spaces of computational pipelines are optimized by an exhaustive search. For example, the pipeline in Figure 5-22 was optimized per FOV using Dice Similarity Coefficient (DSC) (Dice, 1945) over intensity thresholds in the range [20, 105]; $\Delta=5$; and over minimum object size in [25, 305]; $\Delta=10$. The optimal values are calculated as the average over individual optimal values per FOV. In this case, the average optimal intensity threshold was 61 ± 20 (one standard deviation), and the average minimum object size was (247 ± 57) pixels. For the K-means clustering shown in Figure 5-23, fixed seeds were used, starting at 40, and spaced by 30 intensity levels which leveraged our *a priori* knowledge about SEM and experiments with random seeds. By fixing the clustering seeds, we could predict semantic labels found in each FOV and make the algorithm deterministic.

The optimization step also includes the fusion order of contextual masks generated by multiple computational pipelines. The damage and aggregate classes have the highest invariance of their region intensity properties while volcanic and paste classes have the smallest intensity invariance. In general, the higher region invariance implies the higher confidence in spatial and semantic algorithmic accuracies.

By comparison, the dissolution and air voids pipelines directly derive labels from the aggregate and damage masks respectively and hence their accuracies are conditional on the source masks. Thus, one can derive the fusion order by starting with a damage mask, and overwriting damage and non-damage pixels with low-confidence volcanic mask, followed by writing high-confidence aggregate mask, and then dissolution and air voids sorted by their average DSC over the 12 manually annotated images. All remaining pixels that are still labeled as non-damage are then relabeled as paste.

5.7.4 Evaluate AI-Based Semantic Image Segmentation Models

U-Net (Ronneberger et al., 2015) and SegNet (Badrinarayanan et al., 2015) architectures were constructed with the published default parameters. The input images were (a) normalized, (b) augmented with rotation, translation and flip models, and (c) balanced using class sampling when preparing batches. Each image dataset was randomly split into 80 % of images for training and 20 % of images for testing. The Adaptive Moment Estimation optimizer (Kingma and Ba, 2015) was used, instead of stochastic gradient descent, and the rest of the parameters remained the same as in the original U-Net publication. The training was repeated three times to capture the contribution of randomness in model estimation.

Accuracy: Three modeling accuracy metrics were used: a misclassification error rate (MER) (Kundu, 2004), adjusted rand index (ARI) (Hubert and Arabie, 1985), and a four-class confusion matrix. For the mathematical definitions of the metrics, see Section 5.7.5. All metric values are reported as averages over three training runs with the same data. Table 5-5 summarizes the three metrics for the two training data sets and the U-Net model. In addition, the maximum standard deviation is calculated from three runs per metric. The SegNet model perform similarly to the U-Net model with MER=0.035 and MER=0.045 for training sets #1 and #2, respectively

Speed: The implementation of the AI models was written in Python and leveraged the TensorFlow library (Abadi et al., 2015) which has been optimized for execution on GPU hardware. The training time for dataset #1 is smaller than for dataset #2 due to the number of training images and the total computational time ranged between (3 to 4) h, depending on the GPU card specifications. The inference segmentation time is less than a second per FOV. As a rough comparison, the software for automating steps in training dataset creation was written in Java, was leveraging ImageJ libraries (Schindelin et al., 2012), was run on CPU hardware, and took at most 55 s per FOV for the execution of contextual segmentation (without any optimization).

5.7.5 CNN Weak Annotations and Accuracy Metrics

Figure 5-24 (top branch) shows a spectrum of possible spatial annotations applied to SEM images of concrete. The key discriminator for the spectrum of spatial annotations is the amount of time and effort per image spent by one annotator. Ideally, one would like to assign a categorical label to each pixel in an SEM image such that the label is denoting one of the contextual and damage sub-classes. This annotation approach is shown in Figure 5-24 as “Full” semantic image annotations and it is very time consuming. To reduce the time requirements, another approach is “Weak – Semantic” labeling shown in Figure 5-24. One can annotate either a subset of classes (the un-annotated pixels labeled as “un-interesting”) or pre-computed higher-level classes (super-class of the class of interest).

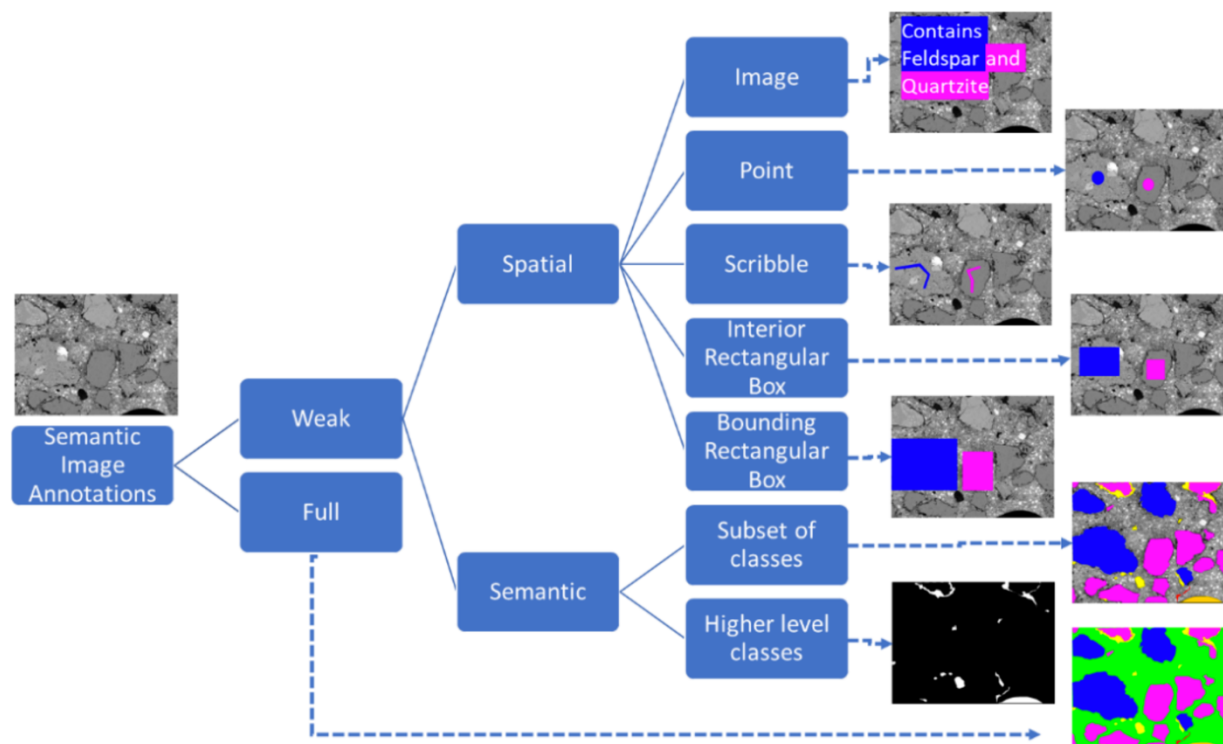


Figure 5-24. Classification of spatial annotation types.

From the spectrum of possible spatial and semantic annotations shown in Figure 5-24, the full annotations of all image pixels were used to establish segmentation references for contextual classes (bottom branch in Figure 5-13) and then the annotations of weak, semantic, higher-level classes, such as the damage super-class (middle branch in Figure 5-13). We also experimented with the annotations of weak, spatial, interior rectangular boxes of contextual classes (see Figure 5-24). However, we did not use them since the incomplete annotations miss accurate object boundary information required to learn segmentation.

The results of semantic segmentation approaches were analyzed for accuracy. The misclassification error rate (MER) is defined as the following ratio:

$$\text{MER} = \frac{\# \text{ of incorrectly classified pixels}}{\# \text{ of all pixels}} \quad (5-1)$$

The misclassification error rate is used to characterize the overall accuracy (α), defined mathematically as follows:

$$\alpha = 1 - \text{MER} \quad (5-2)$$

The Rand Index (RI) (Rand, 1971) is a measure of the percentage of correct decisions made by an algorithm, and is computed using the following equation:

$$RI = \frac{TP+TN}{TP+FP+TN+FN} \tag{5-3}$$

where TP: True Positive; TN: True Negative; FP: False Positive; and FN: False Negative. The adjusted Rand Index (ARI) is corrected-for-chance, and depends on the maximum Rand Index $\max(RI)$ and the expected Rand Index $\langle RI \rangle$:

$$ARI = \frac{RI - \langle RI \rangle}{\max(RI) - \langle RI \rangle} \tag{5-4}$$

In practice, one compares the classification in the predicted output classifications to the annotated input classifications. For input classifications (Ground Truth) X_i where $(1 \leq i \leq r)$ and output classifications (Estimates) Y_j where $(1 \leq j \leq c)$, the intersection of the possible cross-classifications are tallied in a table like that shown in Table 5-5. The value in each table element n_{ij} represents the number of pixels. The sums across each row are a_i , and the sums down each column are b_j .

Table 5-5. Definitions of the entries in Eq. 5-5 via the counts n_{ij} of the predicted labels Y_j (Est) at pixels with known reference labels X_i (Ground Truth (GT)) in multi-label segmentation.

GT/Est	Y_1	Y_2	...	Y_c	Sums
X_1	n_{11}	n_{12}	...	n_{1c}	a_1
X_2	n_{21}	n_{22}	...	n_{2c}	a_2
\vdots	\vdots	\vdots	\ddots	\vdots	\vdots
X_r	n_{r1}	n_{r2}	...	n_{rc}	a_r
Sums	b_1	b_2	...	b_c	

The ARI can be alternately expressed as a function of the elements of Table 5-5:

$$ARI = \frac{\sum_{ij} \binom{n_{ij}}{2} - \left[\sum_i \binom{a_i}{2} \sum_j \binom{b_j}{2} \right] / \binom{n}{2}}{\frac{1}{2} \left[\sum_i \binom{a_i}{2} + \sum_j \binom{b_j}{2} \right] - \left[\sum_i \binom{a_i}{2} \sum_j \binom{b_j}{2} \right] / \binom{n}{2}} \tag{5-5}$$

where the notation $\binom{n}{m}$ is the binomial coefficient: $\frac{n!}{m!(n-m)!}$.

5.7.6 Discussion

Training data preparation and segmentation modeling: While the U-Net and SegNet architectures achieve similar accuracies, the accuracy of these models depends on the quality and quantity of training datasets. According to Table 5-6, the U-Net based on context-assisted training dataset is more accurate based on MER and ARI but less accurate based on confusion matrix (see lower values for air voids and paste damage classes) than the U-Net based on the damage-assisted training dataset. The ranking of damage sub-classes, according to their segmentation accuracy, is paste damage, aggregate damage, and air voids from the lowest to the highest accuracy. Both U-Net models follow the same accuracy ranking of damage sub-classes.

Visual Inspection and Validation of two U-Net Models

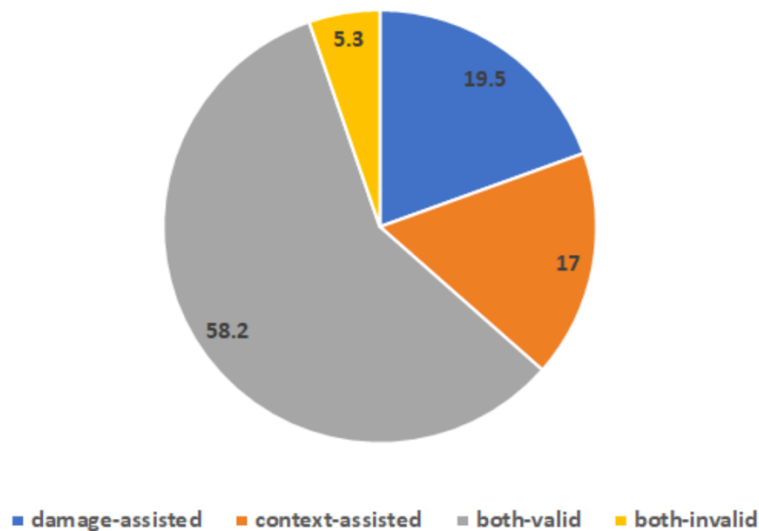


Figure 5-25. Visual inspection and validation of segmentation results obtained from the U-Net models trained on damage-assisted and context-assisted training datasets.

To quantify the amount of inconsistency across these two U-Net models, we designed a web-based validation system and performed visual inspection and validation over 1360 segmentation pairs obtained from the two U-Net models. The results of the two U-Net models is summarized in Figure 5-25. The numerical results are consistent with the results in Table 5-6 and reflect the fact that MER and ARI are less useful metrics. While the context-assisted approach is less time-consuming than damage-assisted approach or full-manual pixel-level approach, it is sensitive to image quality and consistency of image-level labeling during visual inspection.

The segmentation error sources for the paste damage class could be attributed to the smallest occurrence of the class in both training data sets (i.e., class imbalance) and to potential inconsistency of human labeling. While summarizing the set of rules to determine damage sub-classes from contextual labels in Table 5-3, consideration was given to the cases of a damage pixel being surrounded partially by paste, aggregate and air voids, which leads to human uncertainty in assigning one of the damage sub-classes. These uncertainties during training data preparation and segmentation modeling motivated the need to disseminate 4594 raw fields

of view (FOVs) with their damage-assisted, context-assisted, and U-Net predicted target microstructural masks within an interactive web-based validation system at <https://isg.nist.gov/deepzoomweb/data>.

Table 5-6. Summary of test metrics (error, accuracy, and confusion matrix) for two training datasets and U-Net model. BKG: background; PD – paste damage; AD – aggregate damage; and AV – air voids.

Accuracy Metric	Damage-assisted training set 1: 106 FOVs			Context-assisted training set 2: 1232 FOVs		
	Metric Value	St. Deviation		Metric Value	St. Deviation	
MER (Error)	0.033	0.04		0.022	0.03	
ARI (Accuracy)	0.727	0.34		0.799	0.24	

Confusion Matrix	Damage-assisted training set 1: 106 FOVs					Context-assisted training set 2: 1232 FOVs				
	Classes	BKG	PD	AD	AV	Classes	BKG	PD	AD	AV
	BKG	0.98	0.01	0.01	0	BKG	1.0	0	0	0
	PD	0.34	0.29	0.28	0	PD	0.1	0.26	0.59	0.05
	AD	0.09	0.09	0.76	0.03	AD	0.09	0.12	0.77	0.03
	AV	0	0	0.02	0.97	AV	0.01	0.02	0.07	0.89

Chapter 6

FINDINGS AND RECOMMENDATIONS

6.1 CONCRETE MIXTURE DESIGNS

Developing the concrete mixtures to achieve specific target levels of unconfined expansion was more time-consuming than had been originally envisioned. This process was complicated by two factors. Excessive expansion (greater than 0.3 %) was sought, and specific target ultimate expansion values were sought. The concrete industry publishes guides for developing concrete mixtures to achieve performance goals such as compressive strength or workability. There are no corresponding guides, however, for developing concrete mixtures to expand, let alone guides for developing concretes to expand by specified amounts. Moreover, achieving an expansion in excess of 0.3 % is a specialty requirement, like specifying a concrete compressive strength greater than 65 MPa (10 000 psi). It requires specialty materials, often shipped in from afar. As a result, the reactive aggregates had to be procured from Texas (Jobe sand) and New Mexico (Placitas coarse aggregate). Moreover, aggregate is a natural, quarried material, so extended measures had to be taken to ensure that the batch of aggregate shipped had the desired characteristics.

To complicate matters further, analysis of the Placitas aggregate revealed that it is a complex material. It contains a number of different aggregate types, and more than one mineral phase contributed to the ASR expansion. This complexity made finding simple relationships between observable quantities and degree of reaction challenging. For example, variations in temperature changed both the rate and the apparent ultimate expansion. This was likely due to the different reacting phases having different temperature-dependent reaction rates and chemical stabilities.

6.2 EXPANSION MEASUREMENT STATISTICS

Predicting the expansion of the Task 1 Blocks would not have been possible without casting expansion prisms using the concrete mixture materials directly (i.e., crushing and sieving the aggregate for ASTM C1260 testing would not suffice). A number of different prism sizes exist, but as the size of the prism grows, so does the complexity of material handling and processing, and prism storage. Given that the mix design development required “starting from scratch”, many batches had to be made, necessitating a smaller, practical prism. On the other hand, one needs a prism of sufficient size to achieve representative expansion. There were practical upper limits to the size of the prisms, even during the casting of large blocks, because many replicate prisms had to be cast and stored in a conditioned environment.

The minimum acceptable prism size depends upon the ratio of the minimum dimension of the cast prism and the maximum size of the large aggregate. The sieve analysis of the La Placitas large aggregate (Chapter 2) indicates that it entirely passed the 25 mm sieve opening. Therefore, the ratio of prism minimum dimension to the largest aggregate was 3:1 and 4:1 for the 3x3 and the 4x4 prisms, respectively. Unfortunately, the larger 12-in cubes that were

discussed in Chapter 4 gave inconsistent results because their instrumentation and conditioning were not developed for this purpose.

Section 3.1.5 compared the measured expansion from the 3x3 and 4x4 prisms, along with the linear expansion of the 4x8 cylinders. The discussion of the results in that section pointed out the inconclusive nature of the comparison between 3x3 and 4x4 data. For Mix 1, there was excellent agreement between the unconfined expansion measured from the 3x3 and the 4x4 prisms. For the other two mixes, however, there was nearly a 0.1 % difference in the ultimate expansion based on these two prism sizes. Unfortunately, the cast 4x8 cylinders didn't corroborate the results from either prism size: for Mix 2, the 4x8 cylinder data agreed most with the 4x4 prism data; and for Mix 3 the 4x8 cylinder data agreed most with the 3x3 prism data.

The story becomes even more complex when one considers multiple series of tests (i.e., replicate mixing and casting of the same mixture design). The companion Task 1 prisms discussed in Chapter 3 constituted a single series of specimens. By comparison, the temperature-dependent data discussed in Chapter 4 demonstrate the additional series-to-series uncertainty that can arise. This is most evident in the data shown in Section 4.4. For these studies, when multiple series of replicate prisms were tested, there sometimes occurred a complete series of results that contradicted the data from other series. For example, the Mix 1 expansion data at 38 °C contains a series of expansion measurements that were noticeably less than the data from the other two series. It is also important to note that this same series (orange) behaved anomalously for all three mixes. The source of this anomaly is unknown, and were it not for the data from the other series, these observed results would have otherwise appeared to be unremarkable. More importantly, had only this one series been conducted to obtain 38 °C data, the resulting characterization of the mixtures would have been different.

When looking at multiple series, however, a consistent story emerges, and one begins to develop confidence in the expected behavior of a mixture. The recommendation, therefore, is to base one's judgement of future behavior of a concrete mixture on multiple series of tests, not just multiple replicate specimens of a single series.

6.3 TEMPERATURE DEPENDENCE

The temperature dependence of the 3x3 prisms suggested that there may be a universality to the ASR reactions. If changing the temperature merely changes the rate of the reaction, one should be able to scale (multiply by a constant) the time values for data at one temperature and have the data overlap the data at a different temperature. This general behavior was demonstrated in Section 4.4.2. In general, a time scaling could be found to make data from different temperature exposures to overlay upon one another.

Using the *ad hoc* scaling demonstrated in Section 4.4.2, the rates of expansion, relative to 25 °C are shown in Table 6-1 below. As expected, the relative rates increase with increasing temperature. Moreover, there is an exponential character to the data that might suggest an Arrhenius type of temperature dependence.

Table 6-1. Relative expansion rates for each Mix, relative to 25 °C. Values are taken from Figure 4-6 through Figure 4-8.

Mix	Rate Factor		
	25 °C	38 °C	55 °C
1	1	3	8
2	1	5	22
3	1	6	16

Although an Arrhenius approach to characterizing the temperature dependence looks compelling, there are additional features of the temperature dependent data in Chapter 4 that bring into question the validity of the Arrhenius assumption. For all three mixes, the asymptotic value for the 55 °C expansion data appeared to be less than those for the 25 °C and the 38 °C data. This difference suggests that the nature of the reaction at 55 °C was different, thus nullifying this approach. This difference is consistent with the complex nature of the Placitas aggregate, wherein in multiple mineral phases contributed to the ASR reaction. Furthermore, the calorimetry data in Chapter 2 for the individual Placitas phases indicated both exothermic and endothermic behavior.

6.4 DEGREE OF THE REACTION

6.4.1 Damage Rating Index

The Damage Rating Index (DRI) measured on companion cylinders showed a measure of consistency across mixes. The relationship between DRI and expansion were generally consistent with the broad damage classes from Sanchez et al. (2018). Therefore, the DRI does provide some measure of the amount of the reaction that has occurred.

The unconfined expansion for the Task 1 mixtures could be generally broken into three regions: negligible/marginal (less than 0.05 % expansion); moderate (0.05 % to 0.15 % expansion); and high/very high (greater than 0.15 % expansion). A drawback of this study was that only one measurement was done below 0.05 % expansion (due to logistical constraints), so this region was not characterized as thoroughly as the other two regions of expansion.

Because the DRI appears to be related to overall expansion, it is not a direct indicator of the degree of the expansion. Observing a DRI value of 500 does not provide a useful indication of whether the reaction has nearly completed, or whether there will be considerably more expansion.

Furthermore, in practical applications one is often interested in characterizing reinforced concrete. Constraints imposed by the requirements of the structural testing of cores from confined regions of the Task 1 Blocks prevented obtaining data relating DRI to confined expansion. Therefore, there was insufficient data form DRI analysis of a core specimen extracted from the confined regions to yield meaningful results.

6.4.2 Automated Neural Net

The inability of the DRI to quantitatively characterize the degree of the reaction prompted the use of a different petrographic method to better characterize the specific indicators of the different phases of the reaction. For the aggregates used in this study, the reaction included a unique path of aggregate dissolution – a damage indicator not included in the DRI analysis. Therefore, it was thought that a more detailed, material-informed approach would yield a more precise result.

One of the main challenges was sampling. The voids created upon aggregate dissolution are less than 1 mm in size. Moreover, only 10 % of the coarse aggregate, which makes up only 40 % of the volume, is reactive. As a result, one must view a large number of sufficiently magnified images to observe a statistically representative sample of aggregate voids. Creating the large number of images manually is not practical, neither would a DRI-like analysis of each image. Therefore, an automated approach was needed for both collecting the images and analyzing the images. Both of these proved far more challenging than expected.

The automated image collection on the scanning electron microscope required that the sample be both flat and parallel. Standard sample preparation techniques are sufficient for achieving a flat surface on a sample. A means of ensuring that the SEM remained in focus across the entire sample during an automated scan was not found. As a result, the surface of the sample had to be planed flat and oriented to remain at the same height, across the entire 50 mm. The resulting sample preparation procedure was time consuming and required specialized polishing equipment. Even then, the success rate was relatively low.

To automate the image analysis, an artificial intelligence approach was used based on convolutional neural nets. Although the void space was relatively easy to identify, it was contextual information that complicated the procedure. Identifying the void type depended on the spatial context – proximity to paste or aggregate. Given the complexity of the aggregate, petrographic expertise was required to classify the training images, and a method was developed to significantly reduce the amount of time required, given the large number of images.

Although the CNN was developed for this particular concrete mixture, the tool is equally applicable to other concrete mixtures. To facilitate broader use across the concrete community, the Web Image Processing Pipeline (WIPP) system was developed from which one can train the CNN for other concrete mixtures: <https://isg.nist.gov/deepzoomweb/data>.

6.4.3 Ultrasonic Pulse Velocity

The ultrasonic pulse velocity (UPV) of unconfined prisms exhibited measurable change with increasing expansion. For these specimens, the UPV values were measured throughout their lifetime, starting shortly after casting. The initial UPV values increased, consistent with hydration filling in pore space, before the onset of ASR degradation. At approximately 100 d, corresponding to approximately 0.04 % expansion, the UPV values began to steadily decrease until they reached a plateau.

This correspondence between decreasing UPV values and increasing expansion suggested a very useful tool in detecting and monitoring expansion damage in concrete. Moreover, the UPV data at 25 °C were less variable, suggesting that at room temperature the UPV might be a reliable, sensitive detection of damage. In existing concretes, for which early-age UPV measurements do not exist, one could incorporate the UPV into an existing monitoring program, and carefully study trends over time. Moreover, the apparent exponential nature of the UPV

change due to damage suggests that its rate of change may also be a measure of the remaining reaction.

UPV measurements on cored specimens from the Task 1 Blocks were interesting in their lack of a changing value. The cores were extracted after a considerable portion of the expansion (damage) had occurred: at one year and at two years of age. For all three mixes cored at one year of age, the UPV was nearly constant for a period of over 100 days subsequent to the coring; similar results were observed for the coring after two years. This result is consistent with unchanging UPV measurements on unconfined prisms at these ages. This suggests that the UPV data on the unconfined prisms were valid representations of the unconfined regions of the Task 1 Block specimens.

Unfortunately, due to logistical constraints, there were no UPV measurements made on cores from confined regions of the Task 1 Blocks. In addition, measurements made on the bulk Block would have interfering effects from the reinforcement. Therefore, one cannot say conclusively whether the UPV changes in the prisms reflect the changes that one would observe in the confined regions of reinforced concrete structures.

6.4.4 Residual Expansion Potential

The residual expansion potential (REP) was measured on the cores taken from the unconfined regions of the Task 1 Blocks at one year and two years of age. In contrast to a relatively constant UPV, there was measurable residual expansion, in both the one year and two year cores.

The combination of UPV and REP measurements on cores may provide a useful tool for qualitatively characterizing the degree of the expansion. The general classification is depicted in Table 6-2 below. If the UPV changes, the reaction may still be in the early stages. If there is measurable REP, but no change in the UPV, the reaction may be active, but in the later stages of the reaction. If there is a no measurable REP (Null result), the reaction has neared completion.

Table 6-2. A qualitative characterization of the degree of the expansion based on combined UPV and REP measurements from a concrete core.

		REP		
		Null	Small	Large
UPV	Change			EARLY
	Constant	END	LATER	

These findings are based on measurements taken on unconfined concrete specimens, including both companion prisms and cores from unconfined concrete.

6.5 RATE OF EXPANSION

Knowing the current rate of expansion would be helpful in establishing the urgency of any actions that might need to be taken. Furthermore, it helps establish a periodicity in the

monitoring to ensure that critical engineering properties are met. Important components to this monitoring are observation, measurement, record keeping, and data analysis.

It would be extremely difficult to estimate the rate of expansion from an observation made at one point in time. One possible alternative would be to identify where on the degree of expansion curve the structure currently lies. Toward this end, the combined UPV and REP measurement approach discussed above, and summarized in Table 6-2, may provide some measure of initial insight. This information may be sufficient to establish a meaningful period before performing subsequent UPV and REP measurements, both to confirm the previous observations and to better refine the understanding of where on the degree of expansion curve the structure lies. Furthermore, for early stage expansion, the rate of change in the UPV is greatest during the earliest stage of expansion. The relative change in UPV upon subsequent monitoring could provide a more refined insight into the degree of the expansion than the coarse description in Table 6-2.

6.6 ULTIMATE EXPANSION

The REP data, although limited, did generally correlate to the remaining expansion expected from each of the three Mixtures. The linear expansion measured on the cores extracted at one year increased from Mix 1 to Mix 3, as would have been expected: 0.05 % (Mix 1), 0.15 % (Mix 2), and 0.25 % (Mix 3).

The coring from the Mix 3 Block conducted at two years of age resulted in a REP of less than 0.1 %, which was considerably lower than the 0.25 % observed at one year. In a comparative sense, the changing value is consistent with the diminished remaining expansion.

6.7 RECOMMENDED TESTING

The recommendation coming from this work is to use multiple measurement types to gauge the degree of the reaction, or to gauge how much more reaction one should expect. By combining DRI, UPV, and REP one can develop a general understanding of the state of the concrete. This includes some measure of the state of the reaction, from which one might infer the rate of the reaction and the ultimate degree of reaction. At the very least, even if the results from combined measurements at one point in time are not definitive, they should be able to provide sufficient engineering guidance for developing a testing plan from which to generate a more complete picture.

In practice, this combined testing could be accomplished on a core taken from an existing structure, using the following procedure outline:

- Extract a core that is at least 25 cm long
- Cut off at least 1 cm from each end of the core, leaving a central core that is at least 20 cm long
- Remaining central core:
 - Note the location of any steel reinforcement in the core
 - Measure the UPV (while avoiding rebar)
 - Immediately wrap in plastic to minimize drying – note the location of any rebar on the wrapping.
 - Perform expansion measurements, with companion UPV measurements
 - Determine REP, and note any changes in UPV
- Two End Pieces:
 - Use progressive water:ethanol solutions to stop the reaction

- Saturate with low-viscosity epoxy
- Polish the cut surface of each piece
- Perform a DRI analysis, combining the damage counts from both pieces
- Compare REP and UPV measurements to Table 6-2
- Corroborate the Table 6-2 assessment with the DRI measurement
- Determine a prudent subsequent monitoring schedule

Chapter 7

REFERENCES

Abadi, M., Agarwal, A., Barham, P., Brevdo, E., Chen, Z., Citro, C., Corrado, G. S., Davis, A., Dean, J., Devin, M., Ghemawat, S., Goodfellow, I., Harp, A., Irving, G., Isard, M., Jozefowicz, R., Jia, Y., Lukasz Kaiser, Manjunath Kudlur, Josh Levenberg, Dan Mané, M. S., Rajat Monga, Sherry Moore, Derek Murray, Chris Olah, J. S., Steiner, B., Sutskever, I., Talwar, K., Tucker, P., Vincent, V., Vasudevan, V., Viégas, F., Vinyals, O., Warden, P., Wattenberg, M., Wicke, M., Yu, Y. and Zheng, X. (2015) TensorFlow: Large-scale machine learning on heterogeneous systems.

ACI Committee 301. (2010). Specifications for structural concrete (ACI 301-10), American Concrete Institute, Farmington Hills, MI, 77 pp.

Amhaz, R., Chambon, S., Idier, J. and Baltazart, V. (2013) Automatic Road Crack Detection by Selection of Minimal Paths. In *GRETSI 2013*, 1–4. Brest, France: <http://gretsi.fr/colloque2013/>. URL: <https://hal.archives-ouvertes.fr/hal-01197285>.

ASTM C136/136M-14. (2014) Standard Test Method for Sieve Analysis of Fine and Coarse Aggregates. ASTM International. West Conshohocken, PA, 5 pp.

ASTM C150-05. (2005). Standard specification for Portland Cement. ASTM International. West Conshohocken PA , 8 pp.

ASTM C1260-14. (2014). Standard test method for potential alkali reactivity of aggregates (mortar-bar method). ASTM International. West Conshohocken PA , 5 pp.

ASTM C1293-08b. (2008). Standard test method for determination of length change of concrete due to alkali-silica reaction. ASTM International. West Conshohocken PA , 7 pp.

ASTM C1608. Standard test method for chemical shrinkage in hydraulic cement past. ASTM International. West Conshohocken, PA.

Badrinarayanan, V., Kendall, A. and Cipolla, R. (2015) SegNet: A Deep Convolutional Encoder-Decoder Architecture for Image Segmentation. *Arxiv - a repository of electronic preprints*, 1–14. URL: <http://arxiv.org/abs/1511.00561>.

Bajcsy, P., Chalfoun, J. and Simon, M. (2018) Web Microanalysis of Big Image Data. Chann, Switzerland: Springer International Publishing AG, 1st edn.

Ben-Haha, M. (2006) Mechanical effects of alkali silica reaction in concrete studied by SEM-image analysis. Ph.d. thesis, Swiss Federal Institute of Technology Lausanne (EPFL), Switzerland. URL: <papers2://publication/uuid/719DF083-68FA-4514-820B-8805645FB1B7>.

- Ben-Haha, M., Gallucci, E., Guidoum, A. and Scrivener, K. L. (2007) Relation of expansion due to alkali silica reaction to the degree of reaction measured by SEM image analysis. *Cement and Concrete Research*, Vol. 37, 1206–1214.
- Bentz, D.P., Lura, P., Roberts, J. (2005) Mix proportioning for internal curing. *Concrete International* Vol. 27, 35-40.
- Cha, Y. J., Choi, W. and Büyüköztürk, O. (2017) Deep Learning-Based Crack Damage Detection Using Convolutional Neural Networks. *Computer-Aided Civil and Infrastructure Engineering*, Vol. 32, 361–378.
- Chambon, S. and Moliard, J. M. (2011) Automatic Road Pavement Assessment with Image Processing: Review and Comparison. *International Journal of Geophysics*. URL: <https://hal.archives-ouvertes.fr/hal-00612165>.
- Choi, W. and Cha, Y.-J. (2019) Sddnet: Real-time crack segmentation. *IEEE Transactions on Industrial Electronics*, (Pre-Print), 1–1.
- Constantiner, D. and Diamond, S. (2003). Alkali release from feldspars into pore solutions. *Cement and Concrete Research*, 33:549-554.
- Cordts, M., Omran, M., Ramos, S., Rehfeld, T., Enzweiler, M., Benenson, R., Franke, U., Roth, S. and Schiele, B. (2016) The cityscapes dataset for semantic urban scene understanding. In *Proc. of the IEEE Conference on Computer Vision and Pattern Recognition (CVPR)*.
- Dent Glasser, L.S. and Kataoka, N. (1981), The chemistry of alkali-aggregate reaction. *Cement and Concrete Research*, Vol. 11, pp. 1-9.
- Deschenes, D.J., Bayrak, O., and Folliard, K.J. (2009). ASR/DEF-Damaged Bent Caps: Shear Tests and Field Implications, Technical Report No. 12-8XXIA006, University of Texas, Austin, TX, 258 pp.
- Diamond, S., Barneyback, R.S., and Struble, L.J. (1981). On the physics and chemistry of alkali-silica reaction, *Proc. 5th Int. Conf. on Alkali-Aggregate Reaction in Concrete (ICAAAR)*, Cape Town, S252/22, pp. 1-11.
- Dice, L.R. (1945). Measures of the Amount of Ecologic Association Between Species. *Ecology*. 26 (3): 297–302. (doi:10.2307/1932409. JSTOR 1932409)
- Divet, L., and R. Randriambololona. (1998). Delayed ettringite formation: the effect of temperature and basicity on the interaction of sulfate and C-S-H phase. *Cem. Concr. Res.* 28(3):357-363.
- Donovan, J. J., Pingitore, N. E. and Westphal, A. (2003) Compositional averaging of backscatter intensities in compounds. *Microscopy and Microanalysis*, Vol. 9, 202–215.
- Dron, R. and Brivot, F. (1992), Thermodynamic and kinetic approach to the alkali-silica reaction. Part 1: Concepts, *Cement and Concrete Research*, Vol. 22, pp. 941-948.
- Dron, R. and Brivot, F. (1993), Thermodynamic and kinetic approach to the alkali-silica reaction. Part 2: Experiment, *Cement and Concrete Research*, Vol. 23, pp. 93-103.

- Feldman, S.B. 2016. Structural Performance of Nuclear Concrete Structures Affected by ASR: Materials Update. RILEM TC I259-ISR Committee Meeting, 'Prognosis of Deterioration and Loss of Serviceability in Structures Affected by ASR. June 6-8, Boulder CO.
- Feldman, S.B. 2018 (Invited, Keynote Address). Quantifying the performance of nuclear power plant concrete structures affected by alkali-silica reaction (ASR). 9th Advances in cement-based materials: Characterization, processing, modeling, and sensing. Amer. Ceramic Soc, Cement Division, June 2018.
- Feldman, S.B. and R. Eason, Jr. 2018. Reactive aggregate mineralogy in the NIST-NRC large-block study of nuclear concrete structures affected by alkali-silica reaction. ASTM Symposium on Advances in cement analysis and concrete petrography. ASTM International, West Conshohocken, PA.
- Ferraris, C.F., Garboczi, E.J., Davis, F.L., and Clifton, J.R. (1997), "Effect of stress relaxation, self-desiccation, and water absorption on alkali-silica reaction in low water cement ratio mortars," *Cement and Concrete Research*, Vol. 27, pp. 1553-1560.
- FHWA. 2013. Alkali-aggregate reactivity (AAR) facts book. US Dept. of Transportation, Federal Highway Administration Rept. No. FHWA-HIF-13-019, 224 pp.
- Goldstein, J., Newbury, D., Michael, J., Ritchie, N., Scott, J. and Joy, D. (2018) *Scanning Electron Microscopy and X-Ray Micro-analysis*. New York: Springer-Verlag New York.
- Greenspan, L. (1977). Humidity fixed points of binary saturated aqueous solutions, *Journal of Research of the National Bureau of Standard*, 81A(1): 89-96.
- Hansen, W.C. (1944), Studies relating to the mechanism by which the alkali-aggregate reaction produces expansion in concrete, *Journal of the American Concrete Institute*, Vol. 15, p. 213-227.
- Helmuth, R., Stark, D., and Diamond, S. (1993), Alkali-Silica Reactivity: An Overview of Research, SHRP-C-342, Strategic Highway Research Program, Washington, D.C., 106 pp.
- Hesamian, M.H., Jia, W., He, X. & Kennedy, P. (2019), Deep learning techniques for medical image segmentation: achievements and challenges. *J Digit Imaging* 32(4), 582–596.
- Hong, S., Kwak, S. and Han, B. (2017) Weakly Supervised Learning with Deep Convolutional Neural Networks for Semantic Segmentation: Understanding Semantic Layout of Images with Minimum Human Supervision. *IEEE Signal Processing Magazine*, Vol. 34, 39–49.
- Hubert, L. and Arabie, P. (1985) Comparing partitions. *Journal of Classification*, **2**, 193–218.
- Ideker, J.J., A.F. Bentivegna, K.J. Folliard, and M.C.G. Juenger. 2012. Do current laboratory test methods accurately predict alkali-silica reactivity? *ACI Materials Journal*. No. 109-M37. Am. Concr. Inst. Farmingham, MI. 109(4): 395-402.
- Kingma, D. P. and Ba, J. L. (2015) Adam: A method for stochastic optimization. *3rd International Conference on Learning Representations, ICLR 2015 - Conference Track Proceedings*, 1–15.

- Kundu, D. (2004) Neural Network Models for Regression and Classification. In *Statistical Computing: Existing Methods and Recent Developments* (eds. D. Kundu and A. Basu), chap. 10.2, 290–293. Alpha Science Int'l Ltd., illustrate edn. URL: <https://books.google.com/books?id=aDykj8m4Bu0C>.
- Latifee, E.R. and P.R. Rangaraju. 2015. Miniature concrete prism test: Rapid test method for evaluating alkali-silica reactivity of aggregates. *J. Mater. Civ. Eng.* 27(7):04014215(1) - 04014215(10).
- Larive, C. (1998). “Apports Combinés de l'Expérimentation et de la Modélisation à la Compréhension de l'Alcali-Réaction et de ses Effets Mécaniques,” (PhD Thesis) ENPC, 28, Laboratoire Central des Ponts et Chaussées, Paris.
- Le Bas, M.J., and A.L. Streckheisen. (1991). The IUGS systematics of igneous rocks. *J. Geol. Soc.* 148(5):825-833.
- Liu, Y., Yao, J., Lu, X., Xie, R. and Li, L. (2019) Deepcrack: A deep hierarchical feature learning architecture for crack segmentation. *Neurocomputing*, Vol. 338, 139–153.
- Majurski, M., Manescu, P., Chalfoun, J., Bajcsy, P., Brady, M. and Drive, B. (2018) Impact of Sampling and Augmentation on Generalization Accuracy of Microscopy Image Segmentation Methods. In *Computer Vision in Microscopy Imaging Workshop at CVPR*, 1. Salt Lake City: IEEE.
- Malhotra, V.M. and Carino, N.J. (2004) *Handbook on Nondestructive Testing of Concrete, 2nd ed.*, ASTM International, CRC Press LLC.
- Merz, C., and A. Leeman. (2013). Assessment of the residual expansion potential of concrete from structures damaged by AAR. *Cem. Concr. Res.* 52: 182-189.
- Morris, W., Moreno, E.I., and Sagüés, A.A. (1996). “Practical evaluation of resistivity of concrete in test cylinders using a Wenner array probe, *Cement and Concrete Research*, Vol. 26, No. 12, 1779-1787.
- MSHA. (2014). Aggregate Bulletin – Test Data. Maryland State Highway Administration, Office of Materials Technology, Soils and Aggregate Technology Division, Hanover, MD. (<https://www.roads.maryland.gov/OMT/AggBlt.pdf>)
- Papandreou, G., Chen, L. C., Murphy, K. P. and Yuille, A. L. (2015) Weakly-and semi-supervised learning of a deep convolutional network for semantic image segmentation. *Proceedings of the IEEE International Conference on Computer Vision*, 2015 Inter, 1742–1750.
- PCA. (2011) Evaluation of alkali-silica reactivity (ASR) mortar bar testing (ASTM C1260 and C1567) at 14 days and 28 days. Portland Cement Association, Skokie, IL. 4 pp.
- Poyet, S. (2009) Experimental investigation of the effect of temperature on the first desorption isotherm of concrete. *Cement and Concrete Research* 39:11, 1052-1059.
- Poyet S., A. Sellier, B. Capra, G. Tjevenin-Foray, J-M. Torrenti, H. Tournier-Cognon, E. Bourdarot. 2006. Influence of water on Alkali-Silica Reaction: experimental study and numerical simulations. *Materials Journal of ASCE* 18:4(588).

Rand, W. M. (1971). Objective criteria for the evaluation of clustering methods, *Journal of the American Statistical Association*, Vol. 66 (336), 846–850. arXiv:1704.01036. doi:10.2307/2284239

Rigden, S.R., Majlesi, Y., and Burley, E. (1995). “Investigation of factors influencing the expansive behavior, compressive strength and modulus of rupture of alkali-silica reactive concrete using laboratory mixes.” *Magazine of Concrete Research*, Vol. 47, No. 170, pp. 11-21.

Rivard, P., B. Fournier, and G. Ballivy. 2002. The Damage Rating Index method for ASR affected concrete—A critical review of Petrographic features of deterioration and evaluation Criteria. *Cem. Concr. Aggregates* 24(2): 1-11.

Ronneberger, O., Fischer, P. and Brox, T. (2015) U-Net: Convolutional Networks for Biomedical Image Segmentation. In *International Conference on Medical image computing and computer-assisted intervention*, 234–241. URL: <http://arxiv.org/abs/1505.04597>.

Sanchez, L.F.M., B. Fournier, M. Jolin, M.A.B. Bedoya, J. Bastien, and J. Duchesne. (2013). Use of Damage Rating Index to Quantify Alkali-Silica Reaction Damage in Concrete: Fine versus Coarse Aggregate. *ACI Materials Journal* 113(4): 395-407.

Sanchez L.F.M., Drimalas T., Fournier B., Mitchell D., Bastien J. (2018) “Comprehensive damage assessment in concrete affected by different internal swelling reaction (ISR) mechanisms,” *Cement and Concrete Research*, Vol. 107, pp. 284-303.

Saouma, V.E., R.A. Martin, M.A. Hariri-Ardebili, and T. Katayama. (2015). A mathematical model for the kinetics of the alkali-silica chemical reaction. *Cement and Concrete Research* 68: 184-195.

Schindelin, J., Arganda-Carreras, I., Frise, E., Kaynig, V., Longair, M., Pietzsch, T., Preibisch, S., Rueden, C., Saalfeld, S., Schmid, B., Tinevez, J.-Y., White, D. J., Hartenstein, V., Eliceiri, K., Tomancak, P. and Cardona, A. (2012) Fiji: an open-source platform for biological-image analysis. *Nature Methods*, Vol. 9, 676–682.

Simonyan, K., and Zisserman, A. (2015). Very deep convolutional networks for large-scale image recognition. *3rd International Conference on Learning Representations, ICLR 2015 - Conference Track Proceedings*. pp. 1–14. San Diego, CA.

Snyder, K.A., X. Feng, B.D. Keen, and T.O. Mason. (2003). Estimating the electrical conductivity of cement paste pore solutions from OH⁻, K⁺, and Na⁺ concentrations, *Cement and Concrete Research*, Vol. 33, 793 – 798.

Snyder, K.A., H.S. Lew. (2013). Alkali-Silica Reaction Degradation of Nuclear Power Plant Concrete Structures: A Scoping Study. National Institute of Standards and Technology, NIST-IR 7937, 36 pp.

Stanton, T.E. 1940. Expansion of concrete through reaction between cement and aggregate. *Proceedings of the American Society of Civil Engineers* 66 (10): 1781–1811.

Tang, B. 1993. Orthogonal Array-Based Latin Hypercubes. *Journal of the American Statistical Association*, Vol. 88 (Issue 424): 1392—1397.

Taylor, H.F.W. (1990), *Cement Chemistry*, Academic Press, New York.

Thomas, M., B. Fournier, K. Folliard, J. Ideker, and M. Shehata. 2006. Test methods for evaluating preventative measures for controlling expansion due to alkali-silica reaction in concrete. *Cement and Concrete Research*, Vol. 36:1842-1856.

Villeneuve, V, B. Fournier, and J. Duchesne. (2012). Determination of the Damage in Concrete Affected by ASR – The Damage Rating Index (DRI). 14th International Conference on Alkali-Aggregate Reaction (ICAAR), Austin TX, May 2012, 100 pp.

Wenner, F. (1916). "A method of measuring earth resistivity," *Bulletin of the Bureau of Standards*, Vol. 12, Issue 4, 469-478. (<http://dx.doi.org/10.6028/bulletin.282>).

Appendix A

MARYLAND STATE HIGHWAY ADMINISTRATION AGGREGATE BULLETIN (2014)

The following pages provide selected excerpts from the Maryland State Highway Administration (SHA) Aggregate Bulletin that was published in 2014. These pages are provided for historical context because the bulletin is updated quarterly. The most recent bulletin can be found on the SHA web site:

<https://www.roads.maryland.gov/OMT/AggBlt.pdf>



Maryland State Highway Administration

Office of Materials Technology

Aggregate Bulletin

Test Data

Maryland State Highway Administration

**Office of Materials Technology
Soils and Aggregate Technology Division
7450 Traffic Drive
Hanover, Maryland 21076**

Updated: July 31, 2014

Aggregate Bulletin

Keys

- (-) Under test/under evaluation
- (#) In accordance with the Standard Provision Insert (SPI) of Standard Specifications for Construction and Materials, July 2008, Table 901 D, Aggregate Physical Property Requirements for Asphalt Mixes (Note (e)): when carbonate rock is used, it shall have a minimum of 25 percent insoluble residue retained on the No. 200 sieve. Otherwise, the aggregate source does not qualify for use as a high friction aggregate.
- DFV Dynamic Friction Value is defined as a coefficient of friction multiplied by 100. Accordingly, coarse aggregate is categorized as three broad categories: high, standard, and low DFVs, designated as HDFV, SDFV, and LDFV. These categories are presented below in detail:
- HDFV:
- Category I (HDFV I): DFV is equal to 55
 - Category II (HDFV II): DFV is equal to 50
 - Category III (HDFV III): DFV is equal to 45.
- SDFV:
- Category IV (SDFV IV): DFV is equal to 35
 - Category V (SDFV V): DFV is equal to 25
- LDFV:
- Category VI (LDFV VI): DFV is less than 25.

Maryland State Highway Administration: Coarse and Fine Aggregate Test Data

Producer	Aggregate Category	Aggregate Type	Specific Gravity (SSD)	ABS (%)	LA (%)	BPN	Friction Rating(1)	ASR (%)	Soundness (%)	Qualified Use		
										General (HMA Base, GAB, Backfill, etc.)	HMA Surface	High Friction Materials
Aggregate Industries, Inc. Accokeek Sand & Gravel Brandywine, MD	Coarse	#57 Concrete Sand	2.692	1.3	34			0.19	3.3	<input checked="" type="checkbox"/>	<input type="checkbox"/>	<input type="checkbox"/>
	Fine	#57 Concrete Sand	2.610	0.9			0.19	0.9		<input type="checkbox"/>	<input type="checkbox"/>	<input checked="" type="checkbox"/>
Aggregate Industries, Inc. Charles City Sand & Gravel Charles City, VA	Coarse	#57 Concrete Sand	2.692	0.82	38			0.44	1.3	<input checked="" type="checkbox"/>	<input type="checkbox"/>	<input type="checkbox"/>
	Fine	#57 Concrete Sand	2.612	0.9			0.25	1.8		<input checked="" type="checkbox"/>	<input type="checkbox"/>	<input checked="" type="checkbox"/>
Aggregate Industries, Inc. Fulks Sand & Gravel Fredericksburg, VA	Coarse	#57 Concrete Sand	2.636	0.32	38			0.08	1.0	<input checked="" type="checkbox"/>	<input type="checkbox"/>	<input type="checkbox"/>
	Fine	#57 Concrete Sand	2.610	0.85			0.09	1.5		<input type="checkbox"/>	<input type="checkbox"/>	<input checked="" type="checkbox"/>
Aggregate Industries, Inc. Hayfield Sand & Gravel Fredericksburg, VA	Coarse	#57 Concrete Sand	2.665	0.6				0.11	1.9	<input checked="" type="checkbox"/>	<input type="checkbox"/>	<input type="checkbox"/>
	Fine	#57 Concrete Sand	2.626	1.4						<input type="checkbox"/>	<input type="checkbox"/>	<input checked="" type="checkbox"/>
Aggregate Industries, Inc. Kenson Sand & Gravel King George, VA	Coarse	#57 Concrete Sand	2.637	0.37	34			0.22	1.5	<input checked="" type="checkbox"/>	<input type="checkbox"/>	<input type="checkbox"/>
	Fine	#57 Concrete Sand	2.617	1.0			0.12	1.6		<input type="checkbox"/>	<input type="checkbox"/>	<input checked="" type="checkbox"/>
Aggregate Industries, Inc. Kirby Road Sand & Gravel Clinton, MD	Coarse	#57 Concrete Sand	2.697	1.0	34			0.02	3.6	<input checked="" type="checkbox"/>	<input type="checkbox"/>	<input type="checkbox"/>
	Fine	#57 Concrete Sand	2.613	0.9			0.02	1.0		<input type="checkbox"/>	<input type="checkbox"/>	<input checked="" type="checkbox"/>

Note [1]: Category I (HDPV I): DfV-55 Category II (HDPV II): DfV-50 Category III (HDPV III): DfV-45 Category IV (SDfV W): DfV-35 Category V (SDfV V): DfV-25 Category VI (IDfV VI): DfV's less than 25. Updated: July 31, 2014

Maryland State Highway Administration: Coarse and Fine Aggregate Test Data

Producer	Aggregate Category	Aggregate Type	Specific Gravity (SSD)	ABS (%)	LA (%)	BPN	Friction Rating[1]	ASR (%)	Soundness (%)	Qualified Use			
										T-94 & 85	T-96	ASTM D3319 & E303	MSMT 215 & 216
Aggregate Industries, Inc. La Plata Sand & Gravel La Plata, MD	Coarse	#57	2.577	1.8	36			0.04	7.1	<input checked="" type="checkbox"/>	<input type="checkbox"/>	<input type="checkbox"/>	<input checked="" type="checkbox"/>
	Fine	Concrete Sand	2.528	0.9			0.04	1.3		<input type="checkbox"/>	<input type="checkbox"/>	<input type="checkbox"/>	<input checked="" type="checkbox"/>
Aggregate Industries, Inc. Mataponi Sand & Gravel Aylett, VA	Fine	Concrete Sand	2.649	0.3			0.06	0.6		<input type="checkbox"/>	<input type="checkbox"/>	<input type="checkbox"/>	<input checked="" type="checkbox"/>
	Coarse	#57	2.869	0.3	17	22	SDPV V	0.02	0.1	<input checked="" type="checkbox"/>	<input checked="" type="checkbox"/>	<input type="checkbox"/>	<input checked="" type="checkbox"/>
Aggregate Industries, Inc. Rockville Crushed Stone Rockville, MD	Fine	#10	2.839	1.4				1.1		<input checked="" type="checkbox"/>	<input type="checkbox"/>	<input type="checkbox"/>	<input checked="" type="checkbox"/>
	Coarse	#57	2.718	0.9	15	32	SDPV IV	0.01	3.4	<input checked="" type="checkbox"/>	<input checked="" type="checkbox"/>	<input type="checkbox"/>	<input checked="" type="checkbox"/>
Aggregate Industries, Inc. Bedrock Quarry Finisstone, MD	Fine	#10	2.662	1.5				0.01	0.6	<input checked="" type="checkbox"/>	<input type="checkbox"/>	<input type="checkbox"/>	<input checked="" type="checkbox"/>
	Coarse	#57	2.704	0.9	21	31	SDPV V	0.19	2.6	<input checked="" type="checkbox"/>	<input checked="" type="checkbox"/>	<input type="checkbox"/>	<input checked="" type="checkbox"/>
Aggregate Industries, Inc. Short Gap Quarry Short Gap, WV	Coarse	#67	2.711	0.6	24	29	SDPV V	0.08	2.0	<input checked="" type="checkbox"/>	<input checked="" type="checkbox"/>	<input type="checkbox"/>	<input checked="" type="checkbox"/>
	Coarse	#57	2.759	0.4	15		SDPV IV	0.13	0.6	<input checked="" type="checkbox"/>	<input checked="" type="checkbox"/>	<input type="checkbox"/>	<input checked="" type="checkbox"/>
Bluegrass Materials Company, LLC Beaver Creek East Quarry - Formerly Lafarge Hagerstown, MD	Coarse	#57	2.659	2.7				0.11	0.9	<input checked="" type="checkbox"/>	<input checked="" type="checkbox"/>	<input type="checkbox"/>	<input checked="" type="checkbox"/>
	Fine	#10	2.659	2.7				0.11	0.9	<input checked="" type="checkbox"/>	<input checked="" type="checkbox"/>	<input type="checkbox"/>	<input checked="" type="checkbox"/>

Note [1]: Category I (HDPV I): DFC-55 Category II (HDPV II): DFC-50 Category III (HDPV III): DFC-45 Category IV (SDPV IV): DFC-35 Category V (SDPV V): DFC-25 Category VI (IDPV VI): DFC's less than 25. Updated: July 31, 2014

Maryland State Highway Administration: Coarse and Fine Aggregate Test Data

Producer	Aggregate Category	Aggregate Type	Specific Gravity (SSD)	ABS (%)	LA (%)	BPN	Friction Rating[1]	ASR (%)	Soundness (%)	General (HMA Base, GAB, Backfill, etc.)	Qualified Use		
											HMA Surface	High Friction Materials	PCC
Bluegrass Materials Company, LLC Churchville Quarry - Formerly Lafarge Bel Air, MD	Coarse	#57	3.020	0.3	22	28	HDFV (-)	.02	1.1	<input checked="" type="checkbox"/>	<input checked="" type="checkbox"/>	<input checked="" type="checkbox"/>	<input checked="" type="checkbox"/>
	Fine	#10	2.989	0.28					3.3	<input checked="" type="checkbox"/>	<input checked="" type="checkbox"/>	<input type="checkbox"/>	<input type="checkbox"/>
Bluegrass Materials Company, LLC Frederick Quarry - Formerly Lafarge Frederick, MD	Coarse	#57	2.716	0.34	22	34	SDPV IV	0.11	0.3	<input checked="" type="checkbox"/>	<input checked="" type="checkbox"/>	<input type="checkbox"/>	<input checked="" type="checkbox"/>
	Fine	#10	2.692	1.07				0.17	3.0	<input checked="" type="checkbox"/>	<input type="checkbox"/>	<input type="checkbox"/>	<input type="checkbox"/>
Bluegrass Materials Company, LLC Marriottsville Quarry - Formerly Lafarge Marriottsville, MD	Coarse	#57	2.723	0.51	43		SDPV V	0.12	1.6	<input checked="" type="checkbox"/>	<input checked="" type="checkbox"/>	<input type="checkbox"/>	<input checked="" type="checkbox"/>
	Coarse	#57	2.901	0.85	28	39	HDFV I	0.03	0.6	<input checked="" type="checkbox"/>	<input checked="" type="checkbox"/>	<input checked="" type="checkbox"/>	<input checked="" type="checkbox"/>
Bluegrass Materials Company, LLC Medford Quarry - Formerly Lafarge New Windsor, MD	Coarse	#67 Medford Basalt	2.700	0.5	48	24	SDPV V	0.03	1.3	<input checked="" type="checkbox"/>	<input checked="" type="checkbox"/>	<input type="checkbox"/>	<input checked="" type="checkbox"/>
	Fine	#10 Medford Limestone	2.700	0.24					4.1	<input checked="" type="checkbox"/>	<input type="checkbox"/>	<input type="checkbox"/>	<input type="checkbox"/>
Bluegrass Materials Company, LLC Texas Quarry - Formerly Lafarge Cockeysville, MD	Coarse	#57 Concrete Sand	2.818	0.4	41	26	SDPV V	0.04	2.4	<input checked="" type="checkbox"/>	<input checked="" type="checkbox"/>	<input type="checkbox"/>	<input checked="" type="checkbox"/>
	Fine	#10 Concrete Sand	2.827	0.7				0.03	7.3	<input checked="" type="checkbox"/>	<input type="checkbox"/>	<input type="checkbox"/>	<input checked="" type="checkbox"/>
Bluegrass Materials Company, LLC Yall Quarry Yall, Greece	Coarse	#57	2.818	0.4	41	26	SDPV V	0.04	2.4	<input checked="" type="checkbox"/>	<input checked="" type="checkbox"/>	<input type="checkbox"/>	<input checked="" type="checkbox"/>
	Fine	#10	1.583	13.48					2.2	<input checked="" type="checkbox"/>	<input checked="" type="checkbox"/>	<input type="checkbox"/>	<input type="checkbox"/>

Note [1]: Category I (HDFV I): DFV-55 Category II (HDFV II): DFV-50 Category III (HDFV III): DFV-45 Category IV (SDPV IV): DFV-35 Category V (SDPV V): DFV-25 Category VI (IDPV VI): DFV's less than 25. Updated: July 31, 2014




Maryland State Highway Administration: Coarse and Fine Aggregate Test Data

Producer	Aggregate Category	Aggregate Type	Specific Gravity (SSD)	ABS (%)	LA (%)	BPN	Friction Rating(1)	ASR (%)	Soundness (%)	General (HMA Base, GAB, Backfill, etc.)	Qualified Use		
											ASTM D3319 & E303	MSMT 215 & 216	ASTM C1260
Chaney Enterprises, Inc. Riddle Pit Hamwood, MD	Coarse	#57	2.644	0.5	43				0.1	<input checked="" type="checkbox"/>	<input type="checkbox"/>	<input type="checkbox"/>	<input checked="" type="checkbox"/>
	Fine	Concrete Sand	2.637	0.5			0.12	0.12	2.2	<input type="checkbox"/>	<input type="checkbox"/>	<input type="checkbox"/>	<input checked="" type="checkbox"/>
Chaney Enterprises, Inc. Southern Materials Plant Great Mills, MD	Coarse	#67	2.579	1.1	35			0.04	2.4	<input checked="" type="checkbox"/>	<input type="checkbox"/>	<input type="checkbox"/>	<input checked="" type="checkbox"/>
	Fine	Concrete Sand	2.569	0.60			0.10	0.10	2.1	<input type="checkbox"/>	<input type="checkbox"/>	<input type="checkbox"/>	<input checked="" type="checkbox"/>
Chaney Enterprises, Inc. Vienna Sand & Gravel Rhoadesdale, MD	Fine	Concrete Sand	2.631	0.7				0.16	1.1	<input type="checkbox"/>	<input type="checkbox"/>	<input type="checkbox"/>	<input checked="" type="checkbox"/>
	Coarse	#67	2.577	1.3	35			0.20	6.6	<input checked="" type="checkbox"/>	<input type="checkbox"/>	<input type="checkbox"/>	<input checked="" type="checkbox"/>
Chaney Enterprises, Inc. Shore Sand & Gravel Bridge town Facility Henderson, MD	Fine	Concrete Sand	2.609	1.0				0.13	2.7	<input type="checkbox"/>	<input type="checkbox"/>	<input type="checkbox"/>	<input checked="" type="checkbox"/>
	Coarse	#57	2.479	3.6	36			0.12	1.5	<input checked="" type="checkbox"/>	<input type="checkbox"/>	<input type="checkbox"/>	<input checked="" type="checkbox"/>
County Line Quarry, Inc. County Line Quarry Wrightsville, PA	Fine	Concrete Sand	2.604	1.2				0.12	1.4	<input checked="" type="checkbox"/>	<input type="checkbox"/>	<input type="checkbox"/>	<input checked="" type="checkbox"/>
	Coarse	#57	2.767	0.3	26	42	HDPV I	0.09	0.8	<input checked="" type="checkbox"/>	<input checked="" type="checkbox"/>	<input checked="" type="checkbox"/>	<input checked="" type="checkbox"/>
David A. Bramble, Inc. Bridge town Sand & Gravel Ridgely, MD	Fine	#10	2.568	1.81					1.2	<input checked="" type="checkbox"/>	<input type="checkbox"/>	<input type="checkbox"/>	<input type="checkbox"/>

Note [1]: Category I (HDPV I): DfV-55 Category II (HDPV II): DfV-50 Category III (HDPV III): DfV-45 Category IV (SDfV W): DfV-35 Category V (SDfV V): DfV-25 Category VI (IDfV VI): DfV's less than 25. Updated: July 31, 2014

Appendix B CEMENT MILL SHEET

This publication is available free of charge: <https://doi.org/10.6028/NIST.JR.8415>

		Material: Portland Cement Type: I-II (MH)	Material Certification Report Test Period: 01-Feb-2017 to 28-Feb-2017 Date Issued: 09-Mar-2017		
Certification This cement meets the specifications of ASTM C150 and AASHTO M85 for Type I-II (MH) cement.					
General Information					
Supplier: Holcim (US) Inc Address: 1260 Security Road Hagerstown, MD 21742 Contact: AnnaLisa Homan / (240) 452-4908	Source Location: Hagerstown Plant 1260 Security Road Hagerstown, MD 21742 Contact:				
The following is based on average test data during the test period. The data is typical of cement shipped by Holcim; individual shipments may vary.					
Test Data on ASTM Standard Requirements					
Chemical			Physical		
Item	Limit ¹	Result	Item	Limit ¹	Result
SiO ₂ (%)	-	19.3	Air Content (%)	12 max	7
Al ₂ O ₃ (%)	6.0 max	4.1	Blaine Fineness (m ² /kg)	260-430	405
Fe ₂ O ₃ (%)	6.0 max	2.8	Autoclave Expansion (%) (C151)	0.80 max	0.02
CaO (%)	-	61.4	Compressive Strength MPa (psi)		
MgO (%)	6.0 max	4.2	1 day	-	19.1 (2770)
SO ₂ *	3.0 max	3.5	3 day	10.0 (1450) min	28.9 (4190)
Loss on Ignition (%) *	3.5 max	2.3	7 day	17.0 (2470) min	34.5 (5000)
Insoluble Residue (%)	1.50 max	0.30	28 day	-	41.2 (5980)
CO ₂ (%)	-	1.2	Initial Vicat (minutes)	45-375	119
CaCO ₃ in Limestone (%)	70 min	77			
Potential Phase Compositions ² :					
C ₂ S (%)	-	60			
C ₃ S (%)	-	9			
C ₄ A (%)	8 max	6			
C ₃ A (%)	-	9			
C ₂ S + 4.75C ₃ A (%)	100 max	88			
Test Data on ASTM Optional Requirements					
Chemical			Physical		
Item	Limit ¹	Result	Item	Limit ¹	Result
Equivalent Alkalies	-	0.89	False Set (%)	50 min	76
			Mortar Bar Expansion (%) (C1038)	-	0.007
Notes (*1-9)					
1 - Dashes in the Limit / Result columns mean Not Applicable. 2 - It is permissible to exceed the specification limit provided that ASTM Mortar Bar Expansion does not exceed 0.020% at 14 days. 3 - Adjusted per Annex A1.6 of ASTM C150 and AASHTO M85. 5 - Limit = 3.0 when limestone is not an ingredient in the final cement product For Moderate Alkali					
Additional Data					
Item	Limestone	Inorganic Processing Addition	Base Cement Phase Composition	Result	
Amount (%)	3.4	-	C ₂ S (%)	62	
SiO ₂ (%)	13.0	-	C ₃ S (%)	9	
Al ₂ O ₃ (%)	3.1	-	C ₄ A (%)	6	
Fe ₂ O ₃ (%)	1.2	-	C ₃ A (%)	9	
CaO (%)	42.7	-			
SO ₂ (%)	1.3	-			
Printed: 3/9/2017 12:10:19 PM Version: 160627					
				 AnnaLisa Homan, Quality Manager	